Experimental Investigation of the Aerodynamics and Acoustics of Exit Guide Vanes for Future Aircraft Engines

Thorsten Selic

Doctoral Thesis

at the

Institute for Thermal Turbomachinery
and
Machine Dynamics

First Expert:

Prof. Dr.-Ing. Franz Heitmeir

Second Expert:

Prof. Dr.techn. Reinhard Willinger

"It never gets any easier, you just go faster."

Greg LeMond

STATUTORY DECLARATION

I declare that I have authored this thesis independently, that I have not used other than the declared sources / resources, and that I have explicitly marked all material which has been quoted either literally or by content from the used sources.

....

(date) (signature)

EIDESSTATTLICHE ERKLÄRUNG

Ich erkläre an Eides statt, dass ich die vorliegende Arbeit selbstständig verfasst, andere als die angegebenen Quellen/Hilfsmittel nicht benutzt, und die den benutzten Quellen wörtlich und inhaltlich entnommenen Stellen als solche kenntlich gemacht habe.

Graz, am ....

(Unterschrift)

ABSTRACT

This thesis deals with the aerodynamic and acoustic investigation of different designs of turbine exit guide vanes (EGV) in the low pressure test turbine rig (STTF) at the Institute for Thermal Turbomachinery and Machine Dynamics (ITTM) at Graz University of Technology. The facility is a continuously operating cold-flow open-circuit facility driven by pressurised air. The flow path consists of a single stage low pressure turbine followed by the EGV to be investigated.

This thesis investigates four different exit guide vane designs at two different operating points. The four different EGVs were designed in order to understand and evaluate different effects leading to an improvement in acoustic and aerodynamic performance of the EGV itself and the engine as a whole.

The "Datum" EGV is derived from current state-of-the-art designs and serves as the status quo in terms of fluid flow and acoustic performance. The "Leaned" EGV is derived from the "Datum" EGV and incorporates a 20° lean in order to reduce the sound power level of the EGV. The "Inverse Cut-off" EGV is designed to prohibit the propagation of certain airfoil interactions at a distinct frequency with the goal of reducing the sound power level downstream of the test rig. The "High loading" EGV was optimised airfoil was designed applying a multi-point optimisation process to the 33% span profile section of the "Datum" EGV.

Two operating points were investigated. They were selected according to two different objectives: aerodynamic performance and acoustic performance. In terms of aerodynamic performance the operating point ADP is selected which is representative of the flow properties at cruise conditions and for the acoustic performance the operating point "Approach" was selected which is typical of the flow conditions during the landing phase of the aircraft.

The aerodynamic investigations were mainly performed using 5-hole probes in multiple planes up- and downstream of the EGV in order to evaluate its performance. The evaluation of these measurements have shown that the EGVs investigated have the possibility to reduce the total pressure loss of the EGV by up to 20% for the ADP and more than 40% for the operating point "Approach" for a given length of the flow path.

The acoustic investigations, using a 360° rotatable microphone array downstream of the EGV have shown the possibility to reduce the sound power level (PWL) downstream of the EGV by up to 3.3dB for the ADP and, more importantly, by approximately 5.9dB for the operating point "Approach" which is a significant reduction in noise emitted by the turbine during the landing phase. This was achieved by either inhibiting certain interaction modes between the rotor and the EGV from propagating downstream of the vane or by reducing the interaction between the EGV leading edge and the wakes of the upstream rotor.

In addition to this, the EGV designs studied have shown that it is possible to reduce the chord length of the EGV by more than 60% compared to current designs in addition to the aerodynamic and acoustic advantages shown. This results in a decrease in both weight of the EGV as well as axial length of the turbine exit casing allowing for a reduction in the weight of the components surrounding the particular component of the engine.

ACKNOWLEDGEMENT

This work would not have been possible without the help of my colleagues and the members of the Institute of Thermal Turbomachinery and Machine Dynamics. And while the list of people who supported me and helped me keep my sanity during the last years is too long, the people who had a direct impact on this work deserve a special thank you.

First of all I would like to thank Prof. Franz Heitmeir for the supervision and support of this word. A very special thank you to Dr. Andreas Marn who supported my work for almost five years of as was involved in all topics surrounding this thesis.

Furthermore i'd like to thank Dr. Peter Pirker, who relentlessly and without hesitation operated the compressor facility for more than 100 test runs performed over the last two years of this thesis as well as Florian Schönleitner, who's help on performing rig maeasurements was invaluable during the last years.

I would also like to thank Martin Haubenhofer and Forian Plank, members of the workshop at the Institute for hours of work assembling the test rig during the early years of this work. A very special thank you is deserved by Bianca Puntigam and Carina Kunter, secretaries at the Institute for all their organisational help and involvement.

Finally i want to thank my parents and who always supported me through all of my studies leading up to this thesis.

NOMENCLATURE

Abbreviations

ADP	Aero Design Point	AR	Aspect Ratio
BPF	Blade Passing Frequency	BPR	Bypass Ratio
CAD	Computer Aided Design	CDA	Controlled Diffusion Airfoil
CDA	Controlled Diffusion	CFD	Computational Fluid Dynamics
CS	Compressor Station	DB	Decibel
DREAM	Validation Of Radical Engine Architecture Systems	EGV	Exit Guide Vane
GTF	Geared Turbofan	HFTF	Hot Flow Test Facility
HP	High Pressure	HPC	High Pressure Compressor
IGV	Inlet Guide Vane	ITTM	Institute For Thermal Turbomachinery and Machine Dynamics
LDV	Laser Doppler Velocimetry	LE	Leading Edge
LE	Leading Edge	LEAP	Leading Edge Aviaton Propulsion
LP	Low Pressure	LPT	Low Pressure Turbine
LSQR	Least Mean Square Fit	MTF	Mid Turbine Frame
NACA	National Advisory Committee For Aeronautics	NOX	Nitrogen Oxides
OGV	Outlet Guide Vane	SFC	Specific Fuel Consumption
SPL	Sound Pressure Level	STTF	Subsonic Test Turbine Facility
TE	Trailing Edge	TEC	Turbine Exit Casing
TMTF	Turning Mid Turbine Frame	TSWT	Transonic Cascade
TTTF	Transonic Test Turbine Facility	ACARE	Advisory Council For Aeronautical Research In Europe
EPNDB	Effective Perceived Noise In Decibel	HPT	High Pressure Turbine
ICAO	International Civil Aviation Organisation	MTF	Mid Turbine Frame
PWL	Sound Power Level	RMS	Root Mean Square

Symbols

A_{mn}	amplitudes of sound propagation	ρ	density
Δ	Laplace operator	Υ	numerical constant
$<p(t)>$	periodic components	p'	pressure fluctuations
R	real part of a complex number or function	p'	stochastic fluctuation
ω	angular frequency	Ar	Aspect Ratio
$\bar{p}$	averaged value	c_{ax}	axial velocity
σ_{mn}	Bessel coefficients	J_m	Bessel function
x,y,z	Cartesian coordinates	m	circumferential mode
u	circumferential velocity	s	entropy
e	Eulers number	f	frequency
R	gas constant	F,G,H	Generic functions with the property of owning a second derivative
n	harmonic of the blade passing frequency	h	harmonic of the blade passing frequency
κ	heat capacity ratio	k	integer value
δ_{ijk}	Kronecker delta	$\dot{m}$	mass flow
Y_m	Neumann function	B	number of Blades
N_θ	number of circumferential measurement positions	n_{period}	number of samples in the original signal
n_a	number of samples in the original signal	nn	number of samples per revolution
V	number of vanes	α	numerical constant
β	numerical constant	A,B,C	numerical constant
∂	partial derivative	v	particle velocity
φ_0	phase angle	Υ	Pitch angle
p	pressure	r	Radius
R	radius	Re	Reynolds number
n	rotational speed	Ω	rotational speed
RPM	rotations per minute	f_S	sampling frequency
f_{mn}	shape factor	c	speed of sound

i	Sqrt(-1)	D	substantial derivative
T	Temperature	t	time
p_t	total pressure	T_t	total temperature
k	turbulent kinetic energy	ε	turbulet onther thingy
u,v,w	Velocity components	U	Velocity vector
λ	wave length	k	wave number
α	Yaw angle	r,θ,x	Cylindrical coordinates
Ma	Mach number	ω	turbulent something

TABLE OF CONTENT

1 INTRODUCTION

The Advisory Council for Aeronautical Research in Europe (ACARE) defined in their Strategic Research Agenda (ACARAE 2020) that until 2020 the emissions of the whole airplane have to be significantly reduced: CO_2 emissions by 50% and nitrogen oxides (NOx) by 80% in particular. In addition the perceived noise level has to be decreased by 20 EPNdB (effective perceived noise level).

Due to the long history of constant improvements made to modern turbofan engines, the thermodynamic efficiency is at a very high level and the potential of making large improvements without changing the core design is limited. Higher propulsion efficiency can be achieved by e.g. increasing the bypass ratio (BPR) of the engine. Yet this is limited by the maximum velocity at the tip of the fan which means that an increase in fan diameter must lead to a decrease in rotational speed. This is unwanted due to the fact that the fan is linked to the low pressure turbine where a low rotational speed is counter productive. One possible solution for this is a gearbox that is located between the shaft of the low pressure turbine/compressor and the fan as it is used in the Pratt & Whitney PW1000G Series (Figure 1-1 and Figure 1-3, taken from [1]). This allows a decoupling of the rotational speed of the fan and the other components allowing for a lower rotation speed of the fan and a higher speed of LP. Other possible optimisations include improved materials as well as other technologies to improve the aero engine without such a drastic change in engine architecture. One such example is the CFM International LEAP ("Leading Edge Aviation Propulsion", Figure 1-2), a joint venture of GE Aviation and Snecma. This engine involves multiple improvements on each component without a change in the engine architecture offering similar changes in SFC and comparable reduction of noise emission as the GTF-concept.

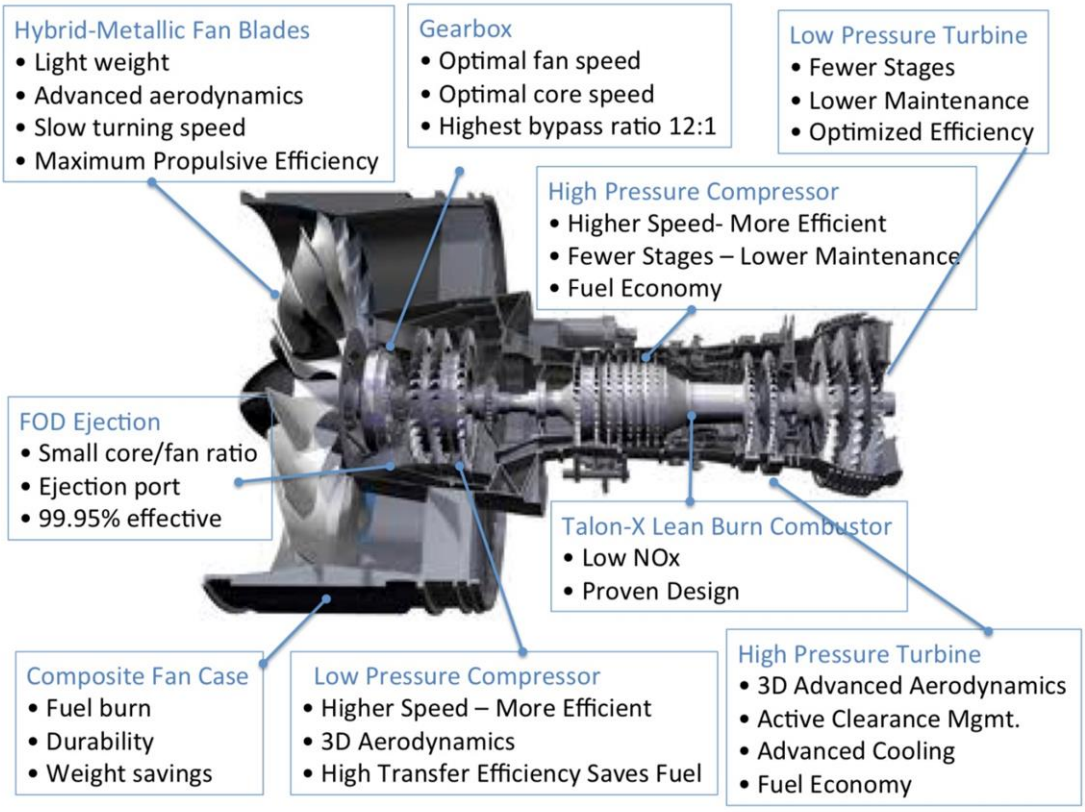

Figure 1-1: Pratt & Whitney PW1000G Series (taken from [1])

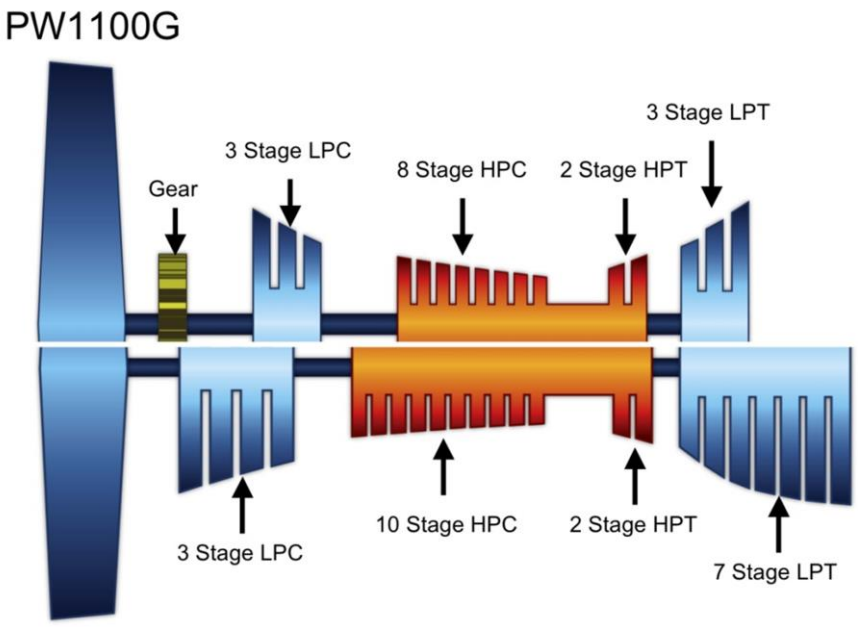

Figure 1-3: Pratt & Whitney PW1000G Series: Effect of the Gear box on stage [1]

Another possible concept that might further decrease the SFC is the so called "Open-rotor". These concepts have already been investigated during the 1980's due to their large potential in reducing specific fuel consumption, but have not been the focus on engine manufactures in the recent years (Figure 1-4). The drawback of these concepts is that they are prone to higher noise levels compared to "closed-rotor" engines and might cause interactions with the fuselage of the plane might lead to unwanted vibrations if not taken into account. These open rotor concepts have recently been investigated in the European framework 7 project DREAM (valiDation of Radical Engine Architecture systeMs) whose main objectives were mainly a reduction of CO2, NOx as well as noise by both novel engine concepts as well as improved component performance.

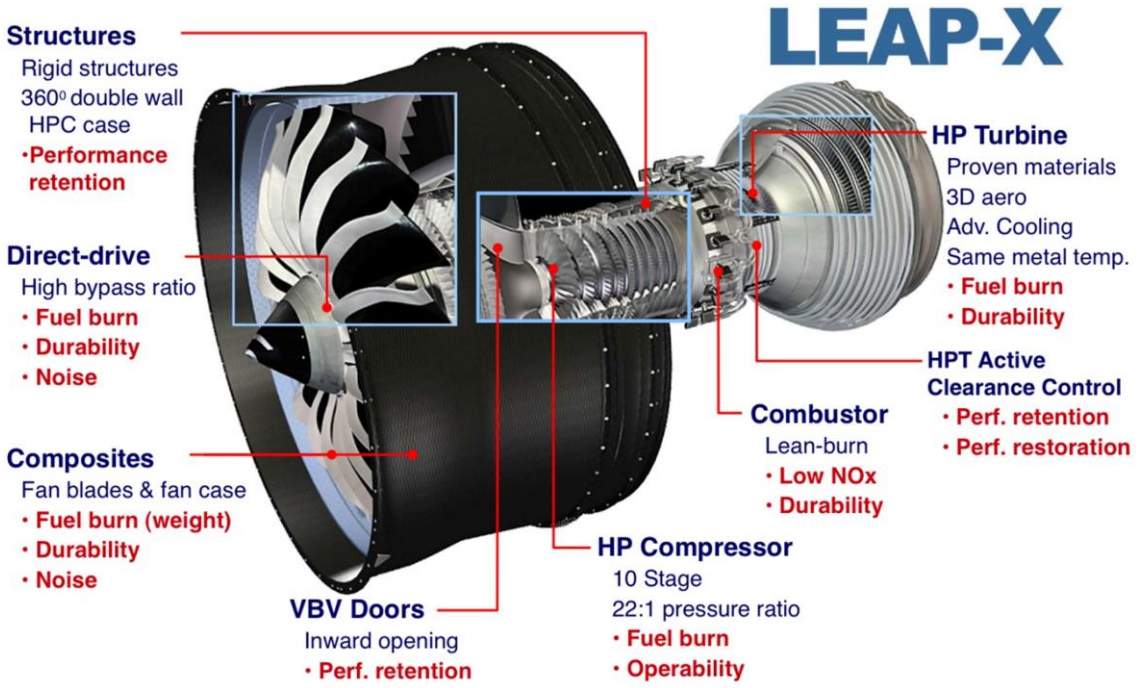

Figure 1-2: CFM International LEAP-X[91]

Figure 1-4: Open rotor concept [92]

One work package within the SP4, namely SP4.3 "Novell Structure for mid Frame" deals with a component that is crucial for the ideas within this thesis. This work package deals with a structure called the midturbine frame (MTF) that is located in the duct between the high pressure turbine (HPT) and the low pressure turbine (LPT). Increasing the bypass ratio requires these ducts to span a wider difference in radius between the HPT and the LPT (given the fact the rational speed of the fan and LPT is identical) leading to the necessity of more aggressive ducts due to the weight of this structure and the whole components surrounding this part (see Marn[2]). These issues were already part of research programs such as e.g. AIDA (Aggressive Intermediate Duct Aerodynamics for Competitive and Environmentally Friendly Jet Engines). These ducts can either be clean or equipped with struts. In the case of the strutted duct, the structures are carefully optimised in order to create a minimum of pressure loss and to provide the following LPT with ideal inlet conditions. In addition, these rigid structures provide the opportunity to also grant an access for oil and cooling air supply. In addition this gives the freedom to shift the position of the engine mount as suggested by Seda [3].

Incorporating these two functions (radial access and engine mounting) into the mid turbine frame has large effects onto the downstream components, namely the LPT as well as the turbine exit casing (TEC). The turbine exit casing usually consists of a large outlet guide vane (OGV or exit guide vane EGV) that also functions as engine mount as seen in Figure 1-5.

Figure 1-6 shows a concept where the engine mount is located right above the mid turbine frame (marked with TMTF for turning mid turbine frame) with a modified position of the LP-shaft bearing. This change in the architecture of the turbine mid frame allows changes to the downstream parts, namely the LPT casing and the EGV itself as already explained. The rigidness of the EGV casing can be severely reduced due to the change in structural requirements in connection with the engine mount. The formerly large and rigid structural component is completely stripped of this function and is now only a device used for aerodynamical and acoustical purposes, but not a structural component. This can be seen when comparing the size and design of the EGV/TEC in Figure 1-5 and Figure 1-6. In Figure 1-5 (taken from [4]) the EGV can be seen as a rigid low aspect ratio (AR) structure with the attached engine mount and the LP-bearing centred on the shaft,

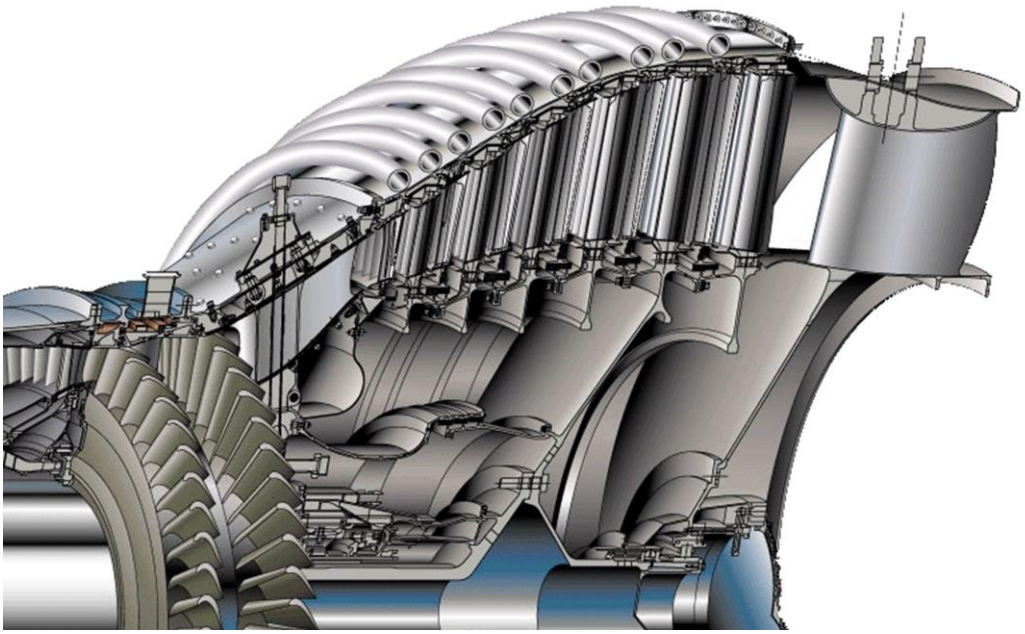

Figure 1-5: Engine Alliance GP7000, turbine section with EGV [4]

whereas in Figure 1-6 the EGV is a comparatively small component that is attached to the LP turbine with a high aspect ratio similar to the upstream turbine components.

Yet this component is different than the upstream components present in the turbine due to the main aerodynamical purpose of the vane: to remove swirl from the LPT exit flow and to increase the static outlet pressure. This is necessary due to the fact that the increased loading of the LPT increases the flow angle downstream of the last blade row. The vane is therefore a compressor vane and needs to be treated as such. The designer now has the opportunity to re-evaluate and optimise the vane without considering the structural needs and restrictions that went into designing this component beforehand.

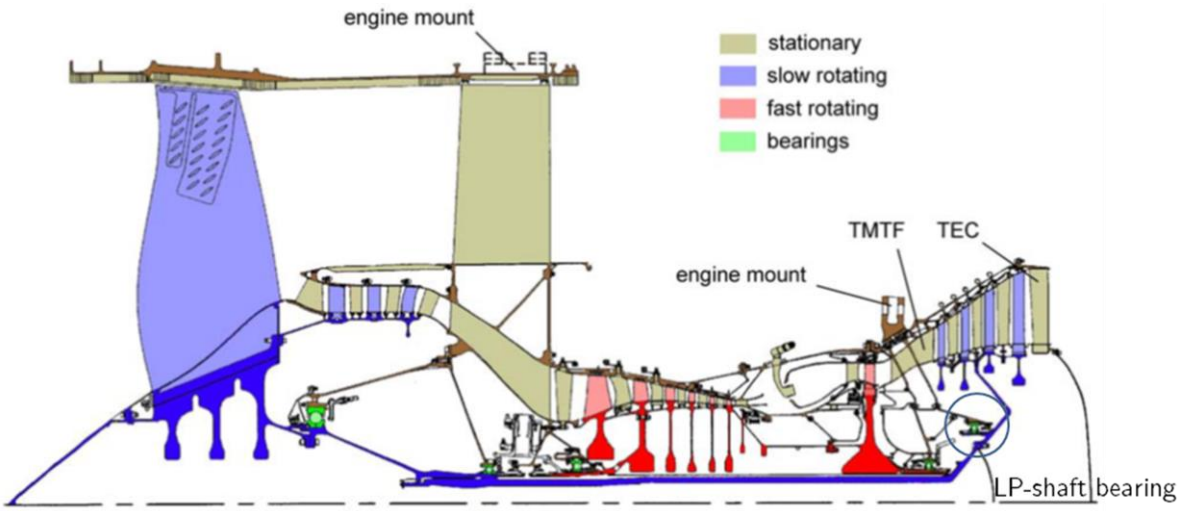

Figure 1-6: High bypass ratio turbofan engine with overhung LPT, miniaturized TEC and TMTF (taken from [3])

1.1 Scope of this thesis

The objective of this thesis is the comparison and evaluation of multiple different EGV configurations for modern aero-engines. Experiments are performed at the subsonic low pressure test turbine facility (STTF) at the Institute for Thermal Turbomachinery and Machine Dynamics.

The goal of this comparison is to show aerodynamical effects occurring within the different EGV setups as well as the quantification of the losses occurring within the EGV passage. In addition to the aerodynamical properties of the EGV the acoustical field downstream of the vane-row is to be evaluated and compared. These acoustical properties are especially important during operational states such as take-off and landing (approach).

In order to be able to perform an aerodynamic comparison the flow conditions upstream of the EGV, coming from the rotor, as well as the flow properties downstream of the vane row have to be characterized and quantified. This will mainly be performed using 5-hole probes as well as total pressure probes. The flow within the vane passage will be evaluated using static pressure tabs on both suction and pressure side of the vane as well as oil-flow visualization.

The acoustical properties are strongly influenced by the flow field of the rig and will be evaluated using 24 flush mounted microphones downstream of the EGV. These microphones are rotatable by 360° in order to measure the full acoustic field that is necessary to evaluate the azimuthal and radial modes present in the acoustic pattern of the EGV. Together with the aerodynamical data these enables the designer a holistic approach to evaluating the performance of the EGV for both its aerodynamical and acoustical performance.

The measurements performed within the test rig provide a data base for the evaluation of the numerical codes used for the aerodynamic and acoustic design of the EGVs.

2 Fundamentals

Before introducing the test facility and discussing the measurements carried out in the test facility, a short overview of the fundamentals of the components involved and the flow through the EGV is given. Since in these tests, an unshrouded LP turbine is positioned upstream of the EGV, a short introduction to LPT and tip leakage flows is required. In addition the basics of compressor flows will be explained due to the fact that the EGV is a compressor blading as explained in the first chapter. At last the acoustic flow field in its basics is described.

2.1 EGV State of the art

There are multiple different EGVs present in an aero engine:

- Downstream of the fan
- Downstream of the high-pressure compressor (HPC)
- Downstream of the low-pressure compressor
- Downstream of the low-pressure turbine

These components share the same responsibility: remove the swirl from the flow and create a uniform exit flow for the downstream components (e.g. the combustor in case of the HPC EGV). The fan and LPT EGV also have a special function when it comes to acoustics since the flow is leaving the engine and special focus has been put on the acoustic field downstream of the vane.

Literature on compressor OGVs can be found in e.g. Stevens and Young [5] or Carrotte et al. [6], where the OGV downstream of a single compressor stage has been investigated. More recently, e.g. Key et al. [7] performed investigations of two different OGV for a compressor. The Design B featured a positive lean to impose a radial shift to the streamlines. In addition, the OGV has been located partway within the downstream diffuser resulting in an increase in radius of both hub and casing leading to a design with both, higher total pressure ratio and efficiency of the whole compressor as well as a shorter duct length.

For fan OGVs the acoustic effect is especially important. Lakshminirayana [8] correlated the sound spectra of a guide vane with aerodynamic measurements, indicating that secondary flow contributes significantly to noise, whereas Posson [9] provided an analytical model for broadband noise accounting for acoustic shielding. In addition manufacturing is an important aspect of fan OGVs as can be seen in e.g. Blecherman et al. [10] who investigated the possibility of manufacturing durable low cost fan EGVs made of a lightweight composite material, providing relevant data for manufacturing and inspection standards of such components.

The literature on EGVs specifically for the application downstream of low pressure turbine is limited. The available open literature dealing specifically with the turbine EGV is shown in the following sections.

2.1.1 Aerodynamics

Sonoda et al. [11] compares two different turbine EGV designs, one traditional controlled diffusion airfoil (CDA) and a second optimised design with extreme frontloading with a peak Mach number at the leading edge. They argued, that if the aerodynamic performance of the EGV at an increased

inlet Mach number of Ma_1=0.7 would be similar to those at Ma_1=0.6, this would correspond to an increase of about 1% for the LP-turbine which would greatly benefit the performance of the engine. Sonoda et al. were able to show, that the CDA profile was more sensitive to free stream turbulence, especially at low Reynolds conditions. The advantage for the optimise profile even held true for high supercritical inlet Mach numbers (Ma_1=0.7) with a suction side peak of Ma=1.25-1.3. The advantage was even more pronounced for off-design incidence angles.

Schreiber et al. [12] and Sonoda et al.[13] performed an optimisation on an OGV airfoil for a single stage LPT for a small turbofan engine. They used different evolutionary strategies to optimise this airfoil and compare it to the baseline controlled-diffusion airfoil (CDA). They were able to reduce total pressure losses at design incidence as well as increase the low loss incidence range. This was done by front loading the profile to achieve a reduced adverse pressure gradient along the suction side in combination with trying a modification of the leading edge to reduce separation. For Reynolds numbers below $2 \cdot 10^5$ it seems to be advantageous to design the airfoil with a steep adverse pressure gradient to promote a fast transition to prevent separation and the risk of bubble burst. They showed that this approach shows advantages compared to a CDA even for higher turbulence levels [13]. The low Reynolds number design of the OGV for Ma_1=0.6 was very critical, because high flow turning and strong diffusion was required at two-dimensional flow conditions because hub and casing contours were nearly parallel and no streamline contraction was present.

In a second step, Sonoda et al. [13] showed an alternative OGV with a unique airfoil Mach number distribution. Their numerical optimisation for the very low Reynolds number conditions resulted in a front loaded cascade having the velocity peak just at the leading edge. The optimisation confirmed the design concept in which "aerodynamic loading should be imposed in a region where the boundary layer is very thin and healthy" and where early boundary layer transition is enforced to prevent too large laminar separation bubbles as seen in Rhoden [14]. Experimental and numerical analysis confirmed the low losses in the entire relevant Reynolds number range [15],

Hjärne et al.[16]–[18] performed experimental and numerical investigations on a highly loaded low pressure turbine outlet guide vane. The authors show the secondary flow and loss development downstream of the OGV for several incidences and turbulence intensities, comparing the flow development as well as averaged loss profiles for different operating points. Hjärne [17] evaluates different turbulence models in terms of mid-span pressure distribution, downstream wake distribution, losses and the outlet flow angles and compares it with the results from [16]. The results shown suggest to use either a $k-\omega$ or $k-\varepsilon$ turbulence model with resolved boundary layers. Hjärne [18] focuses on numerically capturing the secondary flow field presented in [16], suggesting a Reynolds-stress turbulence model is best suited to properly predict the secondary flow evolution of the OGV.

Koch et al. [19] presented numerical and experimental investigations of an optimised profile for a turbine EGV and a comparison with a reference design. The investigations were conducted at low Reynolds numbers ($1.5 \cdot 10^5$) which are typical for turbine EGVs at cruise condition. The experiments show a significant loss reduction for the optimised airfoil over the whole operating range. In addition, the pressure rise of the EGV could be increased, which is due to the reduced wetted surface. This publication is related to the highly loaded EGV presented later in this thesis.

2.1.2 Acoustics

While there is a lot of research on all fields of aero engine acoustics there is only very few publications can be found in the open literature dealing specifically with turbine EGV acoustics. The following shows openly available publications that specifically deal with this topic of turbine exit guide vanes.

Broszat et al. [20] compared the numerical results of two different approaches predicting the sound power level downstream of a 1,5 stage test turbine with EGV with experimental results. The test rig used for the measurements in this publication is the same that is used for this thesis. Three different operating points were discussed in the paper. A linearized Euler approach showed very good agreement for the first BPF, but larger deviations for the second BPF, where an interaction mode is not able to propagate. The semi-empirical model used shows larger deviations compared to the experimental results.

Moser et al. [21] presented numerical investigation in the same LPT test rig as Broszat et al. [20]. Moser et al. discussed the flow field within the acoustic measurement section and showed the modal decomposition for the operating point cutback.

Broszat et al. [22] presents the design and validation of an acoustically optimised EGV. The optimisation of a datum EGV presented in the paper results in a new EGV design with a 20° lean of the EGV. The negative lean means that the EGV is inclined against the rotational direction of the rotor. The numerical design and experimental investigations are compared for multiple operating points. The optimisation results in a reduction of sound power level of up to 3 dB depending on the operating point. The predicted numerical and measured experimental PWLs show a very good agreement.

Broszat et al.[23] presented the application of an acoustic absorber lined in the hub and casing of the EGV passage. The lining uses a classical $\lambda/4$ absorber setup that is setup to have its peak efficiency for two selected acoustic certification points, Cutback and Approach. The results show a generally good agreement between the numerical approach used to setup the liner and the measurement results acquired in the test rig. The liner works well for all three operating points investigated, resulting in a reduction of the overall sound power level of the 1^{st} BPF by more than 3 dB for approach and more than 5dB for the operating point "Sideline".

Serrano and Torres [24] presented a numerical optimisation of lining applied on the suction and/or pressure side of the EGV. After presenting their numerical approach and validating with test cases they used their numerical approach to calculate the sound field downstream of a three stage LPT with OGV. The results show that acoustic lining for the 1^{st} BPF is more effective on the pressure side whereas the 2^{nd} BPF is strongly influenced by the suction side. The changes in PWL are between 1dB and 3dB. They also compare the EGV lining with traditional lining downstream of the EGV. This comparison shows that the suction side treatment gives an overall similar decrease in PWL than the downstream lining, but is more effective in terms of reduction per treated surface area.

2.2 Compressor Aerodynamics

Due to the fact that the EGVs main purpose is identical to a compressor blading the important topics are identical to what can be found on other compressors. The research on compressor aerodynamics is a constant topic of investigation in the last decades. The following section gives an insight into the main topics surrounding the EGVs used within this thesis such as secondary flow and the importance of the Reynolds number.

In addition to a lot of books dedicated to compressors such as Cumpsty [25], multiple reviews on compressor literature are available such as Lakshminarayana et al. [26] who reviewed compressor secondary flow, early empirical and semi-empirical correlations regarding secondary losses, as well as the basics of tip clearance flow in compressors. A model of the secondary flow suggested in [26] can be seen in Figure 2-1, where the secondary flow and the vortices present in a compressor rotor are depicted including the tip leakage vortex.

Another example of an extensive papers focusing on multiple important topics is Halstead et al. [27]–[30] where comprehensive experiments and computational analyses were conducted to understand boundary layer development on airfoil surfaces in multistage, axial-flow compressors and LP turbines. The tests were run over a broad range of Reynolds numbers and loading levels in large, low-speed research facilities which simulate the relevant aerodynamic features of modern engine components. Measurements of boundary layer characteristics were obtained by using arrays of densely packed, hot-film gauges mounted on airfoil surfaces and by making boundary layer surveys with hot wire probes. Computational predictions were made using both steady and an unsteady flow code. This is the first time that time-resolved boundary layer measurements and detailed comparisons of measured data with predictions of boundary layer codes have been reported for multistage compressor and turbine blading.

Kang and Hirsch [31] investigated the three dimensional flow in a linear compressor cascade at

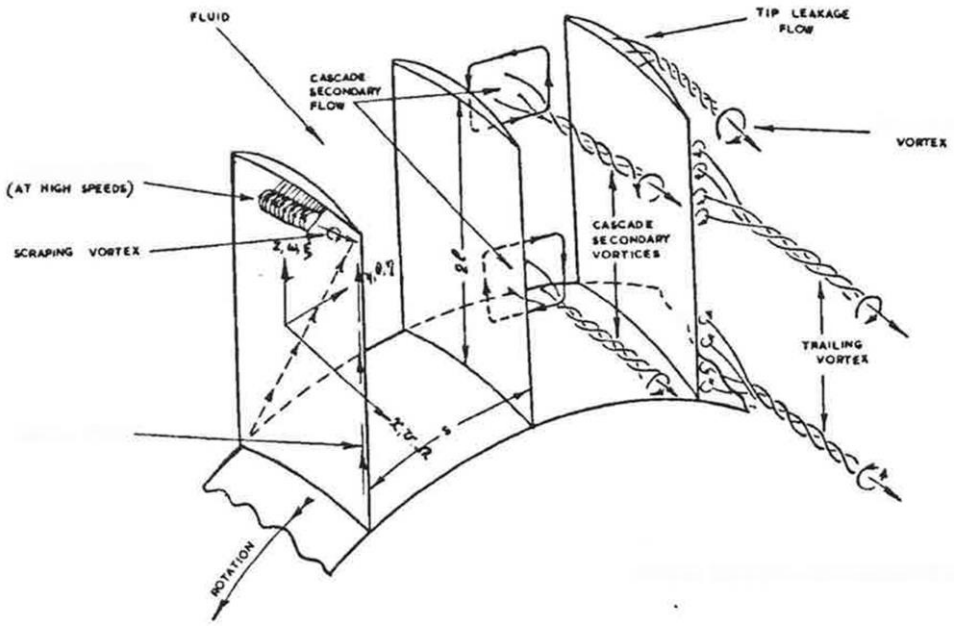

Figure 2-1: Secondary flow and vortices in an axial flow compressor [26]

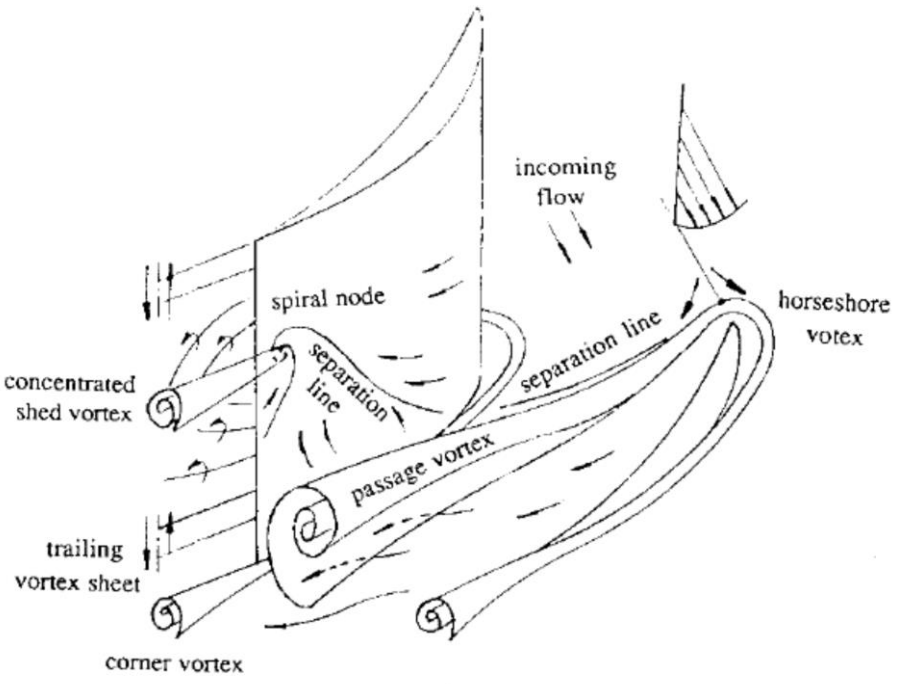

Figure 2-2: Secondary flow structure taken from Kang and Hirsch [31]

design conditions. They observed that the flow is not only characterized by conventional aspects such as horseshoe and passage vortices but also two spiral nodes points that form a three dimensional separation line on the suction side vane surface. Within the blade wake they were able to identify two distinct vortices and a vortex sheet, rotating in the same sense, but opposite to the passage vortex. The shed vortex is originating from the spiral node point formed by the separation lines on the suction side of the vane as seen in Figure 2-2. A comprehensive introduction to flow separation can be found in e.g. Chang [32].

Wisler et al. [33] investigated a multi-stage compressor setup in order to determine the importance of secondary flows and diffusion for mixing in multi stage compressors. It was shown, that considerable fluid motion can occur and that both secondary flow and turbulent diffusion play important roles in mixing, depending on location and loading. The free stream region is dominated by turbulent diffusion whereas the endwalls and airfoil surfaces, the convective effects of secondary flows are in the same order of magnitude and even greater than diffusive mixing

Influence of Reynolds number

Ashpis [34] has shown, that the Reynolds number for the LPT can drop below 10^5 during high altitude cruise conditions. This in extend means that the Reynolds number for the EGV can drop to equally low numbers, making the influence of the Reynolds number onto the flow field an important topic in compressor aerodynamics.

Sonoda et al. [11] noted that the range of working Reynolds number for the EGV itself ranges between 10^6 for take-off and $<10^5$ for cruise condition. This makes the influence of Reynolds number on the flow an important topic for turbine EGV flows.

Rhoden [14] reported that for low-speed cascades a fairly steep pressure gradient immediately after the suction peak near the leading edge seems to be effective in preventing laminar separation, however Rhoden [14] only tested this concept in low-speed cascades. The Reynolds numbers covered a range of $3 \cdot 10^4$ and $5 \cdot 10^5$.

Citavy and Jilek [35] e.g., tested low speed compressor cascades at low Reynolds numbers in a range of $1.8 \cdot 10^4$ to 10^5 and proposed semi empirical models for the growth and bursting of laminar separation bubbles. They found a separation bubble was present at their NACA 65-1210 profile for $Re > Re_B = 7.5 \cdot 10^4$ with a reattachment of the flow downstream of the bubble. For smaller $Re_B = 1 \div 8 \cdot 10^4$ a backflow could be observed with a minimum at $Re = 3 \cdot 10^4$. At $Re < Re_D = 3 \div 4 \cdot 10^4$ a separation of the boundary layer takes place on the pressure side of the bvane near the trailing edge. This point moves upstream with decreasing Re. They found that the loss coefficient of the compressor cascade increases down to Re_M and then is approximately constant until the Reynolds number reaches Re_D where a separation on the pressure surface occurs and the loss coefficient increases with decreasing Re.

Hobson et.al [36] investigated the effect of Reynolds number on separation bubbles in CDA cascades. LDV was used to characterise the flow field of the suction side boundary layer for Reynolds numbers between $2 \cdot 10^5$ and $3 \cdot 10^4$. They showed that for low Reynolds numbers a laminar separation bubble formed at mid-chord and reattached turbulent within 20% chord. At higher Reynolds numbers, the boundary layer upstream of the bubble was transitional and the bubble significantly decreased in size. At high Reynolds number, the flow was shown to be turbulent from close to the leading edge and flow reversal appeared at 80% chord as a result of endwall effects.

Mukhraiya and Ahmed [37] investigated the performance of an axial compressor cascade for low Reynolds numbers ($0.8 \cdot 10^5$) for various inlet turbulences. They showed that for a given incidence, an increase in turbulence level increases lift and decreases drag, indicating turbulence is favourable delaying flow separation. In addition they posted that for low incidences an increase in turbulence level slightly increases stagnation pressure loss whereas for high incidence angles pressure loss decreases.

Cyrus [38] performed investigations on a AR=2 linear compressor cascade with low Reynolds numbers in a range of $0.45 \cdot 10^5$ to $1.5 \cdot 10^5$ for low Mach numbers(Ma_1=0.12). Cyrus showed that for a drop in Reynolds number below a critical level (for the investigated case: approximately $1.35 \cdot 10^5$), the flow regime on the suction side of the vane changes dramatically, namely a large region of separation occurs. In addition the overall loss coefficient will rise, while the losses due to secondary flow effects will be reduced with respect to the overall losses. Cyrus was able to provide simple correlations for these losses.

Horlock et al. [39] tested a series of guide vanes and compressor cascade with varying Reynolds number and aspect ratios. They found that there is a critical Reynolds number, below which the losses and flow deviation increase rapidly. This is only true for aspect rations larger than 3:1 whereas for lower aspect ratios these effects do not appear, but rather the deviation correlates with the axial velocity change cross the cascade. Tests on a two stage compressor showed, that for high Reynolds number, the pressure rise can be accurately predicted from cascade measurements. The effect of low

Reynolds number does also appear in the compressor tests. These results agree with results by Preston[40], suggesting a minimum Re for turbulent boundary layers.

Corner separation

A feature that is often found in compressor vanes is the so called corner separation occurring mostly on the intersection between the suction side and the hub and casing. This effect is most dominant close to the hub and has been investigated multiple times.

Gbadebo et al. [41] investigated three dimensional separations in axial compressors. They showed that reversed flow always occurs on the end wall as well as on the blade suction surface, irrespective of the pitch-wise extent of the separated region. In connection to another effect, separation always occurs, but does not imply stall. This means that separation can occur with no reverse flow and nonzero friction.

Lei et al. [42] presented a criterion for estimating the onset of three dimensional hub-corner stall in compressors. The criterion consists of a diffusion parameter defining conditions where stall will occur and a stall indicator that defines whether a large magnitude flow reversal exists on the suction surface and the hub. Here, hub corner stall is characterized by extreme excursions of the surface streamlines and a large flow reversal on both the suction side and the endwall. While suction surface separation can occur frequently, the magnitude of flow reversal on the hub can be small. They found good agreement between their criterion and available data.

Dong et al. [43] investigated the flow in a low speed high reaction single stage axial compressor. They tried to provide a link between the suction surface hub corner separation, their loss mechanisms and the blade loading. They showed that the introduction of a small clearance between the hub and the stator can increase the efficiency of the stator compared to a no-clearance case. This is due to a significant reduction of suction surface separation caused by the tip leakage flow on the hub, but only when the secondary flows within the passage are very severe such as in the presented case.

Joslyn and Dring [44] investigated the stator of a two stage compressor test facility with a Reynolds number $Re = 2.6 \cdot 10^5$. The found that the presence of a corner stall on the rotor caused an increase in incidence angle on the stator, leading to a severe separation on the stator suction surface hub endwall. This corner separation is present for all three operating points investigated in the publication. Similar to [43] they found that the pressure surface flow is nearly two-dimensional for all flow coefficients, however, they notice that the streamlines become more diffused with decreasing flow coefficient which they link to low momentum fluid from the rotor being pushed towards the pressure surface by the slip velocity.

Vane Design

Another important aspect is the overall design philosophy of the EGV. In the early 1980s sub- and transonic controlled-diffusion airfoils (CDA) made their way into modern compressor designs, which were based on both experimental and numerical research as described by Hobbs and Weingold [45]. In subsonic blade rows the CDA, that has a velocity maximum around 20–30% of the chord, has been applied to many aero-engines and land-based gas turbines.

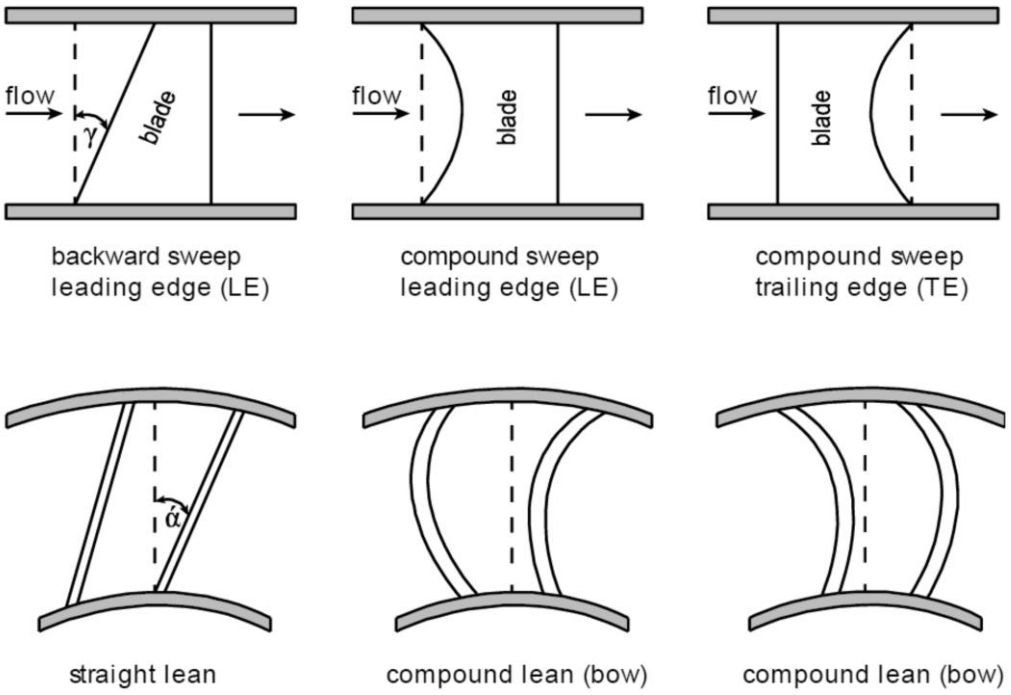

Figure 2-3: Basic possibilities of 3D-blade design: sweep and lean

While this approach has been successfully applied for a long time modern aero-engines strive to reduce the number of turbine components using new ultrahigh-loaded LP turbine technology. While this technology is still under development, it requires the use of a high turning EGV just downstream of this extremely high loaded turbine rotor (Sonoda et al. [11]). Using a higher loaded EGV, a turbine aerodynamic designer can freely load up the rotor performance and adjust the velocity triangles to an optimal stator, rotor and EGV combination. This leads to a considerable increase of the reaction of the turbine rotor[11].

Recently, Köller et al.[46] and Schreiber et al. [12] showed in their optimisation and experiments that the CD airfoils, that have been primarily developed for aero-engine applications, are not the optimal solution, if directly transferred to the land-based gas turbines, since at very high Reynolds numbers nearly no laminar boundary layer is present on the front portion of the airfoil.

Similar optimised airfoils were already found by Sieverding et al. [47], who showed the "ski-slope" pressure distribution that has its peak velocity shortly after the leading edge at about 5% of the chord length. The effectiveness of these profiles, especially the increase of the working range, is confirmed in their three-dimensional CFD simulation and compressor experiments.

An important method in the optimisation of modern airfoil design is the use of three dimensional features such as sweep, lean and endwall profiling. A sweep is radial displacement of the blade profiles in axial direction, whereas a lean is defined as a displacement of the blade profiles in circumferential direction. These displacements do not need to be constant along the span of the blade, can be combined as needed and might be applied to the leading edge and trailing edge of the blade (Figure 2-3).

An overview of the possibilities of these features can be found in Denton and Xu [48] where the basic features and the results of the effects of applying these features are described. A sweep of the

blade leading edge can be used in order to reduce the loading of the blade. A backward sweep such as seen in Figure 2-3 can reduce the loading of the blade at the casing while increasing the loading at the hub. A lean of the blade results in a displacement of fluid from the endwalls towards the middle of the passage causing a reduction in losses close to the endwall. A variable lean as seen in Figure 2-3 is used to reduce the loading close to the endwalls to further facilitate the displacement of fluid. In addition, the flow at the exit of the passage shows a greater homogeneity causing a decrease in mixing losses and improved flow conditions for the next stage [48].

2.3 LPT AERODYNAMICS AND TIP LEAKAGE FLOWS

As shown later, the rig-setup used within this work has an unshrouded low pressure turbine that is located upstream of the EGV to be investigated. Due to the fact that this unshrouded configuration is rather unusual for a low pressure turbine, the effects of the tip leakage vortex have to be taken into account for this very work.

The flow through a low pressure turbine has been studied extensively. A review of secondary flows in axial turbines was e.g. published by Langston [49].

While the effects discussed these papers are mostly interesting for the flow within the turbine blade itself the tip leakage presents a forceful effect that strongly influences the flow field in the downstream rows and in this case the EGV. Turbine tip leakage flows have been studied extensively, and a review of experimental as well as numerical studies on tip leakage flow can be found in e.g. Sjolander et.al [50] and Langston [49].

Heyes and Hodson [51] described a two-dimensional model for the calculation of the tip leakage flow and compared the results with data obtained from experiments in linear turbine cascades. The authors showed the importance of pressure gradients along the blade chord and highlighted it as a main factor of influencing the tip leakage flow.

Yaras and Sjolander [52] examined the total pressure losses in the tip leakage flow of a planar cascade. They altered the tip gap size from zero to 5.5 % blade chord. The authors clarified the role played in the propagation of the tip leakage losses by several mechanisms. Further, they found out that the direct loss in the gap is relatively unimportant for all investigated clearances.

Sell et al. [53] investigated and compared four different tip gap sizes including a zero gap size (0%, 1%, 3% and 5%) in an annular cascade. These tip clearances were chosen by the authors because they represent three conditions where the tip clearance is below, approximately equal to and substantially larger than the inlet boundary layer displacement thickness. At the leading edge this produced different behaviours, with the smallest gap producing a stagnation point, equivalent to the case without tip clearance, while the largest clearance allows through flow over the leading edge into the tip gap. In the presence of larger tip clearances, the tip leakage flow induced a stagnating flow in the trailing-edge region, which resulted in a large area of blocked flow in the blade passage downstream the trailing edge.

An investigation of the physics of tip leakage flows can be found in Tallman et.al [54][55]. Tallman et.al performed numerical investigations on a linear turbine cascade with realistic clearance, inlet conditions as well as endwall motion. The first part of the paper [54] concludes, that the core of the leakage flow is composed entirely of fluid passing through the clearance gap between the leading

edge and mid-chord. Vortex rollup begins between 30 and 40% axial distance from the leading edge. Their results indicate that vorticity convection from the gap is most responsible for the roll-up of the leakage vortex in cases with smaller tip clearances, such as 1% of the span whereas for larger tip clearances the interaction between the leakage jet and the freestream flow is responsible for the rollup.

The second part of the paper [55] investigates the influence of the relative motion between the outer casing and the blade. The tip clearance is set for 1% span which is of the same size as for the rotor investigated within this thesis. It is shown that the relative motion reduces the mass flow through the gap and decreases the loss coefficient. Another effect is that for a moving casing not all of the leakage flow is entrained around the vortex, but rather around and underneath the vortex, developing a strong secondary flow in span-wise direction as well as reducing the size of the roll-up vortex.

While the linear cascade is a useful tool to study the basics of leakage flow, some phenomena that occur due to rotation e.g. centrifugal forces cannot be simulated in cascades. The rotational effects and coriolis forces modify the turbulence structure in the tip leakage flow and secondary flow as compared to cascades (McCarter et al.[56]). Therefore, it is most important to investigate the flow in rotating turbines.

Xiao et.al [57] investigated the pressure distribution as well as the flow field of a low pressure rotor with a tip leakage flow. They used pressure tabs, fast response pressure probes, rotating 5-hole probes as well as Laser-Doppler-velocimetry. The authors stated that regions with lowest pressure and highest loss indicate the trace of the tip leakage vortex. Furthermore the effect of the leakage jet decreases the loading at the tip of the blade due to the lack of turning, while increased the loading just below the tip gap due to the formation of the tip leakage vortex in the rear region of the blade.

It was observed that the loss near the tip leakage region is nearly twice as high as within the passage vortex region. However, the passage vortex produces more losses than the tip leakage vortex in total.

McCarter et al. [56] conducted experimental investigations within the same geometry as Xiao et.al [57] to better understand the flow physics of the tip leakage flow. The focus of this investigation was the origin as well as the development of the leakage flow including its interaction with secondary flow features. The authors stated that the vortex originates for the given geometry in the last half chord of the blade and is confined to the suction side corner near the blade tip. Furthermore, the authors found that the tip leakage flow clings to the endwall and the blade suction surface until approximately 80% chord, and then lifts off the surface to interact with the main flow forming a vortex.

They observed that due to the relative motion between blades and casing a scraping vortex is developed. The authors stated that the propagation of the tip leakage flow into the main flow is reduced by the scraping vortex along with the secondary flow.

The effect of clearance on shrouded and unshrouded turbines at two levels of reaction was performed by Yoon et al. [58]. The effect of seal clearance on the efficiency of a turbine with a shrouded rotor is compared with the effect of the tip clearance when the same turbine has an

unshrouded rotor. The shrouded versus unshrouded comparison was undertaken for two turbine stage designs one having 50% reaction, the other having 24% reaction. It was shown, that when the clearance of the unshrouded rotor is reduced to below a certain threshold, the so called "break-even-clearance", the same efficiency can be achieved for both the shrouded and the unshrouded rotor. If the clearance is reduced further the unshrouded rotor performs better than the shrouded rotor. Secondly, the use of a lower degree of reaction reduced the efficiency penalty for both shrouded and unshrouded rotor.

Lengani et al. [59] performed unsteady measurements with a fast response pressure probe downstream of an unshrouded low pressure test turbine with an uneven blade/vane count. He was able to identify the importance of the tip leakage vortex for the flow field downstream of the stage. The goal of the paper was to show that the interactions between blade and vanes of the stage can be explained by means of rotating pattern according to the aero-acoustic theory by Tyler and Sofrin [60]. The fluctuations downstream of the rotor can be seen as a superposition of rotating patterns due to so called spinning modes.

Arndt [61] studied the unsteady blade row interaction in multi stage low-pressure turbines with hot-film probes downstream of every blade row. The results of his investigations showed that the rotor-rotor interactions have a profound influence on the flow through the LPT. These wake-induced interactions result in strongly modulated periodic and turbulent velocity fluctuations downstream of the rotor blades. There is a significant difference in wake depth and turbulence level measured downstream of each stage.

Binder et al. [62] reported on Laser Measurements in a single stage cold air turbine at off-design conditions with an outlet Mach number of Ma=0.8. They found that the cutting of the stator wakes by the rotor caused an increase in velocity fluctuation within the intersected wake, whereas outside of the wake no such effects occurred. Downstream of the rotor, high fluctuations in the velocities near the pressure side of the rotor resulted in high values of turbulence intensity.

Tiedemann and Kost [63] investigated the rotor stator interactions within a single stage HP-turbine test rig. They concluded that when the rotor wake interacts with the upstream stator wake, the wake decreases in depth and increases in width. During this interaction, the maxima of the random components (turbulence and the RMS of the total pressure) decreases in height and width). The assumed reason for this is the reduction in the velocity and total pressure difference between the passage flow and the rotor wake flow when portions of the NGV wake are present in the passage. This reduces the wake mixing intensity, which in turn results in lower random fluctuations.

An important note on LPT Reynolds number was given by Ashpis [34]. He showed that the operating Reynolds number for the LP turbine can drop below 100,000 at high-altitude cruise condition, which leads to a 2% drop in efficiency from take-off to cruise. It has been observed that the boundary layers are largely laminar, even in the presence of free-stream turbulence and wakes. As a result, the boundary layers are susceptible to flow separation near the aft portion of the blade suction surface. This makes low Reynolds number investigations of the LPT an interesting topic. As a result of this, the EGV downstream of the LPT also experiences Reynolds numbers of similar magnitudes at these operating conditions

2.4 Acoustics

Another important topic within this thesis is the acoustic field downstream of the EGV. The following section deals with the fundamental mechanisms of noise generation and propagation in aircraft engines and components.

2.4.1 Sound generation in turbines

Prior to the application of turbofan engines the dominant sources of noise have been the first compressor stage and the jet of the engine. The introduction of larger bypass engines lead to a significant decrease in the average jet exit velocity. Due to this increase in bypass ratio the noise emitted by the turbine as well as the influence of the compressor noise gets more dominant in current applications.

In addition the introduction of acoustic lining in the inlet of the fan leads to an additional decease in emitted noise (see e.g. Lansing and Zorumski [64] as well as Unruh [65]).

The relative importance of the components in typical noise certification points can be seen in Figure 2-4. The two operating points in Figure 2-4 use a different scale. During the approach condition, the noise emitted by the turbine is only second to the noise emitted by the fan, and due to different directions of propagation contribute a significant amount of noise.

Considering the noise emission within the test rig used in this thesis is due to the LPT, this will be the focus of this section. A typical frequency spectrum of a turbine can be seen in Figure 2-5 where the spectrum of a low bypass turbofan engine can be seen. The spectrum contains multiple peaks that are due to the blade passing frequencies (BPFs) of the respective components and their harmonics. Due to the fact that the turbine and the compressor consist of multiple stages not only the peaks due to the BPFs can be seen in the figure but also the interactions of these BPFs. While the noise generated by the HPT is being dampened by the LPT and can be influenced by a lot of effects, it is difficult to decrease the noise of the LPT and therefore represents a special challenge.

The mechanisms of noise formation in the turbine are similar to noise generation in compressors [66] and are in general divided into broadband noise and tonal noise. They are both due to different phenomena and are being discussed separately in the following sections.

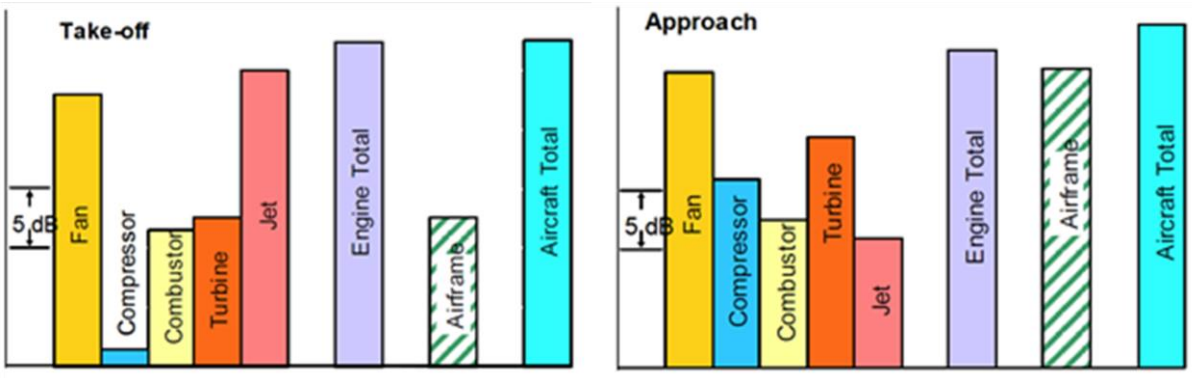

Figure 2-4: Aircraft noise source breakdown (taken from [93]); relative values of the operating points not to scale

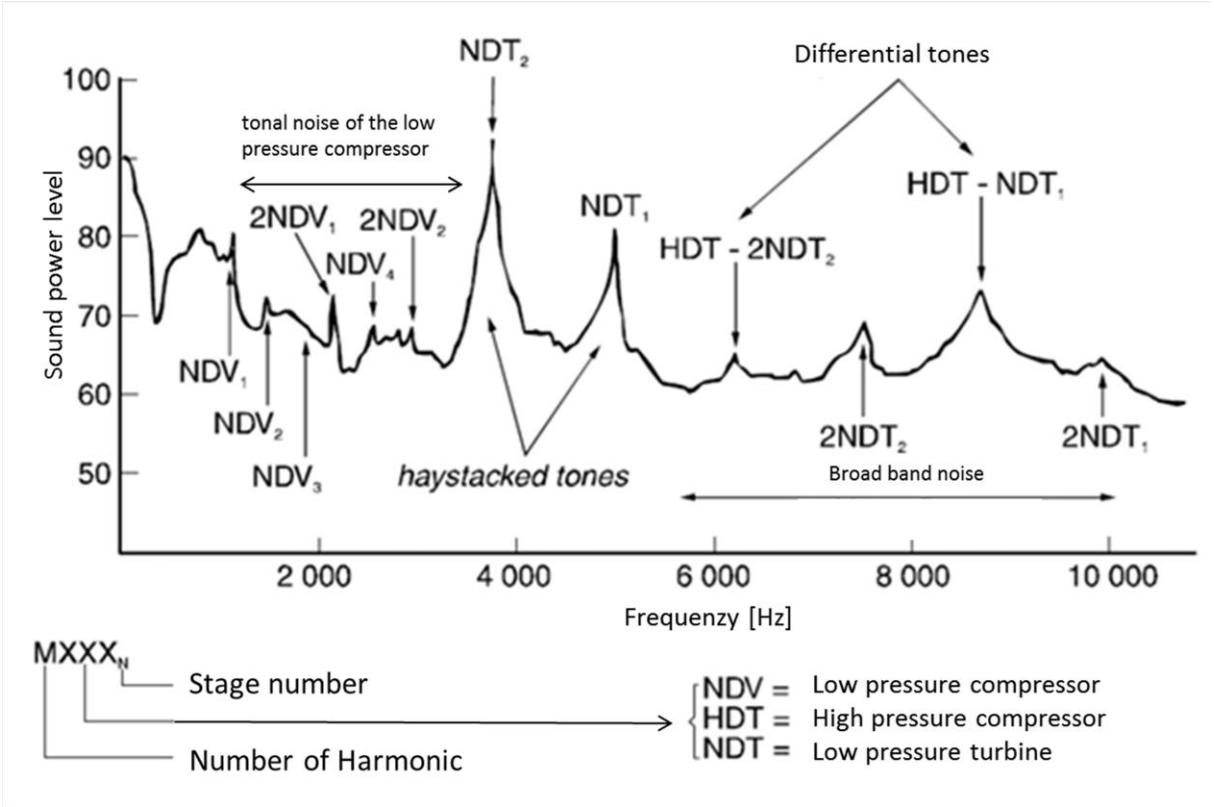

Figure 2-5 : Exemplary noise spectrum of the turbine of a low bypass turbofan, adapted from [67]

2.4.2 Tonal Noise

Tonal noise is the most important part of the nose generated by the engine. When e.g. looking at Figure 2-5 it can be seen that the tonal noise generated is significantly higher than the broadband noise. Tonal noise is being generated by periodic non- uniformity of the flow field [67]. This can be due to a rotating blade row and its interaction with vane rows or pressure discontinuities such as shocks. The easiest case for the generation of tonal noise is the so-called "rotor alone noise" as described by Benzakein and Smith [66]. This generates a tonal noise that is dependent on the rotational speed and the number of blades. The frequency of the periodic pressure fluctuations created by the rotor is called blade passing frequency (BPF) and is defined as follows:

$$BPF = \frac{n_{RPM}}{60} \cdot B \tag{2.1}$$

In addition to this BPF tonal noise is also generated at harmonics h of this frequency. The amplitude of these harmonics decreases with increasing order. These fluctuations generated by the rotor at the BPF rotate with a rotational speed Ω

$$\Omega = n_{RPM} \frac{\pi}{30} \tag{2.2}$$

The usual setup of a stage in an engine consists of a rotor and a stator resulting in an interaction of these two components. Tyler and Sofrin [60] investigated the interaction between a rotor and its interaction

They named three main sources of noise generation:

- The cutting of the upstream stator wakes by the rotor

- The impingement of the rotor wakes on downstream stator vanes
- The influence of the potential effect of the stator vanes onto the rotor

The pressure patterns of these interactions can be expressed as coefficients of a circumferential pressure pattern

$$p(\theta,t)=\sum_{n=1}^{\infty}\sum_{m=-\infty}^{\infty}p_{mn}\cdot\cos(m\theta-n\omega t+\phi) \tag{2.3}$$

In this formula, n is the harmonics of the blade passing frequency, m is the circumferential mode,

According to Tyler and Sofrin the value m is restricted to the following values:

$$m=h\cdot B+k\cdot V \tag{2.4}$$

The value m describes the circumferential mode of the pattern, B the number of blades, V the number of vanes, and h is the harmonic of the blade passing frequency (h=1,2,3….). The variable k is an integer value ranging with k=±∞. For a vane count of V=0 and the first blade harmonic the circumferential mode order is identical to the number of blades and the pressure pattern rotates with the rotational speed of the rotor. For a given circumferential mode m the rotational speed of said mode can be calculated as follows:

$$\Omega_m=\Omega\cdot\frac{h\cdot B}{m}=\Omega\cdot\frac{h\cdot B}{h\cdot B+k\cdot V} \tag{2.5}$$

The rotational direction of a given mode m is not necessarily identical to the rotor. When k is <1 and $|k|>h\cdot B/V$ the resulting mode m is smaller than zero and the resulting rotational speed Ω_m is smaller than zero.

Describing the pressure fluctuations (noise) for a whole engine requires an extension of equation (2.4) for a larger number of vane rows, where these mode m generated by a rotor-stator interaction is scattered by a vane row with a number of vanes V_2, where k_2 is the integer value for the second vane row

$$m^*=m+k_2\cdot V_2 \tag{2.6}$$

This results in a formula for the scattered mode m^*

$$m^*=h\cdot B+k_1\cdot V_1+k_2\cdot V_2 \tag{2.7}$$

The theoretical number of interaction mode is unlimited; the practical number of modes is restricted by the limits of mode propagation in ducts. The modal interaction between a rotor and a stator is now explained with an example taken from Sutliff [68]. Figure 2-6 shows a schematic depiction of a rotor-stator interaction with the number of vanes V=6 and the number of blade B=8. For the base harmonic h=1 and the integer values k = {-3,-2,-1,0,1,2,3} the modes m resulting from equation (2.4) are m=1*8+k*6={10,-4,2,8,14,20,26 }. The mode m=8 results from k=0 and presents the base mode of the rotor. Figure 2-6 shows the interaction for the mode m=2 resulting from an integer k=-1. The figure shows the stator in black and the rotor in red. The temporal evolution of

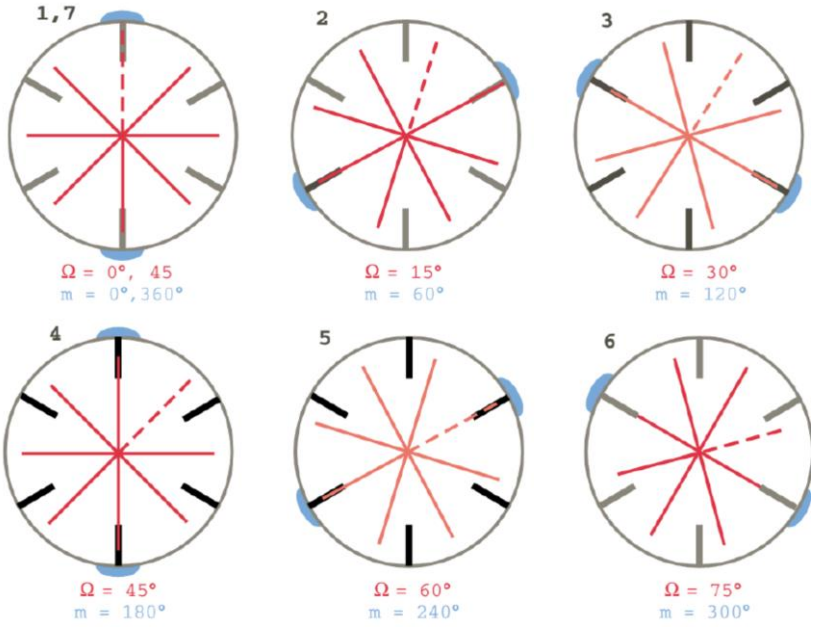

Figure 2-6 : Depiction of the Stator-Rotor interaction; Ω is the circumferential position of the rotor, m is the position of the interaction [68]

the interaction is shown in clockwise direction. One of the blades is shown as a dashed line in order to better see the revolution of the rotor.

In time step one (top-left) the position of the dashed rotor blade and the top stator (as well as another blade with the bottom stator) are in line. The resulting interaction of a blade and a vane being superimposed is marked with a blue dot on the outer circle. The two interaction positions are located at 0° and 180°. For the time step 2 the rotor is moving 15° in clockwise direction. Due to the ratio of vanes to blades another blade/vane combination is now in line in the picture. This results in a movement of the interaction by 60°, four times the rotational speed of the rotor. Timestep 3 moves the rotor another 15° in clockwise direction. Now a third blade pair is superimposing with the stator, the blue dot symbolising the rotating pattern has moved another 60°. This pattern continues until a full rotation of the rotor is reached.

When looking at the rotational speed of the mode according to the formula by Tyler and Sofrin we receive the rotational speed of the mode m=2 as follows:

$$\Omega_{m=2} = \Omega \cdot \frac{h \cdot B}{m} = \Omega \cdot \frac{1 \cdot 8}{2} = 4\Omega$$

This reveals that the rotational speed of the interaction mode m=2 has 4 times the rotational speed of the rotor, and the fact that the value is larger than zero shows that the rotational speed is identical to the rotational speed of the rotor. Due to the fact that equation (2.4) relates the emitted noise to a specific interaction, the analysis and decomposition of a flow field allows for an identification of the source of a specific noise.

2.4.3 Broad Band Noise

The second part of the overall noise is the so called broad band noise. This is caused by e.g. fluctuating pressure distributions along the blades and vanes. This is, amongst other things caused

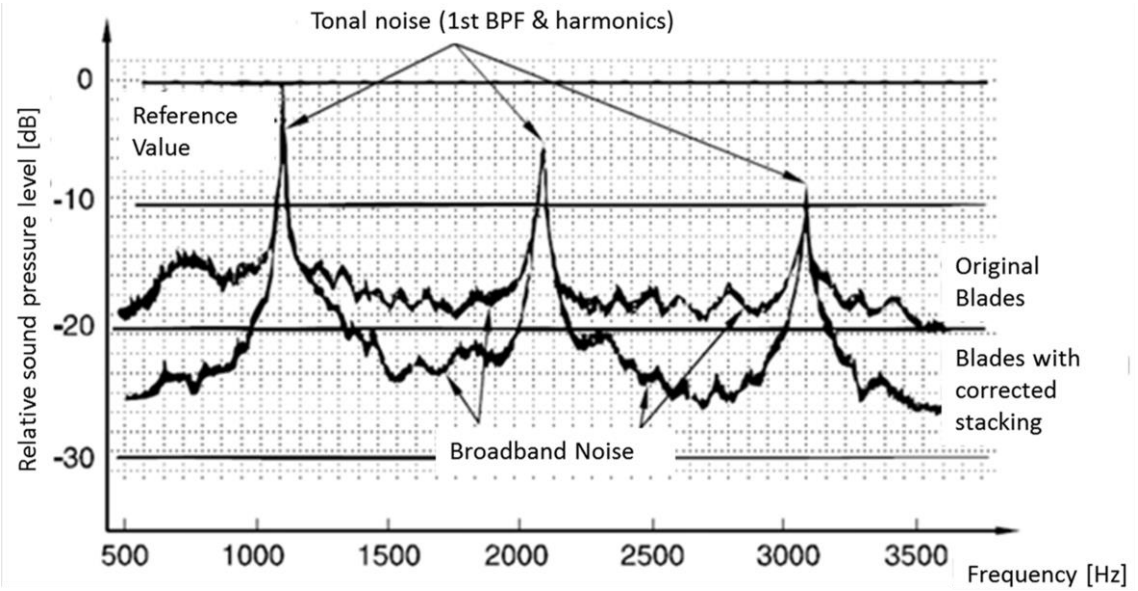

Figure 2-7: Influence of an incidence change of 4° onto the broad band noise generation of a fan (adapted from [69]

by a change in incidence angle on the leading edge of the blading causing flow non uniformities resulting in things such as flow separation, vortices and other turbulent structures [67].

Within stages the turbulent wakes emanating from a blade row play an important part in the generation of not only tonal but also broad band noise, as they change the incidence angle of the downstream stages. In addition these structures are chopped by downstream rows creating structures that have a strong interaction with the blades and vanes.

An important part in the generation of broad band noise is the incidence angle of a blade/vane. In an ideal operating point the incidence angle of a structure is zero, but most operating points of engines either show a positive or a negative incidence. A change in incidence angle of one degree can cause a change in broad band noise by 1 to 2 dB [66]. Smith [69] has shown (see Figure 2-7) that a 4° change in incidence angle of an optimised fan blade results in a strong increase in broad band noise but the tonal noise remains almost unchanged.

2.4.4 Sound propagation

The acoustic properties explained in the previous chapter are fluctuations that propagate in time and space. In fluids this is accomplished by longitudinal waves. In order to explain this propagation of (in this case) small perturbations in a fluid the laws of conservation have to be applied to the thermodynamical properties of the fluid, resulting in the derivation of wave equations for these properties. The derivation of these wave equations used in acoustics is extensively done in literature (e.g. [70][71][72]) so that within the following sections, the equation will be applied to the sound propagation in ducts. In addition the conditions that need to apply in order for a sound wave to propagate within a duct will be shown.

The wave equation for fluids is derived from the Euler equations using the continuity equation on a material law $p = p(\rho)$. The simplifications and assumptions are as follows:

- In the beginning, the equations assume no fluid motion; all motion is due to acoustic fluctuations

- It is assumed that the acoustic perturbations are small leading to a linearization of the equations
- Due to the use of the Euler equations the viscous terms are neglected meaning there is no friction
- All changes in fluid properties are assumed to be adiabatic; the change is significantly faster than the heat transfer
- Constant entropy: the speed of sound can be calculated as follows:

$$\left(\frac{\partial p}{\partial \rho}\right)_{s=const} = c^2 \;\Rightarrow\; c = \sqrt{\kappa \frac{p}{\rho}} = \sqrt{\kappa R_s T} \tag{2.8}$$

Considering these points the wave equation for sound-pressure, sound energy density and particle velocity can be obtained. Considering sound pressure is very easily measurable and describes the sound propagation very well this is the property that will be used for further explanations. The wave equation for the sound-pressure is now:

$$\frac{1}{c^2}\frac{\partial^2 p'}{\partial t^2} - \Delta p' = 0 \tag{2.9}$$

With Δ being the Laplace operator $\Delta = \frac{\partial^2}{\partial x^2} + \frac{\partial^2}{\partial y^2} + \frac{\partial^2}{\partial z^2}$ for Cartesian coordinates. The equation shows that the pressure perturbation p' is propagating with a characteristic velocity, the speed of sound c. For a simple one dimensional case the acoustic properties are only dependent on one spatial dimension. If this dimension is called x the equation looks as follows:

$$\frac{1}{c^2}\frac{\partial^2 p'}{\partial t^2} = \frac{\partial^2 p'}{\partial x^2} \tag{2.10}$$

The solution to this equation according to d'Alambert is

$$p' = F(ct + x) + G(ct - x) \tag{2.11}$$

where F and G are real functions with the property of owning a second derivative. The function 'F' describes the propagation of the wave in negative x-direction and 'G' in positive x-direction. When looking at a periodic propagation of a wave moving in positive x-direction one solution is seen in the following equation:

$$p' = p \cdot \cos(\omega t - kx + \varphi_0) = \Re(p \cdot e^{-i(\omega t - kx + \varphi_0)}) \tag{2.12}$$

In this equation, p is the amplitude of the pressure fluctuation, ω the angular frequency and φ_0 the phase shift. The variable k is called the wavenumber and is calculated from the angular frequency and the velocity of propagation c respectively the wavelength λ.

$$k = \frac{\omega}{c} = \frac{2\pi f}{c} = \frac{2\pi}{\lambda} \tag{2.13}$$

2.4.5 Propagation through a cylindrical duct without hub contour

This section explains the solution of the wave equation for a cylindrical duct without a hub contour. The wave equation is being transformed into cylindrical coordinates. The Laplace operator for

cylindrical coordinates is $\Delta = \frac{1}{r}\frac{\partial}{\partial r}\left(r\frac{\partial}{\partial r}\right) + \frac{1}{r^2}\frac{\partial^2}{\partial \theta^2} + \frac{\partial^2}{\partial x^2}$. When introduced into the equation (2.9) the wave equation looks as follows:

$$\frac{1}{c^2}\frac{\partial^2 p'}{\partial t^2} - \frac{1}{r}\frac{\partial}{\partial r}\left(r\frac{\partial p'}{\partial r}\right) - \frac{1}{r^2}\frac{\partial^2 p'}{\partial \theta^2} - \frac{\partial^2 p'}{\partial x^2} = 0 \tag{2.14}$$ (2.15)

This partial differential equation is solved by separating the variables and uses a harmonic time-dependency

$$p'(x, r, \theta, t) = F(x) \cdot G(r) \cdot H(\theta) \cdot e^{i\omega t} \tag{2.16}$$

Using the solution (2.16) in equation (2.15) yields the following:

$$\left(\frac{\omega}{c}\right)^2 + \frac{1}{F}\frac{d^2F}{dx^2} + \frac{1}{G}\left(\frac{1}{r}\frac{d}{dr}\left(r\frac{dG}{dr}\right)\right) + \frac{1}{H}\frac{1}{r^2}\frac{d^2H}{d\theta^2} = 0 \tag{2.17}$$

Bringing the term $\frac{d^2H}{d\theta^2}$ to the right and multiplying the equation with r^2 yields:

$$r^2\left(\frac{\omega}{c}\right)^2 + r^2\frac{1}{F}\frac{d^2F}{dx^2} + r^2\frac{1}{G}\left(\frac{1}{r}\frac{d}{dr}\left(r\frac{dG}{dr}\right)\right) = -\frac{1}{H}\frac{d^2H}{d\theta^2} \tag{2.18}$$

The solution of such equations requires the left and the right side to be identical, which is only possible when the left and the right side of the equation are constant. It is therefore required that the function$H(\theta)$ satisfies the following equation:

$$\frac{1}{H}\frac{d^2H}{d\theta^2} = -\gamma^2 \tag{2.19}$$

The same approach leads to the following relationship for the function $F(x)$:

$$\frac{1}{F}\frac{d^2F}{dx^2} = -\alpha^2 \tag{2.20}$$

The solution of third function $G(r)$ is not as simple and requires the knowledge of one of the variables γ or α in order to eliminate one of the variables. If e.g. the variable γ is known then $H(\theta)$ can be eliminated resulting in the following equation for$G(r)$:

$$\frac{1}{G}\left(\frac{1}{r}\frac{d}{dr}\left(r\frac{dG}{dr}\right)\right) - \frac{\gamma^2}{r^2} = \beta^2 \tag{2.21}$$

Using the equations (2.21) and (2.20) and substituting them into the wave equation (2.18) leads to the following simple equation:

$$\left(\frac{\omega}{c}\right)^2 = k^2 = \alpha^2 + \beta^2 \tag{2.22}$$

A generalised solution for $H(\theta)$ and F(x) can be given as follows:

$$H(\theta) = C_1 e^{-i\gamma\theta} + C_2 e^{i\gamma\theta} \tag{2.23}$$

$$F(x) = A_1 e^{-i\alpha x} + A_2 e^{i\alpha x} \tag{2.24}$$

The determination of the constants C_1 , C_2 and γ requires meeting the boundary conditions for the function $H(\theta)$ as well satisfying the circumferential periodicity of the function. This requires γ having an integer value. Yet this value is not fixed but is variable.

As seen the value of the variable γ strongly influences the solution of the radial function $G(r)$. When rearranging equation (2.21) the equation takes the form of a so called Bessel differential equation

$$r^2\frac{d^2G}{dr^2}+r\frac{dG}{dr}+r^2\beta^2-\gamma^2G=0 \tag{2.25}$$

The solution of this equation consists of the so called Bessel function 1st kind J_m and the Bessel function 2nd kind Y_m. Both of these functions have

$$G(r)=B_1J_m(r\beta)+B_2Y_m(r\beta) \tag{2.26}$$

As boundary conditions for the evaluation of these functions, the position r=R (the outer wall of the duct) is hard walled. This means that the particle velocity at r=R is zero. In addition, this requires for the pressure gradient to satisfy $\frac{dp\prime}{dr}\Big|_{r=R}=0$. The centre of the duct at r=0 results in a singularity as can be seen from the equation (2.14). In this case this would result in a source term in this position which is not possible. This therefore requires the variable B_2 in equation (2.26) to be zero, eliminating the Neumann function Y_m. The solution is now $G(r)=B_1J_m(r\beta)$. Due to the fact that $\frac{dp\prime}{dr}\Big|_{r=R}=0$ this requires that $\frac{dG}{dr}\Big|_{r=R}=0$ as well as $\frac{dJ_m}{dr}\Big|_{r=R}=0$. This means that the Bessel function needs to have an extreme at r=R. This is possible by using the variable β as a scaling function for r. Due to the fact that the Bessel function as an infinite number of local extema the constant β needs to be properly defined in order to describe the nth extreme of the mth order of the function. This requires the introduction of a variable of the form $\beta=\frac{\sigma_{mn}}{R}=\beta_{mn}$, introducing the variable σ_{mn}. This results in a solution

$$G(r)=B_1J_m(r\beta_{mn}) \tag{2.27}$$

When introducing β_{mn} into equation (2.22) the result for the variable $\alpha=\sqrt{k^2-\beta_{mn}^2}=\alpha_{mn}$. If now, one combines the equations (2.23), (2.24) and (2.27) with equation (2.16) this results in the following solution for the sound pressure:

$$\begin{aligned}p'(x,r,\theta,t)=\sum_{m=0}^{\infty}\sum_{n=0}^{\infty}&\left(C_{mn,1}e^{-im\theta}+C_{mn,2}e^{im\theta}\right)\cdot B_{mn,1}\cdot J_m(r\beta_{mn})\cdot\ldots\\&\ldots\left(A_{mn,1}e^{-i\alpha_{mn}x}+A_{mn,2}e^{i\alpha_{mn}x}\right)\cdot e^{i\omega t}\end{aligned} \tag{2.28}$$

This solution is a linear superposition of solutions dependent on the variables m and n. These variables are called modes with every pair (m,n) representing another characteristic pressure distribution. An exemplary selection of these characteristic pressure distributions can be seen in Figure 2-8. The variable m indicates the number of lobes in circumferential direction whereas the number n indicates the lobes in radial direction. Due to this, the modes m are called azimuthal modes and the modes n are referred to as radial modes. The base mode (m,n)=(0,0) is not depicted due to the fact that the pressure of this mode is constant across the whole channel.

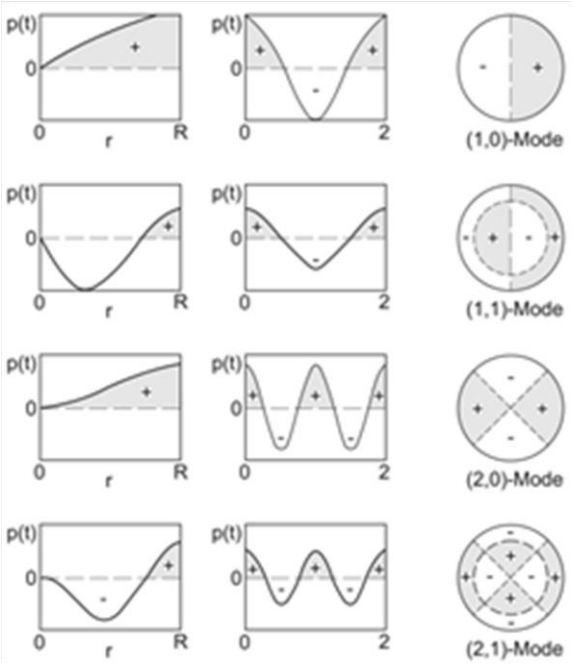

Figure 2-8: Characteristics of sound pressure distributions in a cylindrical channel for a number of modes (m,n) taken from Möser [94]

The effect of the axial propagation in a cylindrical channel are influenced by the values of $A_{mn,1}$ and $A_{mn,2}$, whereas the propagation in circumferential direction is influenced by $C_{mn,1}$ and $C_{mn,2}$. If, e.g. the variable $C_{mn,2}$ and $C_{mn,1}$ is zero this means the pressure field is rotating in positive direction. Depending on the circumferential mode m the angular velocity is fixed resulting in a spiral pressure field with a constant phase relation. If the constants $A_{mn,1}$ and $A_{mn,2}$ are identical a standing wave with no rotation is forming.

2.4.6 Propagation through a cylindrical duct with hub contour and superimposed flow

Up until this point the propagation of sound in a stationary fluid was analysed. In a turbomachine the fluid has an average velocity well above zero and this fluid motion needs to be taken into account. In addition, there is a hub geometry present meaning that the inner contour of the duct has a radius $r = R_i$ that is not zero.

In order to incorporate a non-zero velocity in equation (2.9) the partial derivative of the sound pressure is replaced by the substantial derivative $\frac{D}{Dt} = \frac{\partial}{\partial t} + \nabla\vec{U}$ resulting in the following equation

$$\frac{1}{c^2}\frac{D^2p'}{Dt^2} - \Delta p' = 0 \tag{2.29}$$

This is then transformed into cylindrical coordinates. One of the simplifications made is that the fluid only has a velocity in one direction resulting in a velocity vector $\vec{U} = (U, 0, 0)$ and allowing for$\nabla\vec{U} = U\frac{\partial}{\partial x}$. The wave equation then looks as follows:

$$\frac{1}{c^2}\left[\frac{\partial^2 p'}{\partial t^2} + 2U\frac{\partial^2 p'}{\partial t \partial x} + U^2\frac{\partial^2 p'}{\partial x^2}\right] - \frac{1}{r}\frac{\partial}{\partial r}\left(r\frac{\partial p'}{\partial r}\right) - \frac{1}{r^2}\frac{\partial^2 p'}{\partial \theta^2} - \frac{\partial^2 p'}{\partial x^2} = 0 \tag{2.30}$$

After introducing the axial Mach number $M_x = \frac{U}{c}$ the equation can be written as follows:

$$\frac{1}{c^2}\left[\frac{\partial^2 p'}{\partial t^2}+2U\frac{\partial^2 p'}{\partial t\partial x}\right]-\frac{1}{r}\frac{\partial}{\partial r}\left(r\frac{\partial p'}{\partial r}\right)-\frac{1}{r^2}\frac{\partial^2 p'}{\partial \theta^2}-(1-M_x^2)\frac{\partial^2 p'}{\partial x^2}=0 \tag{2.31}$$

This equation can be solved using the same process already seen in chapter 2.4.5 resulting in an almost identical solution. The important difference lays in the fact that the equation (2.22) is no longer valid, but replaced by the following term:

$$\beta^2=k^2\left(1-U\frac{\alpha}{\omega}\right)^2-\alpha^2 \tag{2.32}$$

This means that superimposing a mean flow not only influences the axial propagation of sound but also the radial propagation. The solution of the Bessel equation now needs to take into account that all positions within the channel have an r>0, which requires the solution to take the Neumann function into account (see equation (2.26)). The boundary conditions for the hard wall at $r=R_i$ and $r=R_a$ are as follows:

$$v_r|_{r=R_i}=\left.\frac{dp'}{dr}\right|_{r=R_i}=0 \;\; und \;\; v_r|_{r=R_a}=\left.\frac{dp'}{dr}\right|_{r=R_a}=0 \tag{2.33}$$

This results in the following form for equation (2.26):

$$\left.\frac{dG}{dr}\right|_{r=R_i}=\beta\left(B_1\left.\frac{dJ_m(r\beta)}{dr}\right|_{r=R_i}+B_2\left.\frac{dY_m(r\beta)}{dr}\right|_{r=R_i}\right)=0 \tag{2.34}$$

One possible singular solution to this equation is $\beta=0$. The variable B_2 can be determined by setting the term within the bracket to zero and introducing this solution to the equation (2.26). This results in the following when doing this for the boundary conditions at$r=R_a$:

$$\left.\frac{dG}{dr}\right|_{r=R_a}=\beta\left(B_1\left.\frac{dJ_m(r\beta)}{dr}\right|_{r=R_a}+B_2\left.\frac{dY_m(r\beta)}{dr}\right|_{r=R_a}\right)=0 \tag{2.35}$$

The solution of this two equation requires the determinant of the resulting system of equations to be zero resulting in the following equation:

$$J_m'(R_a\beta)\cdot Y_m'(R_i\beta)-J_m'(R_i\beta)\cdot Y_m'(R_a\beta)=0 \tag{2.36}$$

When introducing the hub-to-tip ratio $\eta=R_i/R_a$ and using the outer radius $R_a=R$ the equation transforms to:

$$J_m'(R\beta)\cdot Y_m'(\eta\beta)-J_m'(\eta\beta)\cdot Y_m'(R\beta)=0 \tag{2.37}$$

This equation can be numerically solved using the so called Bessel coefficients $\sigma_{mn}=R\beta_{mn}$. For every circumferential mode m there is an infinite discrete sequence of solutions σ_{mn}. This means that for a given geometry the values of β_{mn} can be calculated from the eigenvalues σ_{mn}. This results in equation (2.32) being used to determine the variable α

$$\left(\frac{\sigma_{mn}}{R}\right)^2=k^2\left(1-U\frac{\alpha}{\omega}\right)^2-\alpha^2=k^2-2kM_x\alpha+(M_x^2-1)\alpha^2 \tag{2.38}$$

This results in a quadratic equation for α:

$$\alpha^2 + \frac{2kM_x}{1-M_x^2}\alpha - \frac{1}{1-M_x^2}\left(k^2 - \left(\frac{\sigma_{mn}}{R}\right)^2\right) = 0 \tag{2.39}$$

The solution of this equation for an axial Mach number $M_x \neq 0$ provides the axial wave numbers of the modes m and n for positive and negative directions of propagation.

$$\alpha_{mn}^{\pm} = k_{mn}^{\pm} = \frac{k}{1-M_x^2}\left[-M_x \pm \sqrt{1-(1-M_x^2)\left(\frac{\sigma_{mn}}{kR}\right)^2}\right] \tag{2.40}$$

2.4.7 The cut-off condition

The axial wave number plays an important part in the sound propagation in ducts. The number determines whether propagation in axial direction is able to take place or not. The sound wave is only able to propagate if the wave number $\alpha_{mn}^{\pm}$ is a real number. When looking at equation (2.40) it can be seen that in order this to be the case the term underneath the square root needs to be larger than zero.

$$\frac{\omega}{c} = k > \sqrt{1-M_x^2} \cdot \frac{\sigma_{mn}}{R} \tag{2.41}$$

This equation can also be applied to a flow without a mean velocity by setting $M_x = 0$. If this equation is not fulfilled, the value for α is imaginary and the perturbation either dissipates or grows. Since a higher circumferential modal order m leads to a higher value of σ_{mn} for a given radial mode n, at some point a mode is not able to propagate anymore. These modes that are not able to propagate are called "cut-off". Another limit in terms of propagation is the so called "cut-off frequency" this is the minimum frequency in order for a sound wave to propagate. The cut-off frequency is obtained by rearranging the equation (2.41):

$$f_{cut} = \sqrt{1-M_x^2} \cdot \frac{c\sigma_{mn}}{2\pi R} \tag{2.42}$$

It can be seen that the cut-off frequency scales with $\sqrt{1-M_x^2}$ in the presence of an average flow velocity.

If a mode is cut-on and the axial Mach number is smaller than one (sub-sonic flow) both possible solutions, $\alpha_{mn}^{+}$and α_{mn}^{-}, are able to propagate. The direction of propagation is dependent on the sign of the wave number k. For a Mach number $M_x > 1$ the square root in equation (2.40) cannot be negative and therefore all modes are able to propagate.

3 Experimental Facilities

This section discusses the experimental facilities available and used at the Institute for Thermal Turbomachinery and Machine Dynamics used in this thesis. A schematic view of the experimental facilities available at the Institute can be seen in Figure 3-1.

The backbone of these facilities is an electrically driven 3,3 MW compressor station (CS) providing pressurised air for all test rigs and is located in the second basement of the building. The compressor provides both low pressure (LP) and high pressure (HP) air to supply four different experimental facilities. The compressor station consists of two turbo and one double screw compressors with two coolers. The electrically driven machines can be connected in a highly flexible configuration (serial, parallel and mixed types, with and without cooling) so that air can be provided continuously from 2.5 kg/s up to nearly 16.0 kg/s with a pressure ratio up to 2.9 bar in parallel operation and up to 7.0 kg/s at 10.0 bar in serial operation. The compressed air temperature can be adjusted from about 140°C down to 35°C in the coolers. The air enters the building through mufflers installed in a concrete duct and is sucked into the compressors. After the air is compressed and - if required - cooled it gets to an air distribution system were the compressed air can be delivered to several test facilities. After the air distribution system a bypass line branches off the main pipe. In the case of an emergency, for example collapse of the brake, the bypass valve opens automatically, so that the air flow to the test facility is interrupted. Details on the compressor station can be found in Pirker et al. [73].

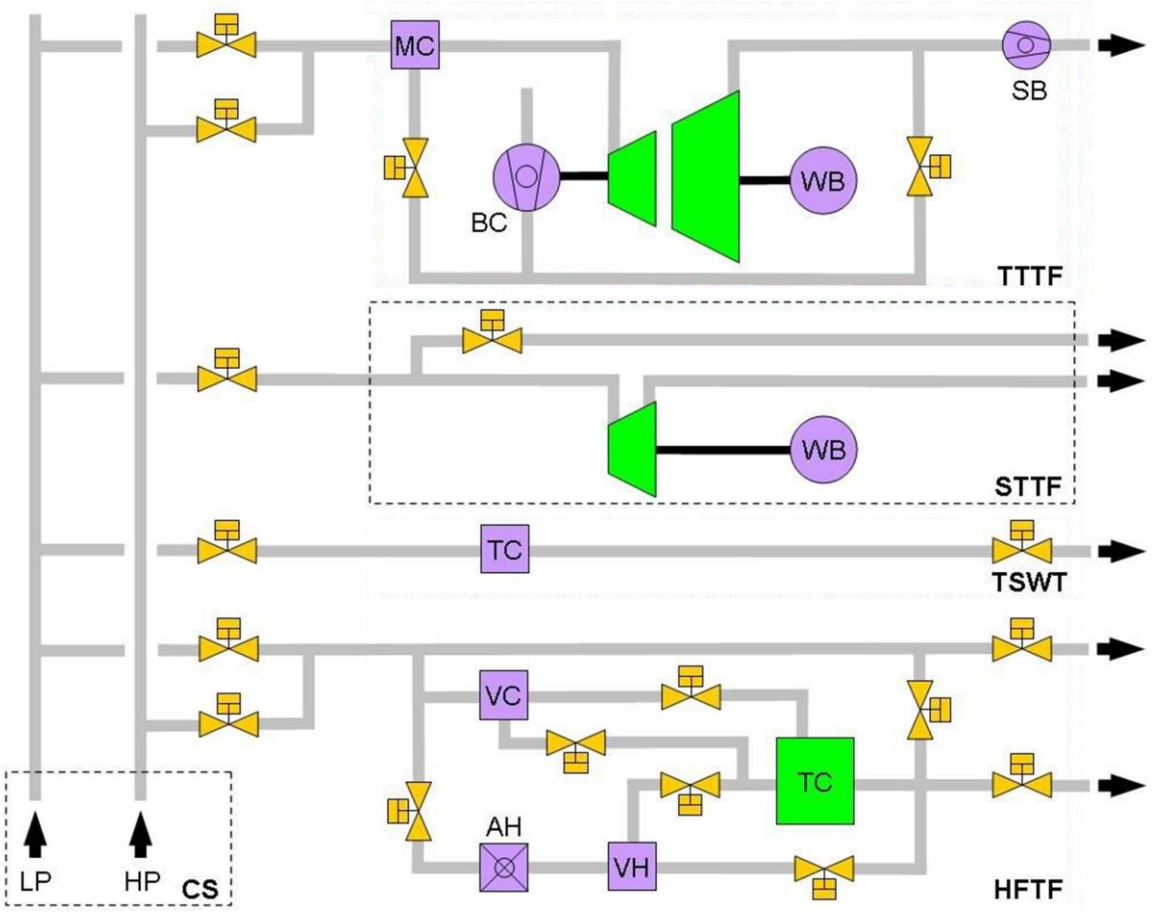

Figure 3-1: Schematic view of the experimental facilities at the ITTM

3.1 Subsonic test turbine facility

The facility used in this thesis is the so called subsonic test turbine facility (STTF). The facility was put in operation during the European project VITAL.

The STTF is supplied with air via the LP supply of the compressor station. This allows for a massflow between 2.5 and 15 kg/s. The maximum inlet pressure of the rig is 2 bar with an inlet temperature of 35°C to 140°C. The inlet pressure is limited due to the admission of the supply piles as well as the inlet casing. The rig is designed for a maximum operating rotational speed of 6300 rpm and a maximum power of 500 kW.

A general arrangement of the test rig can be seen in Figure 3-2. The airflow enters through a spiral inlet casing (3) into the test facility, because the overall arrangement with a water-brake on the inflow side requires a radial inflow to the turbine. In the spiral inlet casing the flow turns into axial direction under generating of an unavoidable swirl in the flow. To provide well defined and controllable inflow conditions a deswirler device (4) is arranged after the spiral inlet casing. As an additional device to achieve uniform flow a perforated metal plate is installed downstream the deswirler. Downstream of the inlet guide vane (IGVs), low pressure turbine stage (5) and the TEC the acoustic measurement section (6) is arranged. The air leaves the rig through the exhaust casing (7). The rotational speed of the facility is controlled by a water-brake (2). The limitations of the rig in terms of torque and rotational speed are largely due to the operating range of this component. In addition, a flywheel has been designed as an additional security measure in case of a break failure (not depicted).

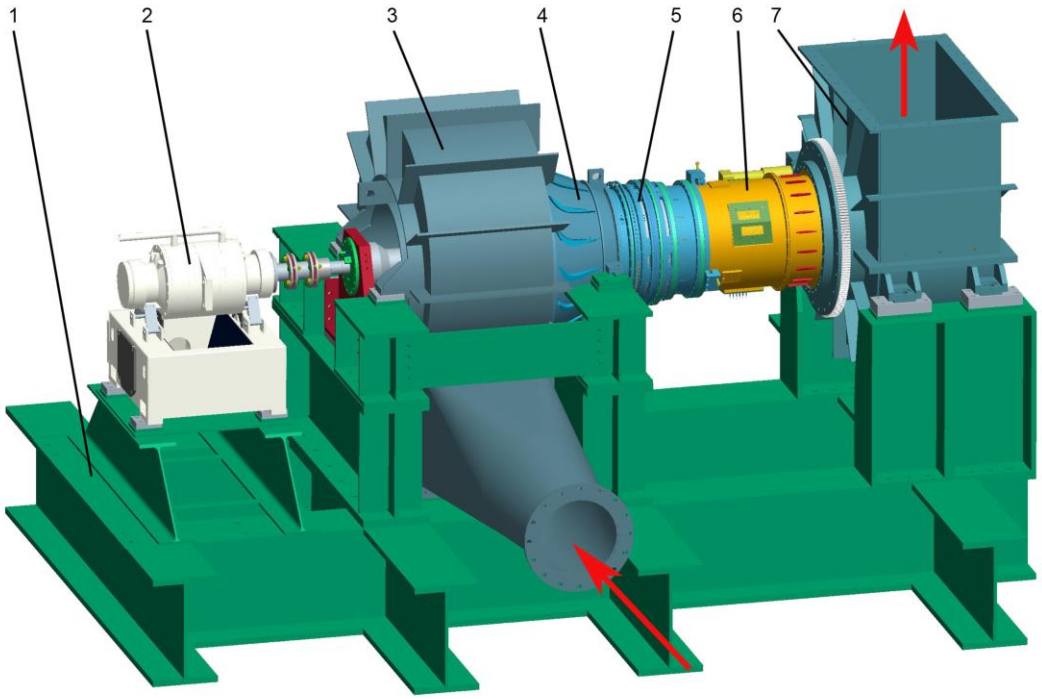

Figure 3-2: subsonic test turbine facility

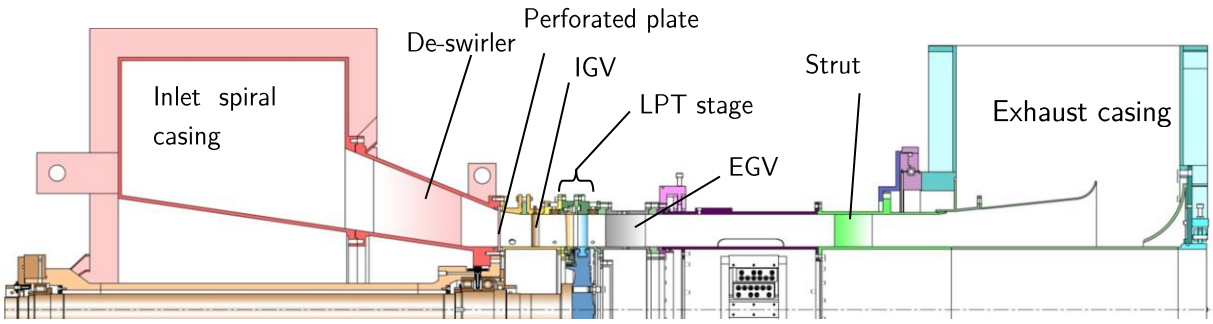

Figure 3-3: cross section of the STTF

The IGVs are used to provide a typical pre-swirl to the LPT stage. The LPT stage itself is designed with an overhung type turbine disk to allow for an easy change of the rotor geometry as well as the stator. This is possible due to the way LPT, TEC and the acoustic measurement section are designed. The acoustic measurement section is not mounted on the rotor casing but rather on the exhaust casing which allows for an axial movement of the section enabling easy access to the TEC/LPT section. The TEC is mounted on the rotor casing and can easily be removed allowing for simple stage access. Details on the construction can be found in Moser [74] and Moser et al. [75].

A cross section of the STTF can be seen in Figure 3-3 where flow path of the rig including the blading can be seen. The flow enters the facility through the inlet casing, the deswirler and the perforated metal plate. The IGV gives a typical pre-swirl for the LPT stator and the following rotor, where the energy is removed from the flow. The EGV turns the flow into the axial direction before entering the acoustic measurement section. This section includes microphone plates on both hub and casing, and is rotatable by 360°. At the exit of the measurement section 17 struts are mounted.

Figure 3-4 shows a sketch of the blade profiles and their arrangement. The profiles are depicted not to scale. The flow direction is shown as a black arrow, the rotational direction of the LPT as a blue arrow. The exit guide vane shown in Figure 3-4 is the so called "Datum" EGV that is used in this thesis and will be further commented on in chapter 3.3.1 .

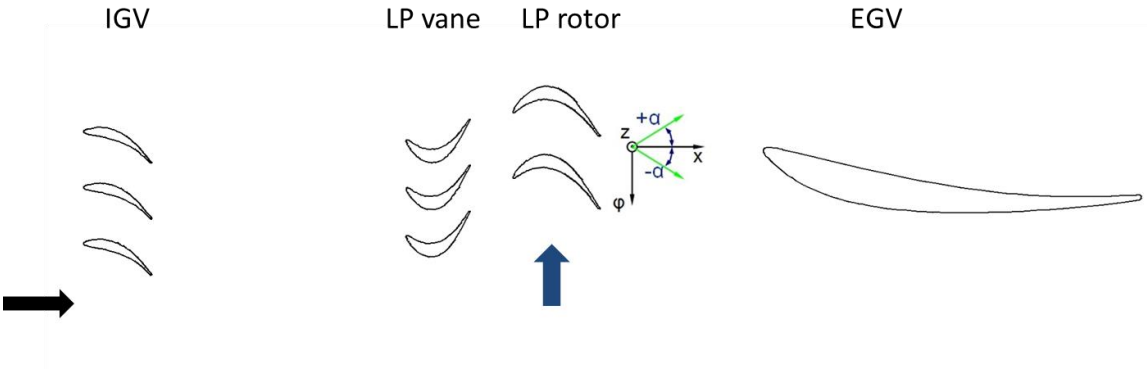

Figure 3-4: Sketch of the profile sections at midspan, not to scale

3.2 Stage setup and operating conditions

This section discusses the geometry details of the turbine setup used for the investigations presented within this thesis. As already explained the test rig consists of an IGV with 83 vanes followed by an LPT stage. The IGV upstream provides the stator of the stage with a typical pre-swirl of approximately 46° across the span.

The stage itself consists of a 96 blades and a rotor with 72 blades. The axial chord length and aspect ratio of the components can be seen in Table 3-1. In addition, the hub to tip ratio of the rig and the axial distance between rotor and stator can be seen. A cross-section of the profiles at midspan can be seen in Figure 3-4. They have been defined using an aero design point of the last stage LPT, derived from current LPT design practice using scaling along reduced speed, reduced mass flow (both referred to 288.15 K and 1013.25 mbar) and pressure ratio.

Table 3-1: Stage geometry details

		IGV	Stator	Rotor
Blade count	-	83	96	72
Axial chord length	mm	20	17	23
Aspect ratio	-	4	4.71	3.48
Turning (at ADP)	deg	45.5	107.1	92.3

Stator rotor axial gap	mm	13
Hub to tip ratio		0.6596

An uncommon feature of the LPT blade used in this rig is the fact that the rig uses an unshrouded rotor. In this case, this results in a tip gap of 1% channel height for the operating points presented later on in this chapter. This results in the formation of a tip leakage vortex that influences the downstream stages. The effect of this tip leakage vortex is discussed in a later chapter.

3.2.1 Operating Conditions

There are two different operating conditions presented in this paper, called "Aero Design Point" (ADP) and "Approach" with different intents. The operating point ADP is designed to present a zero degree of incidence case for the EGV that provides similar Reynolds numbers as the cruise condition whereas the operating point Approach is representative of the conditions found during the landing phase of the airplane. This operating point is one of the operating points for the noise certification of an aircraft according to the ICAO.

Table 3-2 shows the operating conditions for the stages. Due to the fact that the facility is open loop only the stage pressure ratio is set and not the absolute pressure levels for the inlet of the stage.

Table 3-2: Stage operating conditions for Approach and ADP

			Approach	ADP
Total Temperature Inlet	$T_{t,IN}$	°C	370	370
Stage Pressure ratio	$p_{t,IN}/p_{t,OUT}$	-	1.155	1.131
Mass flow	$\dot{m}$	kg/s	7.11	7.1
Reduced massflow			7.07	7.18
Rotational speed	n	rpm	4600	3400
Reduced rotational speed			4059	2997
Stage Loading	dh/u^2	-	1.546	2.358
Flow Coefficient	c_{ax}/u	-	0.787	1.048
Rotor Reynolds number	-	-	150000	165000

These two different operating points result in rather similar Reynolds number but different rotor exit flow angles respectively EGV flow inlet angles. In addition the different Mach numbers result in different Reynolds numbers for the EGVs. The different EGV inlet conditions can be seen in Table 3-3.

Table 3-3: EGV Incidence Conditions

		Approach	ADP
Averaged absolute inlet yaw angle	°	-8.5	-23.45
Averaged relative inlet yaw angle	°	-15	0
Averaged Inlet Mach number		0.21	0.20

3.3 Exit guide vane geometries

As described in the introduction, the main focus on this work is the comparison of multiple EGV geometries for low pressure turbines. Within this thesis a number of EGV geometries are investigated that are presented in this chapter.

3.3.1 Datum EGV

The so called "Datum" EGV is derived from a state of the art EGV that can also be found in current aero engines. During the design process the profile was stripped from a lot of 3D-features usually found in these modern EGV types resulting in a regular radial stacking of the EGV.

shows the vane count and other geometry details of the EGV including the Reynolds number for both operating points. The Reynolds number is calculated using the inlet Mach number and axial chord length.

Table 3-4: Geometry details Datum EGV

Vane count	-	15
Axial chord length	mm	100
Aspect ratio	-	0.8
Diffusion number for ADP	-	0.5
Reynolds Number ADP	-	375000
Reynolds Number Approach	-	340000

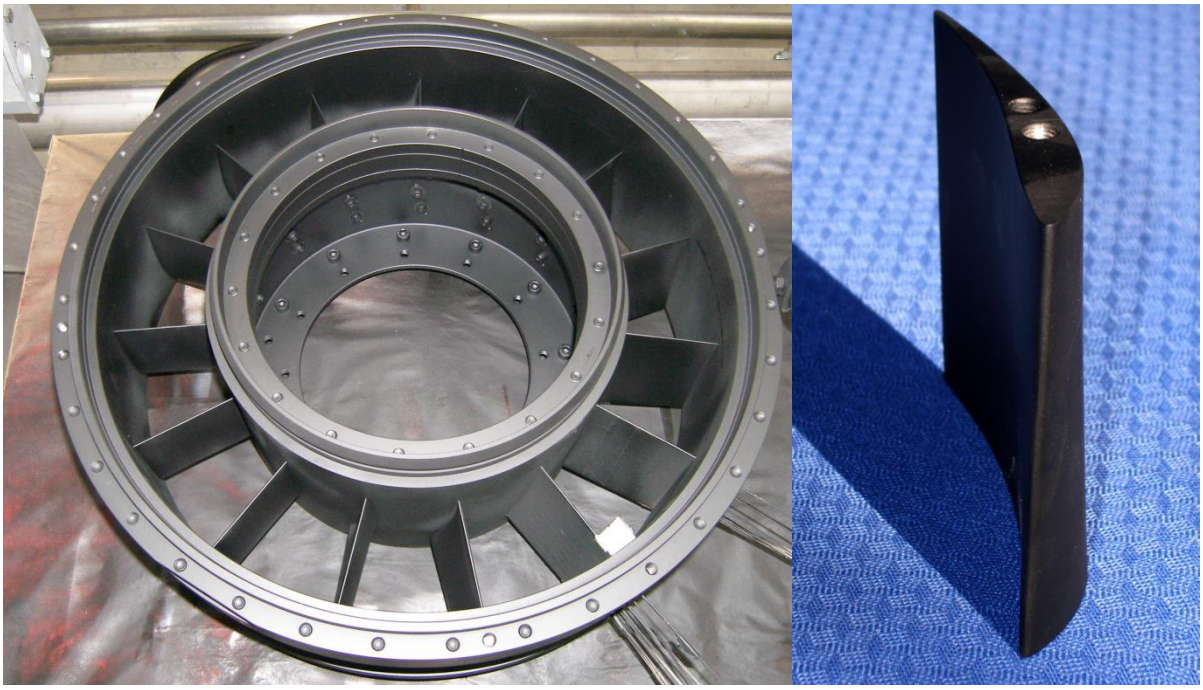

Figure 3-5: Datum EGV; Assembly (left) and single vane (right)

3.3.2 LEANED EGV

The "Leaned" EGV is a modification of the Datum EGV. The modification was performed in order to reduce the overall sound power level downstream of the EGV. An optimisation was performed by Broszat et al. [22]. The work in [22] shows a parametric study of different types of lean and vane count and the influence thereof on overall sound power level. It was shown that a lean that corresponds with the inclination of the wakes of the upstream rotor results in a maximum sound power level whereas a strong difference in inclination decreases overall SPL. Due to the fact that the wakes of the upstream rotor show a 30° inclination in rotational direction of the rotor, this resulted in a EGV lean of 20° against rotational direction of the rotor, the maximum lean investigated in the publication. The vane profiles are similar to the Datum EGV.

Table 3-5: Geometry details Leaned EGV

Vane count	-	15
Axial chord length	mm	100
Aspect ratio	-	0.8
Diffusion number for ADP	-	0.5
Reynolds Number ADP	-	375000
Reynolds Number Approach	-	340000

Figure 3-6: "Leaned" EGV assembly

3.3.3 Inverse Cutoff EGV

The so called "Inverse Cut-off" EGV is based on the idea that the interactions between two airfoils can be designed to be either cut-on or cut-off, meaning the acoustic energy created can either propagate or quickly decay.

It is now possible to design blade row interactions with the specific goal to supress the propagation of one or multiples mode m at a given frequency. For the "Inverse Cut-off" EGV, the main interest is in removing the interaction between the rotor and the EGV for both operating points. After a manipulation of the cut-off condition found in equation (2.41) it can be seen that the suppression of the interaction modes requires the vane (EGV) to blade ratio of the stage needs to be within the limits given in the following equation:

$$\frac{n}{k}\left(\frac{\frac{\omega \cdot r}{a}}{M_\varphi - \sqrt{1-M_x}} - 1\right) \leq \frac{V}{B} \leq \frac{n}{k}\left(\frac{\frac{\omega \cdot r}{a}}{M_\varphi + \sqrt{1-M_x}} - 1\right) \tag{3.1}$$

Further details on the design philosophy and process can be found in [76]. For the rotational speed of the operating point approach, 4600 rpm, this requires the modes to be larger than m = ±21. This is not only necessary for the first interaction k=1 but also the second interaction k=2. The

number of vanes has thus been optimised for these two interactions to not propagate, resulting in a number of vanes that is approximately 3 times the number of vanes for the "Datum" EGV.

Table 3-6: Geometry details "Inverse cut-off" EGV

Blade count	-	>40
Axial chord length	mm	35
Aspect ratio	-	2.28
Diffusion number for ADP	-	0.6
Reynolds Number ADP		131000
Reynolds Number Approach		119000

Figure 3-7: "Inverse Cut-off" EGV, single vanes (left) and assembly (right)

3.3.4 High Loading EGV

This particular EGV was designed based on the original profiles from the "Datum" EGV. The aerodynamically optimised airfoil was designed applying a multi-point optimisation process to the 33% span profile section of the original low aspect ratio EGV. The result of this optimisation was evaluated in multiple 2D-cascade tests at TU Braunschweig (see Koch et al. [19]). The EGV has been designed for the required working range using a loss criterion of 1.5 times minimum loss (compared to e.g. 2 times minimum loss requirement suggested in the NASA SP36 standard definition [77]) to take into account possible real engine effects as e.g. manufacturing tolerances and engine aging. Some details on the vane as well as Reynolds number for the operating points can be found in Table 3-7. The number of vanes is one third of the number of stage stator vanes in order to have identical inlet conditions for all EGVs.

Table 3-7: Geometry details high loading EGV

Blade count	-	>30
Axial chord length	mm	37
Aspect ratio	-	2.16
Diffusion number for ADP	-	0.6
Reynolds Number ADP		139000
Reynolds Number Approach		126000

Figure 3-8: Highly loaded EGV; Single vane (left) and assembly (right)

4 Measurement Setup

The following section explains the measurement techniques used for this thesis. This chapter is split into two main parts: aerodynamic and acoustic measurement techniques.

4.1 Aerodynamic

In this chapter, the equipment and setup used for the aerodynamic measurements is discussed. This includes the 5-hole probe, static pressure taps, Preston tubes, the data acquisition system as well as the oil flow visualisation.

4.1.1 5-Hole Probe

The five-hole probes were used to obtain the flow parameters like total and static pressure, total and static temperature, Mach number, as well as yaw and pitch angle. The probes were manufactured and calibrated at the "Institut für Strahlantriebe und Turboarbeitsmaschinen" at the Rheinisch Westfälische Technische Hochschule (RWTH) Aachen. The probe includes a type K thermocouple mounted on the bottom of the probe head (Figure 4-1) to enable the calculation of the static and total temperature (using provided calibrated recovery factor) as well as the flow velocity. A CAD drawing of the 5-hole probe used can be found in Figure 4-2. The calibration ranges for the five-hole-probe are shown in Table 4-1.

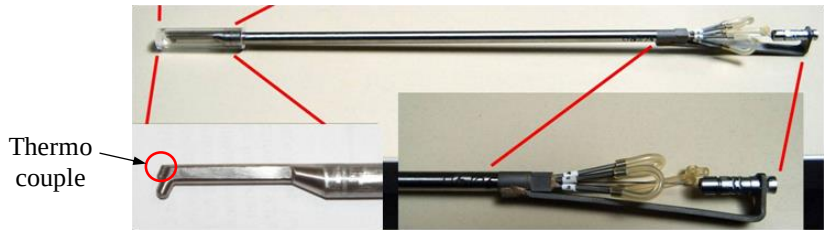

Figure 4-1: Five-hole-probe

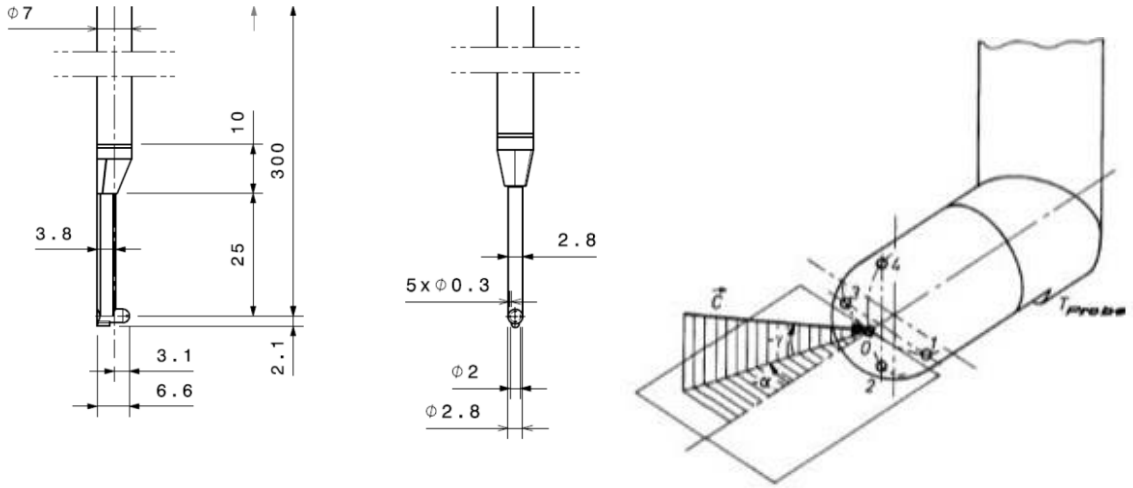

Figure 4-2: CAD Drawing of the five-hole probe

Table 4-1 Calibration range of the 5-hole probe

Flow parameter	Minimum	Maximum	step
Mach number Ma	0.1	0.8	0.1
Yaw angle α	-20	20	4
Pitch angle γ	-20	20	4

To be sure that the probe was always within the calibration range (for the yaw angle) the probe was turned into the flow. Data evaluation is done according the calibration/evaluation report provided by RWTH Aachen [78].

The 5 pressures acquired with the probe are used to define the following non-dimensional parameter:

- Mach number parameter

$$k_{Ma} = \frac{\Delta p}{p_0} \tag{4.1}$$

- Yaw angle parameter

$$k_{\alpha} = \frac{p_3 - p_1}{\Delta p} \tag{4.2}$$

- Pitch angle parameter

$$k_{\gamma} = \frac{p_4 - p_2}{\Delta p} \tag{4.3}$$

With Δp being defined as:

$$\Delta p = p_0 - \frac{p_1 + p_3}{2} \tag{4.4}$$

With these parameters the Mach number, yaw angle, pitch angle, recovery factor a static pressure and a total pressure parameter can be calculated according to the multi-parameter approximation given in [78].

$$Y = \sum_{i=0}^{l} \sum_{j=0}^{m} \sum_{k=0}^{n} \delta_{ijk} c_{Y,ijk} k_{Ma}^{i} k_{\alpha}^{j} k_{\gamma}^{k} \tag{4.5}$$

δ_{ijk} is the well-known Kronecker Delta and $c_{Y,ijk}$ are the calibration coefficients.

Additionally, a static pressure parameter can be defined as well. With these values the static and total pressure can be calculated.

- Total pressure parameter

$$k_{pt} = \frac{p_t - p_0}{\Delta p} \tag{4.6}$$

- Static pressure parameter

$$k_p = \frac{p_0 - p}{\Delta p} \tag{4.7}$$

However, according to the calibration report (Arnold et al. [78]) it is more accurate to calculate the static pressure according the following equation:

$$p = \frac{p_t}{\left(1 + \frac{\kappa-1}{2} Ma^2\right)^{\frac{\kappa}{\kappa-1}}} \tag{4.8}$$

With the included type K thermocouple at the probe tip the total and static temperature as well as the flow velocity can be calculated. These parameters are calculated from the probe temperature, Mach number and the recovery factor.

- Recovery factor

$$r = \frac{T_{probe} - T}{T_t - T} \tag{4.9}$$

- Total temperature

$$T_t = \frac{1 + \frac{\kappa-1}{2} Ma^2}{1 + r\frac{\kappa-1}{2} Ma^2} \tag{4.10}$$

- Static temperature

$$T = \frac{T_{probe}}{1 + r\frac{\kappa-1}{2} Ma^2} \tag{4.11}$$

From this the absolute velocity can be calculated as follows:

$$c = Ma\sqrt{\kappa R T} \tag{4.12}$$

Definition of Flow Parameters

Figure 4-3 shows a general sketch of the flow angle definitions. The direction of flow is defined as x in this figure. The radial direction is r and the circumferential direction φ. The positive direction φ of φ is identical to the rotational direction of the rotor. The green arrow depicts the flow direction that is split into an axial componentc_x, a radial component c_x and a circumferential (tangential) component c_x

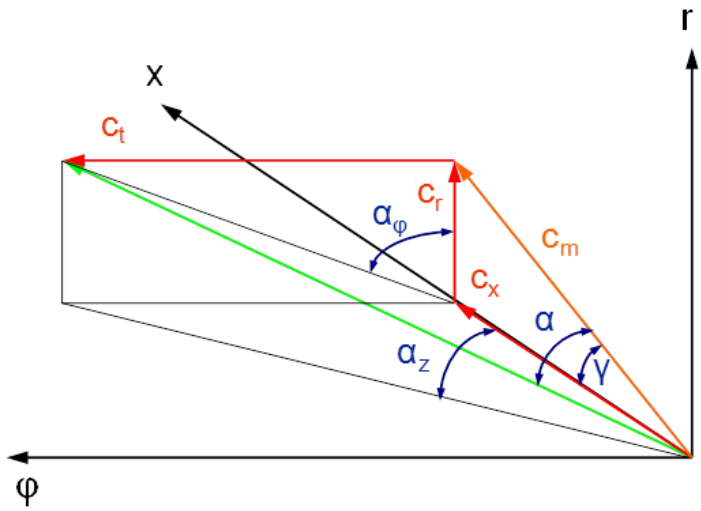

Figure 4-3 Flow angle definition

Angle Definition

The yaw angle (also known as swirl angle) is defined as:

$$\tan \alpha = \frac{c_t}{c_m} \tag{4.13}$$

Where c_m is perpendicular to the measurement plane. This is important for inclined measurement planes. The yaw angle is positive, if c_t shows in the same direction as the circumferential velocity u of the rotor=direction of rotation of the turbine (see Figure 4-4, grey arrow).

Alternatively the yaw angle can be calculated by using $c_x = c_m \cos \gamma$; c_x is parallel to the Machine axis. If the measurement plane is perpendicular to the machine axis $c_m = c_x$.

$$\tan \alpha_z = \frac{c_t}{c_x} \tag{4.14}$$

The pitch angle (radial angle) is defined as:

$$\tan \gamma = \frac{c_r}{c_x} \tag{4.15}$$

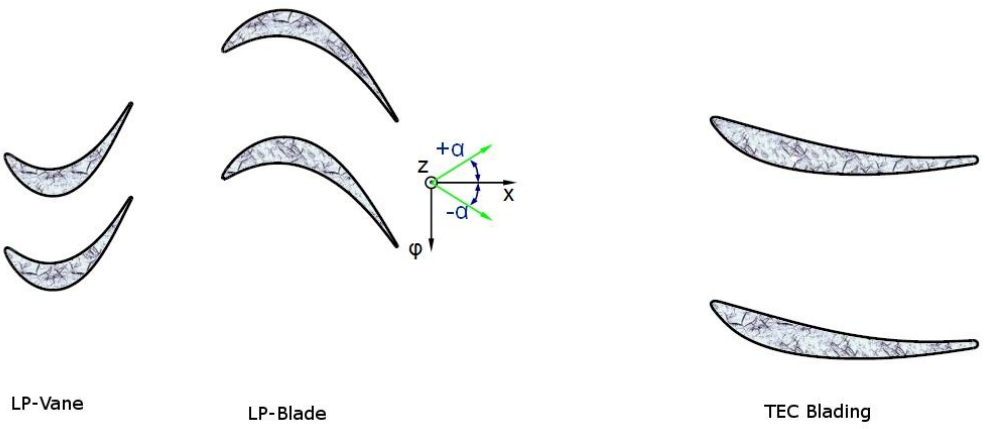

Figure 4-4 Definition of positive direction of yaw angle

γ is calculated in the meridional plane as can be seen in Figure 4-4. The pitch angle is positive, if the velocity vector (exactly the radial component c_r) shows upwards (away from the Machine axis, from hub to tip).

Measurement Systems and Measurement error

The five pressures of the 5-hole probe are evaluated using one of the PSI 9016 modules with a range of 30psi/ 2.068bar. The system is calibrated and has a guaranteed error according to the manufacturer of $\pm 0.05\%$ of full scale, $\pm$1,034 mbar. The full measurement uncertainties can be seen in Table 4-2. Due to the approximation surface received during calibration the probe uncertainties are not symmetrical.

Table 4-2: 5-Hole-Probe measurement uncertainties

Mach number	Ma	0.005	-0.004	[-]
Yaw angle	α	0.3	-0.3	[deg]
Pitch angle	Υ	0.5	-0.4	[deg]
Total Pressure	p_t	3	-3	[mbar]
Static Pressure	p	5.4	-5.1	[mbar]
Total Temperature	T_t	0.6	-0.5	[K]
Static Temperature	T	0.7	-0.8	[K]

Probe Measurement Planes

The test rig has a number of planes that are suitable for probe measurements. The location of these measurement planes can be seen in Figure 4-5. Figure 4-5 shows the available measurement planes, named 0, A, C, D0 and D.

Plane 0 is located approximately 48mm upstream of the IGV leading edge and is equipped with total pressure and temperature rakes for measuring the rig inlet conditions.

Plane A is located approximately 30mm downstream of the IGV/ 26 mm upstream of the stator vanes. This plane is used to characterise the inlet conditions of the stage.

Plane C is located 10mm downstream of the rotor trailing edge and is used to measure the rotor exit conditions. With respect to the leading edge of the EGV, the plane is located approx. 26mm upstream of the EGV.

The plane D0 is unique since it only exists for the two low chord EGVs, the "Inverse Cut-off" EGV and the "Highly Loaded" EGV. The plane is located approx. 20mm downstream of the EGV trailing edge. This distance is identical for both EGVs even though they have a different chord length.

The plane D is identical for all EGVs and is located 230 mm downstream of the leading edge of the EGVs. The distance from the trailing edge is different for each EGV.

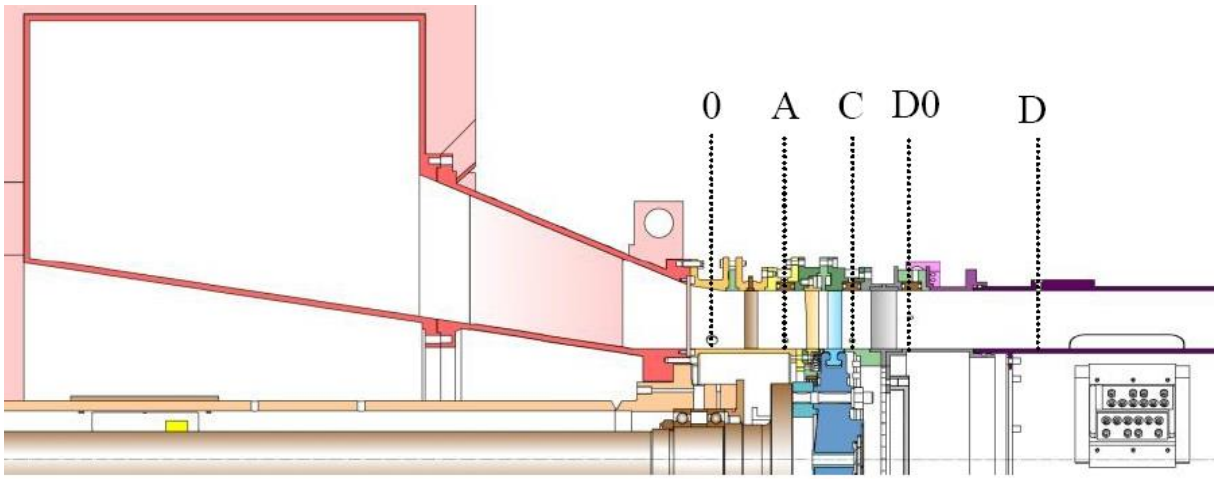

Figure 4-5: Test rig cross-section with probe measurement planes

Measurement sectors and Measurement Grid

As mentioned earlier, there are several measurement planes available within the rig, called 0, A, C and D. Depending on the configuration of the rig an additional plane, called D0, is available.

There are two different types of measurement planes. The planes A, C, and D0 are designed with a rotating ring that is attached to the traversing system. These planes need a separate traversing system to be able to traverse in circumferential direction. The plane D is located in the acoustic measurement section and does not need a separate system for circumferential traversing since the acoustic measurement section itself is rotatable by 360° degree. The measurement sectors are explained in the following section.

Figure 4-6 shows the location of the measurement sectors for the measurement planes available. The view in the picture is from downstream towards upstream (aft looking forwards) as are all the other measurement results in this thesis. Starting at the top of the test rig, the centre of the measurement sectors are located 45° in counterclockwise direction (against the rotational direction of the rotor.

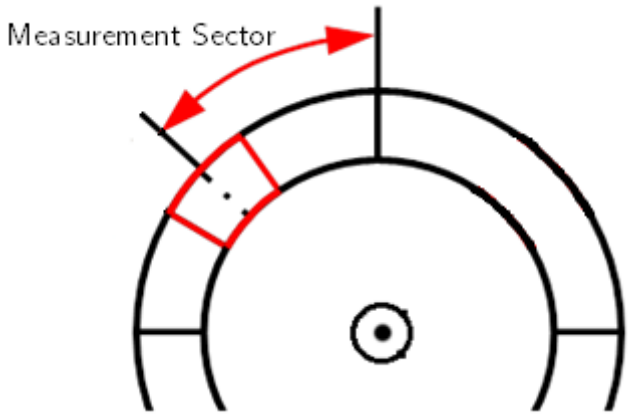

Figure 4-6: Schematic drawing of the location measurement planes within the duct; the planes are marked in red with the angular coordinates, View is from downstream towards upstream

5-Hole Probe Circumferential Measurement Grid

Plane C is located downstream of the rotor, where the influence of the tip leakage flow is the dominant flow feature. The number of upstream vanes is 83/96 and the number of rotor blades is 72. The respective pitches are 4.337°, 3.75° and 5°.

Considering these EGV angles, the rig periodicity including EGV is as shown in Table 4-3. The IGV is not considered for this matter. The periodicity for the high AR vanes (Datum and leaned) is 120° since this is the only common denominator with the 15 vanes of these configurations. The number of vanes of the „Inverse Cut-off" EGV has no common denominator with the stator/rotor count so the periodicity of the rig is 360° for most cases.

Table 4-3: rig periodicity including EGV

EGV geometry	vane/blade count for the whole rig	periodicity
"Datum"/"Leaned" EGV	96/72/15	120°
"Inverse Cut-off" EGV	96/72/>40	360°
"High Loading" EGV	96/72/>30	

Considering these angles, the measured circumferential 5-hole probe pitches are identical to an EGV pitch for all planes. The probe traversing was always performed in counter-clockwise direction.

Radial Measurement Grid 5-hole probe

The radial measurement Grid for the 5-hole probe is identical for all planes, and consists of 21 measurement points as shown below. The radial measurement positions in % of the channel height can be seen in Table 4-4

Table 4-4: radial measurement grid for the 5-hole Probe in % of the channel height

4.125	6.375	8.875	13.875	18.875	23.875	28.875
33.875	38.875	43.875	48.875	53.875	58.875	63.875
68.875	73.875	78.875	83.875	88.875	92.625	95.125

4.1.2 Static Pressure Measurements

All EGVs are equipped with surface static pressure taps. The taps are manufactured at identical radial positions for all geometries. The 4 different radial positions can be seen in terms of absolute and relative channel height.

Table 4-5: Static pressure tabs; radial positions

Relative channel height (%)	20	30	50	80

The axial positions are different for each EGV considering they all have different axial chord lengths. The position of the static pressure taps for the Datum EGV and Leaned EGV can be seen in Table

4-6. Due to the chord length of 100mm the absolute and relative axial position are identical. These positions are the same for all 4 radial positions.

Table 4-6: Static pressure tabs; axial positions in % axial chord

5	14	23	32	41	50	70	90

The axial position of the static pressure taps for the "Inverse Cut-off" EGV can be found in Table 4-7, and for the highly loaded EGV in Table 4-8.

Table 4-7: "Inverse Cut-off" EGV Static Pressure Tabs, axial positions

% axial chord	2.8	8.6	17.1	25.7	34.3	42.9	51.4	60.0	68.6	77.1	94.0

Table 4-8: "Highly Loaded" EGV Static pressure tabs, axial positions

% axial chord	1.5	4.5	7.5	10.5	13.5	16.5	19.5	22.5	25.5	28.5	31.5	34.5

An example of static pressure surface taps can be seen in Figure 4-7 where the static pressure taps of the Datum EGV for three different radial positions can be seen for both suction and pressure side.

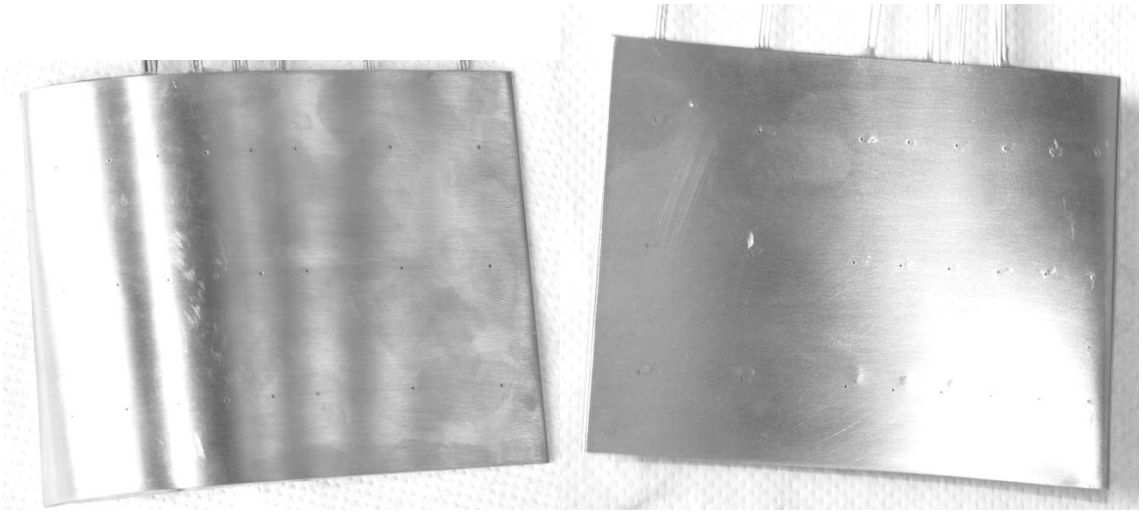

Figure 4-7: Surface pressure tabs

All static pressure taps use a PSI 9016 module with a range of 30psi/ 2.068 bar. The system is calibrated and has a guaranteed error according to the manufacturer of $\pm$0.05% of full scale ($\pm$1,034mbar).

4.1.3 Oil Flow Visualisation

A so called "Oil Flow Visualisation" can be performed to get a qualitative insight into the flow at the vane surface. However, because of the low shear stresses during the operation of this particularly facility the oil film has to have a very low viscosity. This however results in problems during the stat-up of the facility where different flow features can be observed (see Annex) .Figure 4-8 shows an example of an oil flow.

A mixture of titanium oxide and motor oil was applied on the strut (white and/or blue) and the endwalls (pink) in order to distinguish the origin of the identified structures. The result is more or less the trajectories of the wall shear stress.

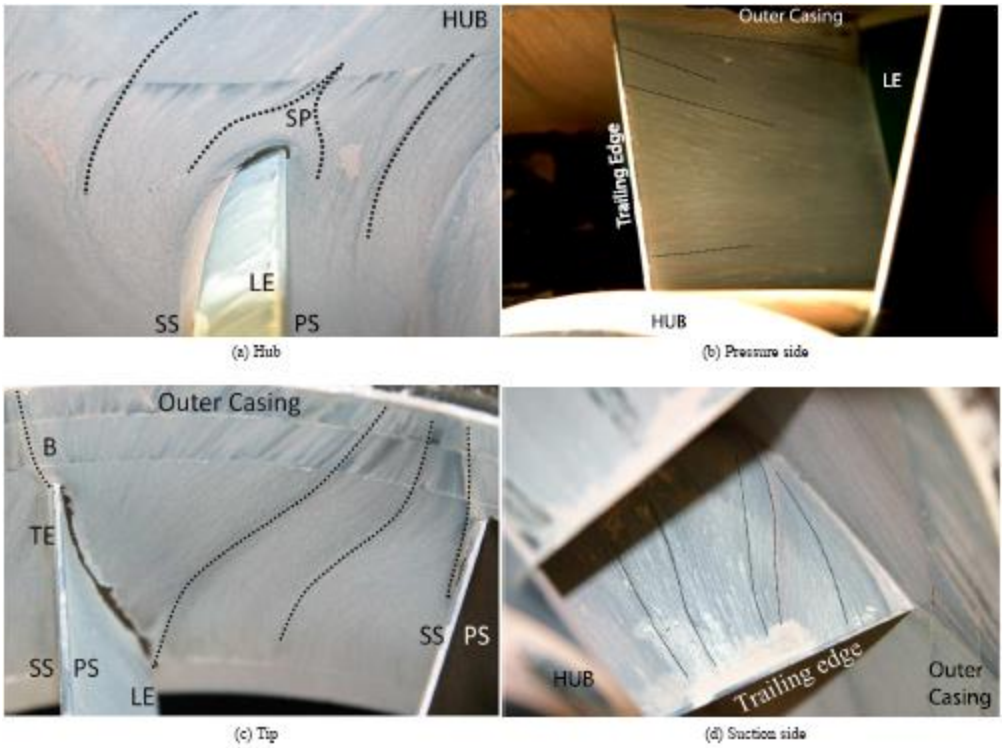

Figure 4-8 Example of an oil flow visualisation for operating point cut-back (not presented in this thesis)

4.2 Acoustic Measurement Setup

In order to perform acoustic measurements in the test rig an acoustic measurement section is placed downstream of the EGV. Due to the fact that for a proper evaluation the fluid properties (Mach number, temperature, and pressure) are needed, the measurement plane D is located in the immediate vicinity of the acoustic measurement section to provide this data. Whenever acoustic measurements are performed, the aerodynamic instrumentation is reduced to a minimum level for acoustic measurements in order to reduce flow disturbances and additional interactions. Figure 4-9 shows the acoustic measurement section. The acoustic measurement section is rotatable by 360° in order to perform full circumferential measurements. There are microphone plates mounted at three different positions at hub and at the casing where microphones can be inserted yet only one of these three circumferential positions is used.

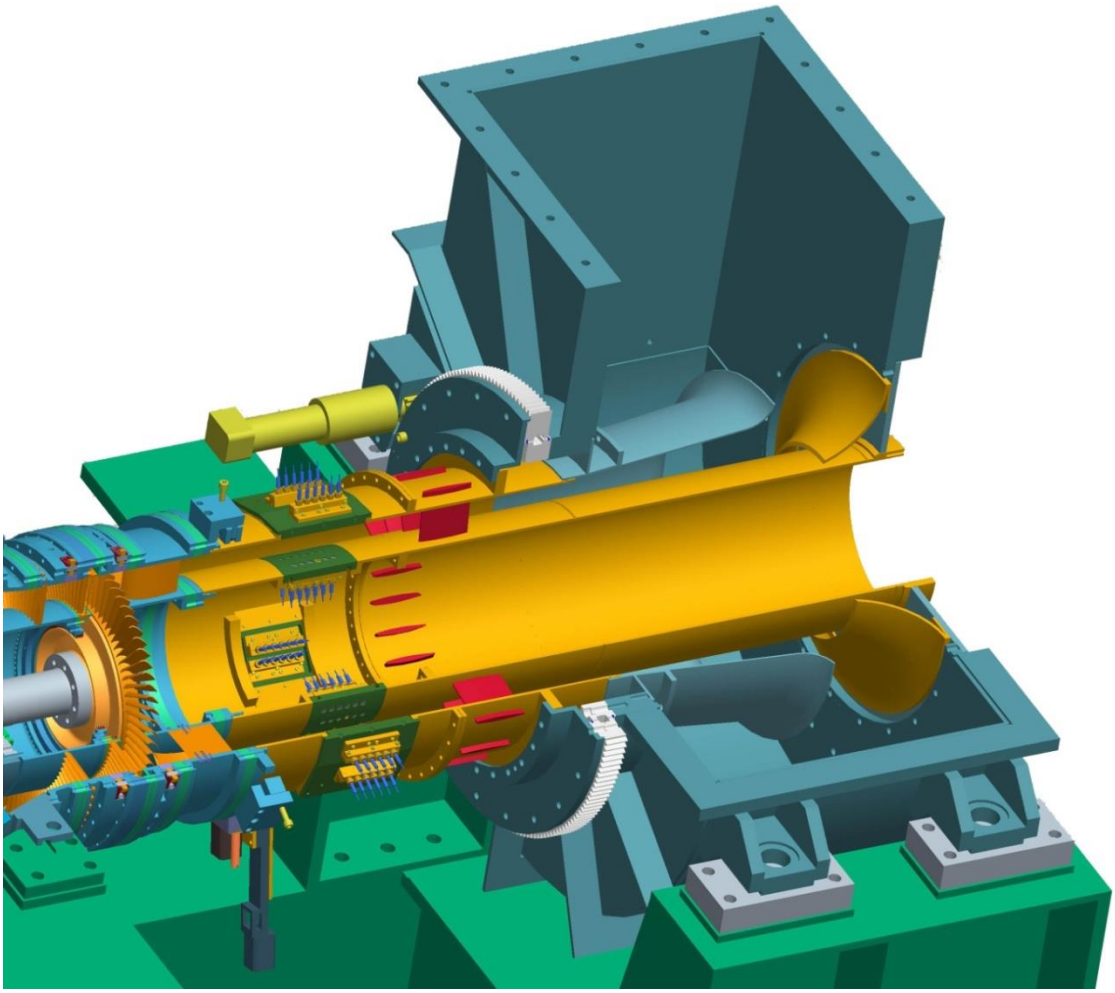

Figure 4-9: Acoustic measurement section

For the acoustic measurements presented in this thesis 24 microphones are used. 12 microphones are mounted at the hub and 12 at the tip. The design of the microphones arrays was performed by DLR Berlin and further details can be found in Moser et al. [21], [75] and Enghardt et al. [79] as well as Broszat et al. [20].

These microphones are mounted in a steel insert, however each microphone is protected by a plastic bush as can be seen in Figure 4-11. The axial distance between each microphone is 7.5 mm. It was

decided to realise this setup in two rows of microphones (named "a" and "b" in Figure 4-10). The distance between microphones in each row is 15 mm. The two rows are angled at 12 degrees and are shifted axially by 7.5 mm. The white arrows in the figure indicate the flow direction.

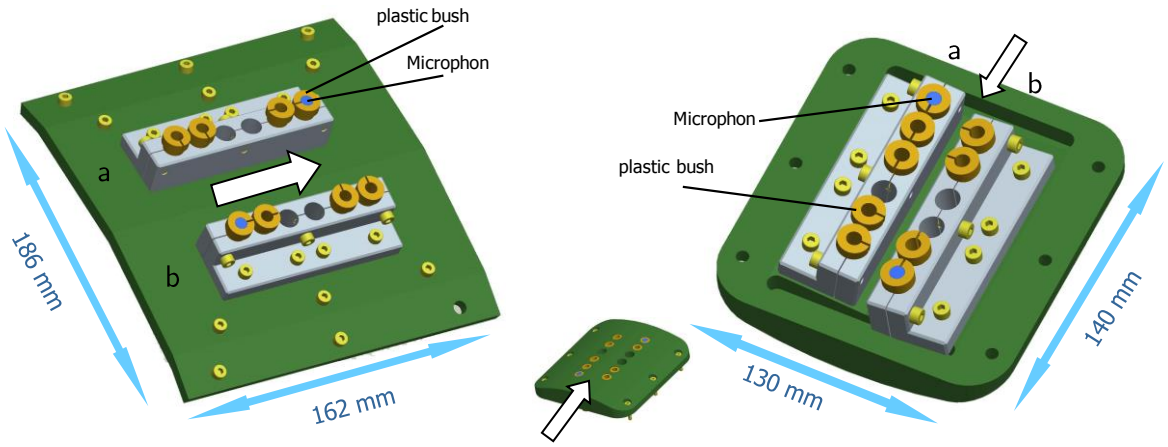

Figure 4-10: Drawing of the steel microphone plates (left: hub, right: casing)

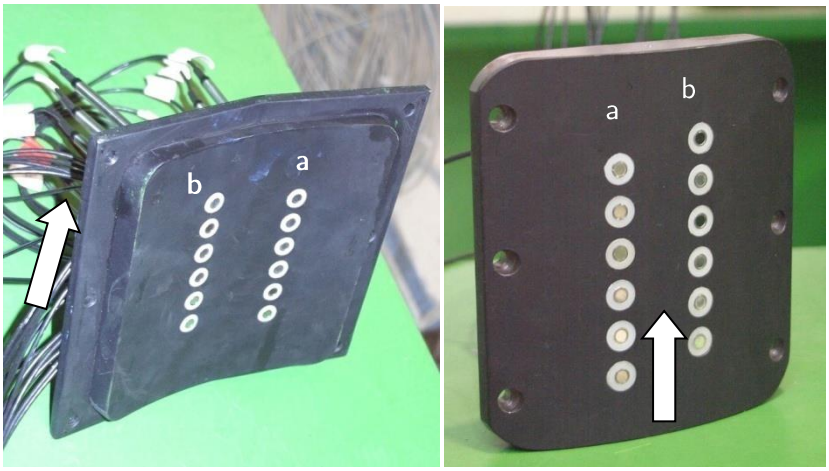

Figure 4-11: Steel plate for the tip microphones (left) and the hub microphones (right)

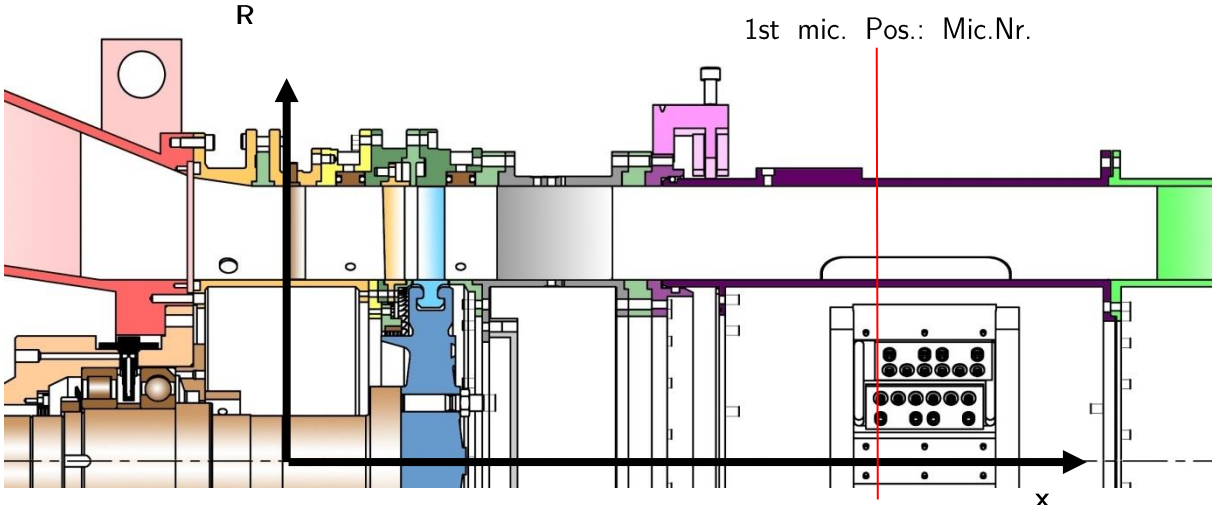

Figure 4-12: Position of the first microphone

The distance from IGV leading edge to the first microphone is +508.50 mm (see Table 4-9 and Figure 4-12).

Table 4-9: Microphone distance from the IGV leading edge

Microphone Distance from IGV LE in mm												
Micro.	Microphone Number											
Row	1	2	3	4	5	6	7	8	9	10	11	12
a	508.5		523.5		538.5		553.5		568.5		583.5	
b		516.0		531.0		546.0		561.0		576.0		591.0

For this investigation one microphone plate at the hub and one at the tip are equipped with microphones, there 360° have to be traversed with step width of 2°. Figure 4-13 shows the full measurement grid.

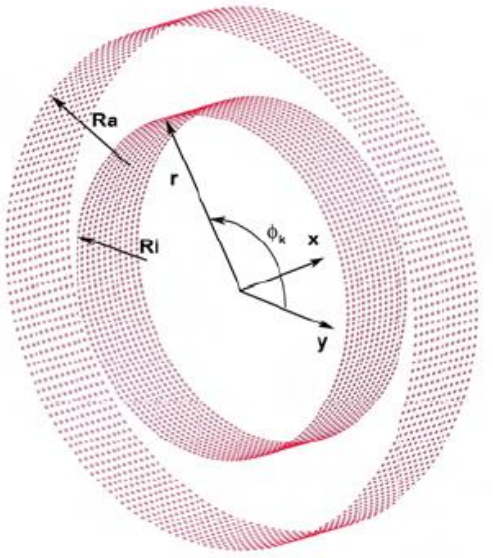

Figure 4-13: Acoustic Measurement Grid

The acoustic measurement arrangement is the same for all setups described in this document.

4.2.1 Measurement hardware

The microphones used are ¼" GRAS 40BD polarised condenser microphones with a GRAS 26AC preamplifier and a GRAS 12AN power module.

The microphones have a frequency range of 4 Hz to 70kHz and a dynamic range of 44dB(A) to 166dbB(A). The microphones have a linear frequency response from 10 Hz up to 25 kHz (±1dB). The sensitivity of the microphones is 1,45 mV/Pa at 250Hz. The preamplifier 26AC has a very low noise level and a large dynamic range. The frequency response ranges from 2 to 200 kHz (± 0.2dB).

The microphones are calibrated with a GRAS 42AA pistonphone before each measurement. The pistonphone generates a 250Hz tone with amplitude of 114dB.

Figure 4-14: Microphone (left) and preamplifier (right)

Data acquisition

The data acquisition is performed using a National Instruments PXI chassis including two PXI 4498 Modules with a total of 32 channels. The PXI 4498 is a high-accuracy data acquisition module with a sampling rate of up to 204.8 kSamples/s including a 24-bit analog to digital converter (ADC)[80]. The chassis uses a PXIe8375 module in order to transfer the acquired date to a PC via fibre-optic cabling. In addition to the 24 Microphones in use, a reference microphone is acquired on channel 25 and the shaft trigger of the rig at channel 26. The sampling rate used is 51.2 kHz resulting in a maximum frequency of 25.6 kHz according to the Nyquist-Shannon sampling theorem. This theorem can also be applied to the maximum circumferential mode that can be detected. The increment between two measurement points $\Delta\theta = 2°$ resulting in $N_\theta = 180$ circumferential measurement positions. This results in a maximum circumferential mode m= ± 90 that is detectable.

The measurement time is dependent on the operating point. The time acquired for the operating point approach ($n = 4600\ 1/\mathrm{min}$) is 15s resulting in 1150 revolutions of the rotor. Due to the fact that the rotational speed of operating point ADP is lower ($n = 3400\ 1/\mathrm{min}$) the time acquired is 20s in order to achieve a similar amount of revolutions acquired, namely 1133 revolutions.

4.2.2 Acoustic Post-processing

The post-processing routine used for post-processing the measurement data is elaborated in the following section. The post-processing consists of the following steps:

- Adaptive resampling
- Phase averaging
- Fourier Transformation
- Azimutal mode analysis
- Radial mode analysis

The methods explained are implemented in this very order to net the results seen in this thesis.

Adaptive resampling

During the measurement process the test rig used in this thesis undergoes a small variation of rotational speed that is usually smaller than $\pm 1\%$ of the rotational speed of the operating point. This leads to an uneven distribution of samples for each revolution of the rig. The adaptive resampling is a procedure to deal with this uneven distribution of samples. It requires a trigger giving a once-per revolution signal in order to resample the recorded raw signal. The necessary trigger signal is obtained from the Bentley Nevada shaft surveillance system. This signal is used to resample

the raw signal to a new signal with a constant number of samples per revolution. In order for this procedure to work properly the following equation has to be satisfied

$$nn = 2^k < \frac{f_s \cdot t}{n_{period}} = na \tag{4.16}$$

In this equation, nn is the number of samples per revolution in the resampled signal, which is preferably a number that results from a power of 2. While this is not necessary for the procedure, it accelerates the procedures following the resampling when using Matlab [81]. The variable f_s is the original sampling frequency, t is the measured time of the raw signal and n_{period} is the number of revolutions in the original signal. The variable na is the calculated number of samples per revolution in the original signal. The variables n_{period} and na are not necessarily integer numbers. This means that the number of samples in the resampled signal needs to be smaller than the original number of samples.

Phase Averaging

After the adaptive resampling of the raw signal a phase averaging is performed. In general, a measured signal can be decomposed into three major components [82]:

$$p(t) = \bar{p} + \langle p(t) \rangle + p'(t) \tag{4.17}$$

In this formula, $p(t)$ is the time-dependent measured fluid property, $\bar{p}$ is the time averaged value, $\langle p(t) \rangle$ is the periodic component of the signal and $p'(t)$ is the stochastic fluctuation in the time dependent signal. The phase averaging procedure averages the previously resampled revolutions into one single representative revolution. Since the stochastic fluctuations $p'(t)$ are different for each revolution, the averaging procedure significantly reduces or, if the number of revolutions is large enough, removes the stochastic fluctuations from the signal resulting in a new signal $\tilde{p}$ that only consists of the average and periodic components:

$$\tilde{p}(t) = \bar{p} + \langle p(t) \rangle \tag{4.18}$$

Modal Analysis

Based on the concepts explained in chapter 2.4.4 the routine used for extracting this information is explained in the following section. As already discussed, the solution of the wave equation (2.29) is necessary in order to be able to achieve a solution for the sound field. Another solution to this problem was introduced by Munjal [83]. He states the solution as follows:

$$p'(x, r, \theta, t) = \sum_{m=-\infty}^{\infty} \sum_{n=0}^{\infty} \left(A_{mn}^{+} e^{ik_{mn}^{+} x} + A_{mn}^{-} e^{ik_{mn}^{-} x} \right) f_{mn}\left(\sigma_{mn} \frac{r}{R}\right) e^{im\theta} e^{-i\omega t} \tag{4.19}$$

This complex Fourier series describes the time and space dependent sound pressure p' in a duct at an angular frequency ω through a superposition of solutions called modes. Every mode (m,n) consists of a circumferential mode m and a radial mode n and describes a characteristic pressure distribution within the channel. A_{mn}^{+} and A_{mn}^{-} describe the amplitudes of the sound propagation in (+) and against (-) flow direction with the corresponding wave numbers k_{mn}^{+} and k_{mn}^{-}. The shape

factor $f_{mn}\left(\sigma_{mn}\frac{r}{R}\right)$ describes the geometry of the channel and consists of Bessel functions for hard walled boundary conditions. It is defined as follows:

$$f_{mn}\left(\sigma_{mn}\frac{r}{R}\right)=\frac{1}{\sqrt{F_{mn}}}\left(J_m\left(\sigma_{mn}\frac{r}{R}\right)+Q_{mn}Y_m\left(\sigma_{mn}\frac{r}{R}\right)\right) \tag{4.20}$$

In this formula J_m is the Bessel function 1st kind and Y_m the Bessel function 2nd kind of the respective mth order. These are functions of the respective eigenvalues σ_{mn} and the hub-to-tip ratio$\eta = r/R$, where R is the outer radius and r the inner radius. The definition of Q_{mn} is as follows:

$$Q_{mn}=-J'_m(\sigma_{mn}\eta)/Y'_m(\sigma_{mn}\eta) \tag{4.21}$$

This variable is zero for a duct without hub. The variable F_{mn} is a normalising factor transforming the orthogonal system into an orthonormal eigensystem [68][82].

$$F_{mn}=\begin{cases}\frac{1}{2}[1-\eta^2], & m=n=0\\ \frac{1}{2}\left[\left(1-\frac{m^2}{\sigma_{mn}^2}\right)\hat{f}_{mn}^2(R)-\left(\eta^2-\frac{m^2}{\sigma_{mn}^2}\right)\hat{f}_{mn}^2(\eta R)\right], & otherwise\end{cases} \tag{4.22}$$

with:

$$\hat{f}_{mn}(r)=J_m(\sigma_{mn}\eta)+Q_{mn}Y_m(\sigma_{mn}\eta) \tag{4.23}$$

As seen in chapter 2.4.6 the presence of an axial mean flow gives the following wave number:

$$k_{mn}^{\pm}=\frac{\tilde{k}}{1-M_x^2}\left[-M_x\pm\sqrt{1-(1-M_x^2)\left(\frac{\sigma_{mn}}{\tilde{k}R}\right)^2}\right] \tag{4.24}$$

All these equations assume a swirl free exit flow. In real world examples this cannot always be assumed so that the swirl has to be taken into account. One of the easiest cases is by assuming a rigid body swirl with an angular frequency ω that modifies the wave number.

$$\tilde{k}=\frac{\omega}{c}-\frac{m\Omega}{c} \tag{4.25}$$

Due to the fact that the topic of this thesis are EGVs, structures whose purpose is to remove swirl from the flow it is assumed that the swirl component downstream of the EGV is negligible.

Azimuthal mode analysis (AMA)

When looking at the solution to the wave equation according to Munjal (see equation (4.19)), the unknown amplitudes A_{mn}^{+} and $A_{mn}^{-}$of the modes (m,n) can be determined. This is done by measuring the sound pressure p' using a procedure called the azimuthal mode analysis that is being performed for certain frequency. This is usually only done for frequencies of interest, in our case the BPF and its harmonics. For every circumferential mode m, the complex amplitude $A_m(x,r)_f$ at a frequency f can be expressed as follows.

$$A_m(x,r)_f = \sum_{n=0}^{\infty} \left(A^+_{mn,f} e^{ik^+_{mn}x} + A^-_{mn,f} e^{ik^-_{mn}x} \right) f_{mn}\left(\sigma_{mn}\frac{r}{R}\right) \tag{4.26}$$

Introducing this formula into equation (4.19) this results in:

$$p'(x,r,\theta,t) = \sum_{m=-\infty}^{\infty} A_m(x,r)_f e^{im\theta} e^{-i\omega t} \tag{4.27}$$

The first step of this procedure is a transformation of the signal into the frequency domain using a discrete Fourier transformation (DFT).This results in the complex sound pressure at a given frequency for a certain measurement position (axial, radial, circumferential) of a microphone. The amplitude A_m of a given circumferential mode m at the frequency f can be calculated according to [84]:

$$A_m(x_0,r_0)_f = \frac{1}{N_\theta} \sum_{k=1}^{N_\theta} p(x_0,r_0,\theta_k)_f e^{-im\theta_k} \tag{4.28}$$

In this formula, N_θ is the number of circumferential measurement positions and x_0 and r_0 are radial position of the microphone. An alternative post-processing procedure using cross correlation with a reference microphone is also explained by Sijtsma and Zillmann [84]. The amplitudes A_m are calculated using the reference pressure p_0 and it's conjugated p_0^* as follows:

$$A_m(x_0,r_0)_f = \frac{1}{N_\theta} \sum_{k=1}^{N_\theta} \frac{p(x_0,r_0,\theta_k)_f \cdot p_0^*}{\sqrt{p_0 \cdot p_0^*}} e^{-im\theta_k} \tag{4.29}$$

When performed for all modes m this procedure results in the modal amplitudes for all circumferential modes at a given frequency.

Radial mode analysis (RMA)

In order to gain a full insight into the sound field another post-processing step is necessary. This is due to the fact that the AMA only nets the circumferential mods m, but not the radial modes n as seen in Figure 2-8. The goal of the so called "radial mode analysis" (RMA) is to provide the amplitudes A^+_{mn} and A^-_{mn}. This can be done using the results of the AMA to transform equation (4.26) into a system of linear equations of the order m [85].

$$\boldsymbol{A}_m = \boldsymbol{W}_m \boldsymbol{A}_{mn} \tag{4.30}$$

In this equation, $\boldsymbol{A}_m$ is a vector of the length m containing the azimuthal modes from the AMA. The vector has, for an axial positioning of the microphones the size $(N_x \times 1)$ with N_x being the number of axial microphone positions. The term $\boldsymbol{A}_{mn}$ is the vector of the radial modes for both directions of propagation and has the size $(1 \times 2n_{max})$ with n_{max} being the highest radial mode able to propagate. The matrix $\boldsymbol{W}_m$ therefore needs to be the size $(N_x \times 2n_{max})$ and contains terms containing the form factor f_{mn}, the axial wave number $k^{\pm}_{mn}$ and the axial position of each microphone:

$$W_{mn} = f_{mn} e^{ik^{\pm}_{mn}x} \tag{4.31}$$

Due to the fact that the unknown term $\boldsymbol{A}_{mn}$ is on the right of equation (4.30) leads to an inverse problem of the following form:

$$\boldsymbol{A}_{mn} = [\boldsymbol{W}_m^H \boldsymbol{W}_m]^{-1} \boldsymbol{W}_m^H \boldsymbol{A}_m \tag{4.32}$$

In this equation the pseudo-inverse of $\boldsymbol{W}_m$ is calculated using the adjunct Hermitian matrix$\boldsymbol{W}_m^H$. Due to the fact that this system of equations is overdetermined, meaning there are more equations than unknown, and the solvability of the system is strongly dependent on the conditioning of the square matrix $\boldsymbol{W}_m^H \boldsymbol{W}_m$ the system is unstable. The conditioning f the matrix $\boldsymbol{W}_m^H \boldsymbol{W}_m$ is dependent on the number of radial modes n, the frequenzy f, the hub-to-tip ratio η as well as the flow properties and the geometry of the microphone array used. The solution of this system of equations is only solvable up to a given frequency and radial mode order for a given microphone setup. This is limited by the order of the numerical error in the post-processing [85]. This is why a "least-mean-squares fit" LSQR is used, which solves the problem $\boldsymbol{Ax} = \boldsymbol{b}$ by minimizing the error for x.

$$min\|\boldsymbol{Ax} - \boldsymbol{b}\|^2 \tag{4.33}$$

For a matrix with a bad conditioning or who's rank is smaller than the number of columns a method is proposed in [86]. This method uses a dampening term to stabilise the system and, instead of using the results of the AMA for the RMA directly computes the modes of the RMA from the sound pressure. This requires the entries in the matrix $\boldsymbol{W}_m$ to be extended with the term $e^{-im\varphi_k}$ and the equation (4.30) is rearranged to:

$$\boldsymbol{p}' = \boldsymbol{W}_m \boldsymbol{A}_{mn} \tag{4.34}$$

The solution of the equation yields the amplitudes $\boldsymbol{A}_{mn}$.for the radial mode analysis. For the evaluation of a sound source the whole sound power level of this source is evaluated.

The energy transported in axial direction with each mode in a cylindrical hard walled duct can be calculated according to Morfey [87] when the modal amplitudes A_{mn} are known:

$$\begin{aligned} P_{mn}^{\pm} &= \frac{\pi R^2}{\rho c} \frac{\alpha_{mn}(1 - M_x^2)^2}{(1 \mp \alpha_{mn} M_x)^2} \left| A_{mn}^{\pm} \right|^2 \\ \text{mit } \alpha_{mn} &= \sqrt{1 - (1 - M_x^2) \left(\frac{\sigma_{mn}}{\tilde{k} R} \right)^2} \end{aligned} \tag{4.35}$$

5 Discussion of Results

The following section discusses the measurement results of the different EGV configurations presented in section 3.3 for both operating points, ADP and Approach.

At first the rotor exit / EGV inlet conditions will be discussed for a given operating point and it will be validated that all EGV have similar inlet conditions in order to be comparable. Thereafter the flow field of each EGV will be discussed separately, followed by a comparison of the EGVs for each operating point.

5.1 Aero Design Point (ADP)

5.1.1 Rotor Exit Flow Field

The following section details the flow field downstream of the rotor. Figure 5-1 shows the total pressure distribution in plane C downstream of the rotor. When looking at the total pressure distribution in Figure 5-1 three different sections can be identified. One section is located between the hub and approximately 20% span. This section is dominated by the secondary flows of both the rotor and the upstream stator as well as the interaction of these two structures. The region between 20% and approximately 85% span is dominated by the 2d-interaction between the stator and the rotor as described in literature. The flow field shown in the figures below shows radial structures that are due to the upstream stator wakes. Structures emanating from upstream vanes are always shown as radial structures whereas structures that are due to the rotor are seen as circumferential bands due to the pneumatic probe functioning as a low pass filter. This means that while the radial distribution is very strongly dependent on the rotor, the effects of the rotor in the 2d-flow field will be seen as circumferential bands. Close to the casing a region of low total pressure stretching in circumferential direction can be identified that is due to the tip leakage vortex present in this region of the blade. At the casing, the total pressure increases due to the jet generated by the tip gap. The maximum total pressure can be seen at approximately 25% span.

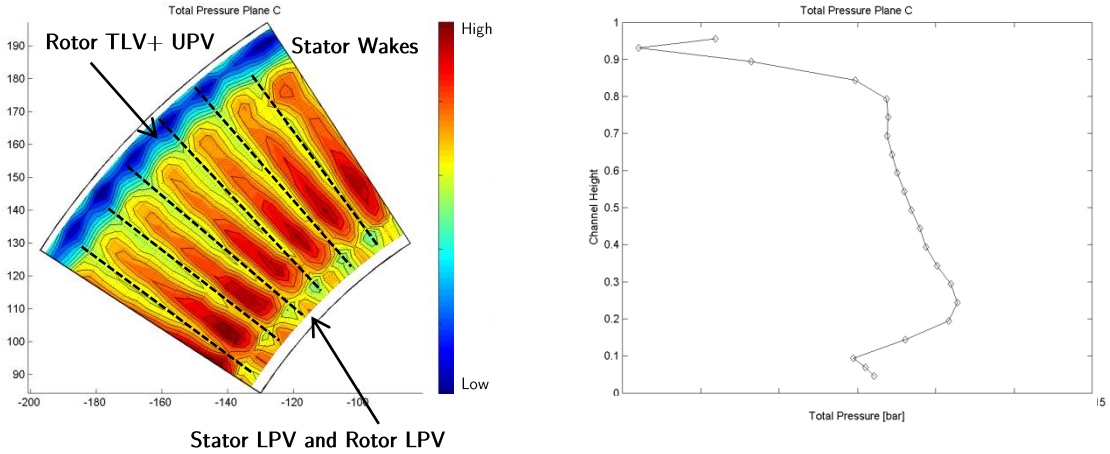

Figure 5-1: Total Pressure distribution plane C

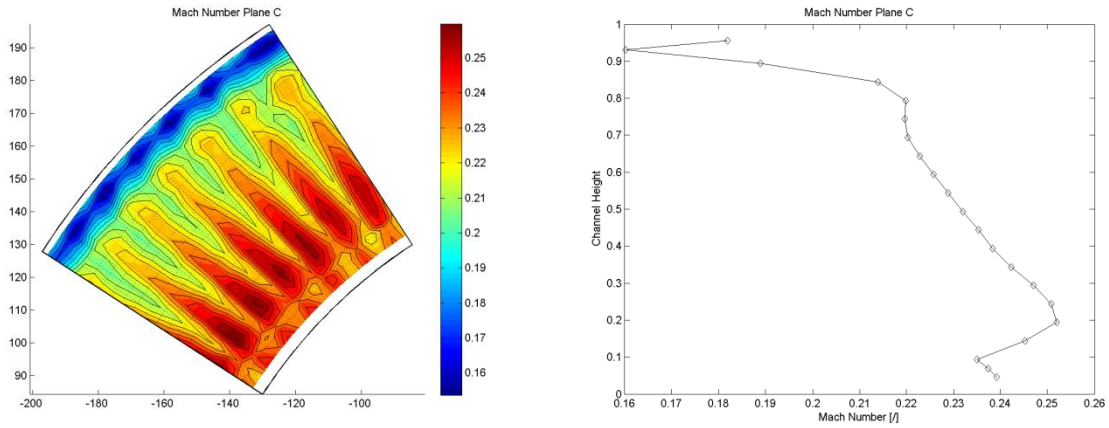

Figure 5-2: Mach number distribution plane C

This is also the location where the maximum Mach number can be found as seen in Figure 5-2. The radial as well as circumferential distribution of the velocity is similar to what was seen in the total pressure distribution. There is a strong decrease in Mach number close to the casing where the influence of the tip leakage flow can be identified as well as close to the hub where the hub secondary flow influences the flow field.

The static pressure distribution in Figure 5-3 shows an almost linear radial pressure distribution as required by the radial equilibrium of the swirling flow. Close to the endwalls this distribution is influenced by the secondary flows as well as the tip leakage flow. This leads to a flattening of the otherwise present static pressure distribution in these areas.

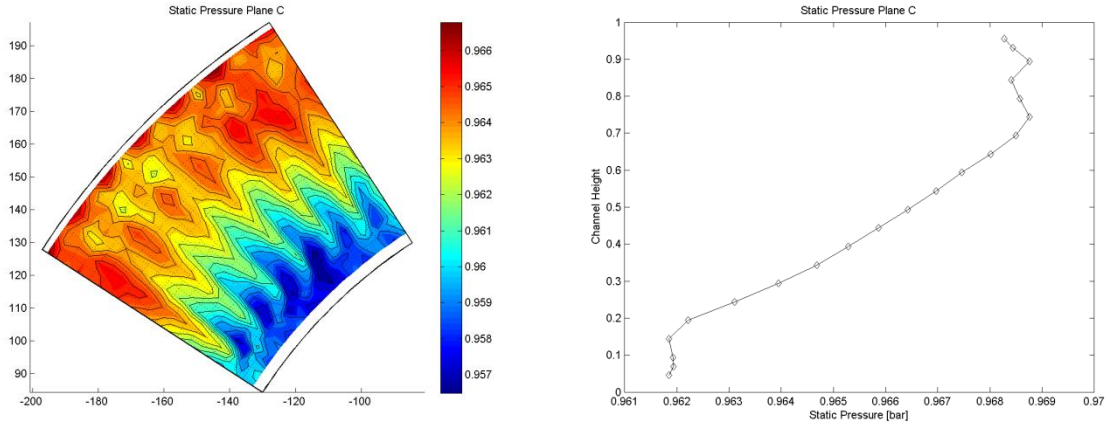

Figure 5-3: Static pressure distribution plane C

The total temperature distribution in Figure 5-4 shows a strong increase in total temperature close to the endwalls where there is a lack of work being performed by the rotor due to secondary flows and the tip leakage flow. At approximately midspan the rotor shows the lowest total temperature due to the high work performed in this region.

The yaw angle distribution is shown in Figure 5-5, where a steady increase in yaw angle from the hub towards the casing can be identified. This is largely due to the design intent of the stage. Close to the casing the influence of the leakage flow can be seen. This results in a lack of turning in this region resulting in a strong increase in yaw angle close to the casing. Close to the hub the influence of the secondary flow can be seen as small variations in the circumferentially averaged distribution.

The influence of the upstream stator onto the circumferential variation of the averaged yaw angle is in the magnitude of $\pm$ 1.5 degree.

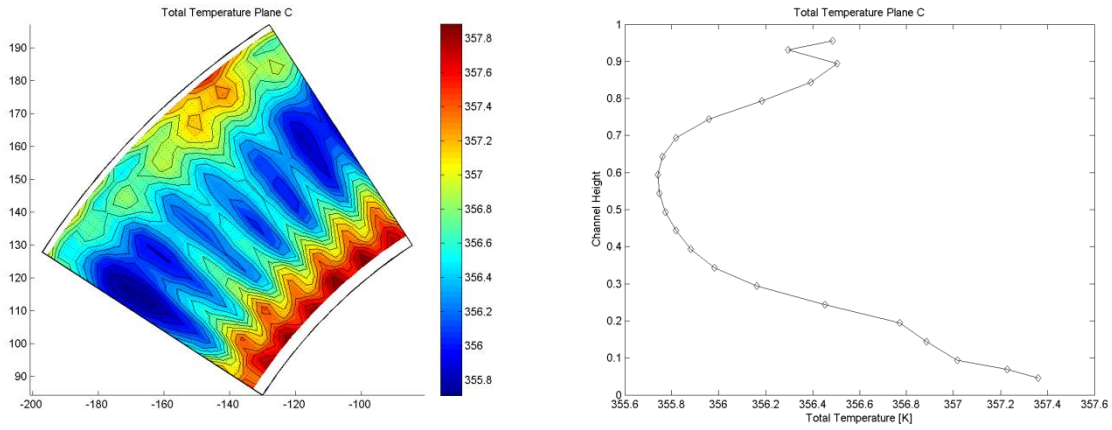

Figure 5-4 Total temperature distribution plane C

The pitch angle distribution can be seen in Figure 5-6. As already seen in the total pressure distribution the flow field is split into three distinct regions. Close to the hub the secondary flow causes a change in pitch angle towards a more negative value. The same can be seen close to the casing where the tip leakage flow results in the tip leakage vortex.

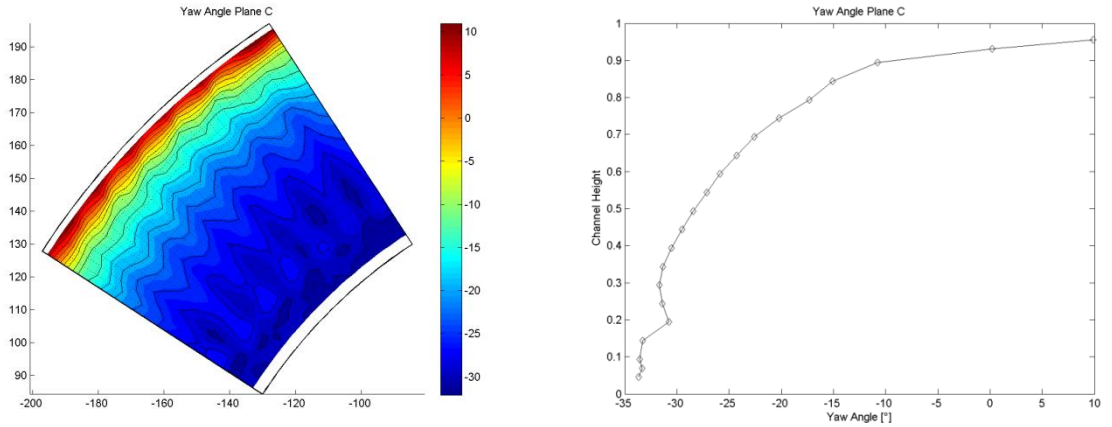

Figure 5-5: Yaw angle distribution plane C

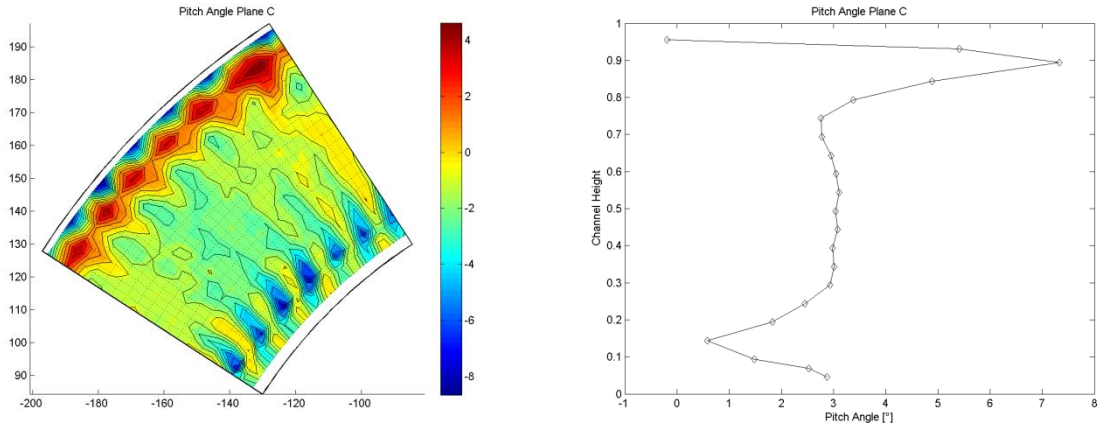

Figure 5-6: Pitch angle distribution plane C

Comparison plane C Flow properties for different EGV

The following section compares the different EGV exit flow fields in order to show all EGVs have similar inlet conditions in order to be comparable. The Figure 5-81 shows the comparison of yaw angle (left) and total pressure (right) for all four different EGVs used in this thesis.

The yaw angle distribution is shown on the left of Figure 5-7 and shows an identical radial distribution for all four EGV. In terms of absolute values the difference in mass averaged yaw angle between the operating points for the different EGVs is ±1.1 deg with respect to the operating point of the "Datum" EGV. This difference is largely due to two reasons, the open loop facility and the possibility of control of the compressor facility used to supply the air for the LPT test rig. This shows that the yaw angle has a good agreement between the different operating points.

The total pressure coefficient is shown in the right of Figure 5-7 shows identical radial distributions for all four different EGVs. The radial distribution of the total pressure coefficient is identical for all four different EGVs. The overall agreement for all 4 EGVs is very good and the inlet conditions for all EGV are identical.

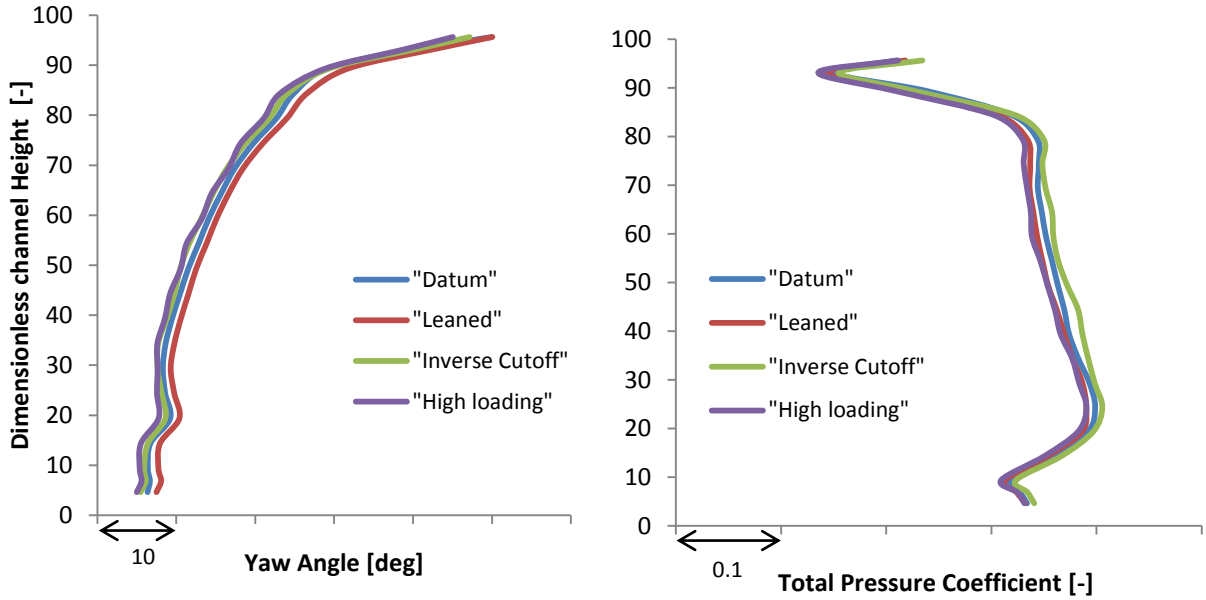

Figure 5-7: Comparison of the ADP rotor exit flow fields for all EGVs; Yaw angle (left) and Total pressure (right)

5.1.2 Discussion of the EGV Flow fields

5.1.2.1 Datum EGV

5-Hole probe plane D

The following section deals with the flow field downstream of the EGV in plane D. The wake of the vane, here defined by the minimum total pressure at a given radial position can be seen as a black dotted line. This wake has also been put into the other depictions of the flow field. The total pressure distribution of the vane exit flow field can be seen in Figure 5-8. In addition to the wake two distinct regions of low total pressure can be identified. One region is located close to the hub within the wake region. This region is joined by another smaller region of lower total pressure located on the suction side of the vane close to the hub. This region is due to the hub secondary flow present close to the casing. This can also be identified by the positive yaw angle in Figure 5-9, where the averaged yaw angle gets progressively positive close to the casing. This region is confined to a region very close to the casing due to the dominance of the upper passage vortex and the tip leakage flow of the vane. The low total pressure is due to the hub secondary flow pushing the fluid from the pressure towards the suction side and along the suction side surface towards midspan of the vane. This structure stays confined to the hub and is responsible for the low total pressure region.

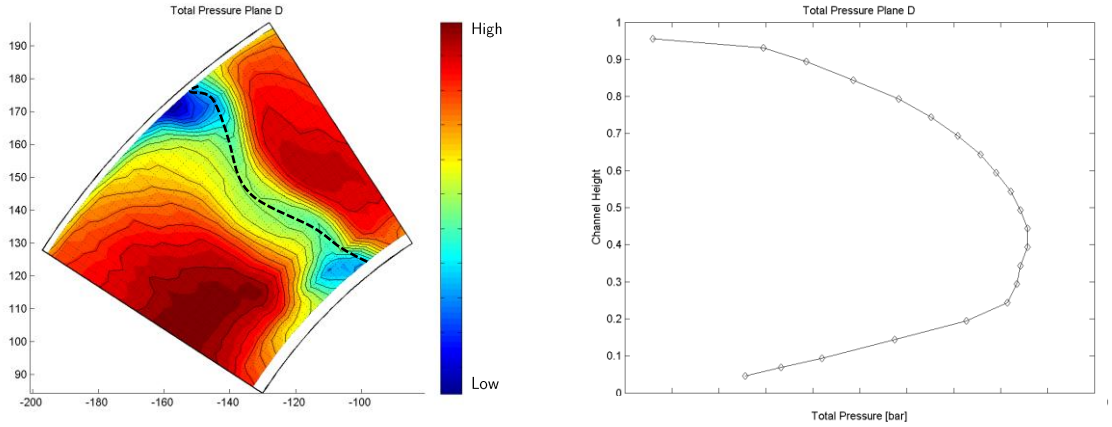

Figure 5-8: Total pressure distribution plane D, "Datum" EGV, operating point ADP

The second region is located close to the casing at the intersection with the trailing edge. The casing region of the flow is strongly dominated by the tip leakage flow coming from the rotor. This leakage flow superimposes with the upper passage vortex and causes a strong migration of fluid from the casing towards the midspan. This in turn promotes the formation of the upper passage vortex that dominates the flow field downstream of the vane (as in detail explained in the Annex). This movement of tip leakage fluid can also be seen when looking at the total temperature distribution in Figure 5-10 where a large region of high total temperature fluid can be identified on the suction side of the wake at approximately 30% to 70% span. This movement can also be seen in the pitch angle distribution in Figure 5-11 where a large region of negative pitch angle can be identified that is due to the tip leakage fluid being pushed towards the casing of the vane. Close to the hub in Figure 5-11 a small region of high positive pitch angle can be identified that is due to the aforementioned hub secondary flow pushing the fluid from the hub towards midspan.

This flow structure can also be seen when looking at the yaw angle distribution in Figure 5-9 where a large region of positive yaw angle can be seen close to the casing of the vane. Due to the effect of the channel pressure gradient the yaw angle that can be seen in this region is larger than what was seen in plane C upstream of the EGV. The upper passage vortex dominates the flow field and can be identified by the lines of parallel lines tangential to the rotational axis at midspan indicating solid body rotation as pointed out by Binder et al. [62]. An identical structure can be found close to the hub due to the lower passage vortex.

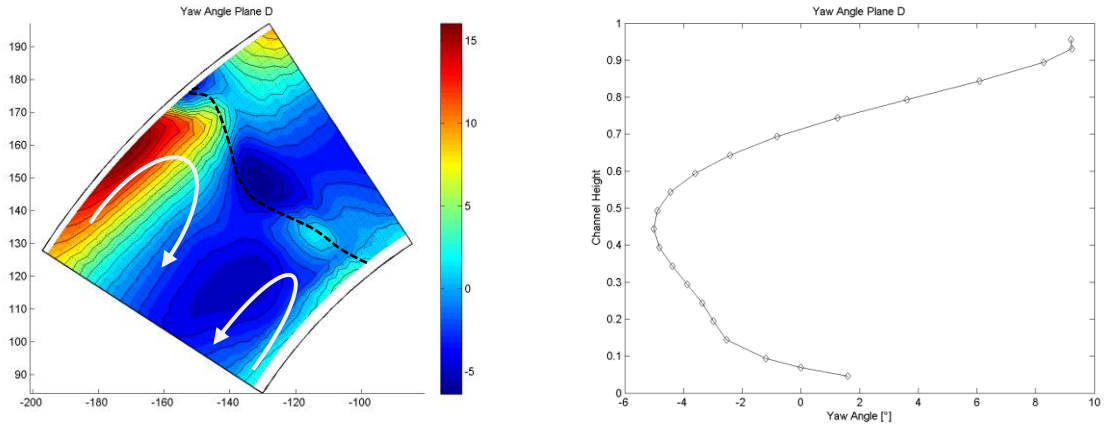

Figure 5-9: Yaw angle distribution plane D, "Datum" EGV, operating point ADP

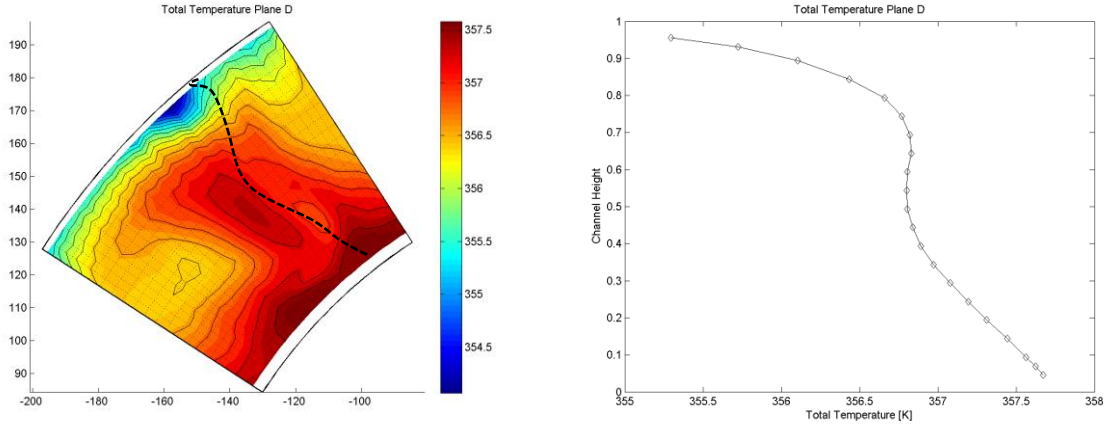

Figure 5-10: Total temperature distribution plane D, "Datum" EGV, operating point ADP

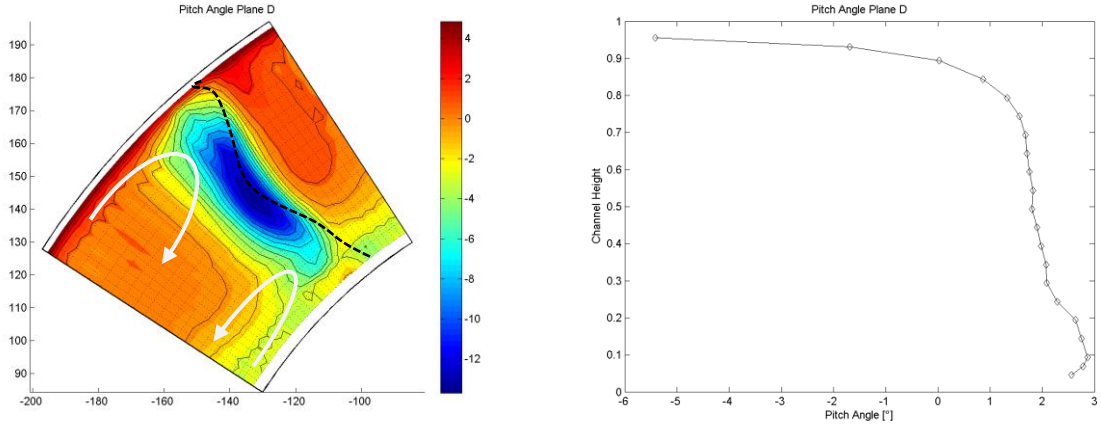

Figure 5-11: Pitch angle distribution plane D, "Datum" EGV, operating point ADP

Static pressure distribution

The static pressure distribution for the "Datum" EGV, operating point ADP is shown in Figure 5-12. The figure shows all four radial positions where static pressure taps are manufactured.

The suction side distributions at 20% and 50% span show a somewhat similar distribution with an increase in velocity from the leading edge towards the suction peak. This suction peak is located at approximately 15% axial chord for these two positions. From this point onwards the 50% span distribution shows a steady decrease in velocity whereas the distribution at 20% span shows a change in slope between 30% and 40% axial chord. Downstream of this position the change in velocity is identical to what was seen at 50% span.

The 30% span position shows a very different picture than the 20% and 50% span distributions. The measured static pressure distribution shows a maximum Mach number/minimum static pressure close to the leading edge of the vane. From the first static pressure tap onwards the velocity decreases. This radial position also shows a change in velocity decrease at a position of approximately 40% axial chord as was seen at the 20% span position.

The data at 80% span shows a similar distribution to what was seen for the other positions on the suction side of the vane. There is an increase in velocity to a minimum static pressure at approximately 16% axial chord. Downstream of this point there is a steady increase in static pressure until the trailing edge of the vane.

The pressure distribution on the pressure side of the vane shows an almost constant static pressure distribution along the axial chord for all radial positions. Only the 50% radial position shows a small decrease in velocity at the leading edge of the vane. The 30% span position shows a slightly higher static pressure compared to the other 3 radial positions.

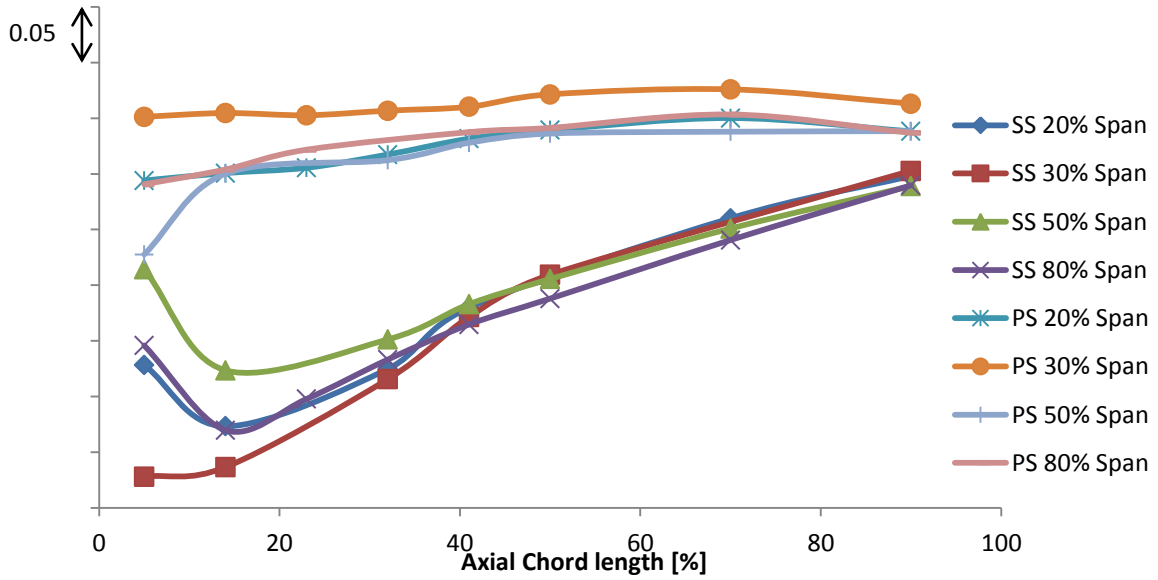

Figure 5-12: Static pressure distribution, "Datum" EGV, operating point ADP

Oil Flow visualisation

The oil flow visualisation for the "Datum" EGV operating point ADP can be seen in Figure 5-13 to Figure 5-15. Figure 5-13 shows the oil flow visualisation on the suction side (left) and the pressure side (right) of the vane. The oil flow visualisation on the suction side shows a multitude of flow features. Close to the casing the influence of the rotor tip leakage flow of the rotor can be identified. The superposition of upper passage vortex, radial pressure gradient and tip leakage flow causes a strong migration of fluid from the casing towards midspan (marked A). This can be seen when looking at the stream line depicted close to the casing that migrates from the casing at the LE towards a position of 55% span at the TE of the vane. Close to the hub two different structures are visible. A lift-off line can be identified close to the hub endwall, starting at approximately 25% axial chord (marked B). The lift-off starts out at the hub endwall and extends further towards midspan. At the trailing edge, the lift-off line extends until approximately 20% span at the trailing edge of the vane. When looking at the hub oil flow visualisation in Figure 5-14 it can be seen that streamlines from the hub in this particular region of the flow extend until the very endwall which means that this particular lift-off on the suction side of the wall is not caused by a reverse flow as it is possible in compressor vanes but rather the hub secondary flow pushing fluid from the hub towards the suction side and as a consequence towards midspan.

A third structure, marked C, can be seen in closer to the leading edge at approximately 20-30% axial chord. There is a straight line from 5% span to approximately midspan. It can be seen that the surface streamlines show a small radial movement followed by a region of very low traces of remaining oil flow, pointing towards a region of high shear stress. Downstream of this region a regular fluid flow with now radial component can be identified. This is an effect of the start-up of the test rig. In this short period of time where the flow is not according the operating point. During this time a strong radial flow with high shear stress influences this region (see section 0). The shear stress during the subsequent operating point is not large enough to significantly alter the appearance of this region. When comparing the position of this effect to the presumed position of the suction peak of the vane it can be seen that this line marked in Figure 5-15 is also in rather good agreement with the predicted position of the spanwise maximum velocity. A closer look shows that while the start-up has a large influence in this region the flow during the operating point shows no features that resemble those of the flow during the startup of the testrig (see chapter 12).

The pressure side of the vane on the right of Figure 5-13 shows only very little identifiable structures. Close to the hub a small separation line marked white is visible that is due to the a small corner vortex forming at the intersection of the hub and the pressure side of the vane.

Figure 5-14 shows the oil flow visualisation on the hub of the passage. The approximate location of the stagnation point can be located in front of the vane is marked with an "S". The fluid is pushed from the pressure towards the suction side of the vane and influences the flow on the suction side as explained earlier.

Figure 5-15 shows the oil flow visualisation on the casing of the vane. The cross passage flow can easily be identified that is caused by the pressure gradient and the tip leakage flow. The position of the stagnation point cannot be identified. It can be seen that due to the underturning of the tip leakage vortex the flow enters the passage with an almost axial flow direction (see also Figure 5-5) and is then turned towards the suction side of the vane.

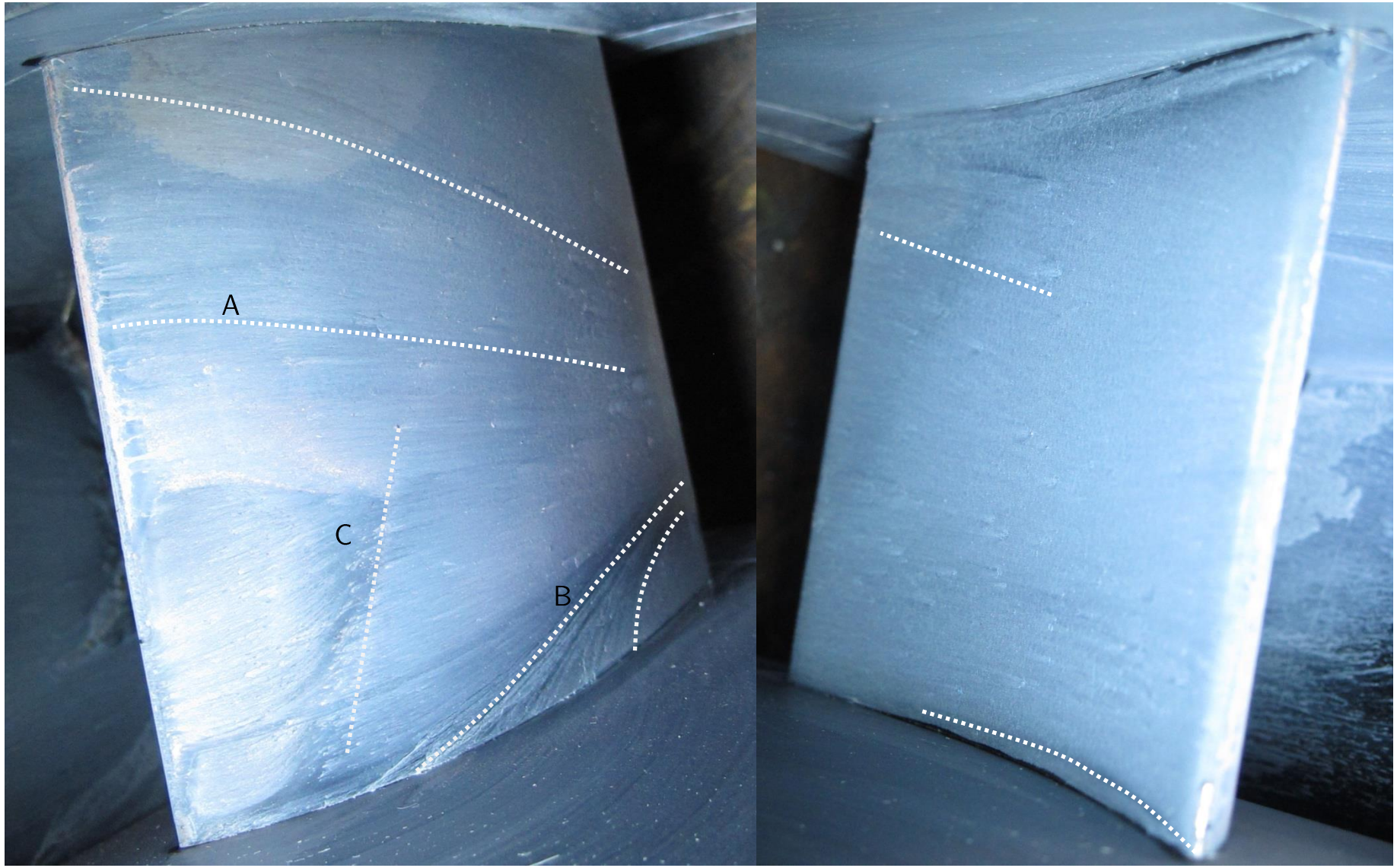

Figure 5-13: Oil flow visualisation "Datum EGV", operating point ADP; Suction side (left) and pressure side (right)

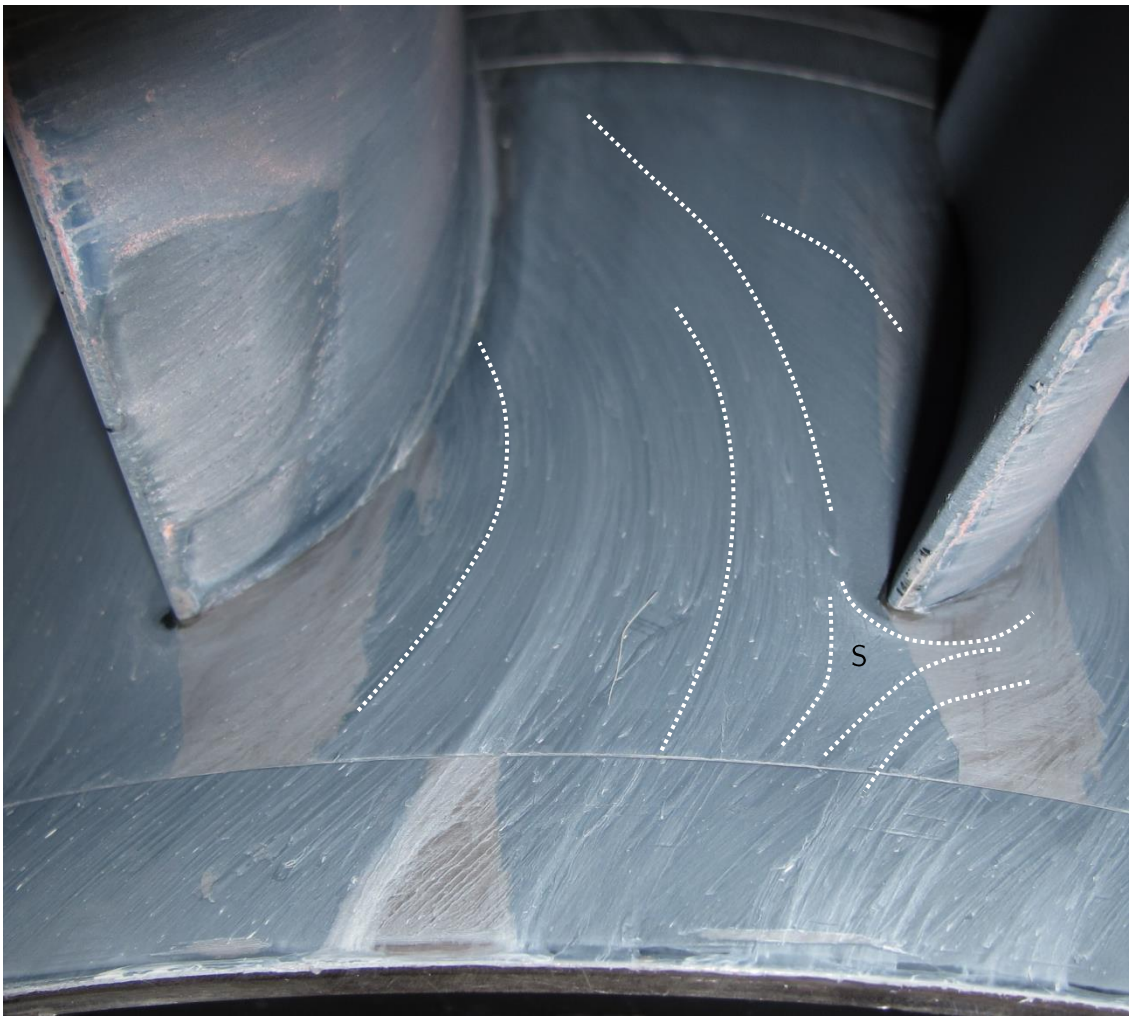

Figure 5-14 Oil flow visualisation "Datum EGV", operating point ADP; hub

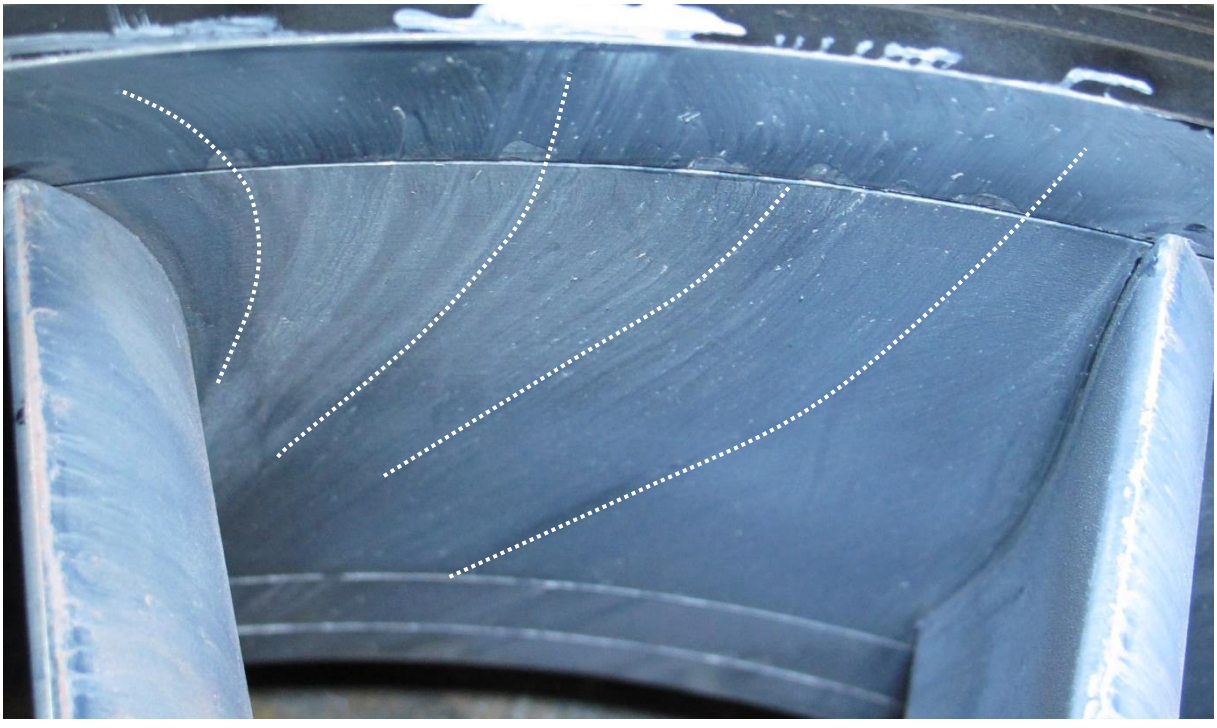

Figure 5-15: Oil flow visualisation "Datum EGV", operating point ADP; Casing

Acoustic

The results of the acoustic post processing can be seen in the following section.

Figure 5-16 shows the averaged FFT of all microphones used in the post-processing. The blade passing frequency of the operating point ADP is 4080 Hz as can be seen in the figure. The second and third blade passing frequency can also be identified at 8160 Hz and 12240 Hz respectively.

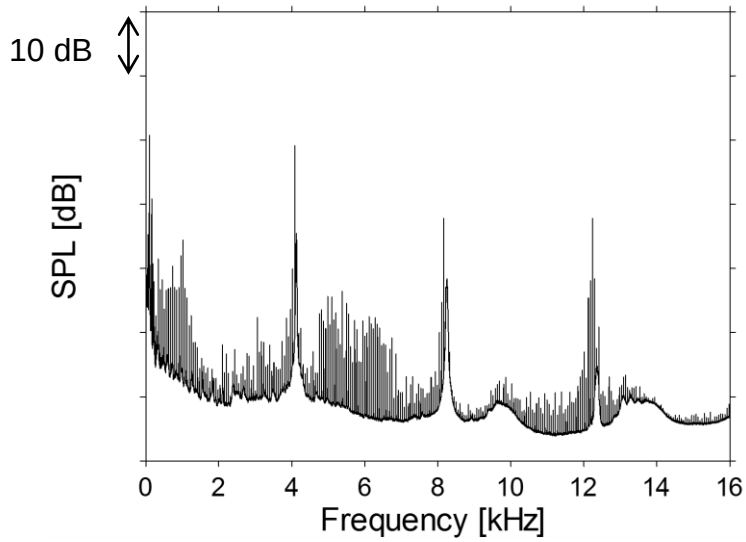

Figure 5-16: Averaged FFT of all microphones, Datum EGV operating point ADP

The results of the azimuthal mode decomposition can be seen in Figure 5-17 where the circumferential modes for the operating point are depicted. According to the theory, modes up to ± 15 are able to propagate and are this boundary is depicted as a red dotted line.

There are three dominant modes to be identified in the Figure 5-17. The two dominant modes are a result of the rotor-stator interaction being scattered by the EGV. The third highest mode is a result of the interaction between the rotor and the EGV itself.

All modes beyond m=$\pm$15 are cut off and significantly lower than the modes smaller than m=$\pm$15

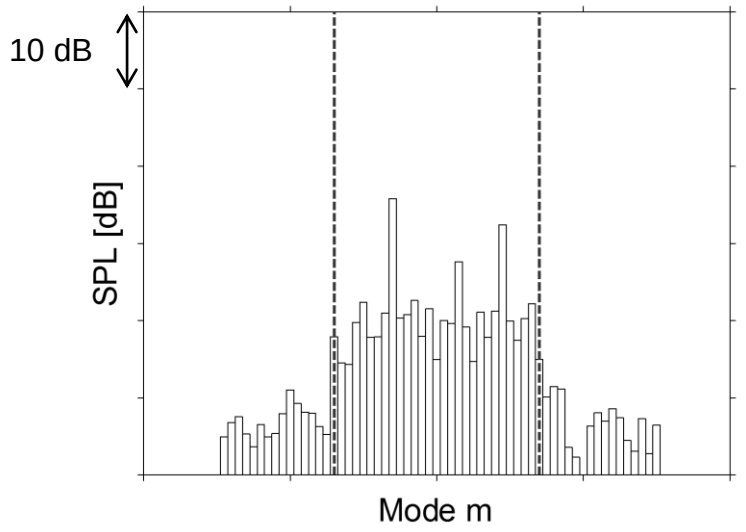

Figure 5-17: Azimutal mode decomposition, "Datum" EGV operating point ADP

The results of the radial mode decomposition can be found in Figure 5-18, where the amplitude of each radial mode n and circumferential mode m can be seen. In addition these modes are split by their direction of propagation (up- and downstream). The maximum number of radial modes able to propagate for the given operating point is n=1 resulting in an overall small amount of modes propagating. The highest mode present in the flowfield for the propagation in streamwise direction is a mode related to the radial order n=0. In this radial mode order only one significant peak can be found that is due to the scattering of the rotor/stator interaction by the EGV. At the radial order n=1 three modes with a high SPL can be identified. These are due to the scattering of the rotor/stator interaction by the EGV as well as the interaction of the rotor and the EGV.

This can be seen in Figure 5-19 where the results of the radial mode decomposition is depicted split by circumferential mode and direction of propagation but summed up over all radial modes are depicted. It can be seen that the mode highest mode is more than 5 dB larger than the other modes present in the flow field.

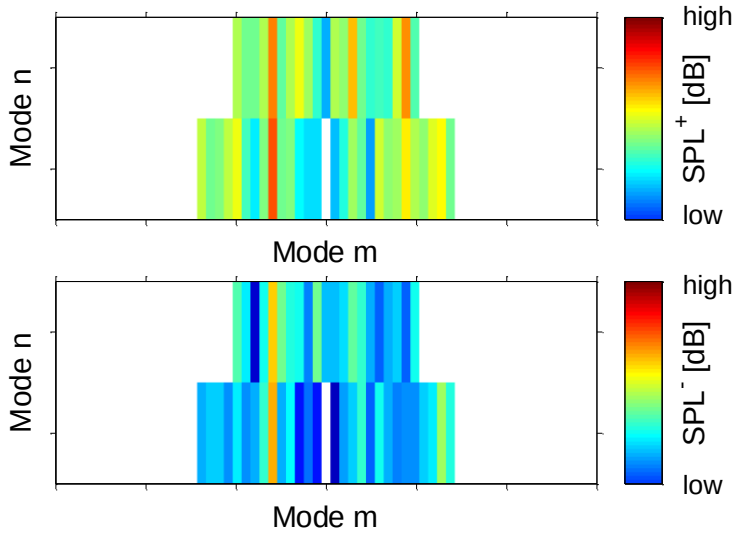

Figure 5-18: Radial mode decomposition, "Datum" EGV, operating point ADP, split by circumferential and radial modes as well as up- and downstream moving modes

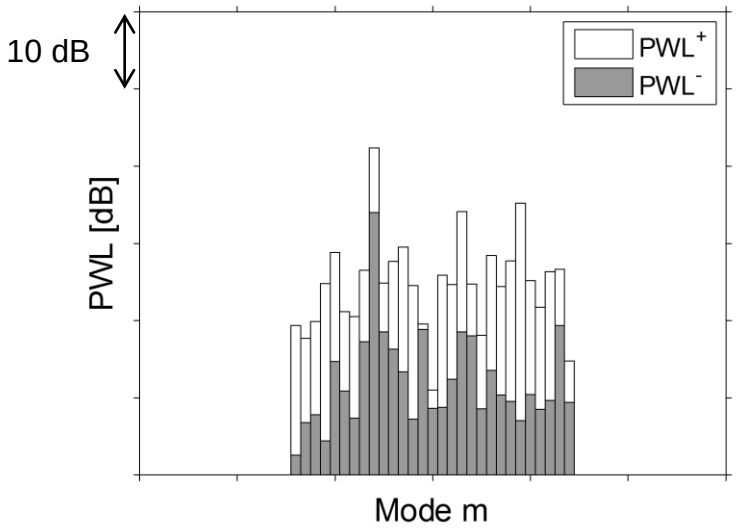

Figure 5-19: Radial mode decomposition, "Datum" EGV, operating point ADP, split by up- and downstream moving modes, sum of all radial modes

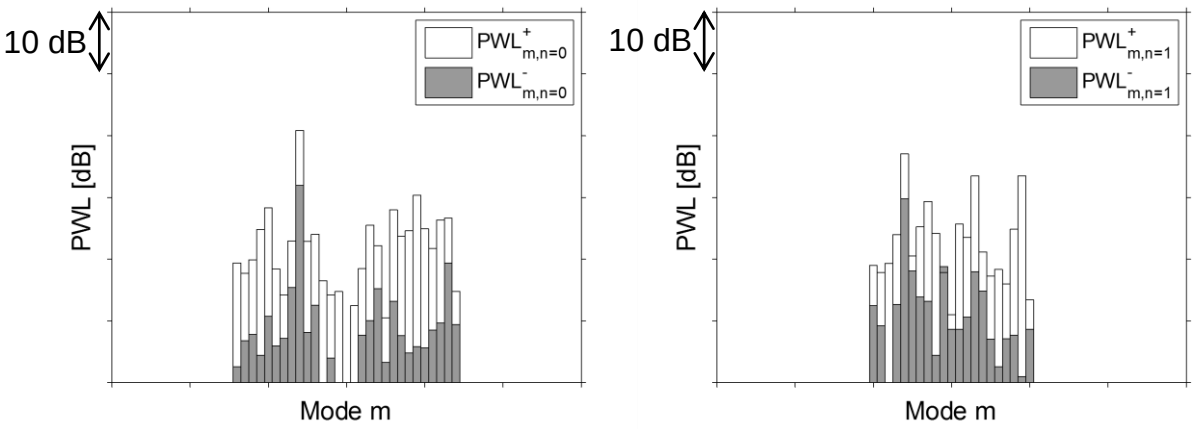

Figure 5-20: Radial mode decomposition split by up- and downstream moving modes, radial mode n=0 (left) and n=1 (right)

5.1.2.2 Leaned EGV

5 Hole Probe results plane D

The flow field downstream of the EGV in plane D will be discussed in the following section. The flow seen downstream of the EGV is, for a large part similar to what was seen for the "Datum" EGV.

The wake of the vane is shown by a white dotted line in Figure 5-21 where the total pressure distribution is shown. The wake here is defined as the local region of minimum total pressure. The wake of the vane consists of three regions of large total pressure: one located close to the casing (marked A), one close to the hub (marked B) and a region of lower total pressure located at approximately 45% span of the wake (marked C). When comparing the overall shape of the wake to what was seen for the "Datum" EGV in Figure 5-21, the two flow fields show the general similar flow features. The big difference is the lean of the wake caused by the vane lean. The low total pressure region close to midspan is more pronounced than for the "datum" EGV. This is due to the large flow separation seen in the oil flow visualization in Figure 5-28. The separation line of this flow feature reaches from the hub towards approximately midspan where it interacts with the strong flow from the casing towards midspan. This can also be seen when looking at the pitch angle distribution in Figure 5-24 where the region of low total pressure is seen as a region of strong change in pitch angle.

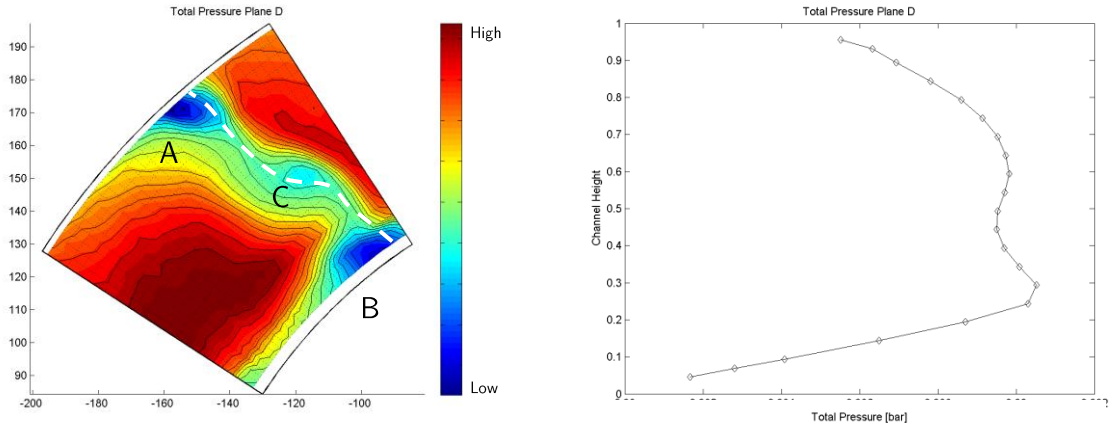

Figure 5-21: Total pressure distribution plane D, "Leaned" EGV, operating point ADP

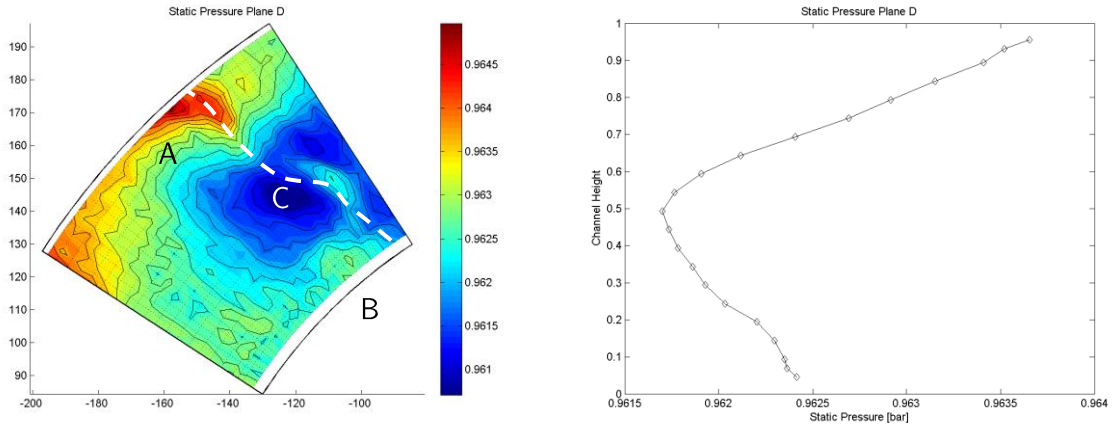

Figure 5-22: Static pressure distribution plane D, "Leaned" EGV, operating point ADP

The total pressure region close to the casing is centred on the wake of the vane and shows only a very small extension towards suction or the pressure side. These small extensions are due to the hub secondary flows.

The static pressure distribution shows only very small differences across the flow field. The maximum difference is approximately 5 mbar. A large region of low static pressure is present close to the region of low total pressure indicating a vertical structure might be present in this region. This is also suggested when looking at the yaw angle in Figure 5-23, where the yaw angle shows a strong change with parallel iso-lines indicating a vertical structure. This structure is due to the rotation caused by the tip leakage flow superimposing with the secondary flows.

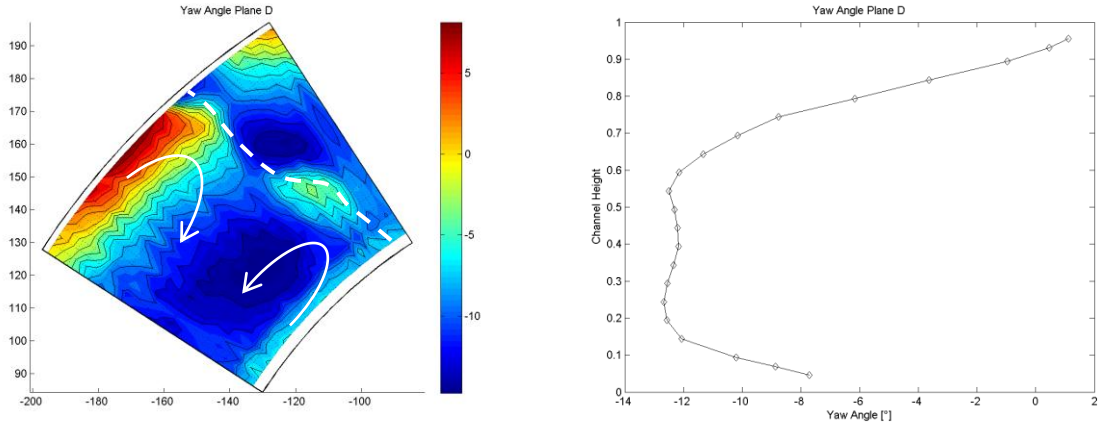

Figure 5-23: Yaw angle distribution plane D, "Leaned" EGV, operating point ADP

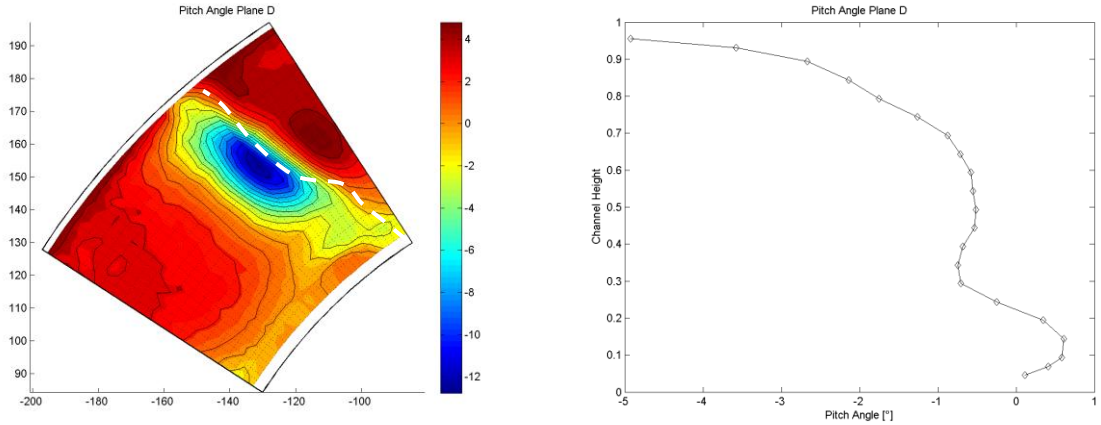

Figure 5-24: Pitch angle distribution plane D, "Leaned" EGV, operating point ADP

Static pressure distribution

Figure 5-25 shows the static pressure distribution along all 4 radial positions equipped with static pressure taps.

The static pressure distribution along the pressure side of the vane shows an identical static pressure distribution for all radial positions. There is a steady decrease of velocity from the leading edge up to approximately 70% axial chord, followed by a small acceleration towards the TE of the vane.

The suction side static pressure distribution at 30% span shows a very strong acceleration from the LE towards the suction peak located at ~20% axial chord. Downstream of this point the static pressure distribution shows a steady increase until the TE of the vane.

The suction side distribution at 50% span shows an acceleration of the flow from the leading edge towards the suction peak of the vane located at 20% axial chord. This is followed by a deceleration towards the TE of the vane. The rate of deceleration slows down with progressing axial chord position.

The pressure distribution closest to the hub, at 20% span shows a different behaviour than the other radial positions. There is a deceleration of the flow from the leading edge towards 25% axial chord where an even stronger deceleration until an axial position of 30% chord takes place. The static pressure tap at 41% axial chord does not show proper results as the value obtained is equal to the ambient pressure and therefore assumed to be wrong. The region of 50-60% axial chord shows this flow acceleration and the subsequent region of constant speed is within the region of flow separation that can be found in the oil flow visualization in Figure 5-28. There a large separated region close to the hub suction side can be observed.

The static pressure distribution at 80% span shows an acceleration of the flow from the leading edge towards 15% axial chord. The two following pressure taps are not valid since the data received from these points is too similar to ambient pressure.

This is again followed by an acceleration of the flow from 40% to 50% chord and decelerating towards the trailing edge of the vane. When comparing this static pressure distribution to the oil flow visualization in Figure 5-28 shows that up until approximately the position of the first "suction peak" at 15% axial chord the flow only shows very little radial movement. At approximately 20% axial chord the influence of the tip leakage region can be seen. There is a strong beginning of radial movement coming from the region above 90% span at shows the strongest influence close to the LE of the vane. This change in flow regime is possibly responsible for the change in static pressure seen in the 20-30% chord region. Further downstream the oil flow visualization shows a flow that has a strong radial component.

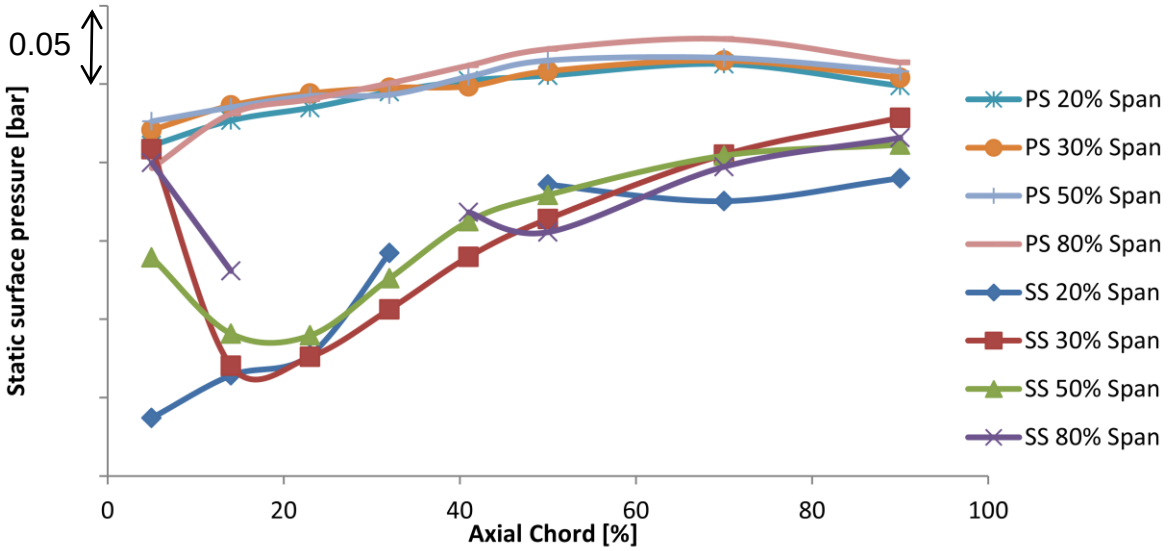

Figure 5-25: Static pressure distribution on the vane surface, "Leaned" EGV, operating point ADP

Oil Flow Visualisation

The oil flow visualization of the "Leaned" EGV operating point ADP can be seen in Figure 5-26 to Figure 5-28.

Figure 5-26 shows the oil flow visualization along the hub of the passage. The stagnation point of the flow can easily be identified in the oil flow visualization and is marked with an S. The stagnation point is followed by two separation lines S_1 and S_2 as described by Sieverding [88]. Downstream of the second separation line the cross passage flow can be clearly seen originating from the pressure side of the vane moving towards suction side. Close to the pressure side of the vane a large separated region with supposedly flow reversal can be seen starting at approximately 40-45% axial chord (marked A). There is a clearly visible separation line extending from the suction side endwall to approximately 20% of the passage. This region extends up to 85% axial chord where the cross passage flow can again be seen moving downstream of the separated flow region towards the suction side. This separated flow region can also be seen on the suction side of the vane in Figure 5-28. The lift of line (marked B) is identical to what was seen on the hub and reaches a span-wise extension of approximately 30% span at the 90% axial chord of the vane (marked C), where the influence of the flow from the casing reattaches the flow at the 30% span position. Close to the casing of the suction side the influence of the tip leakage flow as well as the pressure gradient due to the lean can be seen. The fluid shows a strong radial component moving from approximately 90% axial chord at the TE towards midspan at the TE of the vane. Another flow feature visible on the suction side of the vane is a strong radial movement from the hub towards midspan. This movement is associated with a flow feature starting at the casing of the vane at approximately 10% axial chord. There is a large region of high shear stress stretching in a line from the hub towards a region located at 20% chord at midspan. This region of high shear stress is marked D in the Figure 5-28. At approximately 60% span the regular fluid movement from the casing towards midspan can be identified.

The pressure side of the vane can be seen on the right of Figure 5-28. Only a very limited amount of flow features are visible from this visualization. Close to the hub the influence of the cross passage flow is visible leading to the migration of fluid towards the hub, whereas close to midspan the streamlines show an almost axial direction. Close to the casing a lift-off line (marked E) can be observed.

The casing of the vane shows a strong fluid migration from the pressure towards the suction side of the vane. The stagnation point as well as the separation lines can be identified. The cross passage flow is clearly visible extending to almost 90% of the passage when close to the TE of the vane. There is no flow separation visible in this region of the flow.

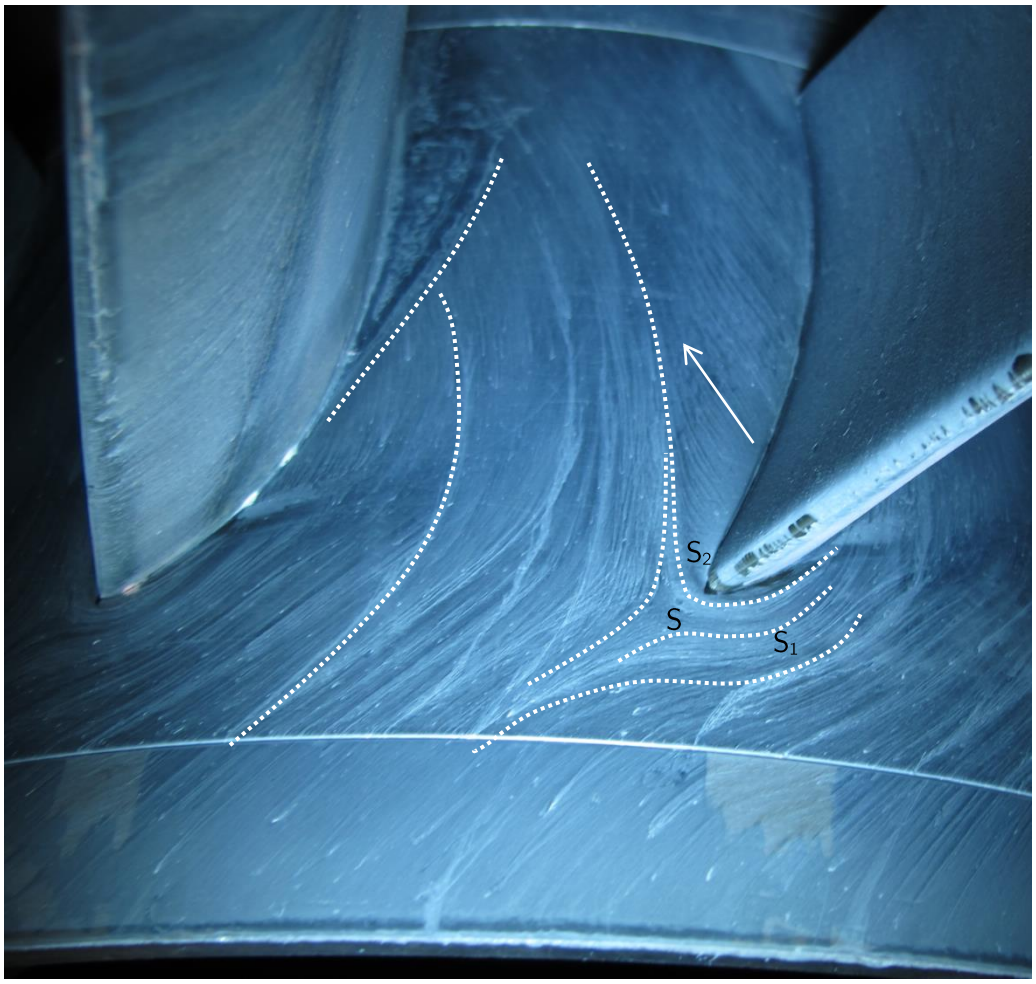

Figure 5-26: Oil Flow Visualisation "Leaned" EGV, operating point ADP, Hub

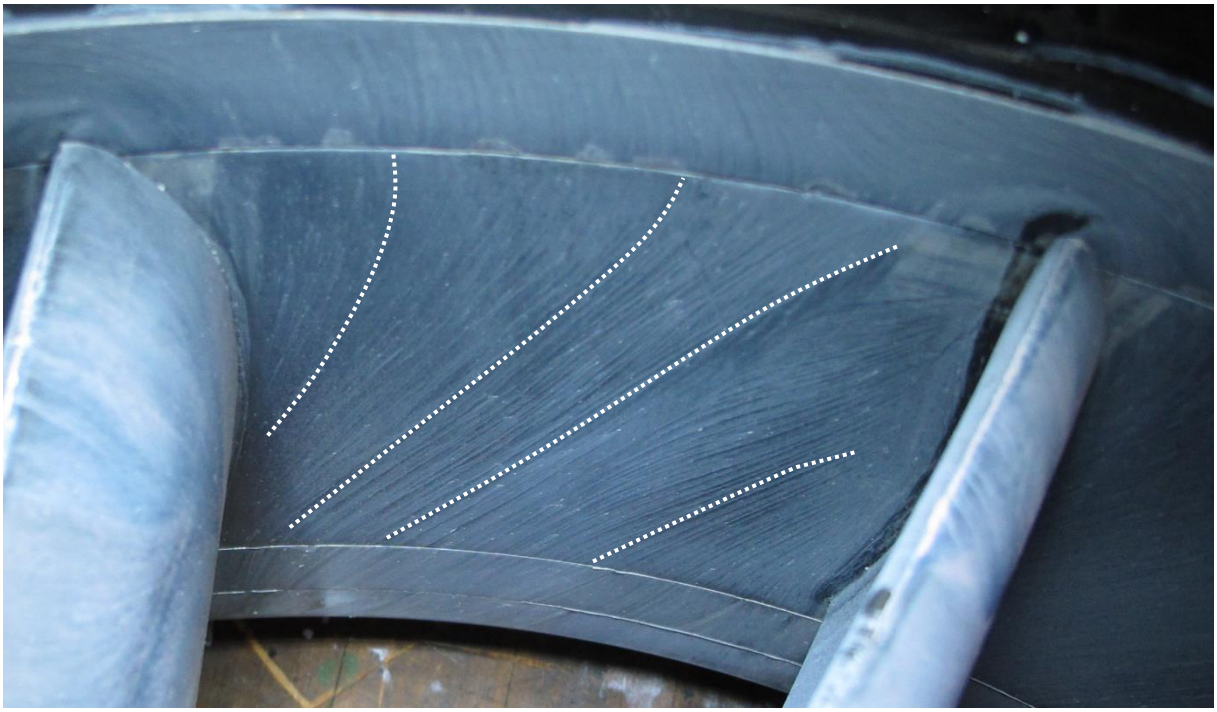

Figure 5-27: Oil Flow Visualisation "Leaned" EGV, operating point ADP, Casing

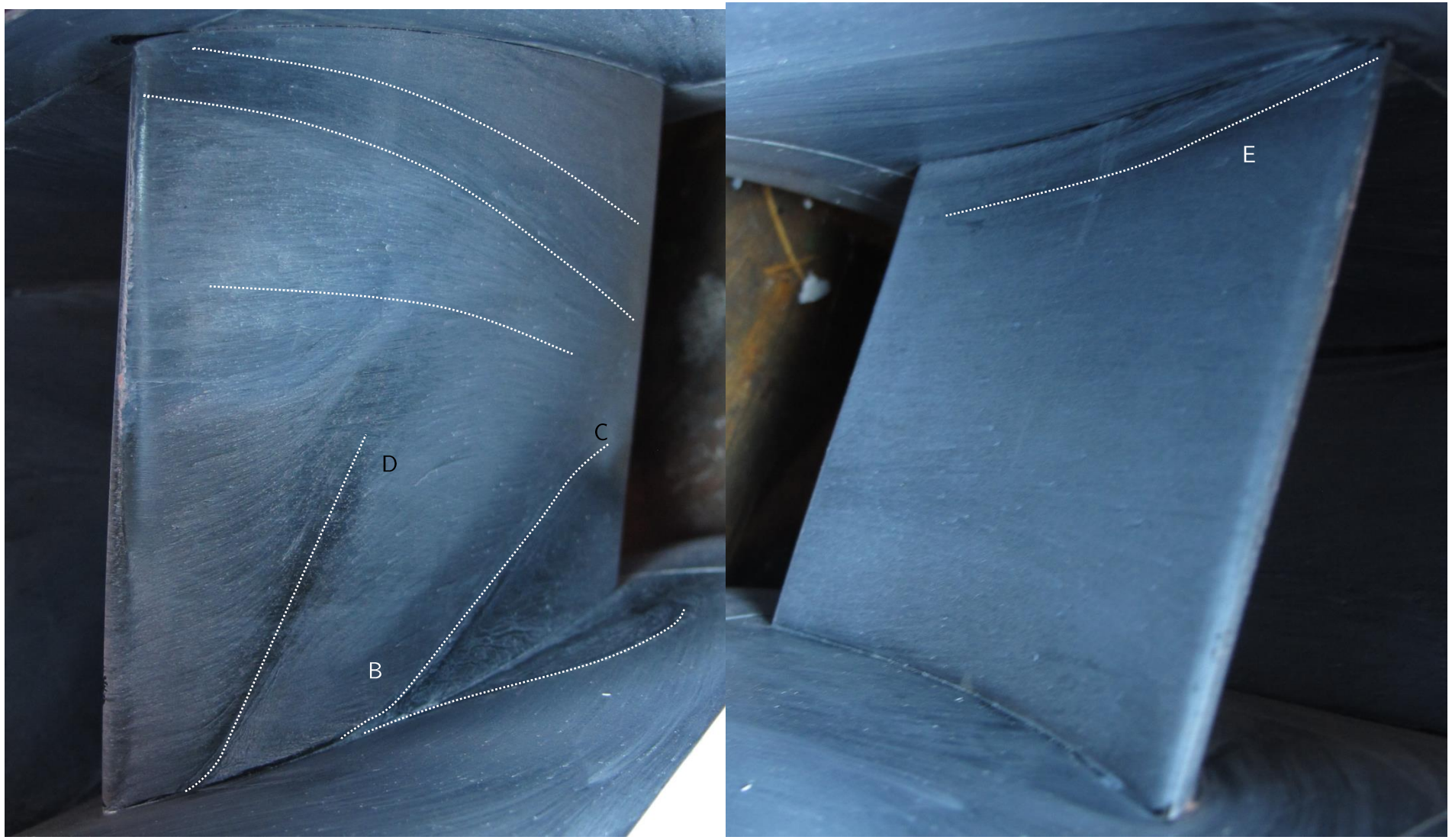

Figure 5-28: Oil Flow Visualisation "Leaned" EGV, operating point ADP, Suction Side (left) and Pressure side (right)

Acoustic

The results of the acoustic post-processing can be seen in the following section.

Figure 5-29 shows an averaged FFT of all microphones used in the post-processing. The blade passing frequency of the operating point ADP is 4080 Hz as can be seen in the figure. The second and third blade passing frequency can also be identified at 8160 Hz and 12240 Hz respectively.

The results of the azimuthal mode decomposition can be seen in Figure 5-30 where the circumferential modes for the operating point ADP are depicted. According to the theory, modes up to ± 15 are able to propagate and are this boundary is depicted as a red dotted line.

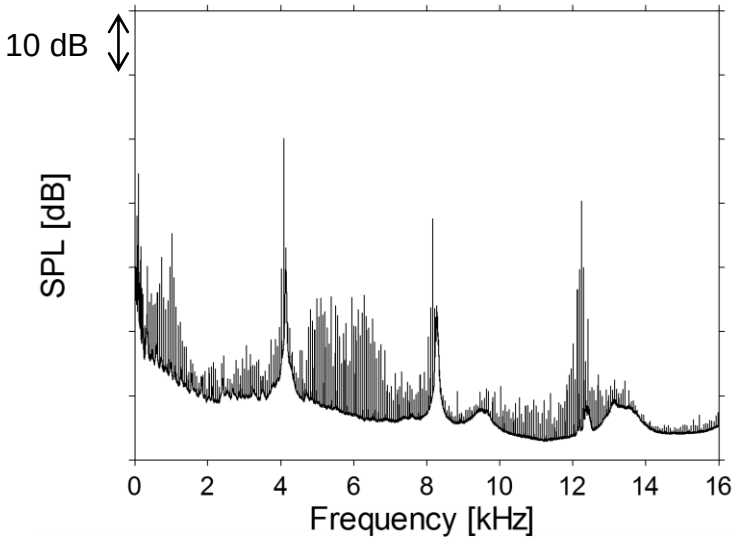

Figure 5-29: Averaged FFT of all microphones used in the post-processing

The dominating mode of the azimuthal mode decomposition is more than 5 dB higher than the second highest mode. Both of these modes are due to the scattering of the rotor/stator interaction by the EGV. The other modes able to propagate show significantly lower amplitudes compared to the dominating modes. When compared to the "Datum" EGV it can be seen that the mode that was due to the interaction between the EGV and the rotor is significantly lowered. This is a result of the lean of the EGV.

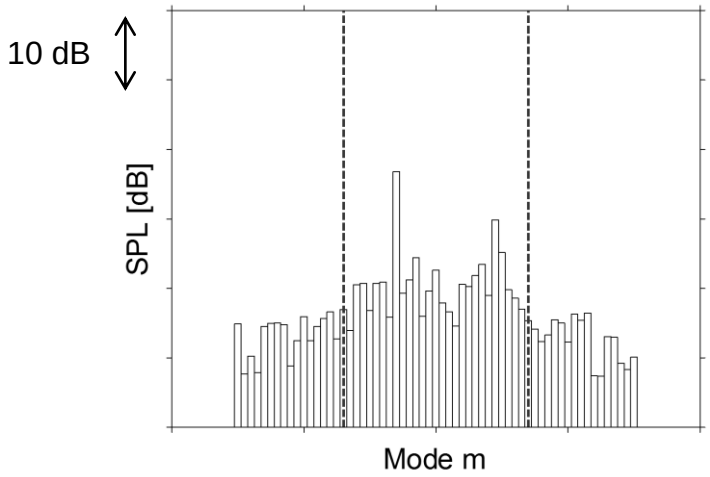

Figure 5-30: Result of the azimuthal mode decomposition, "Leaned" EGV, operating point ADP

The results of the following radial mode composition can be seen in the following section. The Figure 5-31 shows the results split by radial and circumferential modes as well as by up- and downstream propagating modes. A single dominant mode for the propagation in streamwise direction can be identified that is also the dominant mode in Figure 5-30. This mode has its highest amplitude for the radial mode n=1 unlike for the "Datum" EGV where the highest radial mode was the mode n=0. The second third highest mode is more than 5dB below the highest mode. The modes moving upstream are significantly lower than the downstream moving.

The sum of all radial modes for the RMA can be seen in Figure 5-32 split by up- and downstream moving modes. The results are similar to the AMA with the dominant mode being more than 5dB higher than the other modes.

The results for the radial modes n=0 and n=1 can be seen in Figure 5-33. As already described the largest contributor to the overall SPL is the radial mode n=1 where the highest single mode (m,n) can be identified. The modes with a radial order n=0 are approximately 3 dB lower than this mode.

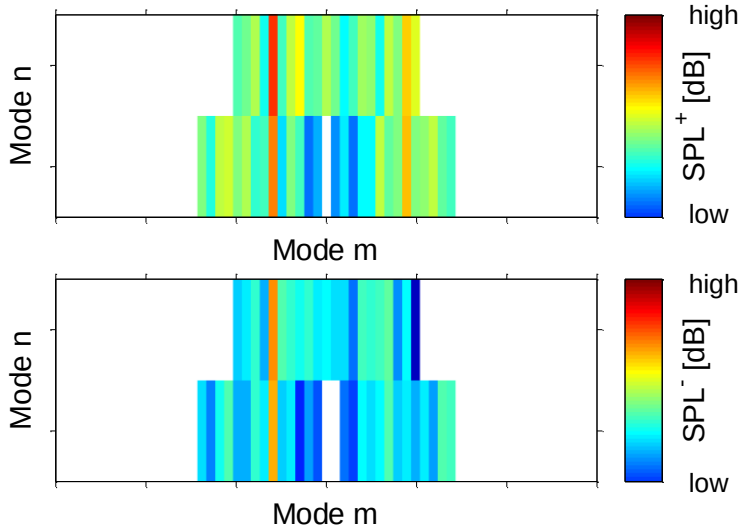

Figure 5-31: Radial mode decomposition, "Leaned" EGV, operating point ADP, split by circumferential and radial modes as well as up- and downstream moving modes

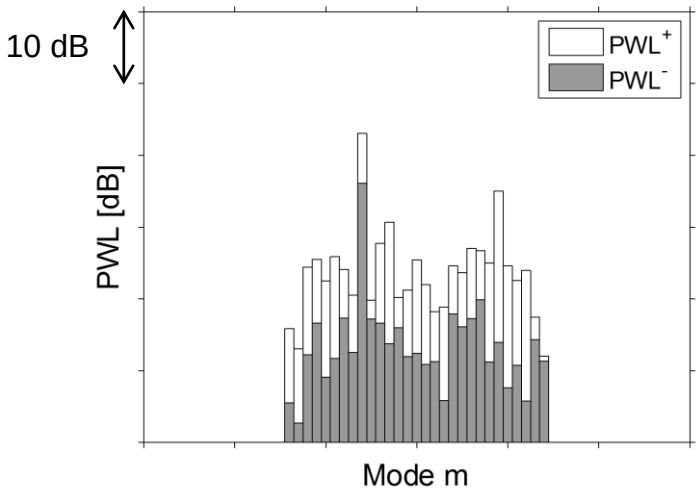

Figure 5-32: Radial mode decomposition split by up- and downstream moving modes, radial mode n=0 (left) and n=1 (right)

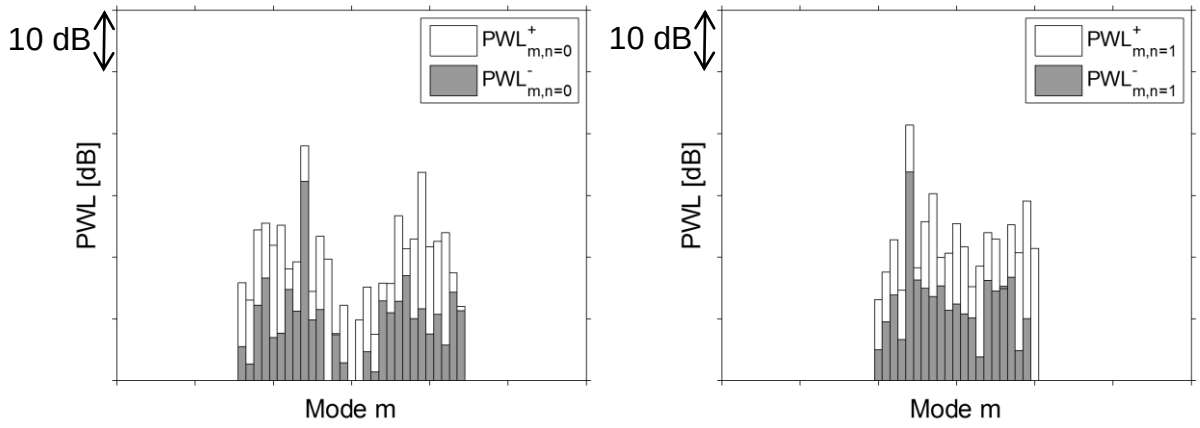

Figure 5-33: Radial mode decomposition split by up- and downstream moving modes, radial mode n=0 (left) and n=1 (right)

5.1.2.3 Inverse Cut-Off EGV

In contrast to what was seen in the "Datum" and "Leaned" EGV the "Inverse Cut-off" and the "High Loading" EGV have two planes downstream of the EGV that will be discussed, "D0" and D. The plane D's location is identical to what was seen in the before discussed EGVs.

5-Hole Probe Results Plane D0

The flow field downstream of the EGV is discussed in the following section. The plane D0 is located 55% axial chord downstream of the EGV trailing edge.

The Figure 5-34 shows the total pressure distribution downstream of the EGV trailing edge. The central structure of the flow field is the wake of the vane. Close to the hub, again a region of low total pressure can be found. This structure is due to the hub secondary flow of the vane pushing fluid onto the suction side of the vane. This causes a vertical structure to form at the intersection of suction side and hub endwall. Close to the outer casing a region of low total pressure, marked A, can be identified. This region is due to the flow coming from the tip leakage region of the rotor. This low pressure region is mainly located at the suction side of the vane and is migrating towards midspan. This process is due to the interaction of the rotor tip leakage flow interacting with natural pressure gradient of the vane passage causing the migration of fluid from the casing towards midspan. At the intersection of the suction side and casing endwall another region of low total pressure can be identified. This structure is a reaction to the fluid migration towards midspan and is rotating against clockwise direction counteracting the clockwise movement of fluid in the upper passage. The structures visible in Figure 5-35 where the Mach number is shown are identical to what can be identified when looking at the total pressure.

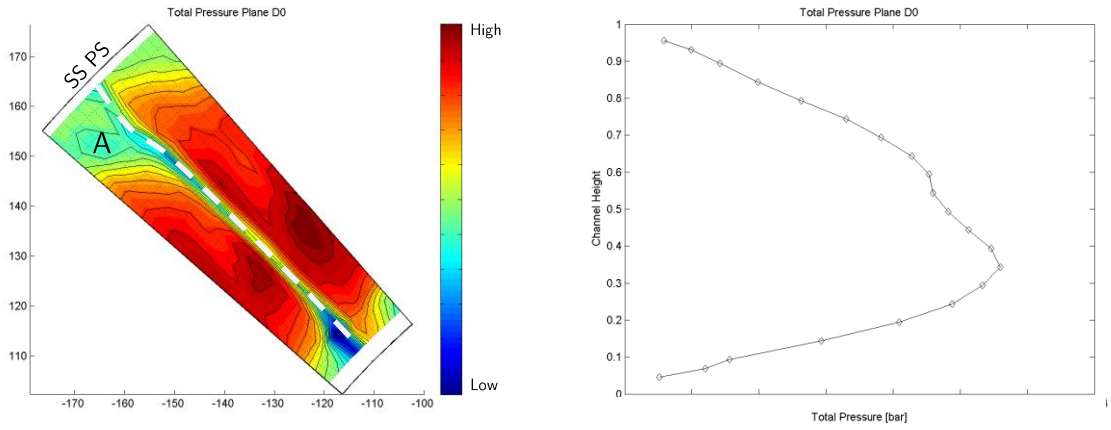

Figure 5-34: Total pressure distribution plane D0, "Inverse Cut-off" EGV, operating point ADP

Figure 5-36 show the total temperature distribution downstream of the vane. A region of high total temperature can be seen that is due to the lack of work performed by the rotor in the tip leakage region (marked A). Another region of high total temperature can be identified close to the hub that is due to the lack of work performed close to the hub of the rotor.

Looking at the yaw angle distribution in Figure 5-37 a region of positive yaw angle can be seen close to the casing that is due to the leakage jet of the rotor as well as the secondary flows imposed by the passage pressure gradient of the channel. Close to the casing another region of positive yaw angle can be identified caused by the hub secondary vortex. The pitch angle distribution in Figure

5-38 shows the movement of fluid in this particular region where the flow is pushed from the hub towards midspan. Due to the strong effect of the tip leakage this flow migration towards midspan on the suction side is much stronger close to the casing. This in turn holds also true for the fluid migration directed towards the endwalls on the pressure side of the vane. There is a much larger pitch angle close to the casing compared to what can be seen near the hub.

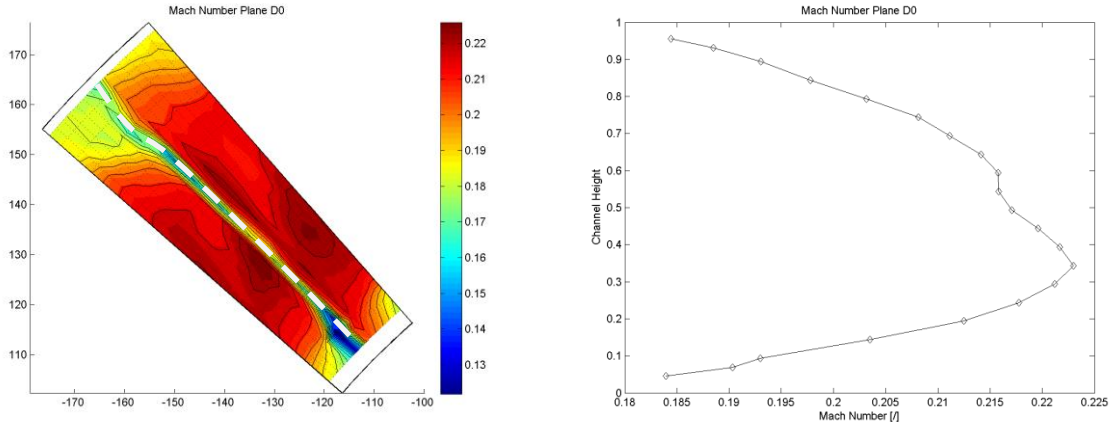

Figure 5-35: Mach number distribution plane D0, "Inverse Cut-off" EGV, operating point ADP

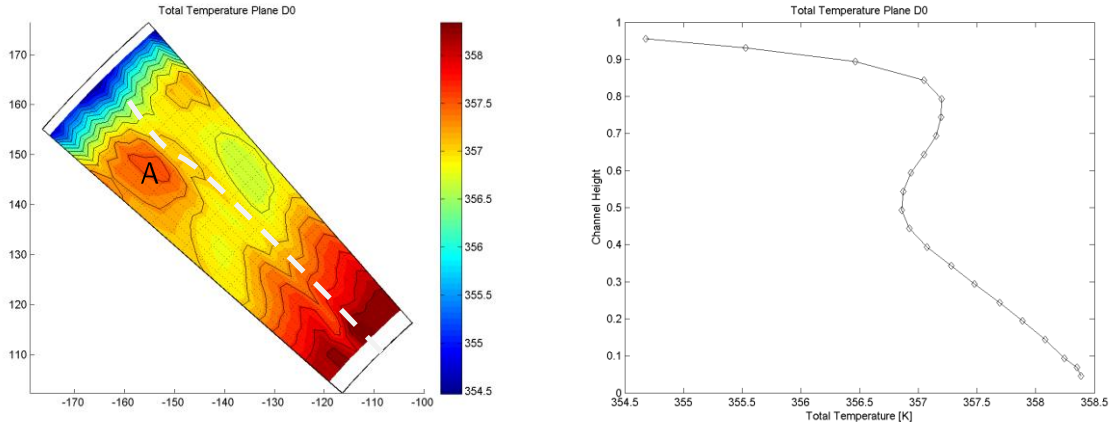

Figure 5-36: Total temperature distribution plane D0, "Inverse Cut-off" EGV, operating point ADP

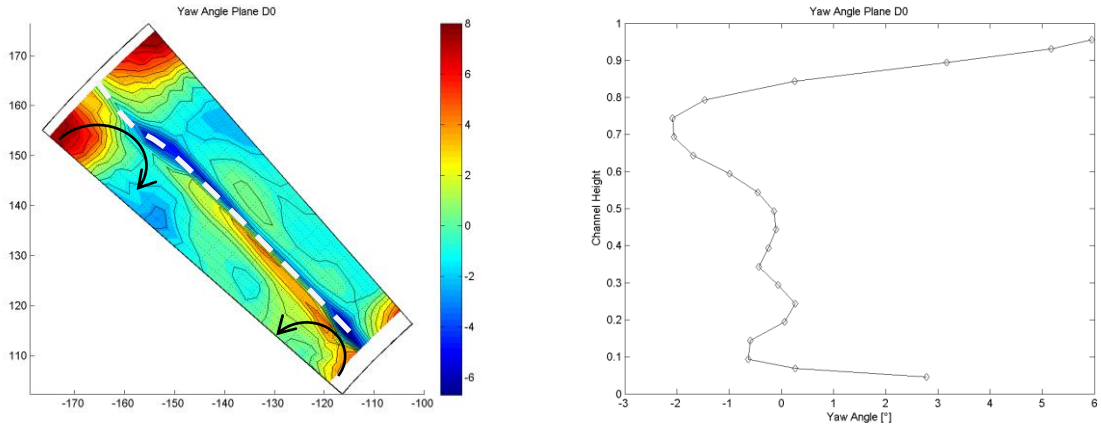

Figure 5-37: Yaw angle distribution plane D0, "Inverse Cut-off" EGV, operating point ADP

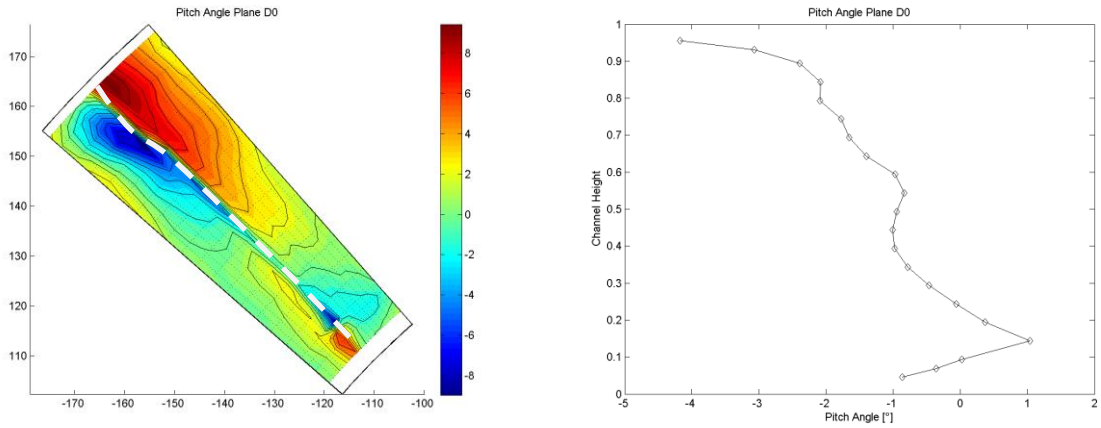

Figure 5-38: Pitch angle distribution plane D0, "Inverse Cut-off" EGV, operating point ADP

5-Hole Probe Results Plane D

The state of the flow field downstream of the plane D0 is shown in the following section. The wake that was identified in plane D0 is shown as a grey dotted line. The total pressure distribution in Figure 5-39 shows a wake that is very wide compared to what was seen in Figure 5-34. This is due to the mixing out of the wake. In addition the wake is not straight anymore but rather has an S-shape. The strong S-shape of the wake is caused by an interaction between the vane secondary flows and the tip leakage flow causing a rollup of the wake. This is due to the tip leakage flow increases the intensity of the upper passage vortex causing a stronger trailing edge shed vorticity which in turn favours the rolling up of the wake into a vertical structure (see chapter 12 and Pullan et. al [89]). Similar features can be seen when looking at the Mach number distribution in Figure 5-40. The static pressure distribution in Figure 5-40 shows that the static pressure is almost constant across the height of the channel with a small increase towards the casing that is due to the remaining pressure gradient caused by the swirling rotor flow. The variation of static pressure is in the order of 2mbar.

The total temperature distribution shown in Figure 5-41 shows no significant difference to what was seen in plane D0 in Figure 5-36. There is a region of low total pressure located close to the outer casing that is due to the high total temperature fluid migrating from the tip region towards midspan. In this plane the difference in total temperature outside of the casing region is significantly reduced, but the casing region still shows a large total temperature deficit that is due to the lack of radial mixing in this region of the vane.

The yaw angle in Figure 5-42 and the pitch angle in Figure 5-43 show similar distributions to what was seen in plane D except for the change in the shape of the wake discussed earlier. The strong bend of the wake at 70% span is located directly at the position where the strong radial flow component towards the hub is located. This region in combination with the strong positive pitch angle located on the pressure side of the wake rolls up to a vertical structure due to the shear layer within this region [89].

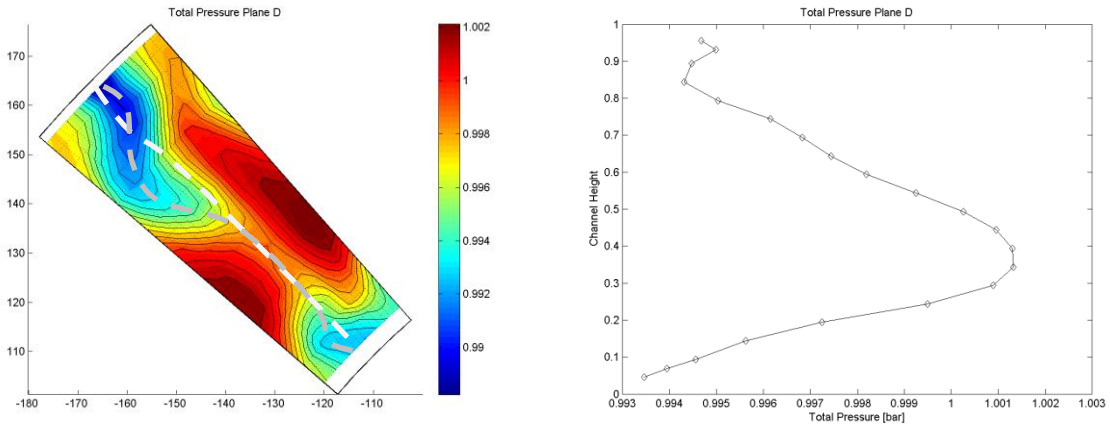

Figure 5-39: Total pressure distribution in plane D, "Inverse Cut-off" EGV, operating point ADP

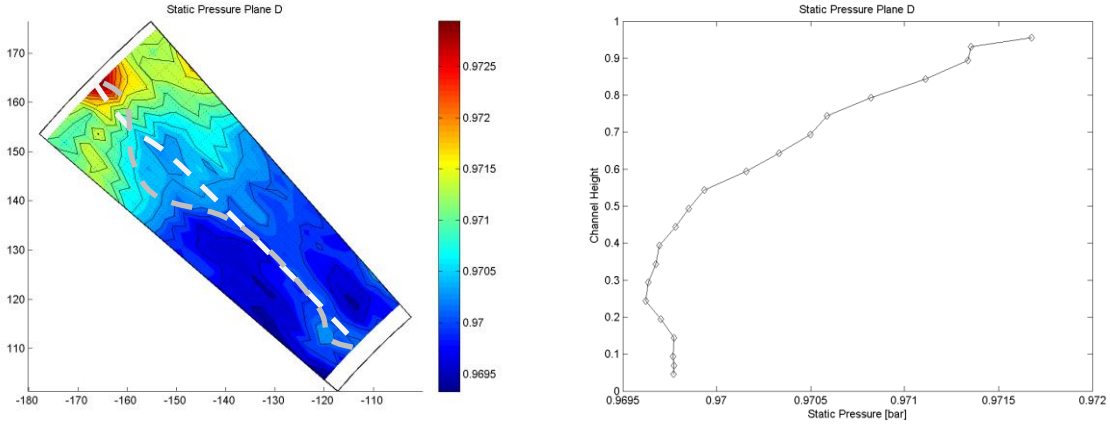

Figure 5-40: Static pressure distribution in plane D, "Inverse Cut-off" EGV, operating point ADP

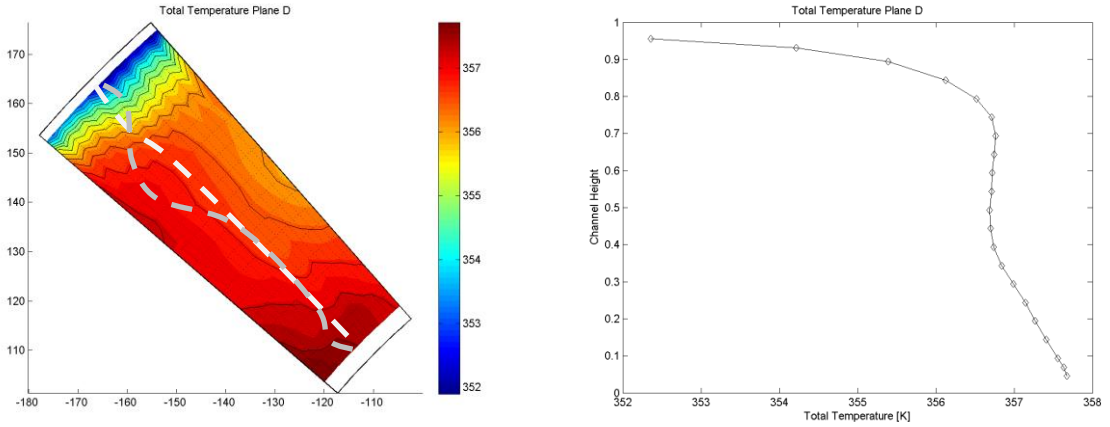

Figure 5-41: Total temperature distribution in plane D, "Inverse Cut-off" EGV, operating point ADP

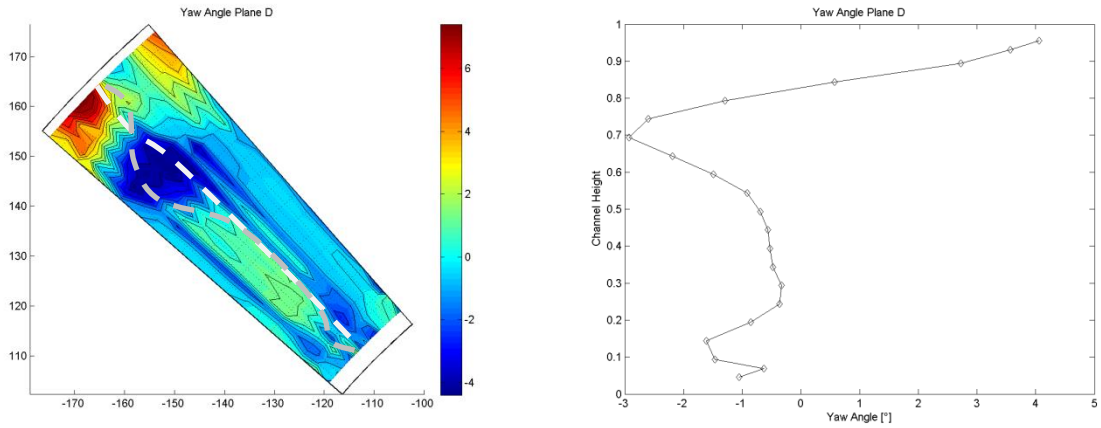

Figure 5-42: Yaw angle distribution in plane D, "Inverse Cut-off" EGV, operating point ADP

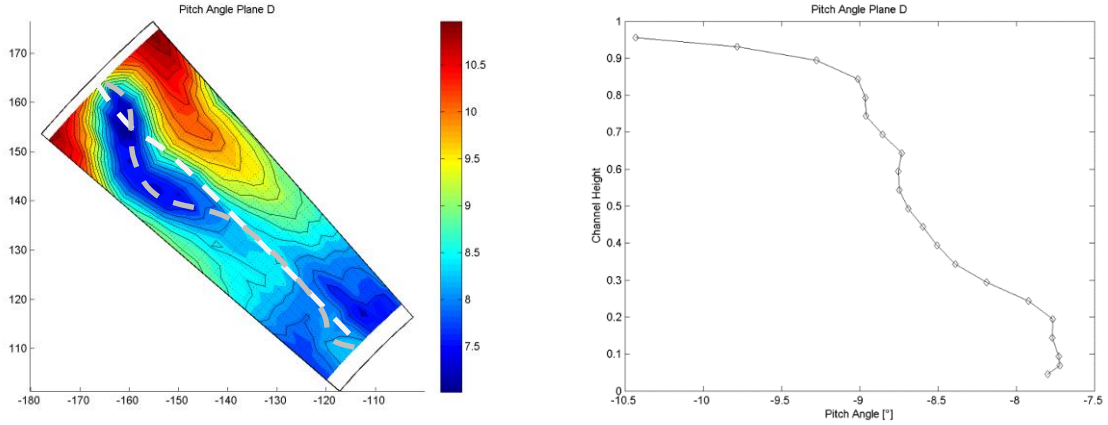

Figure 5-43: Pitch angle distribution in plane D, "Inverse Cut-off" EGV, operating point ADP

Static pressure distribution

The static pressure distribution on the vane surface can be seen in Figure 5-44.

Looking at the static pressure distribution on the pressure side of vane it can be seen that the distribution is almost identical for the three radial positions 20, 30 and 50% span. The distribution at 20% shows a slightly smaller static pressure close to the leading edge, but is otherwise identical. The static pressure distribution at 80% span shows a smaller static pressure than the other pressure side positions.

The suction side shows, again almost identical pressure distributions for 20, 30 and 50% axial chord. One of the main differences lies in the position of the suction peak of the vane. Whereas the 20% and 30% span positions show a suction peak at approximately 15% axial chord, the 50% span position has the suction peak at approximately 20% chord and moves even further downstream for the 80% span position where the suction peak is located at 30% axial chord. The static pressure distributions at 20% and 50% span show an increase in static pressure at 45% axial chord where a small plateau is located which might point towards a separation bubble in this location. A second plateau like feature can be seen at 60% chord for the 20% span position. This cannot be seen for the 30% span pressure distribution where a small change in gradient can be seen at an axial position of approximately 60% axial chord similar to the second plateau seen in the other radial positions.

The 80% span distribution shows a much higher static pressure than the other radial positions. There is a small plateau like flattening at approximately 45% axial chord.

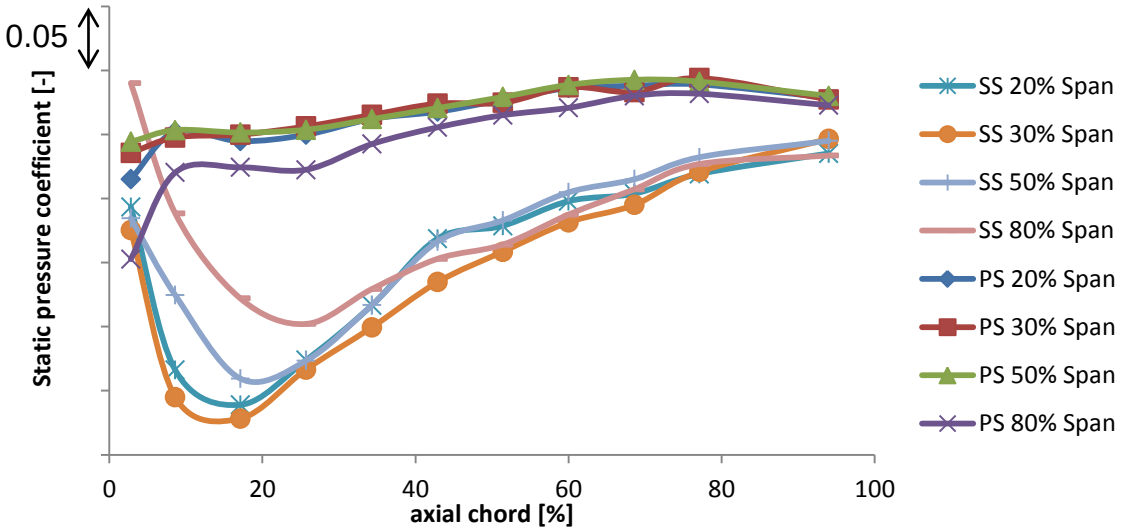

Figure 5-44: Vane surface static pressure, "Inverse Cut-off" EGV, operating point ADP

Oil Flow Visualisation

The oil flow visualisation for the operating point ADP of the "Inverse Cut-off" EGV is show in the following figures. Figure 5-45 shows the oil flow visualisation on the hub of the EGV passage. The stagnation point can be identified by a region of accumulated oil flow located in front of the leading edge of the vane. The main flow features on the hub can be associated to the hub secondary flows due to the pressure gradient between pressure and suction side. There is a strong migration from the pressure towards the suction side and fluid is strongly influencing the flow on the suction side of the vane.

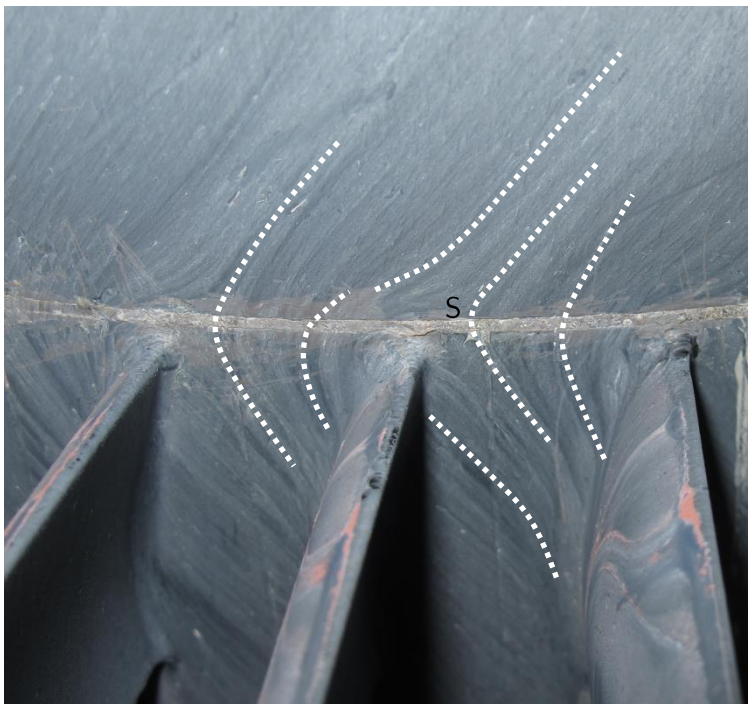

Figure 5-45: Oil flow visualisation on the hub, "Inverse Cut-off" EGV, operating point ADP

Figure 5-46 shows the oil flow visualisation on the casing of the passage. This region is strongly influenced by the rotor tip leakage vortex causing a change in the cross passage flow compared to the hub. The region where the stagnation point is located is marked with an "S" and the separation line accompanying the separation point. The cross passage flow is significantly lower than what can be seen in Figure 5-45, yet there is a clear migration of fluid from the pressure towards the suction side as visible in the oil flow visualisation.

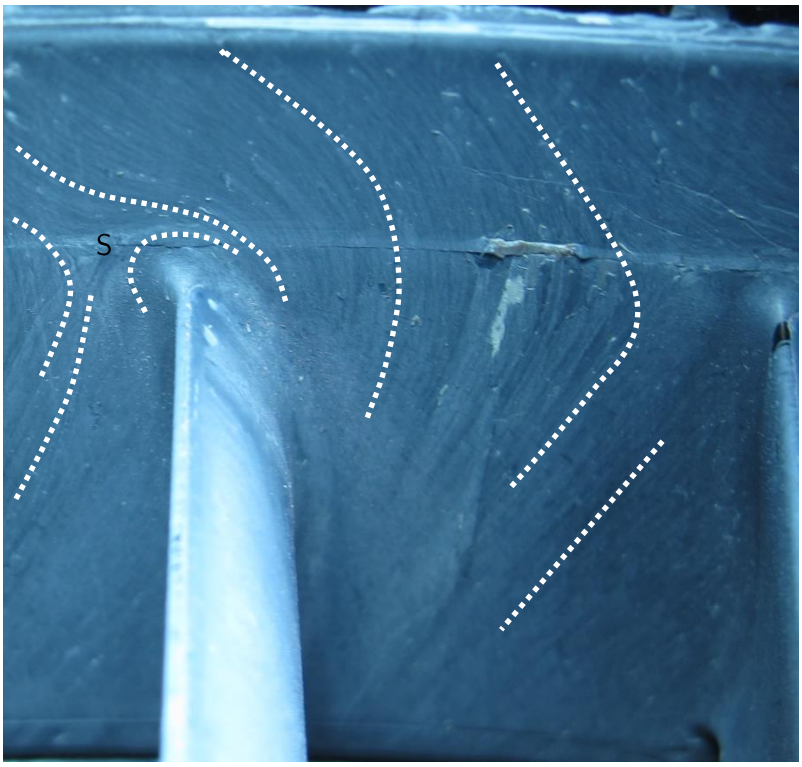

Figure 5-46: Oil flow visualisation on the casing, "Inverse Cut-off" EGV, operating point ADP

The oil flow visualisation on the pressure side of the vane in the left of Figure 5-47 shows no structures to be identified except for a separation line on the intersection of the vane surface and the hub. This is due to the hub secondary flows and is confined to a region very close to the hub.

The right of Figure 5-47 shows the oil flow visualisation on the suction side of the vane. Close to the hub the influence of the cross passage flow can easily be identified when looking at the surface streamlines moving from the hub onto the suction side (marked A). The extension of these streamlines on the suction side is limited to a radial extension of approximately 10% span. Close to the hub two very distinct lines of flow movement can be identified that are marked in green. These show a strong movement of fluid with a component towards the hub (marked B). This is unlike what was seen for the high aspect ratio EGVs, where a movement from the hub towards the casing was seen in this region that was due to the startup procedure of the test rig. For this particular EGV the flow at start-up is different from the low aspect ratio EGV as there is a present that is identical to the structures marked in green dotted lines (marked B). This can be seen in the appendix of this thesis (chapter 12). This in term means that shear stress occurring during the operation is not high enough to extinguish the structures created by the start-up procedure of the rig.

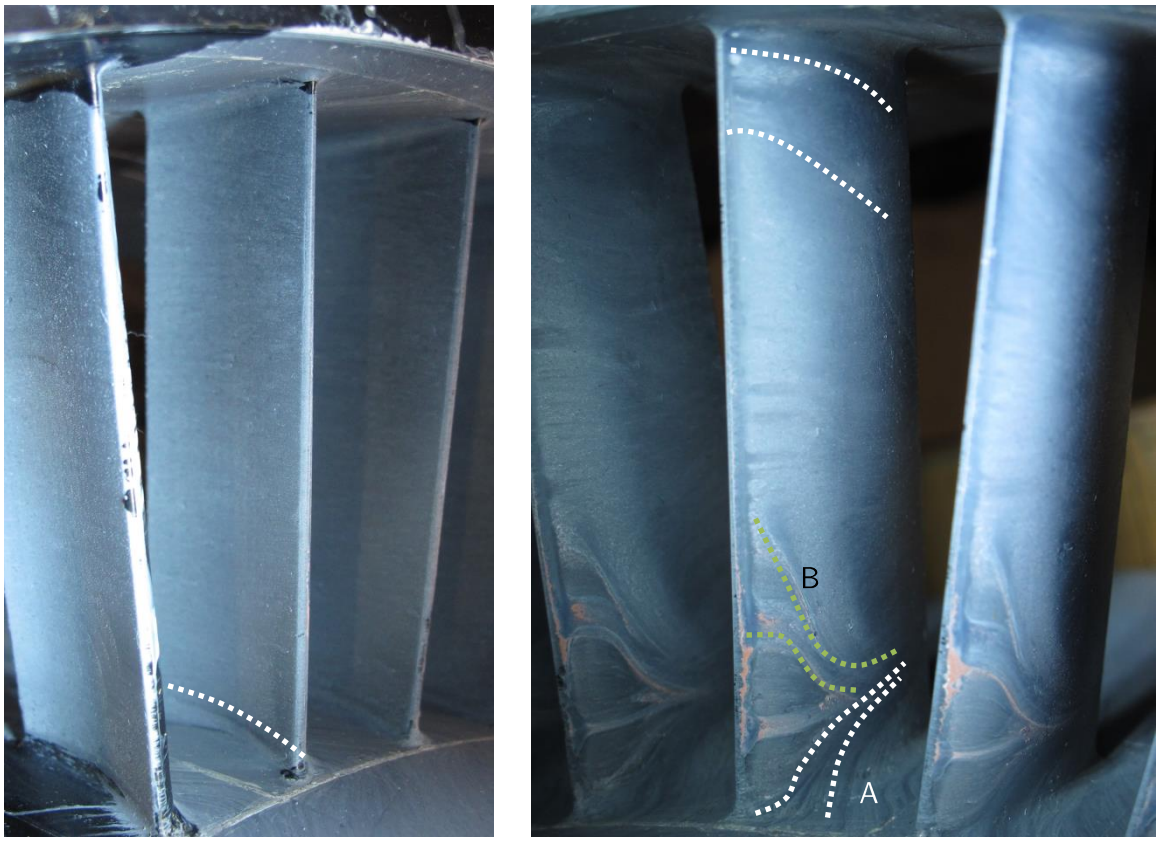

Figure 5-47: Oil flow visualisation on the pressure side (left) and suction side (right), "Inverse Cut-off" EGV, operating point ADP

Acoustic

Figure 5-48 shows the averaged FFT over all microphones used in the acoustic post-processing. The figure shows a large peak at 4080 Hz as well as double and triple this frequency.

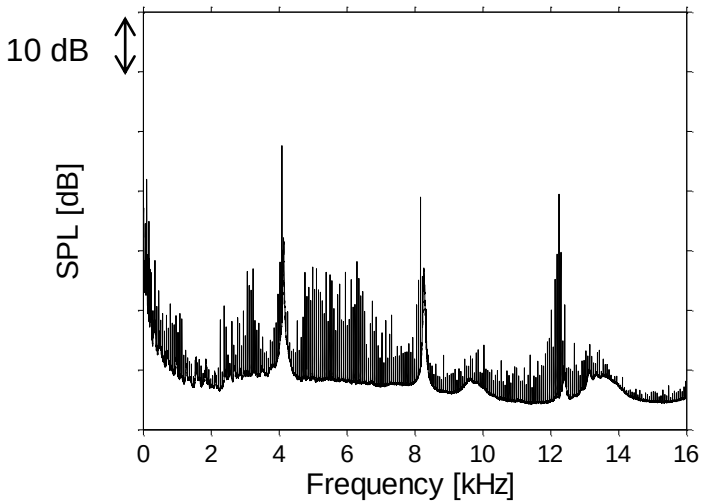

Figure 5-48: Averaged FFT of all microphones for the "Inverse Cut-off" EGV, operating point ADP

The result of the azimuthal mode decomposition can be seen in Figure 5-49. As can be seen the modes able to propagate from the Tyler and Sofrin formula are significantly larger than what is able to propagate. The dominant mode for this operating point is not related to any mode that can be

calculated with the Tyler & Sofrin formula and is approximately 10 dB higher sound power level than the other modes. This means that the modes according to Tyler & Sofrin have been successfully extinguished.

The results of the radial mode decomposition can be seen in Figure 5-50. The figure shows all circumferential modes m able to propagate by their radial mode number n. In addition the modes are split into up- and downstream moving modes. It can be seen that for both directions of propagation the dominant mode is again the mode seen in the AMA with the radial mode n=1 being the dominant order.

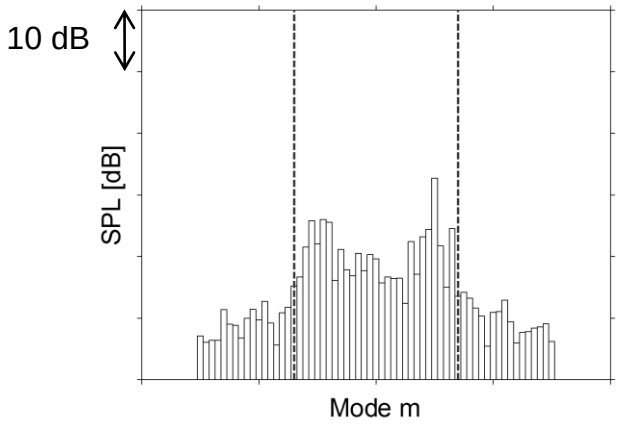

Figure 5-49: Azimuthal mode decomposition for the "Inverse Cut-off" EGV, operating point ADP

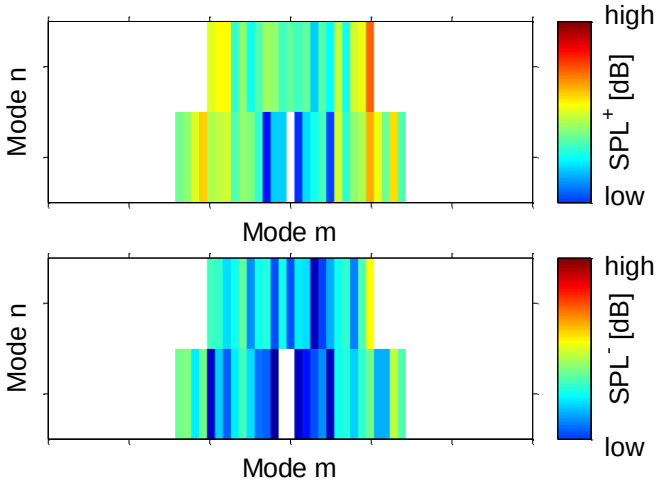

Figure 5-50: Radial mode decomposition for the "Inverse Cut-off" EGV, operating point ADP split by azimuthal, radial, up-and downstream propagating modes

Figure 5-51 shows the results of the radial mode decomposition split by up- and downstream moving modes, but summed up over all radial modes. It can be seen that the dominating mode is approximately 5 dB higher than the other modes in the acoustic field downstream of the vane.

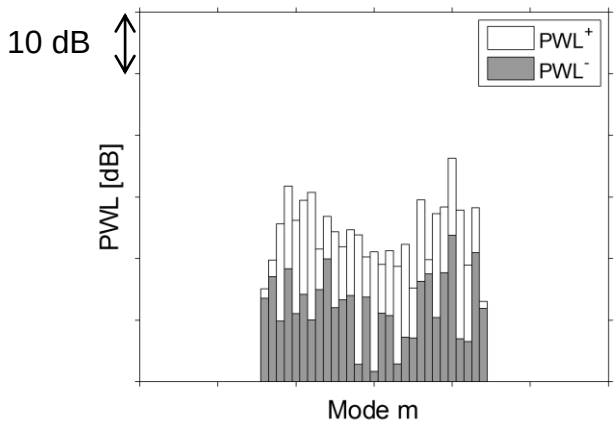

Figure 5-51: Radial mode decomposition, sum of all radial modes split by up and downstream moving modes

5.1.2.4 High loaded EGV

5-hole Probe Plane D0

The flow field in the plane D0 downstream of the EGV is shown in the following pictures. The Figure 5-52 shows the total pressure distribution downstream of the vane. The wake of the vane can easily be identified in the middle of the flow field. On the suction side of the wane-wake close to the casing a large region of low total pressure can be seen (marked with A). This region can be associated with the low total pressure tip leakage fluid in the near wall region as seen in Figure 5-1. This region of low total pressure within the tip leakage region interacts with the cross pressure gradient and is pushed from the pressure side of the vane towards the suction side and starts migrating towards midspan as already explained in the appendix. At around 30% span the maxima of three structures of high total pressure can be identified. These structures are leaned at approximately 30° in clockwise direction that are due to the upstream stators wakes.

This region at approximately 30% span is also the region of maximum total pressure when looking at the averaged values in

Close to the hub a region of low total pressure can be identified (marked B).The region extends from mid-passage towards the centre of the wake. This region is due to the separation that occurs on the hub suction side of the vane due to the hub secondary flow.

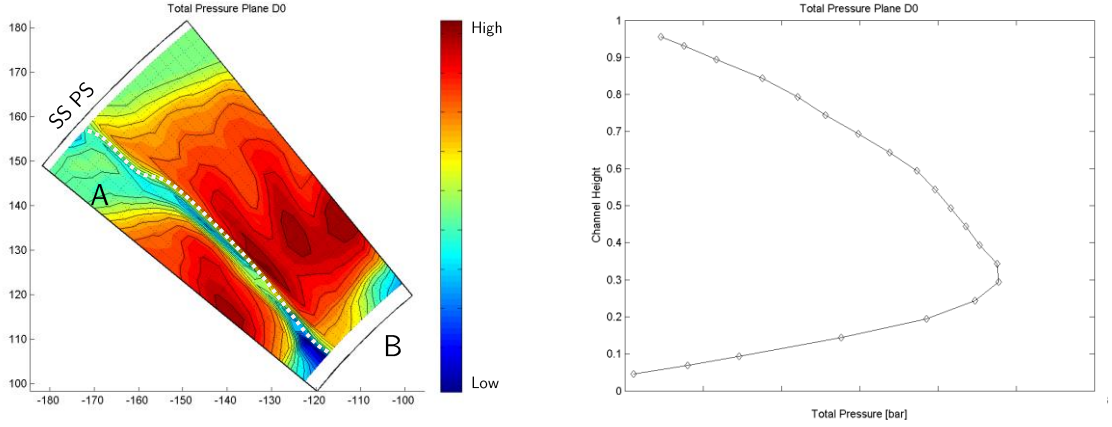

Figure 5-52: Total pressure distribution in plane D0 "High Loading" EGV, operating point ADP

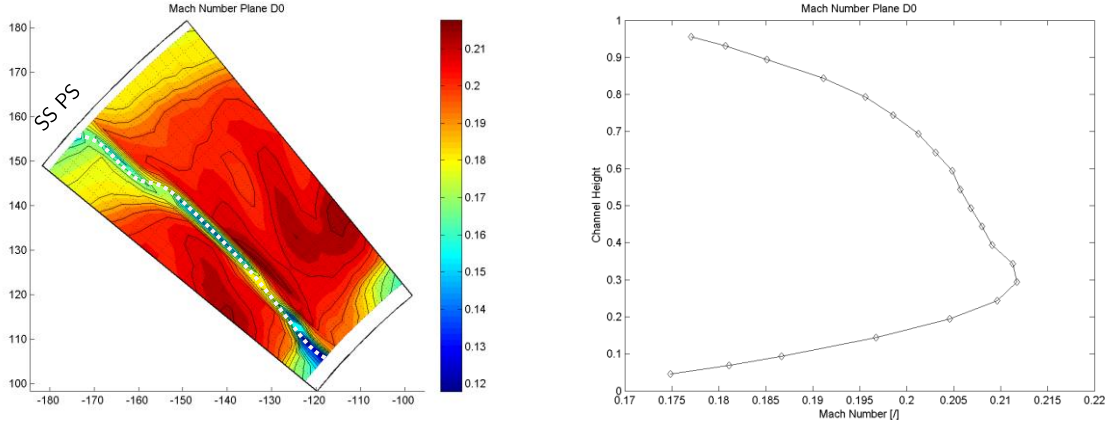

Figure 5-53: Mach number distribution in plane D0 "High Loading" EGV, operating point ADP

The total temperature distribution in Figure 5-54 shows two regions of high total temperature. One of these regions (marked A) can be found on the suction side of the vane at approximately 70% - 80% span and is due to the tip leakage vortex. This is caused by the accumulation of tip leakage fluid on the suction side of the vane due to the secondary flows within the passage of the vane. The second region (marked B) can be found close to the hub where the hub secondary flow of the stage is present in the flow field.

The yaw angle distribution downstream of the wake can be found in Figure 5-55. There is a region of positive yaw angle close to the casing that is due to the tip leakage vortex that extends to approximately 80% span. This tip leakage fluid moves towards the hub as can be seen by the negative pitch angle on the suction side of the wake in Figure 5-56. This is similar to what is seen in Pullan et al. [89] where this flow feature was discussed in context with the formation of a TE shed vortex. Close to the hub, a region of positive yaw angle can be identified that is due to the hub secondary flow present in this region. The wake itself shows a positive yaw angle on the suction side of the wake around midspan and a negative angle on the suction side. In terms of radial flow direction the hub shows a positive yaw angle on the suction side of the wake and a negative angle on the pressure side. This distribution is in contrast to the pitch angle of the wake closer to casing.

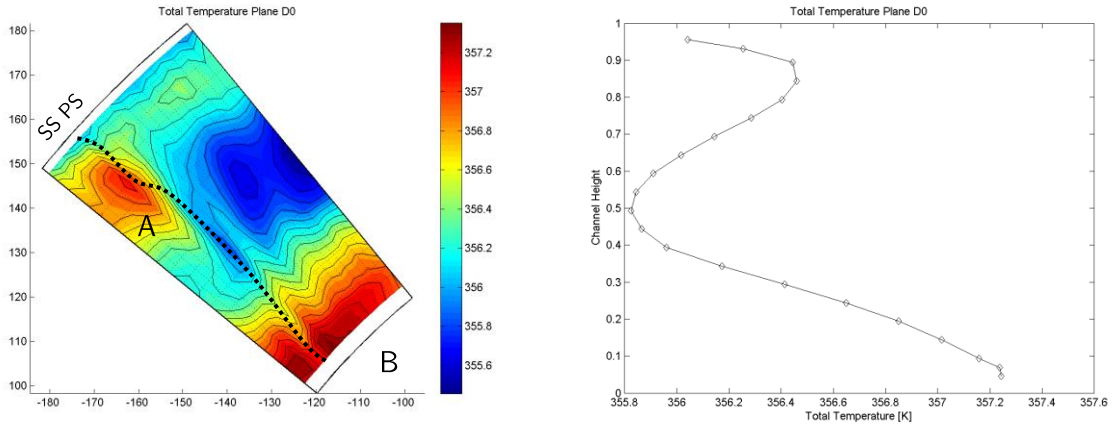

Figure 5-54: Total temperature distribution in plane D0 "High Loading" EGV, operating point ADP

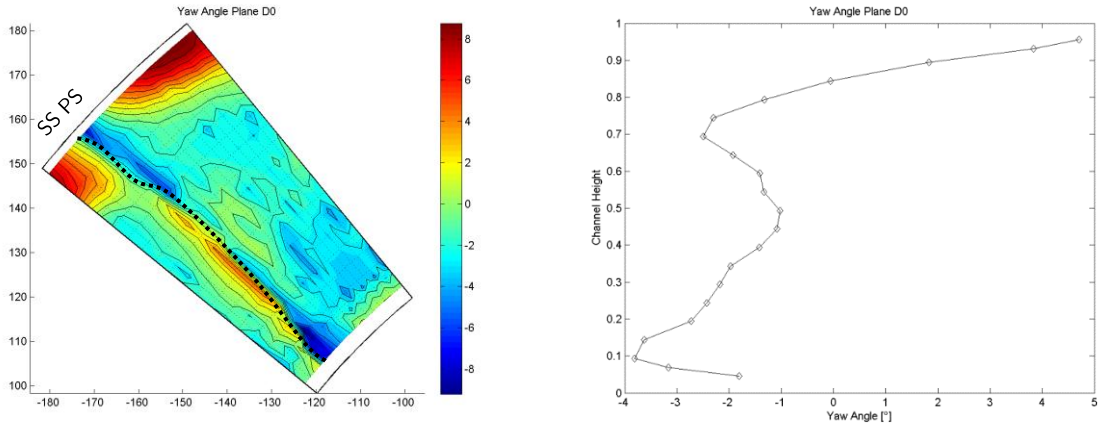

Figure 5-55: Yaw angle distribution in plane D0 "High Loading" EGV, operating point ADP

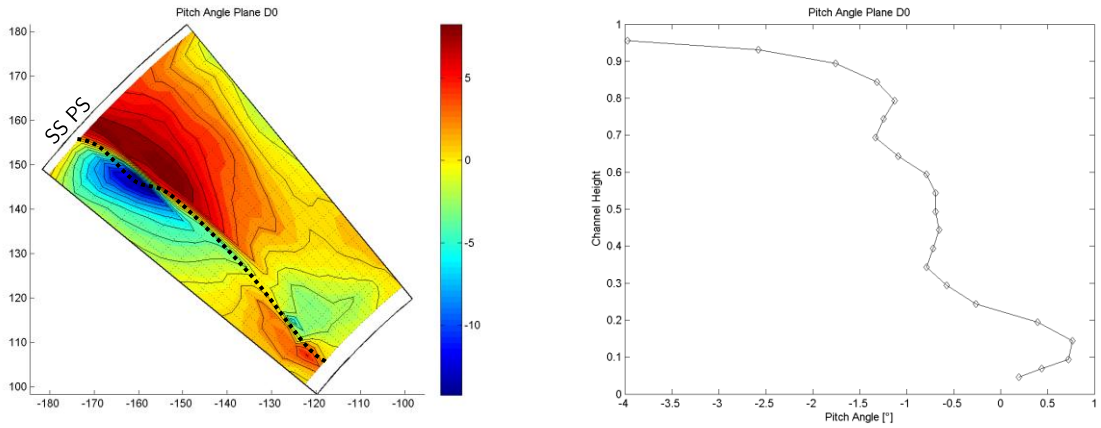

Figure 5-56: Pitch angle distribution in plane D0 "High Loading" EGV, operating point ADP

5-hole Probe Plane D

The result of the five-hole probe measurements downstream of the EGV is shown in the following section. The wake has mixed out to a large extend as can be seen in Figure 5-57. The remainder of the wake is bent towards the pressure side of the vane and consists of a large low pressure are between midspan and the casing and a second region of low pressure close to the hub.

The hub structure is due secondary flow and the resulting corner separation that occurs at the hub suction side of the vane. The structure existing from midspan upwards results from a combination of two different effects: the low total pressure fluid from the rotor tip leakage vortex and the rolling up of the trailing edge shed vorticity. An easier separation of these two effects can be seen in Figure 5-58 where the yaw angle distribution is shown. Close to the casing, a region of positive yaw angle is present that is due to the tip leakage flow. In addition to the two structures, a third structure is present close to the hub at approximately mid-passage. This structure is due to the hub secondary flow of the vane.

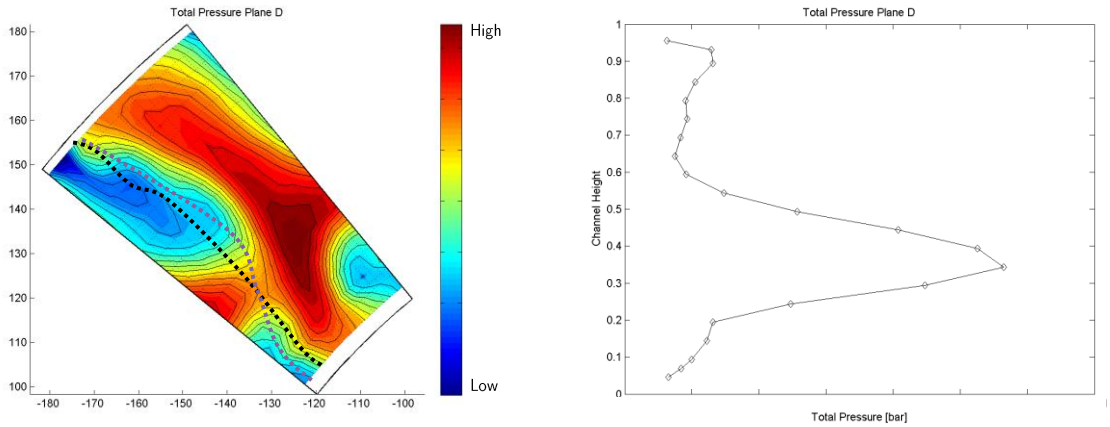

Figure 5-57: Total pressure distribution in plane D "High Loading" EGV, operating point ADP

The pitch angle in Figure 5-59 shows a large region of positive/negative fluid flow between the casing and approximately midspan at the pressure/suction side of the vane. This again shows the trailing edge shed vorticity causing the rolling up of the fluid into a vortex.

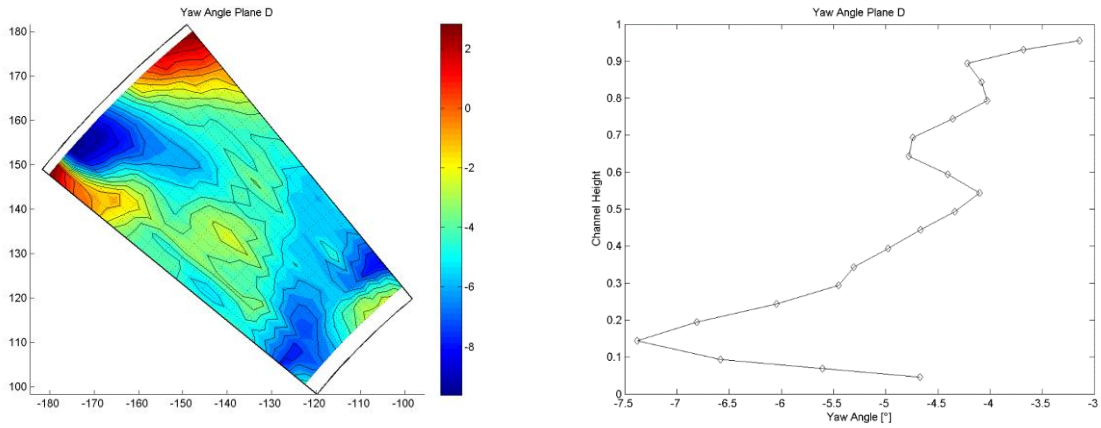

Figure 5-58: Yaw angle distribution in plane D "High Loading" EGV, operating point ADP

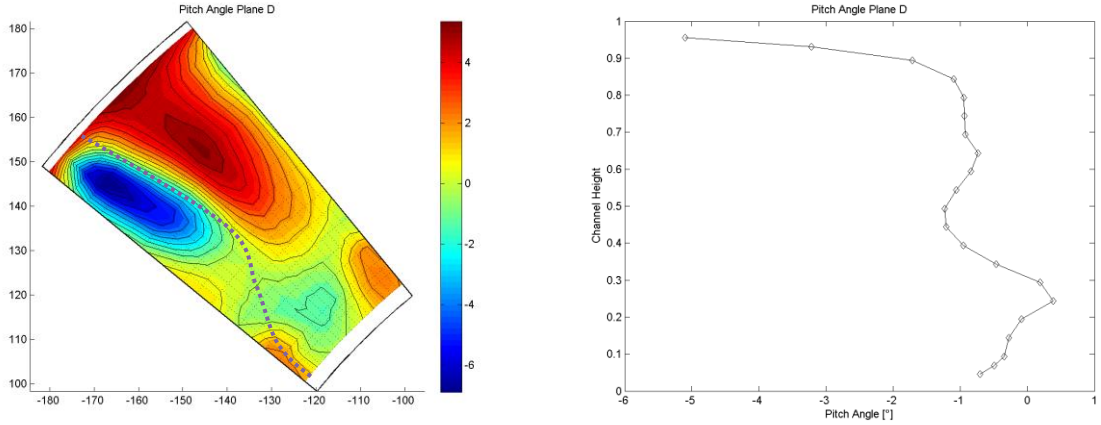

Figure 5-59: Pitch angle distribution in plane D "High Loading" EGV, operating point ADP

Static pressure

The static pressure distribution on the vane surface for the "High Loading" EGV operating point ADP is shown in Figure 5-60. Depicted is the distribution of suction and pressure side for all 4 radial positions. The suction sides distributions for 20% span and 30% span show a rather similar distribution. Both radial positions show a suction peak at approximately 13% axial chord and show a velocity decrease downstream of this point. In the region between 20% and 30% axial chord a region of almost constant static pressure can be observed just downstream of the suction peak for the 20% span pressure distribution. This implies that a separation bubble present in this region. At 20% span the last static pressure point at the trailing edge at 93% axial chord shows a strong increase in static pressure. Another feature can be identified at approximately 50% axial chord for the suction side at 30% and 50% span. A decrease in pressure gradient can be seen for these two positions.

The pressure distribution on the suction side at 50% span shows a suction peak at approximately 20% axial chord and a steady deceleration towards the trailing edge. At 80% span, the suction peak is again located at approximately 20% axial chord, but the overall distribution shows a very small suction peak compared to the other axial positions.

The pressure side shows an almost identical distribution of static pressure for all radial positions. The static pressure is almost constant at all positions. The 80% span position shows a slightly lower static pressure, but otherwise the shows approximately the same features.

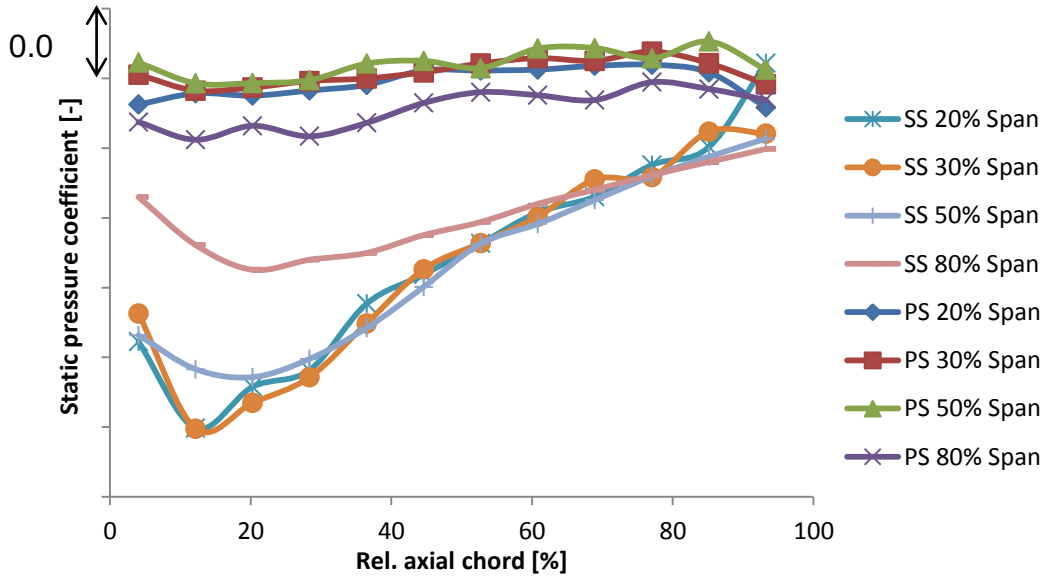

Figure 5-60: Static pressure distribution for suction and pressure side "High Loading" EGV, operating point ADP

Oil Flow visualization

The hub oil flow visualisation of the hub portion of the "High loading" EGV at the operating point ADP can be seen in Figure 5-61. A strong pressure gradient is present as can be seen by the streamlines from the suction to the pressure side. The stagnation point is again marked with an "S", and again it is hard to determine the exact point of separation due to the low shear stress. This strong cross passage flow is responsible for a separation on the suction side hub endwall corner of the vane.

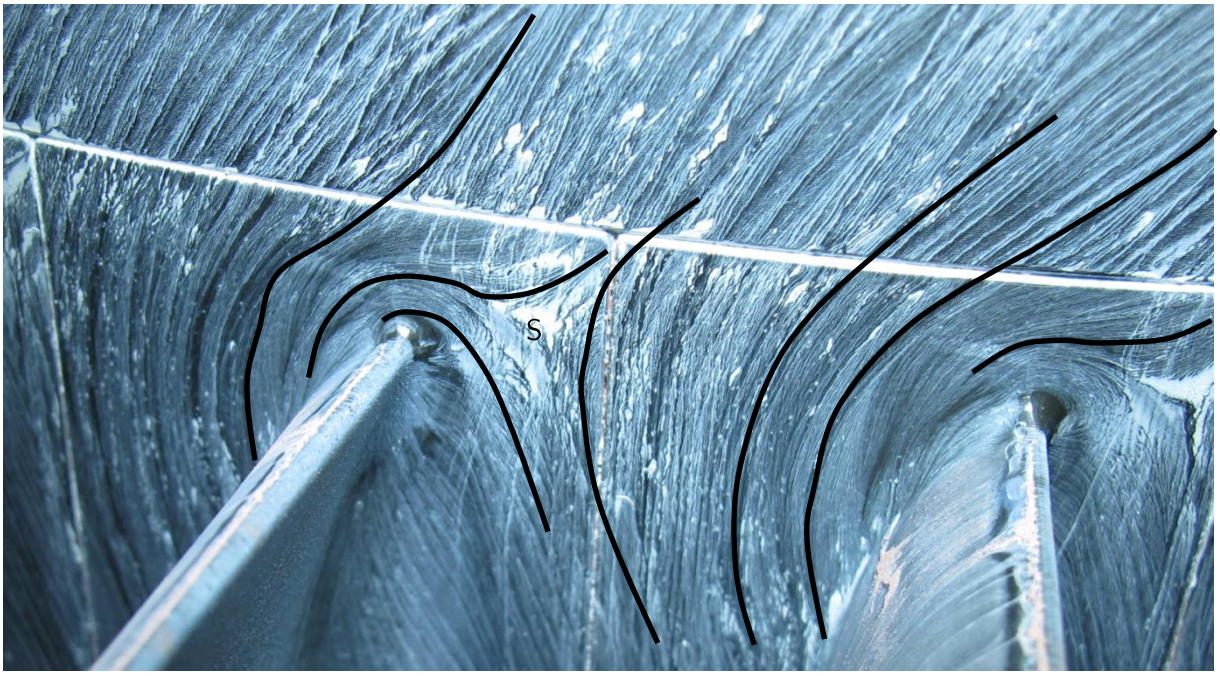

Figure 5-61: Hub oil flow visualisation, "High Loading" EGV, operating point ADP

The oil flow visualisation at the casing of the vane can be seen in Figure 5-62. The separation point on the pressure side of the vane is again marked with an "S". The general features of the oil flow

visualisation are marked as black lines. There is a distinct lack of pressure gradient between the suction and the pressure side present as was also seen in the static pressure distribution in Figure 5-60 and as seen by the surface streamline plotted between the suction and the pressure side.

Figure 5-62: Casing oil flow visualisation, "High Loading" EGV, operating point ADP

The suction side of the vane is shown in Figure 5-63 where the suction side of two different vanes can be identified. At approximately 20% axial chord a lift-off line can be identified (marked A) where the streamlines start to move on the vane up to a height of approximately 15% span. Close to the casing the effect of the tip leakage vortex superimposed with the passage gradient can be seen. The streamlines move from the casing towards approximately 75% span of the vane. Close to the leading edge of the vane, at approximately 10-15% axial chord a region of accumulation of oil stretching from the hub to approximately 80% span (marked B). The onset of this line coincides with the axial position where the streamlines from the hub start to move onto the suction side of the vane. While at 20% span, a static surface pressure plateau could be identified that could point towards a separation bubble, no such structures were found in the static pressure distribution, although the structure in the oil flow visualisation can be identified up to a radial position of 70%. At a radial position of approximately 30% to 60% a region with almost no traces of oil (marked C). This region coincides with a change in pressure gradient that was already mentioned for the two radial positions 30% and 50%. Looking at the pressure side shown in Figure 5-64there is a distinct lack of features visible compared to the suction side of the vane. A black line is shown at an axial position that is being followed by a region of less oil present on the vane.

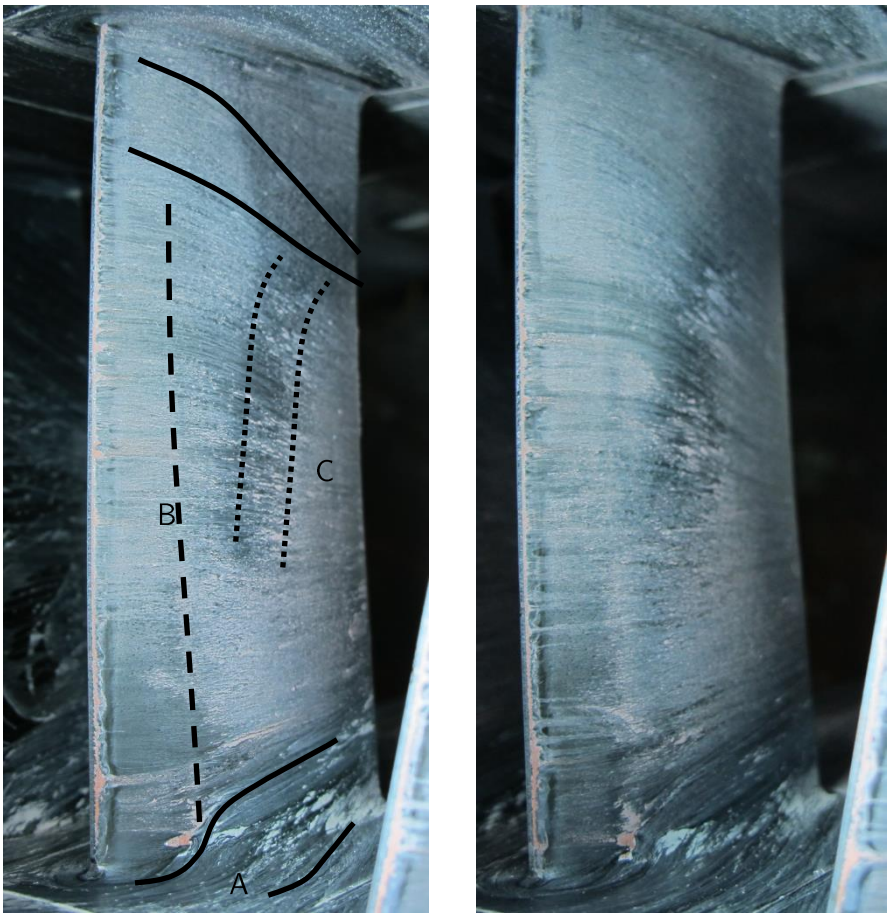

Figure 5-63: Suction side oil flow visualisation, "High Loading" EGV, operating point ADP

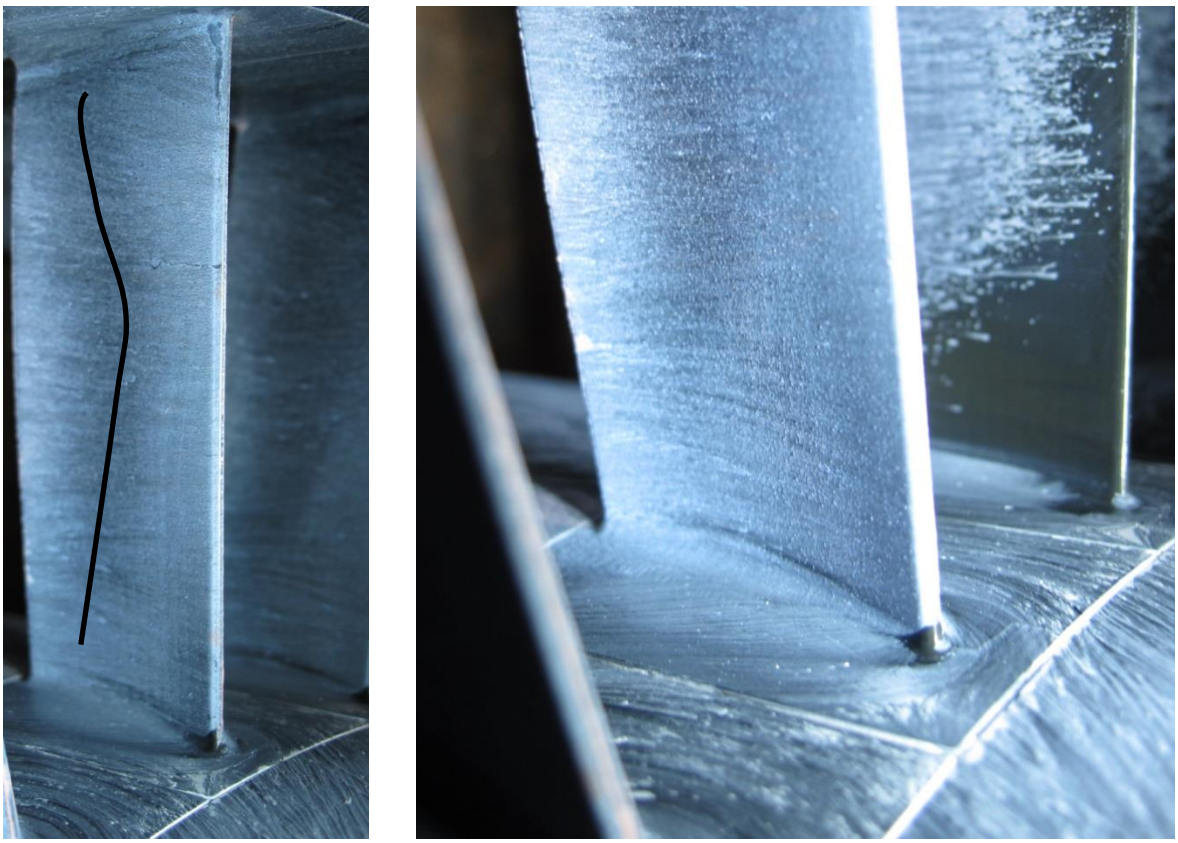

Figure 5-64: Pressure side oil flow visualisation, "High Loading" EGV, operating point ADP

Acoustic

The acoustic results of the "High loading" EGV for the operating point ADP are presented in the following section. The averaged FFT is shown in the Figure 5-65. The blade passing frequency can be identified at a Frequency of 4080 Hz and the 2nd BPF at 8160 Hz and even the third BPF is visible.

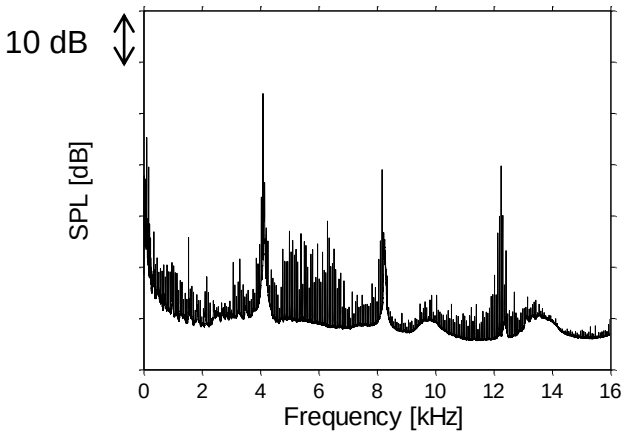

Figure 5-65: Averaged FFT of all microphones "High Loading" EGV, operating point ADP

The results of the averaged azimuthal mode analysis can be seen in Figure 5-66. The modes able to propagate are shown as red, dotted lines. There is a single mode dominating the acoustic field that is a result of two different interactions, a rotor/stator interaction scattered by the EGV as well as a direct interaction between the rotor and the EGV. The SPL of this mode is more than 10dB larger than that of the other modes.

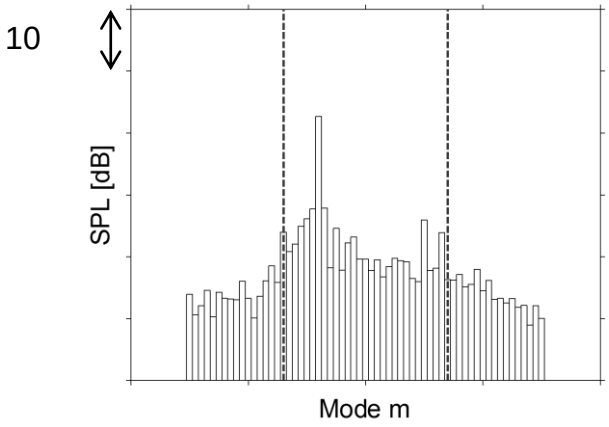

Figure 5-66: Averaged azimuthal mode analysis "High Loading" EGV operating point ADP

The results of the following radial mode analysis can be seen in Figure 5-67. The figure shows all radial and azimuthal modes able to propagate, separated by up and downstream propagating modes. There are only two radial modes able to propagate, the modes n=0 and n=1.

Figure 5-67 shows the sum of all radial modes for each azimuthal mode separated by up- and downstream moving modes. When comparing the radial modes n=0 and n=1 in Figure 5-68 it can be seen that the dominant mode has equal amplitudes for both radial modes.

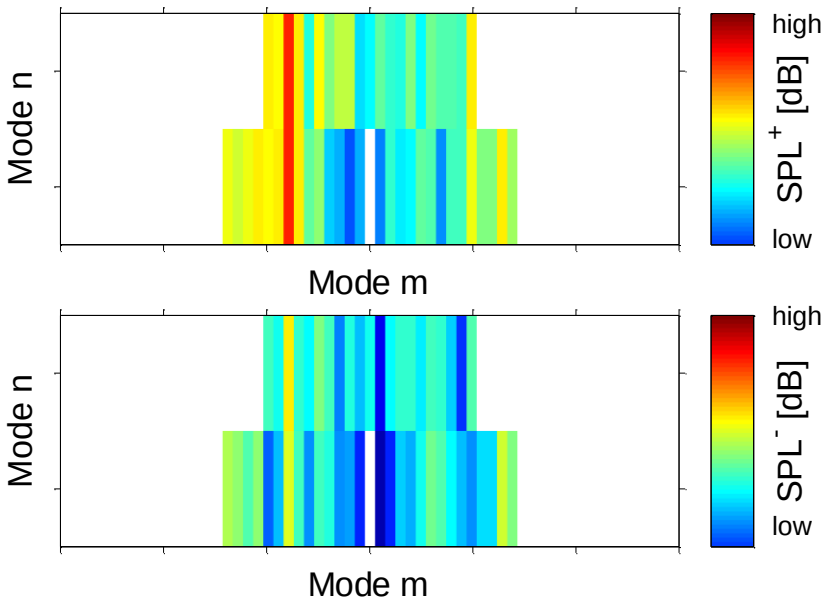

Figure 5-67: Radial mode decomposition of the "High Loading" EGV, operating point ADP; all circumferential and radial modes by up- and downstream propagating modes

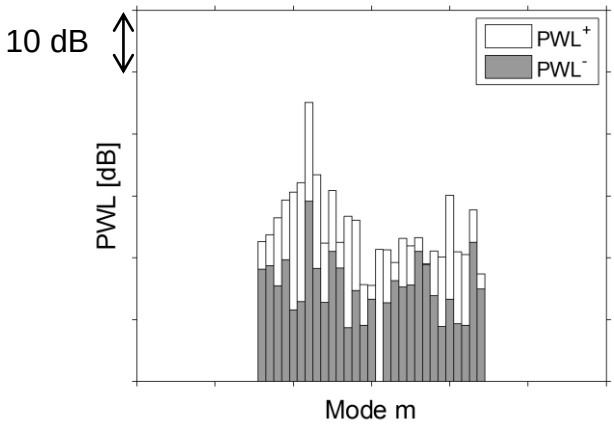

Figure 5-68: Radial mode decomposition, sum of all radial modes split by up- and downstream propagating modes; "High Loading" EGV, operating point ADP

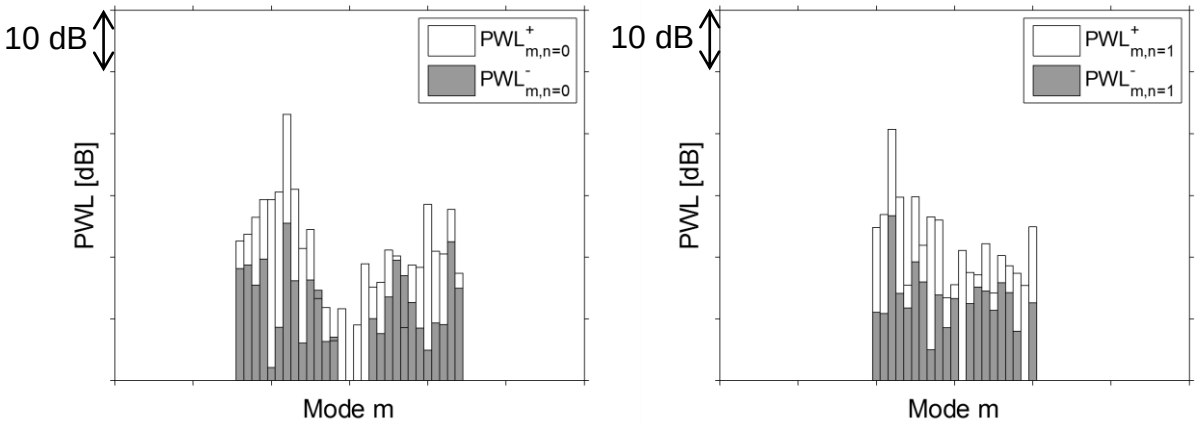

Figure 5-69: Radial mode n=0 (left) and n=1 (right) split by up and downstream propagating modes "High Loading" EGV, operating point ADP

5.1.3 Comparison of the EGVs

The following section directly compares resulting flow and acoustic field downstream of the different EGVs presented in the previous chapters. At first the aerodynamic differences including a comparison of the different total pressure loss coefficients will be presented and then the differences in acoustic performance will be discussed.

Aerodynamic Comparison

The aerodynamic properties of the different EGVs will be discussed in terms of circumferentially averaged distributions of total pressure loss coefficient and yaw angle since these provide the best insight into the flow field downstream of the EGV. Figure 5-70 shows a comparison of the circumferentially averaged total pressure loss coefficient downstream of the EGV for all four EGV configurations for the operating point ADP. The abscissa shows the total pressure loss coefficient with respect to the measurement plane upstream of the EGV and the ordinate the dimensionless height of the channel.

The "Datum" EGV, shown in black, shows an almost constant distribution of total pressure between 25% and 70% span with a maximum at approximately 45% span. Close to the endwalls the influence of the secondary flow can be identified resulting in an increase in total pressure loss. A small plateau in total pressure can be identified in a region between 20 and 35% span. This influence can also be seen in Figure 5-71 where the yaw angle distribution is shown over the dimensionless channel height for all four EGVs. Close to the hub and the casing the "Datum" EGV shows an increase in yaw angle close to the endwalls. For the hub this is due to the hub secondary flow caused by the passage pressure gradient whereas close to the casing this effect is amplified by the change in yaw angle due to the tip leakage flow.

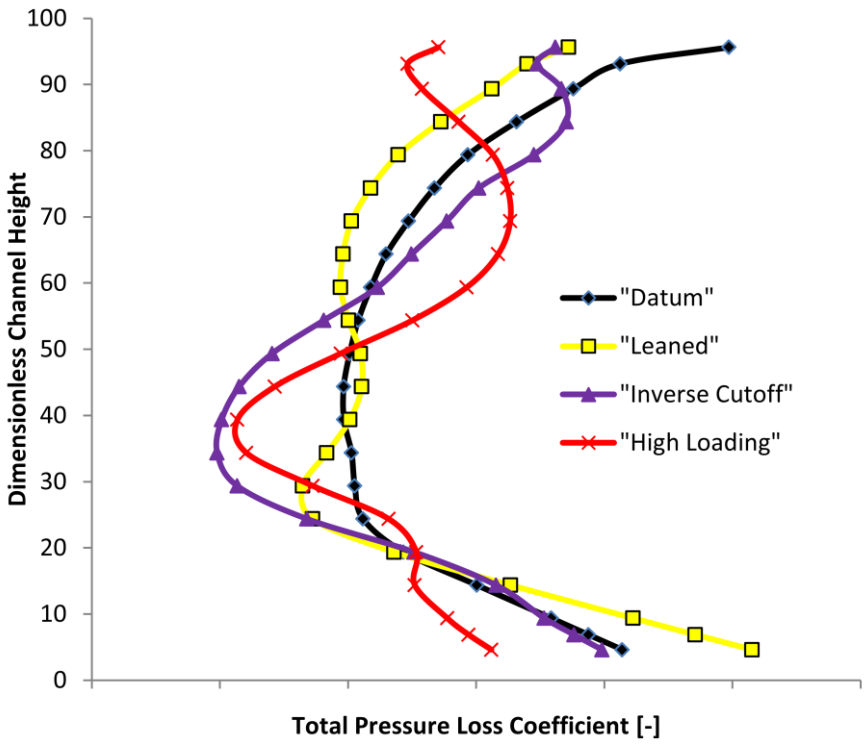

Figure 5-70: Comparison of circumferentially averaged total pressure in plane D, operating point ADP

The "Leaned" EGV shows a similar distribution in total pressure although the average pressure level is lower than for the "Datum" EGV. The influence of the secondary flows close to hub and casing can again be identified by the increased total pressure loss present in these regions. At midspan the plateau like feature that was seen for the "Datum" EGV is not present anymore, but rather a region of minimum total pressure loss can be identified at 30% span that decreases to a local maximum at 45% span and then decreases again. This minimum is due to the region of high total pressure at this region as seen in Figure 5-21 that is then again reduced around midspan by the region of low total pressure located at the centre of the vane that is due to the hub suction side corner separation. The yaw angle distribution in Figure 5-71 shows an almost identical distribution close to the endwalls compared to the "Datum" EGV whereas between 15% and 60% span a large difference can be seen. The region above 15% span shows a lower yaw angle for the "Leaned" EGV that only varies slightly across the span whereas the "Datum" EGV shows a steady decrease in yaw angle until a minimum at 45% span. This effect close to the casing can again be attributed to the suction side corner separation.

The "Inverse Cut-off" EGV is, like the "High loading" EGV, is an EGV with a short (approximately 1/3rd of the "Datum"/"Leaned" EGV) chord length is therefore less prone to the influence of secondary flows. This can be seen when comparing the EGV exit total pressure distribution of the "Inverse Cut-off" and "High loading" EGV with the higher chord EGVs. The short chord EGVs show a significant difference in the distribution of total pressure loss. Whereas the long chord EGVs show a somewhat constant total pressure loss at midspan, the two short chord EGVs show a significant peak in total pressure at approximately 35-40% span reducing the total pressure loss in this regions. This peak results from the total pressure distribution in plane C upstream of the EGV (Figure 5-1) that shows a maximum at 25% height of the channel. This is now influenced by the hub secondary flows and pushed further towards midspan. In addition, the tip leakage flow causes a migration of

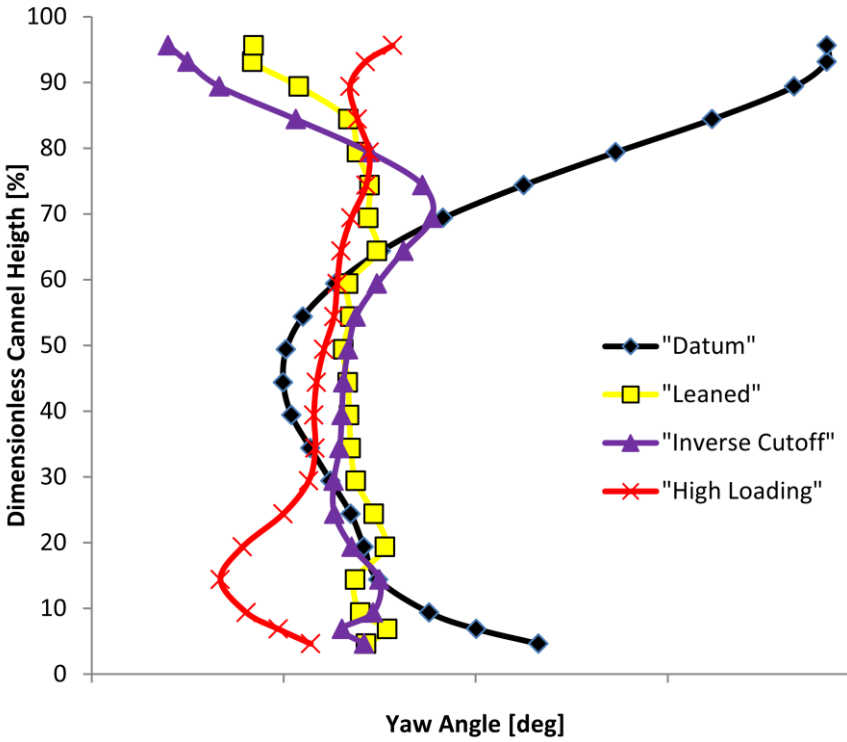

Figure 5-71: Comparison of circumferentially averaged yaw angle in plane D, operating point ADP

fluid from the casing towards midspan resulting in a further increase in total pressure in this region. Looking at the yaw angle distribution of the "inverse Cut-off" EGV in Figure 5-71 it can be seen that the EGV shows a constant exit angle in a region between 25% and 55% span is almost constant. At 70% peak a region of positive average yaw angle can be identified that is due to the effect of the tip leakage flow who's fluid migrates from the casing towards midspan and results in a maximum yaw angle located in this radial position in plane D. Close to the casing a region of strong negative yaw angle can be identified that is a result of the tip leakage flow causing a rollup into a vertical structure and therefore influencing the region close to the casing resulting in a region of negative yaw angle. Close to the hub the yaw angle shows a local maximum at 10% span.

The "Highly loaded" EGV shows a similar minimum in the total pressure loss distribution as seen for the "Inverse Cut-off" EGV. There is a maximum of total pressure loss located at 75% span due to the way the low total pressure fluid associated with the tip leakage migrates from the casing towards midspan as seen in Figure 5-57. Close to the casing there is a minor decrease in averaged total pressure loss again caused by said migration of fluid. Close to the hub a further decrease of total pressure can be identified. This strong reduction in total pressure is due to the hub secondary flows. The yaw angle distribution shows an almost constant averaged distribution across the whole span with a small increase towards the casing. Close to the hub the influence of the secondary flows can be seen by a decrease in yaw angle with a minimum at 15% span. This is caused by the fluid migrating onto the suction side of the vane as seen in Figure 5-63.

The results of the global total pressure loss comparison can be seen in Table 5-1. The table shows the total pressure losses with respect to the loss generated by the "Datum" EGV between measurement plane C and D. The "Leaned" EGV has a calculated relative loss of 0.92 meaning there is only a minor change in total pressure loss between the "Datum" EGV and the "Leaned" EGV. This is despite that the fact that the "Leaned" EGV shows a strong hub suction side corner separation zone.

The "Inverse Cut-off" EGV shows a reduction in total pressure loss coefficient by 15% between plane C and D. The aerodynamically optimised "High Loading" EGV has an additional 4% reduction in total pressure loss resulting in a 19% reduction in total pressure loss compared to the "Datum" EGV.

For these two EGVs there is also the option to compare the losses of the "Datum" EGV to the

Table 5-1: EGV total pressure loss comparison ADP

	Total Pressure Loss $\frac{\zeta}{\zeta_{REF}}$	
Configuration	C-D	C-D0
Ref. EGV	1	-
Leaned EGV	0.92	-
Inverse Cut-Off EGV	0.85	0.47
High loaded EGV	0.81	0.45

losses created from plane C to the plane D0 located close to the TE of the vane. It can be seen that the losses of the "High loading" EGV are only 45% of those created by the "Datum" EGV. This means that the rest of the losses created from D0 to D are largely due to the mixing of the flow as well as wall shear occurring at hub and casing. The calculated losses for the "Inverse Cut-off" EGV are 47% of the "Datum" EGV losses. When comparing the two low aspect ratio EGVs it can be seen that the mixing losses of the "Inverse Cut-off" EGV are higher than those of the "High Loading" EGV. The change in loss coefficient for the "Inverse Cut-off" EGV is 38% whereas an increase of 36% can be seen for the "High Loading" EGV.

Acoustic Comparison

A comparison of the acoustic properties for the four EGV at the operating point ADP will be given in the following section.

Figure 5-72 shows the overall sound power level (PWL) as well as of all four EGVs as already separately shown in earlier chapters. The according values can be seen in Table 5-2.

It can be seen that the highest PWL is caused by the "High loading" EGV. The PLW of this EGV is approximately 1.5dB higher than of the "Datum" EGV. The two EGVs that were optimised for the acoustic performance, the "Leaned" and "Inverse Cut-off" EGV show lower power levels. The "Leaned" EGV, that was not optimised for this particular operating point shows a PWL that is 0.2dB lower than for the "Datum" EGV and the "Inverse Cut-off" EGV has a level that is 3.3dB lower. This can also be seen in Table 5-2.

The reason for this decrease for this EGV is the fact that the modes associated with the formula by Tyler and Sofrin are not able to propagate and are therefore significantly lower than those of the other EGVs. The "High Loading" EGV has significantly higher Tyler and Sofrin modes than the "Datum" and "Leaned" EGV who have a similar Tyler and Sofrin PWL.

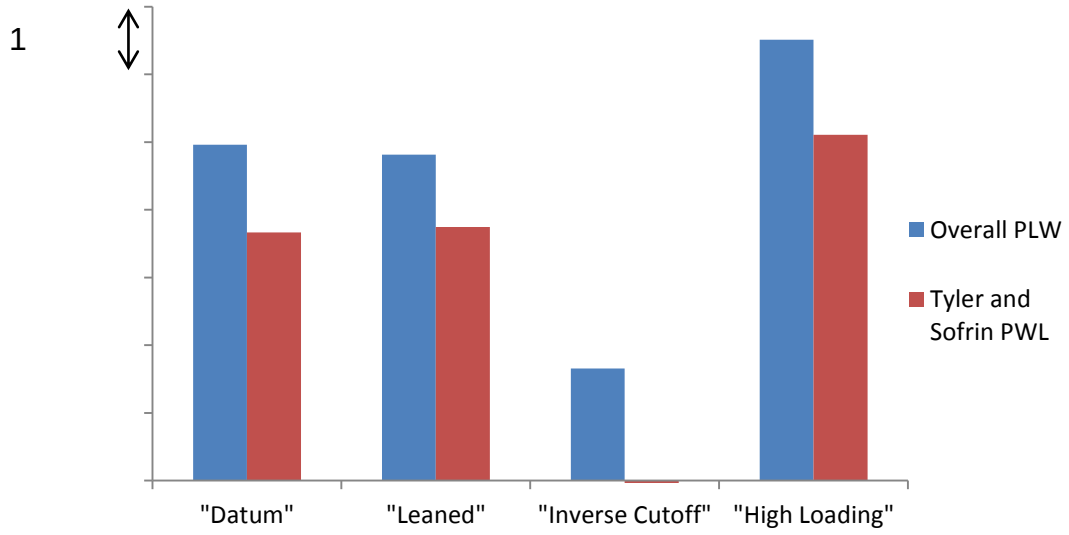

Figure 5-72: EGV Sound Power Level Comparison

Table 5-2: EGV Sound Power Level Comparison

	Datum	Leaned	Inverse Cut-off	High Loading
Overall SPL	Reference	-0.2dB	-3.3dB	+1.5dB
Tyler & Sofrin	-1.3dB	-1.3dB	-	+0.1dB

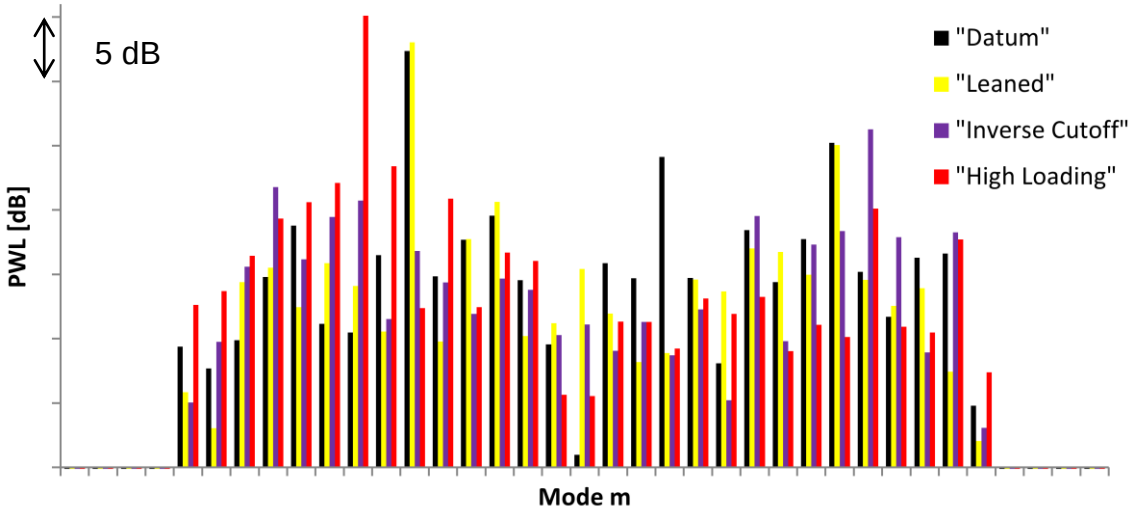

Figure 5-73 shows a comparison of all modes able to propagate from the radial mode decomposition performed for the acoustic field downstream of all four EGVs.

The dominant modes for both the "Datum" and "Leaned" EGV are the modes resulting from the rotor/stator interaction being scattered by the EGV. The rotor-EGV interaction can be identified as the third highest mode for the "Datum" EGV. This mode is not visible for the "Leaned" EGV as the goal of the design was to reduce the interaction between rotor and EGV.

The "Inverse Cut-off" EGV shows a single peak that is higher than the other modes found in the post processing. This mode is not related to any blade or vane number in the configuration. All interactions with the EGV have been successfully extinguished.

For the "High Loading" EGV the dominant mode is a result of two different interactions: the interaction between the rotor and the EGV and the rotor/stator interaction mode being scattered by the EGV. This results in the highest PWL for the operating point ADP.

Overall the goal of reducing the PWL by either a change in vane number ("Inverse Cut-off" EGV) has been successfully applied for this operating point and resulted in a decrease in PWL by 3.3dB. The stacking of the vane profiles ("Leaned" EGV) resulted in no significant change in PWL and does not prove to be a useful tool in this particular operating point. The strong interaction modes occurring for the "High Loading" EGV show to be the dominant source of noise for this EGV.

5.2 Approach

5.2.1 Rotor Exit Flow Field

The 5-hole probe results of the operating point approach are shown in the following section. When looking at the total pressure distribution in Figure 5-74 three different sections can be identified. One section is located between the hub and approximately 20% span. This section is dominated by the secondary flows of both the rotor and the upstream stator as well as the interaction of these two structures. The region between 20% and approximately 85% span is dominated by the 2d-interaction between the stator and the rotor as described in literature. The flow-field shown in the figures below shows radial structures that are due to the upstream stator wakes. Structures emanating from upstream vanes are always shown as radial structures whereas structures that are due to the rotor are seen as circumferential bands due to the pneumatic probe functioning as a low pass filter. This means that while the radial distribution is very strongly dependent on the rotor, the effects of the rotor in the 2d-flow field will be seen as circumferential bands. Close to the casing a region of low total pressure stretching in circumferential can be identified that is due to the tip leakage vortex present in this region of the blade. At the very casing, the total pressure increases due to the jet generated by the tip gap.

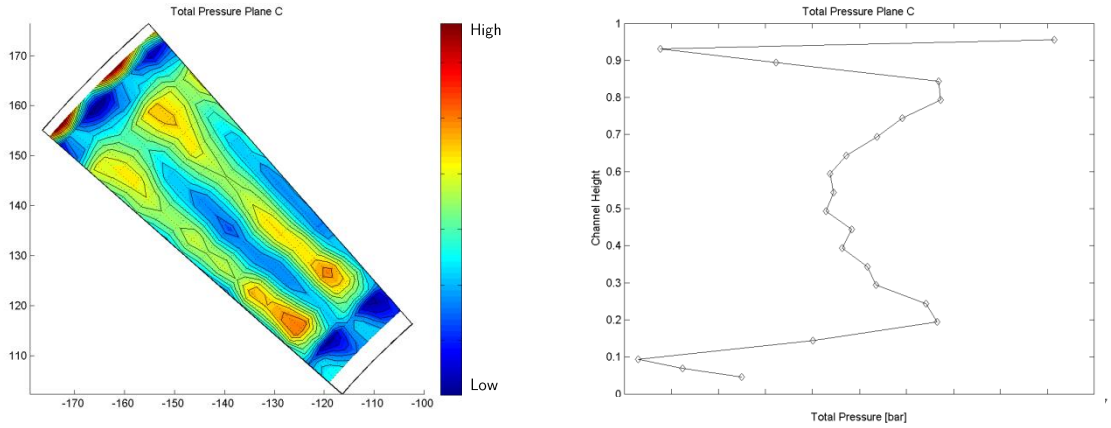

Figure 5-74: Total pressure distribution plane C, "Inverse Cut-off" EGV, operating point Approach

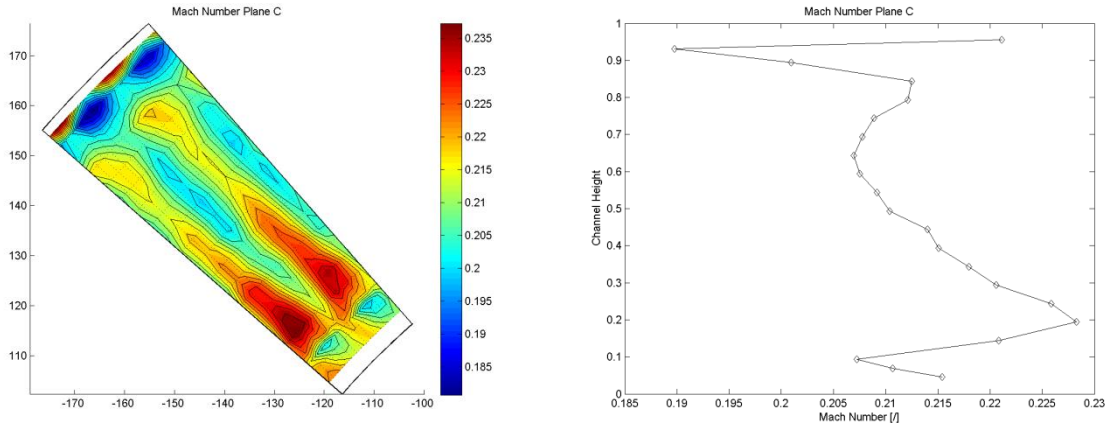

Figure 5-75: Mach number distribution plane C, "Inverse Cut-off" EGV, operating point Approach

Looking at the Mach number in Figure 5-75 identical features can be seen. There is a maximum Mach number at approximately 20% span and another peak close to the tip vortex at 80% span.

The static pressure distribution in Figure 5-76 shows an almost linear radial pressure distribution as required by the radial equilibrium of the swirling flow. Close to the endwalls this distribution is influenced by the secondary flows as well as the tip leakage flow.

The total temperature distribution in Figure 5-77 shows a strong increase in total temperature close to the endwalls where there is a lack of work being performed by the rotor due to secondary flows and the tip leakage flow.

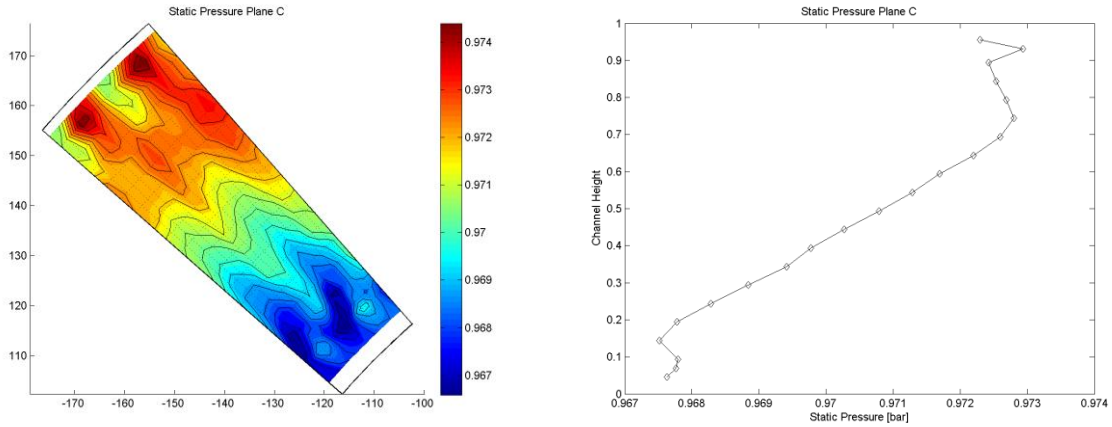

Figure 5-76: Static pressure distribution plane C, "Inverse Cut-off" EGV, operating point Approach

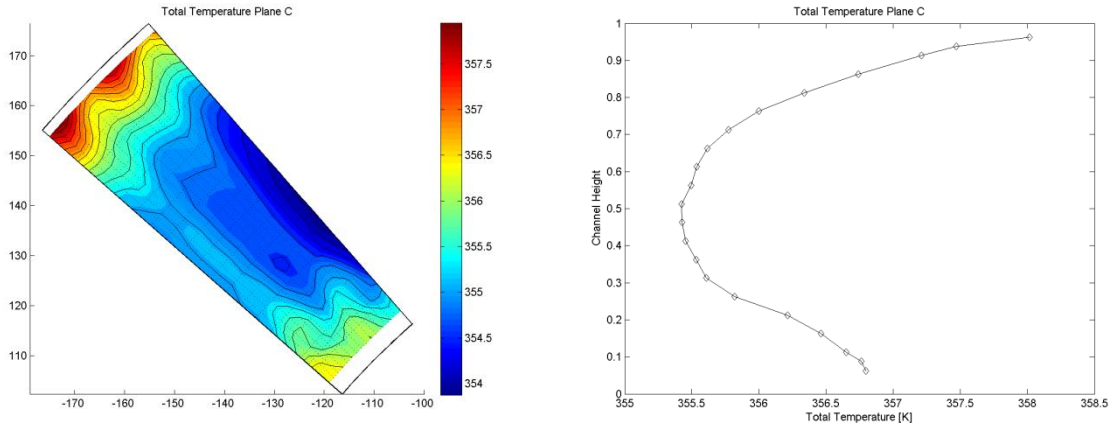

Figure 5-77: Total Temperature distribution plane C, "Inverse Cut-off" EGV, operating point Approach

The yaw angle distribution is shown in Figure 5-78. The region between 20 and 80% span shows an almost linear increase of yaw angle. The presence of the tip leakage flow causes a strong increase in yaw angle close to the casing due to the lack of turning of the leakage flow.

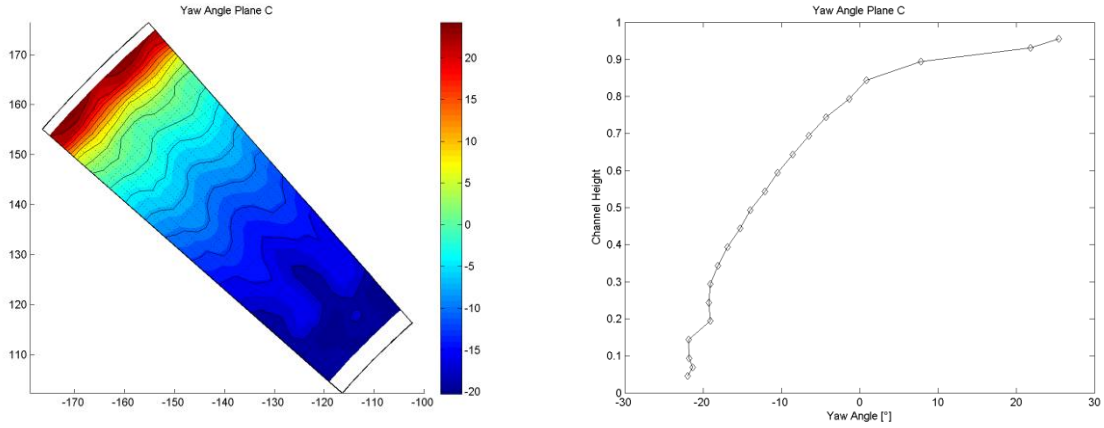

Figure 5-78: Yaw angle distribution plane C, "Inverse Cut-off" EGV, operating point Approach

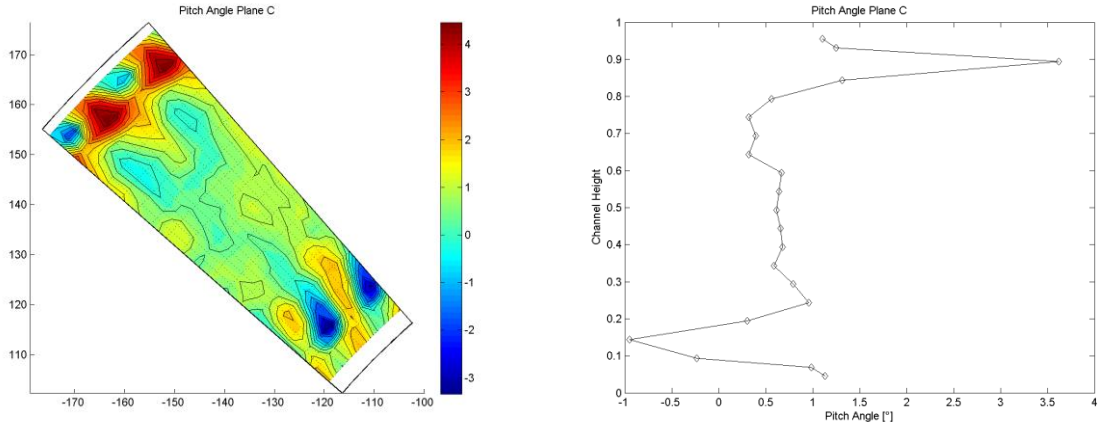

Figure 5-79: Pitch angle distribution plane C, "Inverse Cut-off" EGV, operating point Approach

Comparison plane C Flow properties for different EGV

The following section compares the different EGV exit flow fields in order to show all EGVs have similar inlet conditions in order to be comparable. Figure 5-80 shows the comparison of yaw angle (left) and total pressure (right) for all four different EGVs used in this thesis.

The yaw angle distribution is shown on the left of Figure 5-80 and shows an identical radial distribution for all EGVs. In terms of absolute values the difference in mass averaged yaw angle between the operating points for the different EGVs is less than ± 1 deg with respect to the operating point of the "Datum" EGV. This difference is largely due to two reasons, the open loop facility and the possibility of control of the compressor facility used to supply the air for the LPT test rig. This shows that the yaw angle has a good agreement between the different operating points.

The total pressure shown in the right of Figure 5-80 shows identical radial distributions for all four different EGVs. The absolute value of the total pressure in plane C differs by 10 mbar between the lowest, the "Datum" EGV, and the highest, the "High loading" EGV. This difference can solely be

explained by the open loop type facility. For the "Datum" EGV, the ambient pressure was approximately 10mbar lower than for the "high loading" EGV resulting in a lower overall pressure level for this operating point.

The overall agreement for all 4 EGVs is very good and the inlet conditions for all EGV are identical.

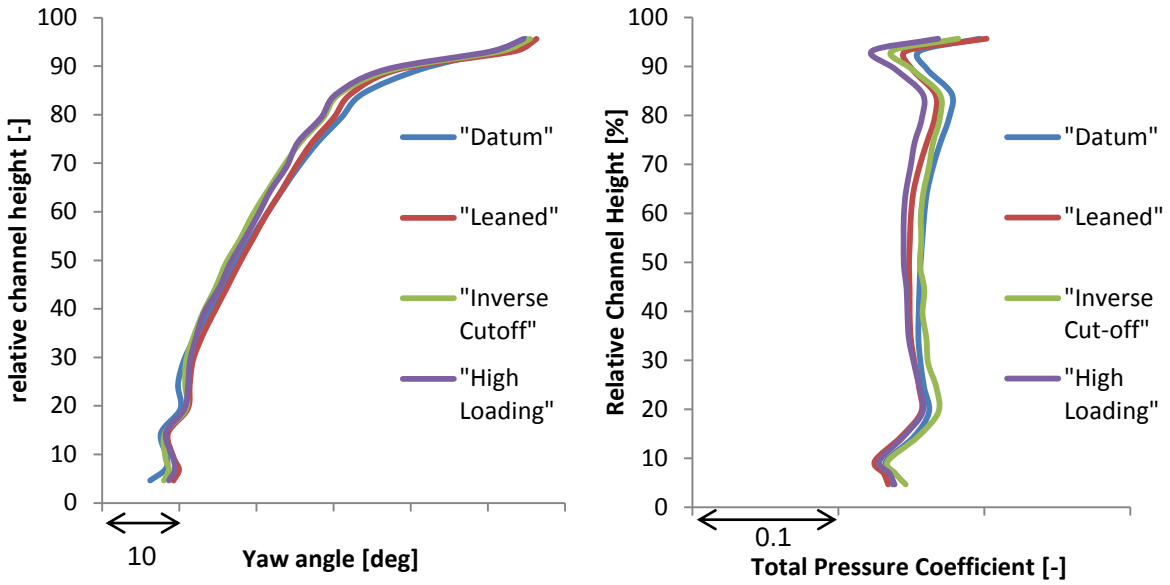

Figure 5-80: Comparison of the ADP rotor exit flow fields for all EGVs; Yaw angle (left) and Total pressure coefficient (right)

5.2.2 Discussion of the EGV flow-fields

5.2.2.1 Datum EGV

The first section deals with the flow field downstream of the "Datum" EGV for the operating point Approach.

5-Hole probe plane D

The flow field downstream of the EGV is show in the following section, with the total pressure distribution depicted in Figure 5-81. The wake of the vane can be seen by the black, dotted lines in all of the following figures. The wake of the vane shows a slight lean to the left (against rotor rotational direction). The wake shows two regions of large total pressure deficits, one located close to the casing and another one located closer to the hub. The structure close to the casing is caused largely by the low total pressure region emerging from the rotor tip leakage region that is migrating from the suction to the pressure side of the vane. This structure is migrating from the pressure towards the suction side of the vane. The superposition of the vane secondary flow with the rotor tip leakage flow causes a strong migration of fluid from on the vane surface from the casing towards midspan. A full explanation of this effect can be found in the appendix in section 12 where the effect of the leakage flow is fully evaluated.

Close to the hub at the intersection of endwall and trailing edge another region of low total pressure can be identified. This region extends further along the wake to midspan where a lower pressure deficit can be seen. This region is due to the movement of fluid along the suction surface from the hub towards the midspan as can be seen in the oil flow visualization. Close to the casing, a second region of low total pressure can be identified at the middle of the passage. This is due to the hub secondary flow caused by the passage pressure gradient that is located within this region of the flow field.

The static pressure distribution is shown in Figure 5-83. The distribution shows a higher static pressure towards the casing that is the remainder of the swirling flow superimposed by the rotor. The static pressure difference between the pressure side and the suction side of the vane can clearly be seen and is especially pronounced close to the casing. A large region of high static pressure can be identified at the intersection of the pressure side of the vane and the casing where large static

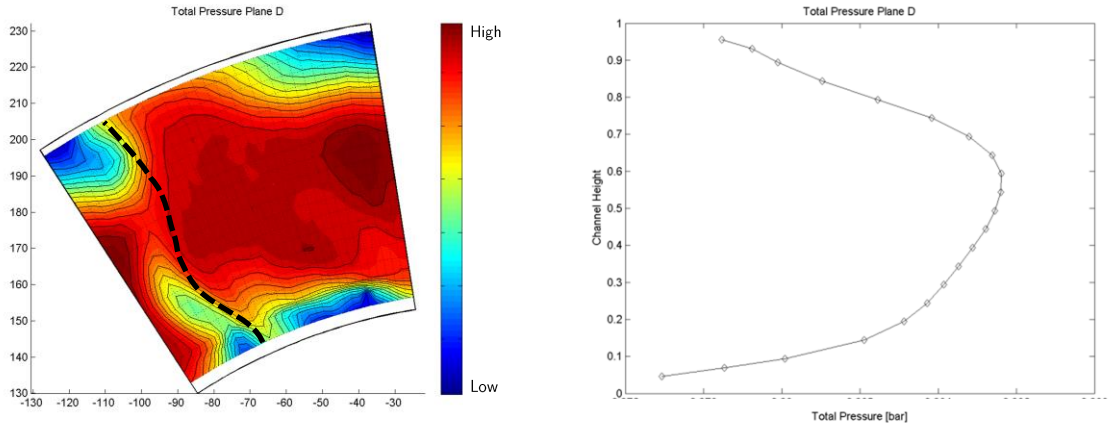

Figure 5-81: Total pressure distribution plane D, "Datum" EGV, operating point Approach

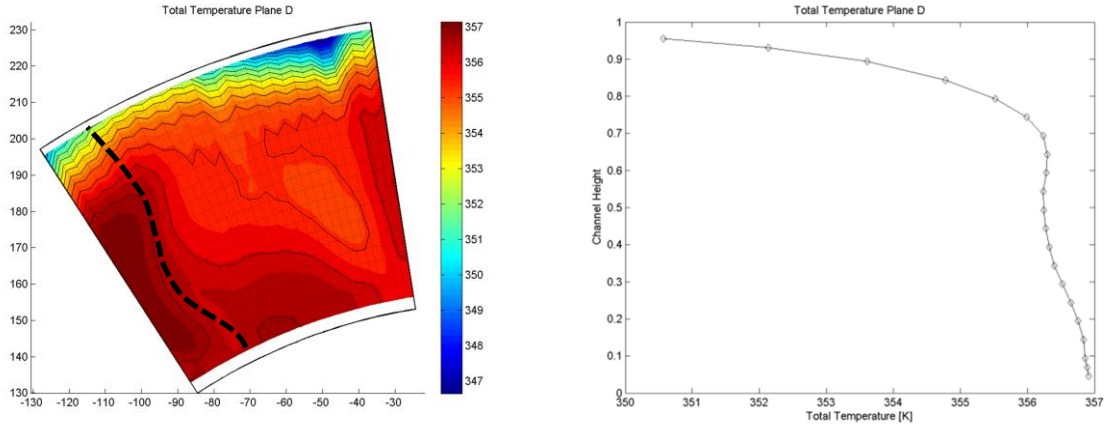

Figure 5-82: Total temperature distribution plane D, "Datum" EGV, operating point Approach

pressure difference can easily be identified. The same is true close to the hub, where a similar difference between suction and pressure side can be identified, but on a lower absolute level.

The total temperature distribution can be seen in Figure 5-82. Close to the casing a low total temperature can be identified. This region is most likely due to the low total pressure fluid coming from the tip leakage region. A region of high total pressure can be identified on the suction side of the vane. This fluid originates from the jet of the leakage flow migrating along the suction side of the vane towards midspan and further towards the hub.

The yaw angle distribution downstream of the vane is shown in Figure 5-84. Close to the casing, a large region of positive yaw angle can be identified that is again due to the under-turning in the tip leakage region as well as the influence of the hub secondary flow that shows it´s influence in this particular region. Close to the hub another region of positive yaw angle can be seen that is due to the hub secondary flow migrating from pressure to suction side. The overall yaw angle distribution in plane C (Figure 5-75) shows a steady increase in yaw angle and this can still be seen in the radial distribution in Figure 5-84 where an overall trend of increasing yaw angle from hub to casing can be observed. This is of course modulated by the secondary flows creating a strong negative yaw angle in the region between 15% and 55% span. Looking at the pitch angle distribution it can be seen that the upper passage vortex and its interaction with the tip leakage flow largely dominates the

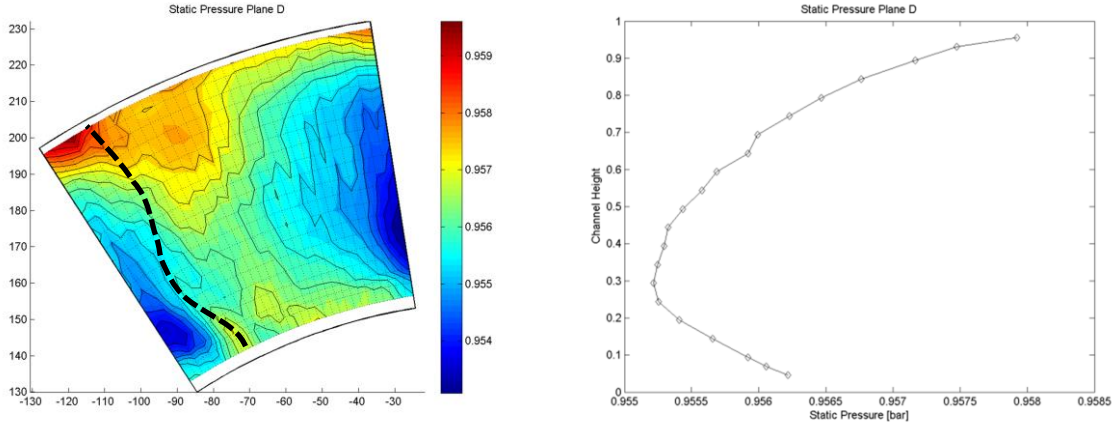

Figure 5-83: Static pressure distribution plane D, "Datum" EGV, operating point Approach

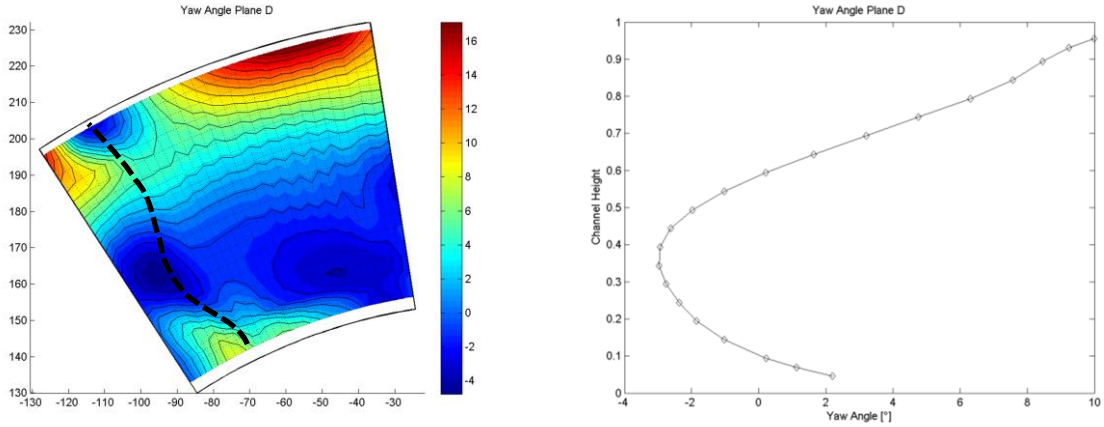

Figure 5-84: Yaw angle distribution plane D "Datum" EGV operating point Approach

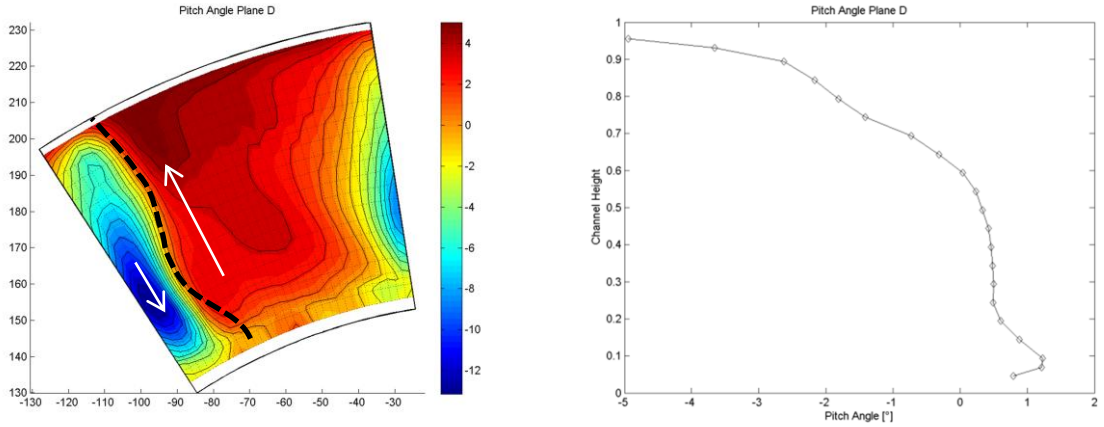

Figure 5-85: Pitch angle distribution plane D, "Datum" EGV, operating point Approach

flow field. There is only a very little trace of the lower passage vortex present in in the whole flow field as seen in the yaw angle distribution, but there is hardly any trace in the pitch angle distribution.

Static pressure distribution

The static pressure distribution of the vane surface is shown in Figure 5-86, where all for four radial positions where static pressure taps have been manufactured for both suction- and pressure side are depicted.

Looking at the pressure side distribution first, it can be seen that the axial distributions of the values at 30, 50 and 80% span are almost identical in terms of quality. There is a strong deceleration close to the leading edge between the first and second static pressure tap. Downstream of this point a steady increase in static pressure can be observed for these three positions. The static pressure along the pressure side at 20% span shows a significantly lower static pressure close to the leading edge of the vane. Again, a strong deceleration can be observed close to the leading edge followed by a steady deceleration towards the trailing edge of the vane.

The suction side of the vane shows a very strong acceleration of the flow close to the leading edge of the vane. The location of the suction peak is different for all radial positions. At 20% span the

suction peak is located at 25% axial chord followed by a steady deceleration towards the trailing edge.

At 30% span the suction peak is located at approx. 18% axial chord and at 50% span the position is 25% chord. No signs of separation bubbles can be identified for this EGV design. The static pressure at 30% span shows a lower absolute level than what is seen at 20% and 50% span. This is in contrast to the radial distribution seen in Figure 5-76where an increase in static pressure from the hub towards the casing can be identified.

The suction side distribution at 80% span again shows an increase in velocity until approximately 25% axial chord, where a region of almost constant static pressure can be identified. Downstream of this point an increase in static pressure can be identified that is followed by an accelerated flow from 70% axial chord towards the trailing edge. This effect is not related to any flow feature seen in either the flow field downstream of the vane or the oil flow visualisation and exists probably due to the fact that the static pressure taps are defect and therefore the measurement value is not valid for the last 3 static pressure measurements at 80% span.

The effect of the change in incidence angle of the vane can be identified by the fact that, unlike what was seen in Figure 5-86, the static pressure at the suction side leading edge of the vane is higher than at the pressure side of the vane due to the stagnation point being on the suction side of the vane.

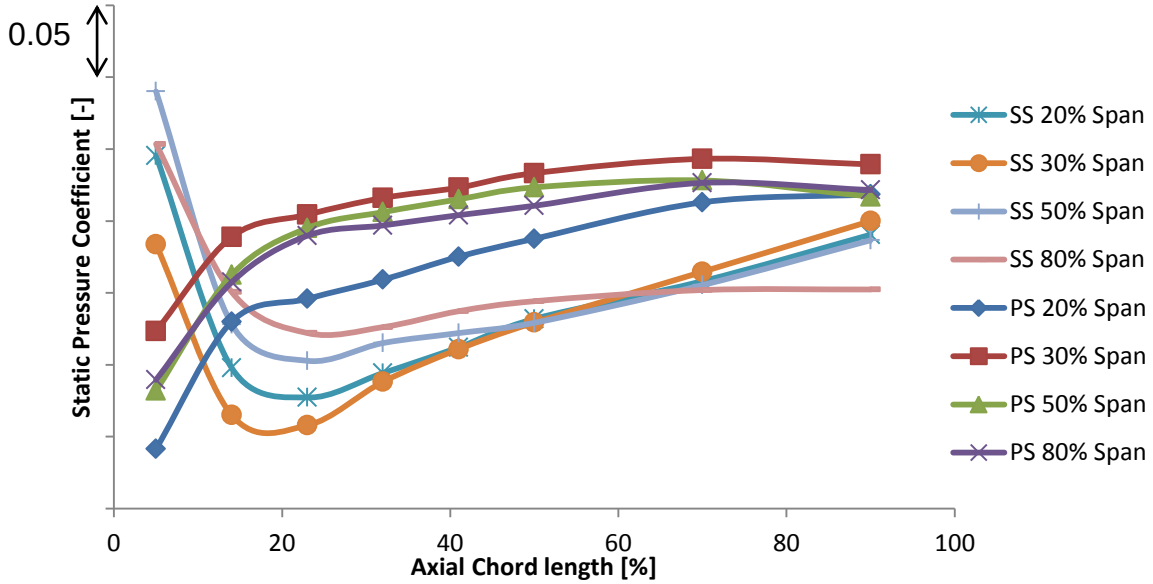

Figure 5-86: Static pressure distribution, "Datum" EGV, operating point Approach

Oil Flow Visualisation

The oil flow visualisation performed for the operating point "Approach" for the "Datum" EGV is described in the following section.

Figure 5-87 shows the oil flow visualisation on the hub of the passage close to the leading edge of the vane. The hub stagnation point is marked with "S" and is located on the pressure side of the vane with the flow splitting up on suction and pressure side of the vane. The separation lines described by Sieverding [88] can be easily identified and are marked S_1 and S_2. The passage cross flow from the pressure towards the suction side downstream of the separation line is clearly visible. The flow migrates from the pressure towards the suction side of the passage where a separation line shown in green is visible. This separation line extents until approximately 30% axial chord of the vane and then disappears due to the influence of the cross passage flow.

The oil flow visualisation along the casing of the vane can be seen in Figure 5-88. The fluid is again pushed from the pressure towards the suction side of the vane. A stream line marked in green shows the effect of this migration when intersecting with the suction side endwall, and as a consequence moving onto the suction side and towards midspan.

This effect can be easier seen when looking at the suction side oil flow visualisation on the left of Figure 5-89. The migration of fluid from the casing towards midspan along the chord of the vane can be easily identified and is marked with two white dotted lines. Close to the hub a lift-off line (marked A) can be identified that starts of close to the leading edge of the vane. The point of origin is identical to the separation line seen on the hub in Figure 5-87 (marked green). The lift-off line continues until the trailing edge of the vane and reaches a radial position of approximately 15% span. Another flow feature can be seen close to the leading edge of the vane. There is a strongly visible line from the hub leading edge extending towards midspan (marked B). This line is due to the start-up procedure of the test facility and cannot be avoided. The shear stresses at the operating point are not high enough to remove this feature from the vane. The details on the flow features during start-up can be found in the appendix of this thesis. While this feature is due to the start-up procedure, downstream of this separation line the oil flow visualisation shows an axial flow direction of the fluid. The pressure side visualisation shown on the right of Figure 5-89 provides only very little information. Close to the casing a separation line can be identified that is due to the hub pressure side horseshoe vortex. Close to the casing at the leading edge of the vane a structure within the oil flow visualisation can be identified that shows no clear sign of fluid flow, but rather a change in the consistency of the oil flow. This might point towards a separation in this region due to the influence of the rotor tip leakage flow.

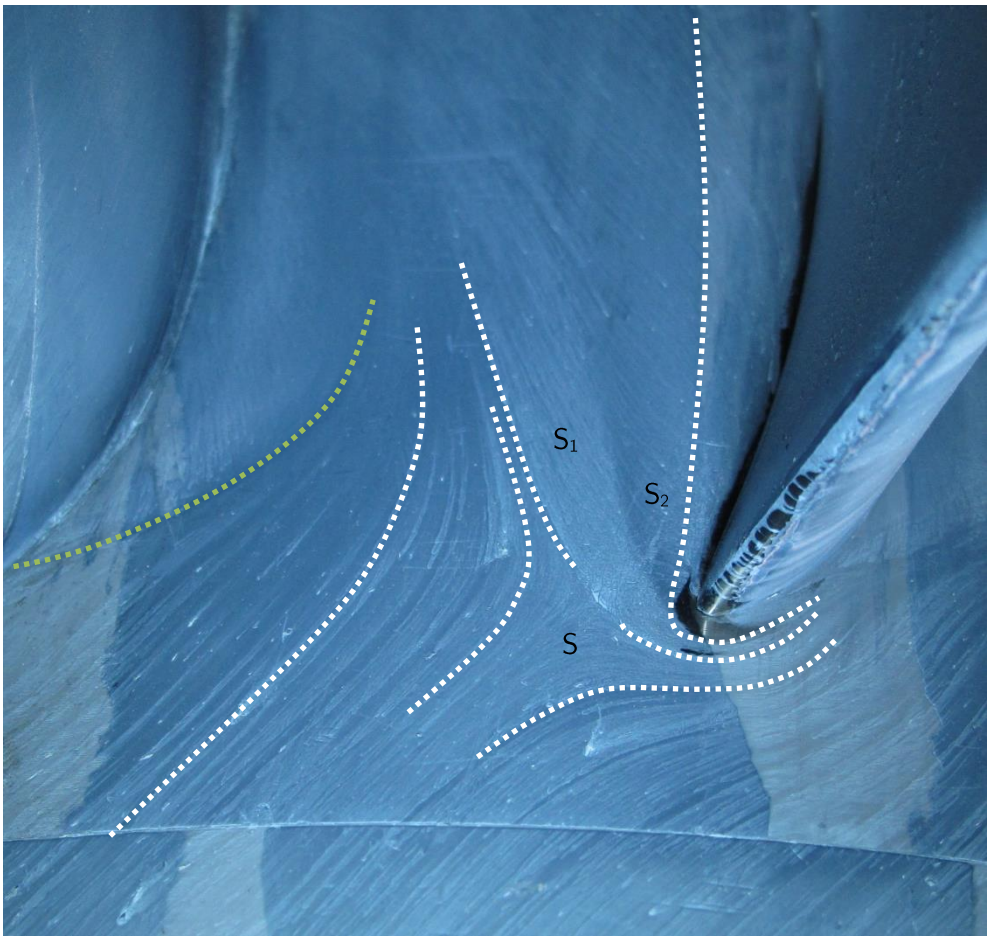

Figure 5-87: Oil Flow visualisation suction side "Datum" EGV, operating point Approach

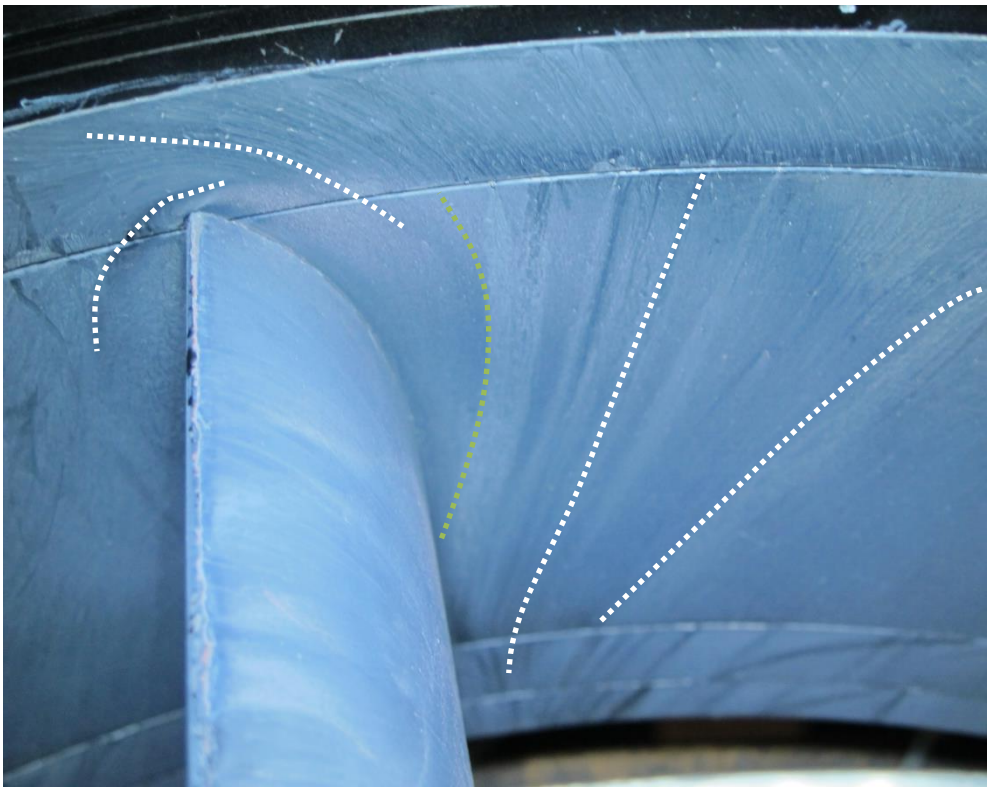

Figure 5-88: Oil Flow visualisation pressure side "Datum" EGV, operating point Approach

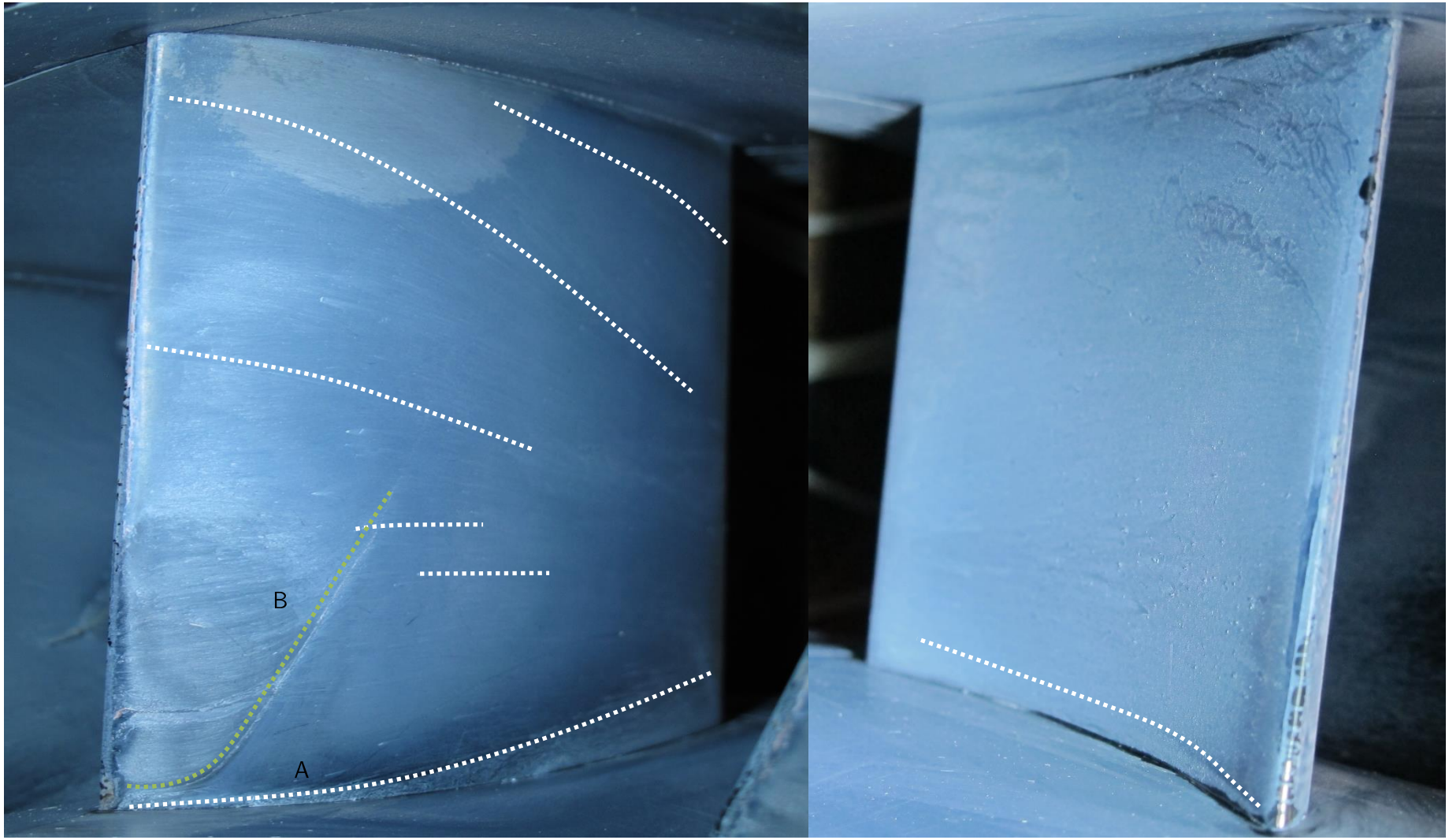

Figure 5-89: Oil flow visualisation "Datum" EGV operating point Approach; suction side (left) and pressure side (right)

Acoustic

The results of the acoustic post-processing can be seen in the following section.

The averaged FFT of all microphones used in the post processing is shown in Figure 5-90. The peak of the blade passing frequency can be identified at 5520 Hz with the second BPF at 11040Hz. Other peaks can be identified at 4080 Hz and 8160 Hz that are due to blade vibrations present in this setup of the test rig.

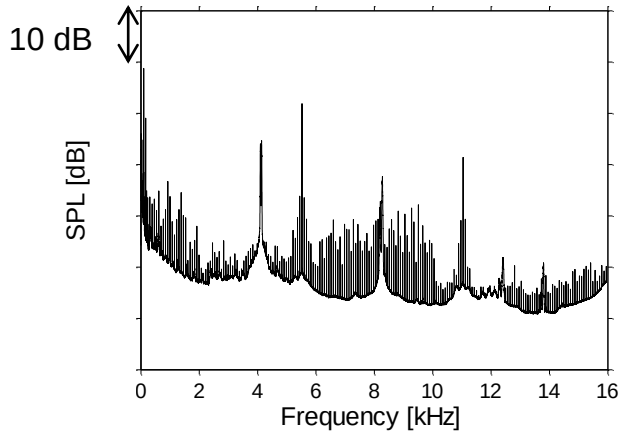

Figure 5-90: Averaged FFT of all microphones, "Datum" EGV, operating point Approach

The results of the azimuthal mode decomposition can be found in Figure 5-91. The limit of modes able to propagate is shown by red dotted lines. It can be seen that the limit of circumferential modes able to propagate is m=±19.The highest mode propagating is the mode m=-6 followed by the modes m=9 and m=-12. The modes m=-6 and m=9 are the scattering of the stator rotor interaction (mode m=24) at the EGV, with m=9 being the interaction with the vane number and m=-6 the interaction with two times the vane number. The modes m=1 and m=3 are significantly lower than the other modes able to propagate. The modes m=-21 and m=24 are not able to propagate for the given operating point.

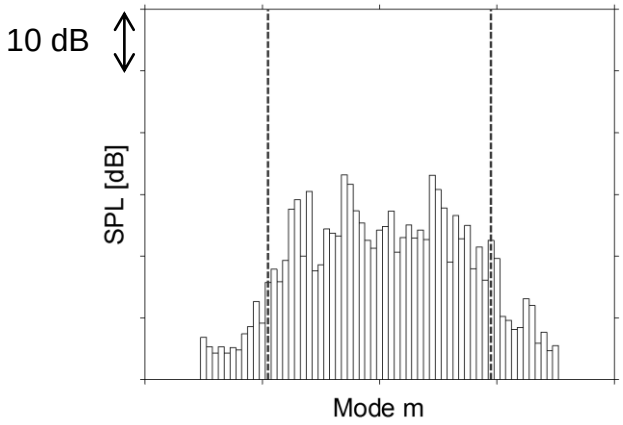

Figure 5-91: Azimutal mode decomposition "Datum" EGV, operating point Approach

The results of the following radial mode decomposition can be seen in Figure 5-92 where all circumferential modes able to propagate are shown split by their radial mode order as well as by their direction of propagation (up- and downstream). It can be seen that the highest mode is the

mode m=9,n=1. The mode m=-6 that was the highest mode in the azimuthal decomposition is now being split into two radial modes n=0 and n=1 and is therefore smaller. The modes propagating in downstream direction are significantly higher than those propagating in upstream direction. These modes are mainly due to reflections from the downstream components.

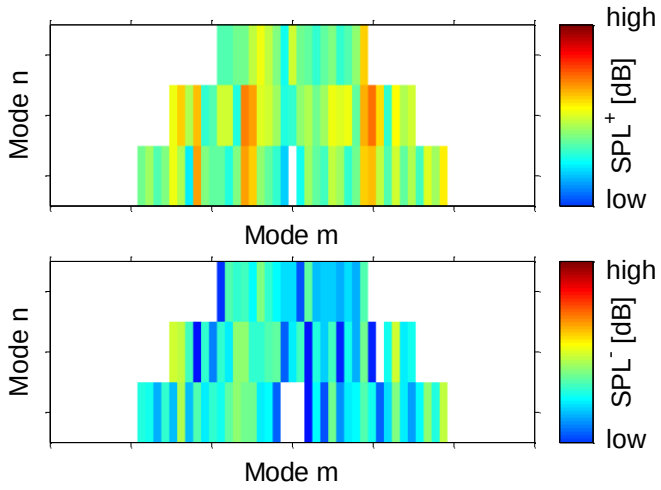

Figure 5-92: Radial mode decomposition "Datum" EGV, operating point Approach, split by radial and circumferential modes as well as up- and downstream moving modes

When summing up each circumferential mode m over all its radial modes n the results obtained can be seen in Figure 5-93 where these sums are shown split by up-and downstream moving modes. The dominating mode when summing up all radial modes is the mode m=-6, followed by the mode m=9. The overall sound power level is 97.4dB. It can be seen that there are neighbouring modes to the ones described by Tyler and Sofrin. This might possibly be to an effect that is due to flow discussed by Astley et al.[90] where flow non-uniformities cause a scattering of modes into "side bands". The effects of these non-uniformities can extend to a point where the main mode excited is not able to be identified but rather modes to the left and right of the excited mode. This is especially notably for the modes m=-6 and m=9.

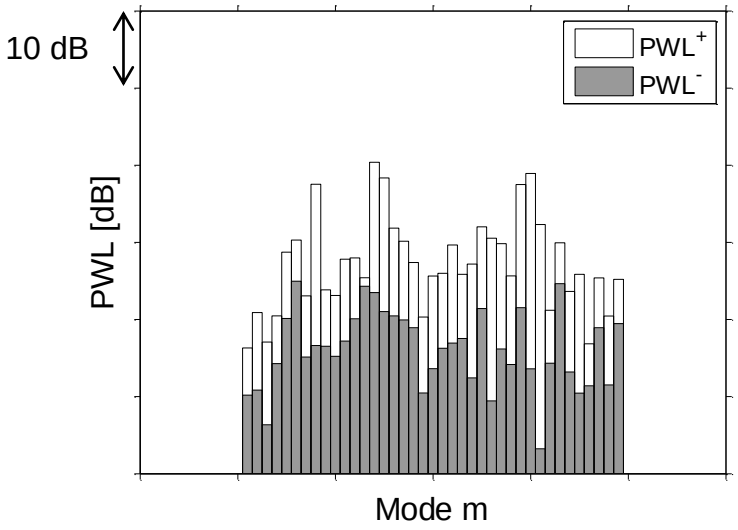

Figure 5-93: radial mode decomposition, sum of all radial modes, split by up- and downstream moving modes

The Figure 5-94 and Figure 5-95 show the azimuthal mode decomposition separated by radial modes. It can be seen that the number of circumferential modes m able to propagate decreases as the radial mode order n increases. For the all radial modes the circumferential modes m=-6 and m=9 are amongst the dominating modes. For the mode n=0 the highest mode is the mode m=-12.

The radial mode n=2 shows only modes up to ±9 that are able to propagate with the mode m=9 dominating.

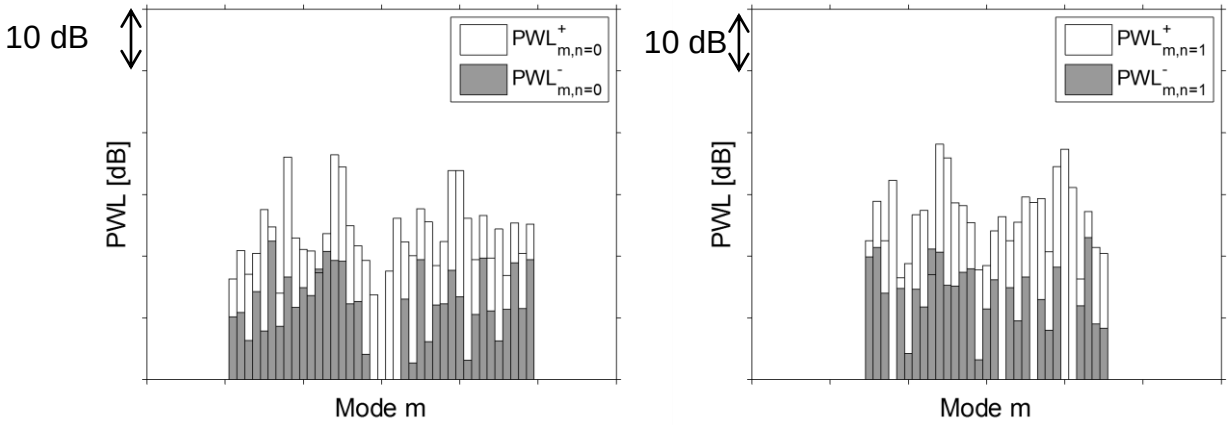

Figure 5-94: Radial mode decomposition, radial modes n=0 (left) and n=1 (right) split by up and downstream propagating modes

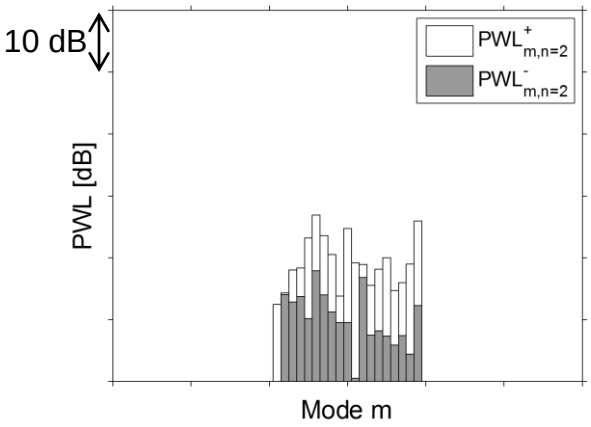

Figure 5-95: Radial mode decomposition, radial modes n=2 split by up and downstream propagating modes

5.2.2.2 *Leaned EGV*

The flow field downstream of the leaned EGV is described in the following section.

5 Hole Probe results plane D

The wake of the vane, here defined as the region of lowest pressure is shown as a black dotted line in the Figure 5-96 where the total pressure distribution in plane D is shown. There are multiple effects present within the EGV passage that influence the evolution of the flow field. In addition to the always occurring secondary flows present in a vane passage and the increase in static pressure due to the removal of swirl from the flow, a negative incidence angle at the leading edge due to the operating point is present as already seen in the "Datum" EGV. In addition the swirl of the vane imposes a pressure gradient onto the flow field that strongly influences the flow field of the vane as e.g. explained by Denton and Xu [48] where the effects of multiple three-dimensional vane features are discussed.

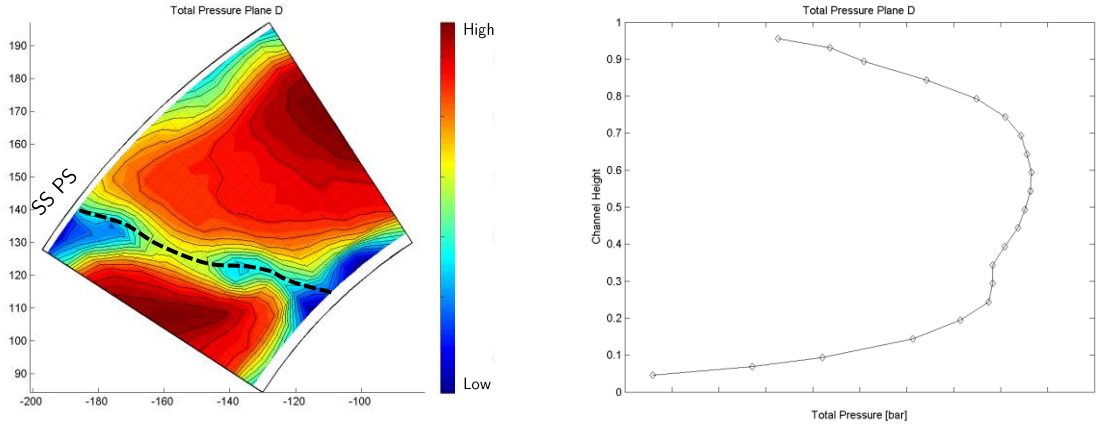

Figure 5-96: Total pressure distribution plane D, "Leaned" EGV operating point Approach

The total pressure distribution shows a wake with a very strong lean against the direction of rotation of the rotor. There are multiple regions of low total pressure present in the flow field. Close to the hub a large region of low total pressure can be identified that is split into 3 separate regions. One region is located on the pressure side of the vane. This region is due to the cross passage flow at the hub. With the fluid migrating from the pressure side towards the suction side of the vane low total pressure fluid is located in this region of the vane. This is better visible when looking at the oil flow visualisation in Figure 5-100 as explained later.

Close to the casing and along the suction side of the vane the influence of the rotor tip leakage flow can be seen. The vorticity of the tip leakage flow superimposes with the upper passage vortex as well as the pressure gradient superimposed by the lean of the blade. This superposition causes a strong migration of fluid from the suction towards the pressure side and consequent a migration of fluid from the hub towards midspan. This can be seen by looking at the positive yaw angle distribution close to the casing in Figure 5-97 as well as the large region of negative pitch angle in Figure 5-98 that is due to the migration of fluid from the suction towards the pressure side. This can also be seen when looking at the oil flow visualization of the suction side in Figure 5-102 where the migration of fluid from the casing towards midspan can be observed with fluid changing its radial position from 80% span at the LE to below 50% span at the TE. This can also be seen when

looking at the oil flow visualization in Figure 5-101 where the streamlines along the casing are depicted. A very strong migration of fluid from the pressure towards the suction side can be seen starting at the LE of the vane. The separation line following the stagnation point is clearly visible and depicted resulting in a strong yaw angle in the near wall region (marked A).

The pitch angle distribution in Figure 5-98 shows a string radial component to the flow downstream of the trailing edge of the wake. This was already seen for the "Datum" EGV and promotes the formation of a trailing edge shed vortex as seen in Pullan et al. [89].

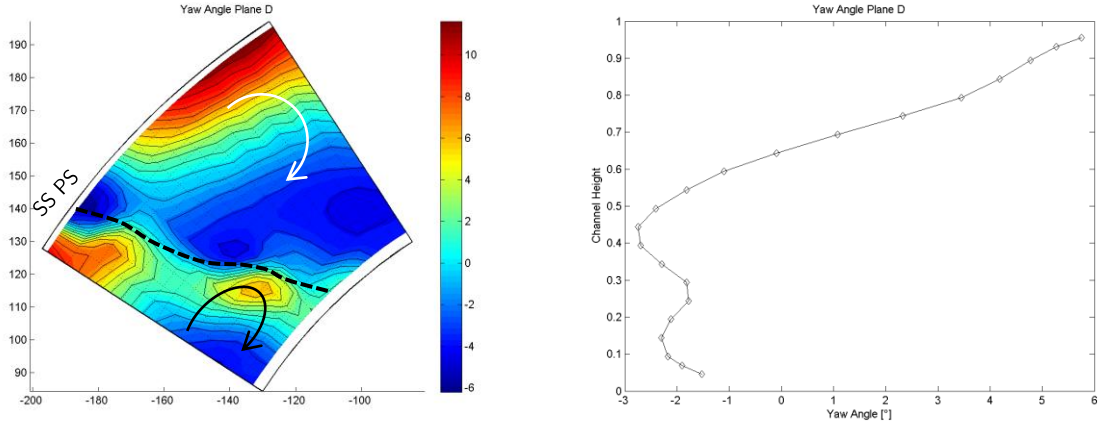

Figure 5-97: Yaw angle distribution plane D, "Leaned" EGV operating point Approach

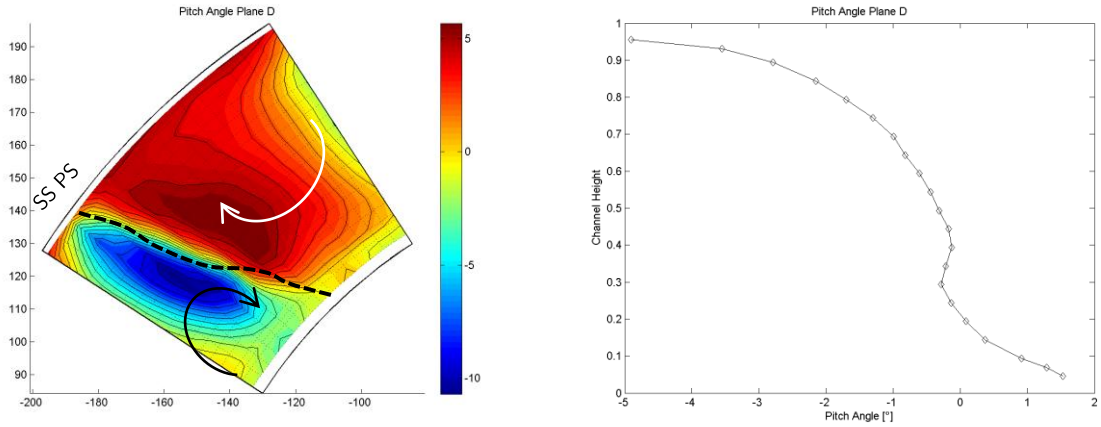

Figure 5-98: Pitch angle distribution plane D, "Leaned" EGV operating point Approach

Static pressure distribution

The static pressure distribution along the vane surface is shown in Figure 5-99. The figure depicts suction and pressure side for all four radial positions equipped with static pressure taps.

The suction side static pressure distributions at 20, 30 and 50% span show a steady increase in surface velocity until a maximum velocity is reached. This is at an axial location off approximately 40-50% chord for the positions at 20, 30 and 50% span. The acceleration up to this point is somewhat constant with only small changes in slope. This is also true for the following deceleration until towards the TE of the vane. The distribution at 80% span shows again an acceleration of fluid from the LE towards the suction peak at approximately 20% followed by an increase in static pressure until the trailing edge. The static pressure distribution at the pressure side shows an identical pressure distribution for the two positions at 20% and 30% span. There is a strong deceleration at the leading edge of the vane followed by a change in pressure gradient at approximately 20% axial chord leading to a smaller pressure gradient. Towards the trailing edge a very small acceleration of the flow can be observed for the last section of the vane.

The pressure side static pressure distribution at 50% span shows again a deceleration of the flow along the first 15% chord of the vane followed by a change in pressure increase at approximately 25%. At this point the static pressure gradient is almost zero, pointing towards a separation bubble. This bubble is finally visible at the 80% span pressure side distribution where a large region of almost constant static pressure can be found in a region between 22% and 40% axial chord. This separation can also be seen when looking at the oil flow visualization of the pressure side of the EGV in Figure 5-102. The intersection of LE and casing shows a large region of circulating flow. That is due to a combination of an increased angle of incidence due to the tip leakage flow as well as an effect of the lean of the vane. When comparing this to the pressure side of the "Datum"-EGV in Figure 5-99 where no (or only minor) flow separation can be seen close to the casing. Downstream of this separated region a movement of fluid from midspan towards the casing can be seen promoting the upper passage cross-flow.

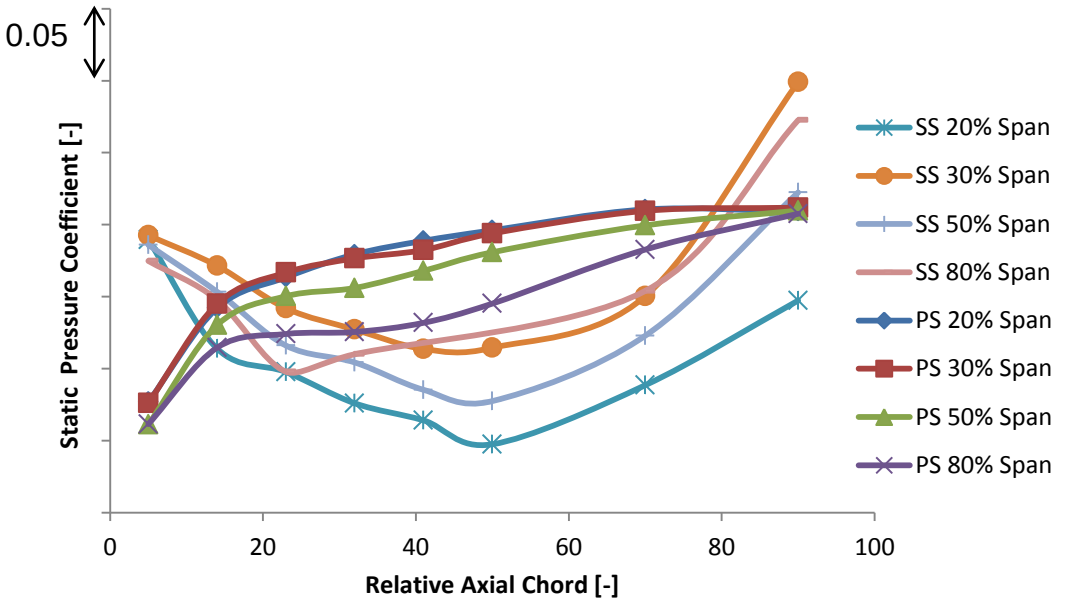

Figure 5-99: Vane static surface pressure "Leaned" EGV, operating point Approach

Oil Flow visualisation

When looking at the oil flow visualization in Figure 5-100, where the hub of the passage is depicted, it can be seen that the fluid on the hub is not being pushed towards the suction side of the vane as strong as for the Datum EGV (Figure 5-87) where a very strong cross passage gradient is present. Due to this effect the hub passage vortex stays confined to the pressure side of the passage and does not cross over to the suction side where it migrates along the vane surface towards midspan. This is an effect of the lean of the wake superimposing a pressure gradient reducing the cross passage pressure gradient on the hub of the passage, while increasing the cross passage gradient on the casing.

The strong cross passage flow close to the casing can be seen when looking at the oil flow visualisation in Figure 5-101. The influence of the rotor tip leakage causes a strong migration of fluid from the pressure to the suction side that is further enhanced by the naturally occurring pressure gradient. This fluid is than migrating from the casing onto the suction side surface and further towards midspan.

This can also be seen when looking at the oil flow visualisation in Figure 5-102 where the suction side of the vane is depicted. The region between the midspan and the casing shows a strong

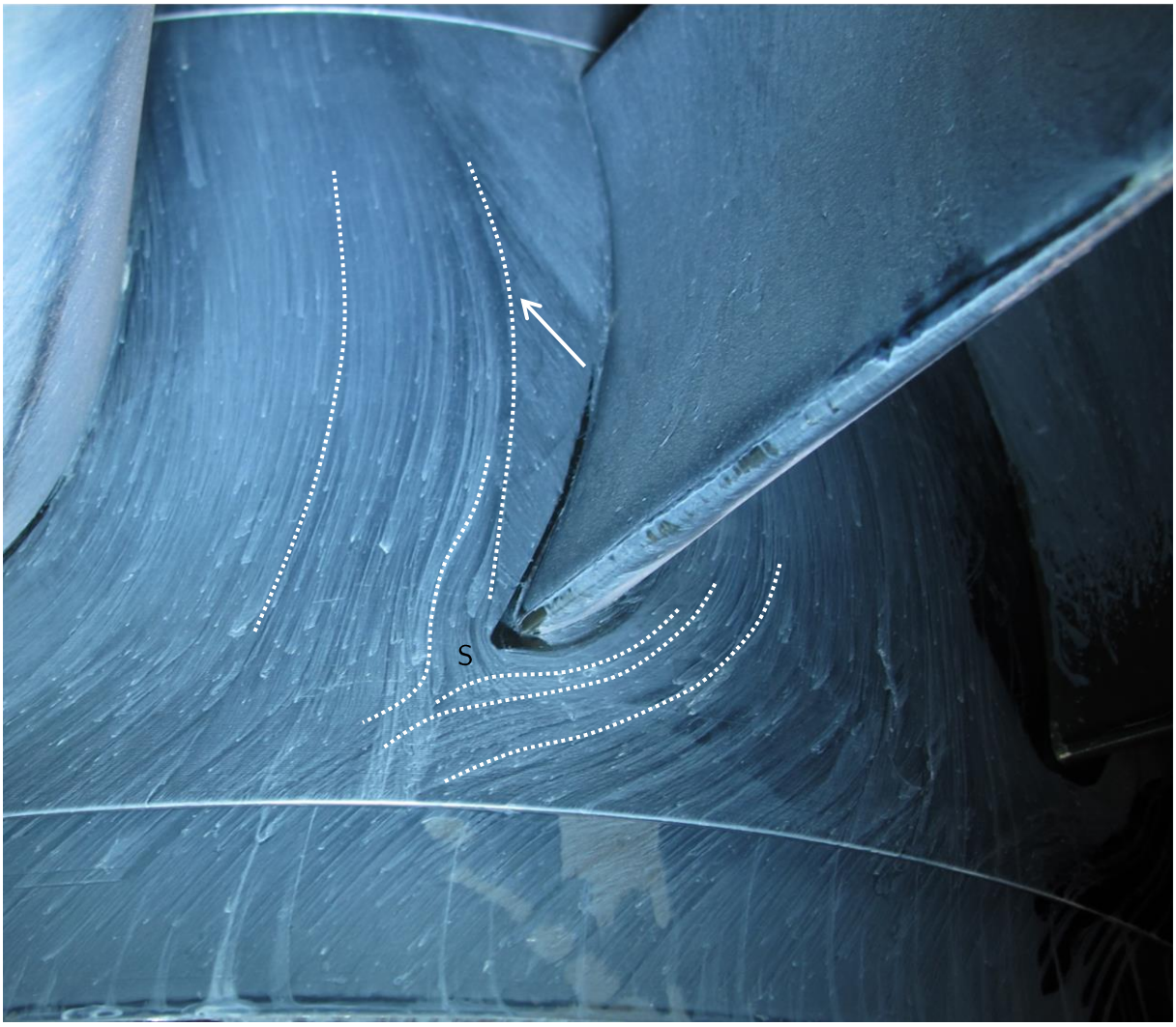

Figure 5-100: Oil Flow visualisation, Hub, "Leaned" EGV, operating point Approach

migration of fluid from the casing towards midspan. Close to the hub a small separated region can be identified close to the hub suction side trailing edge. This region is due to the migration of fluid from the pressure towards the suction side of the vane migrating towards midspan along the suction side surface of the vane. This also shows an almost axial direction of the streamlines leaving the passage on the suction side of the vane.

The oil flow visualisation of the pressure side of the vane can be seen on the right of Figure 5-102. A separated region with a vortex marked S can be seen close to the trailing edge. The structure extends from the casing to approximately 65% span of the vane.

Figure 5-101: Oil Flow visualisation, casing, "Leaned" EGV, operating point Approach

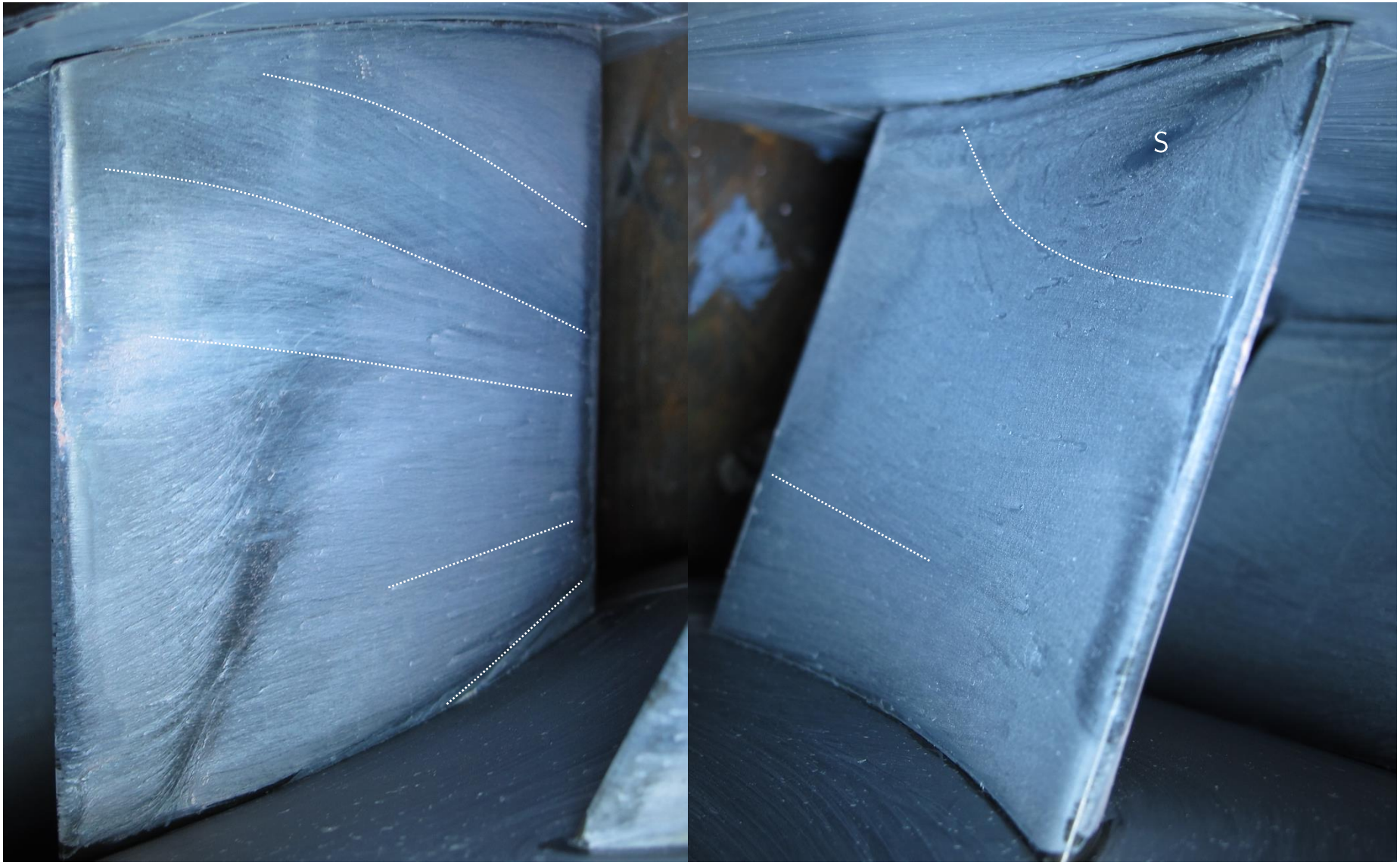

Figure 5-102: Oil Flow visualisation, Suction side (left), pressure side (right), "Leaned" EGV, operating point Approach

Acoustic

The results of the acoustic post-processing can be seen in the following section.

The averaged FFT of all microphones used in the post processing is shown in Figure 5-90. The peak of the blade passing frequency can be identified at 5520 Hz with the second BPF at 11040 Hz. The peaks at 4080 Hz and 8160 Hz that were identified for the "Datum" EGV in Figure 5-90 are not present in this setup of the test rig.

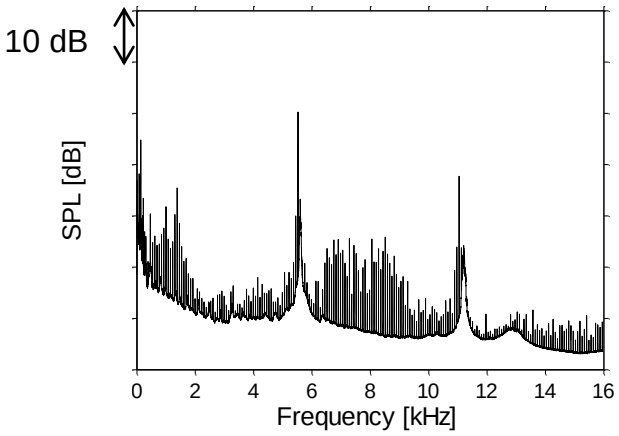

Figure 5-103: Averaged FFT of all microphones, "Leaned" EGV, operating point Approach

The results of the azimuthal mode decomposition can be found in Figure 5-91. The limit of modes able to propagate is shown by red dotted lines. It can be seen that the limit of circumferential modes able to propagate is m=±19. The highest mode propagating is the mode m=-6 followed by the modes m=9. This is similar to what was seen for the "Datum" EGV in section 0. The modes m=-6 and m=9 are the scattering of the stator rotor interaction (mode m=24) at the EGV, with m=9 being the interaction with the vane number and m=-6 the interaction with two times the vane number. The interaction modes m=1 and m=3 and m=-12 are significantly lower than the other modes able to propagate. The modes m=-21 and m=24 are not able to propagate for the given operating point.

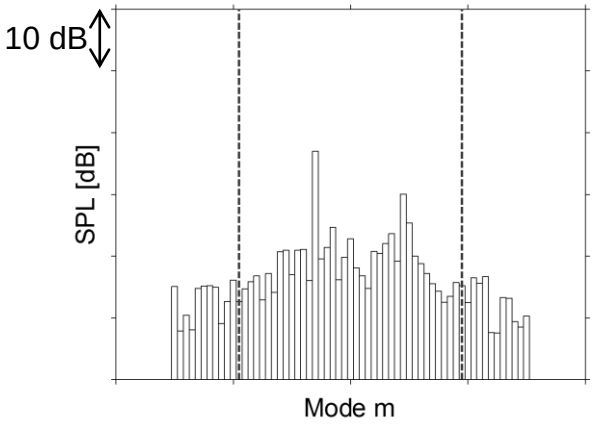

Figure 5-104: Azimutal mode decomposition, "Datum" EGV, operating point Approach

The results of the following radial mode decomposition can be seen in Figure 5-92 where all circumferential modes able to propagate are shown split by their radial mode order as well as by

their direction of propagation (up- and downstream). It can be seen that the highest mode is the mode m=9,n=1. The mode m=-6 that was the highest mode in the azimuthal decomposition is now being split into tree radial modes of almost identical amplitude. The modes propagating in downstream direction are significantly higher than those propagating in upstream direction. These modes are mainly due to reflections from the downstream components. The highest upstream moving mode is the mode m=-6, n=2.

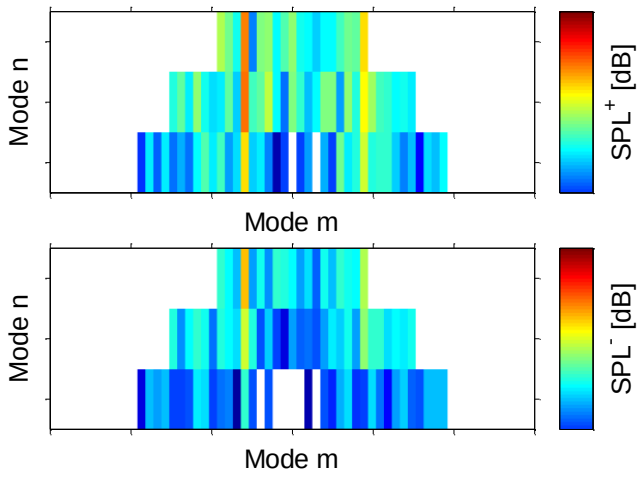

Figure 5-105: Radial mode decomposition, "Datum" EGV, operating point Approach, split by radial and circumferential modes as well as up- and downstream moving modes

When summing up each circumferential mode m over all its radial modes n the results obtained can be seen in Figure 5-93 where these sums are shown split by up-and downstream moving modes. The dominating mode when summing up all radial modes is the mode m=-6, followed by the mode m=9. The overall sound power level is 97.4 dB. It can be seen that there are neighbouring modes to the ones described by Tyler and Sofrin. This might possibly be to an effect that is due to flow non-uniformities as discussed by Astley et al.[100] where this caused a scattering of a main mode into neighbouring mode orders. The effects of these non-uniformities can extend to a point where the main mode excited is not able to be identified but rather modes to the left and right of the excited mode.

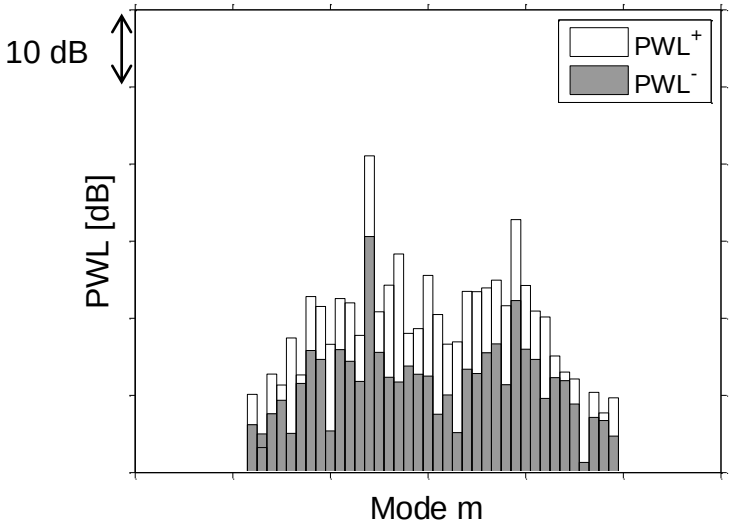

Figure 5-106: radial mode decomposition, sum of all radial modes, split by up- and downstream moving modes

The Figure 5-94 and Figure 5-95 show the azimuthal mode decomposition separated by radial modes. It can be seen that the number of circumferential modes m able to propagate decreases as the radial mode order n increases. For the all radial modes the circumferential modes m=-6 and m=9 are the dominating modes with the mode m=-6/n=1 being the dominating mode.

The radial mode n=2 shows only modes up to ±9 that are able to propagate.

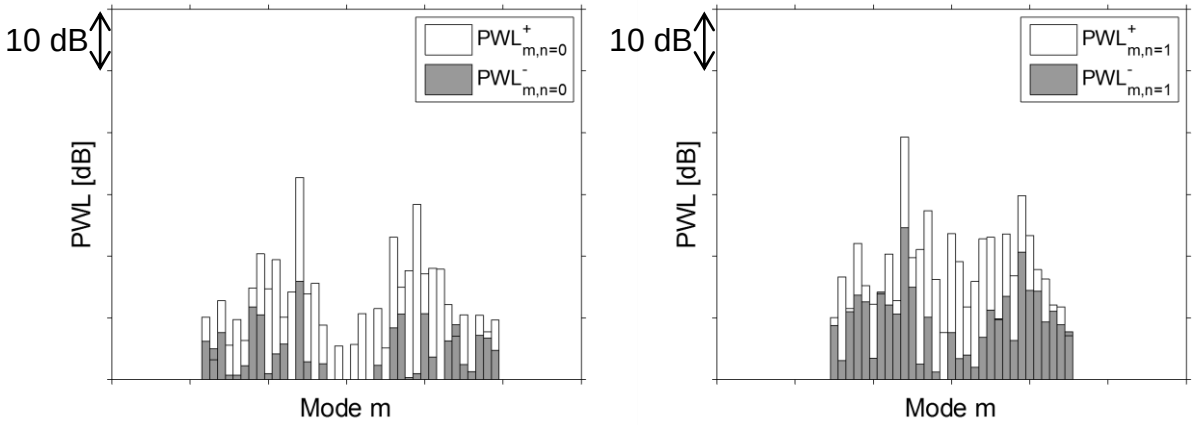

Figure 5-107: Radial mode decomposition, radial modes n=0 (left) and n=1 (right) split by up and downstream propagating modes

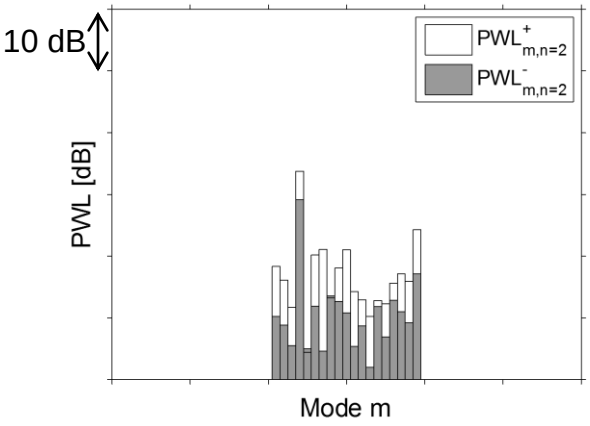

Figure 5-108: Radial mode decomposition, radial modes n=2 split by up and downstream propagating modes

5.2.2.3 *Inverse Cut-Off EGV*

5-Hole Probe Results Plane D0

The flow field downstream of the EGV in plane D0 can be seen in the following section. Figure 5-109 shows the total pressure distribution and Figure 5-110 the Mach number distribution in this plane. Main feature of the flow field downstream of the vane is the wake of the vane. Close to the hub, a band of low total pressure as well as Mach number can be identified. Within the wake region this band shows a very large total pressure deficit. This low pressure region is due to the secondary flows of the hub being pushed onto the suction side of the vane. Close to the casing the influence of the tip leakage flow can be identified. There is a large region of low total pressure as well as Mach number that is due to the leakage flow of the rotor. Close to the suction side of the vane, a region of high Mach number can be identified, that is somewhat separated from the remaining high Mach number flow around midspan and is therefore a separate flow structure present in this configuration. Between 20% and 80% span the remaining structures of the upstream stator are able to be identified. There are two distinct region of large total pressure identifiable in this field that are due to the upstream stators.

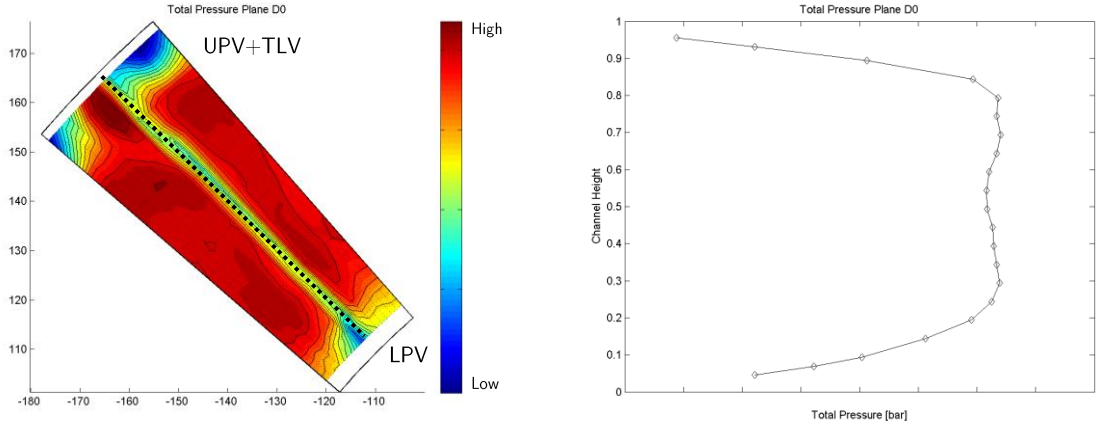

Figure 5-109: Total pressure distribution plane D0, "Inverse Cut-off" EGV operating point Approach

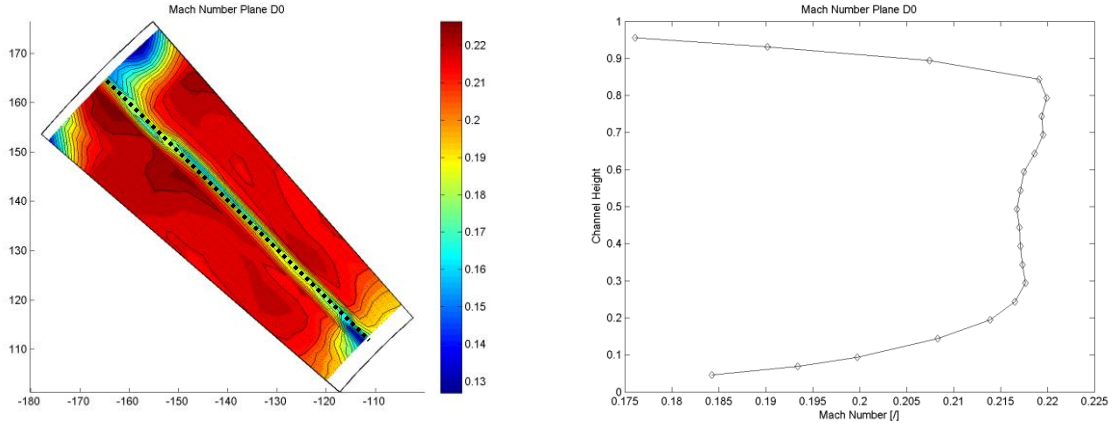

Figure 5-110: Mach number distribution plane D0, "Inverse Cut-off" EGV operating point Approach

The total temperature distribution in Figure 5-111 shows two regions of high total temperature: one is located close the hub (marked A), the second region of high total temperature is located on the suction side of the vane between 70 and 90% span (marked B). This high total temperature fluid is

migrating from the tip leakage region of the blade along the suction side of the vane towards midspan. The migration of the fluid towards this particular location is a result of the tip leakage flow interacting with the casing secondary flow imposing a clockwise rotation onto the flow that causes a migration of fluid along the suction side of the vane towards midspan (see chapter 12).

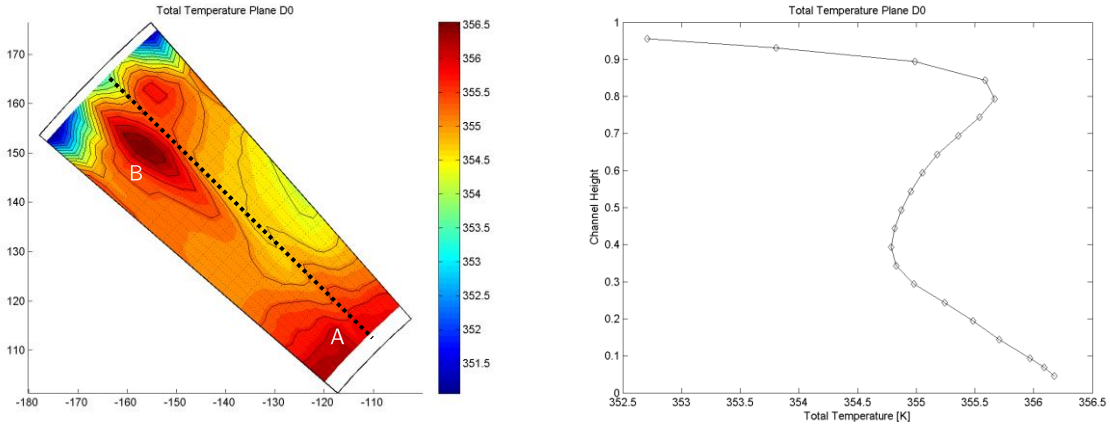

Figure 5-111: Total Temperature distribution plane D0, "Inverse Cut-off" EGV operating point Approach

The yaw angle distribution downstream of the vane is shown in Figure 5-112. There is a large region of positive yaw angle close to the casing that is due to the flow being strongly influenced by the tip leakage flow as well as the secondary flow. Another region of positive yaw angle can be identified close to the hub, where the secondary flow causes a migration of fluid from the pressure to the suction side of the vane.

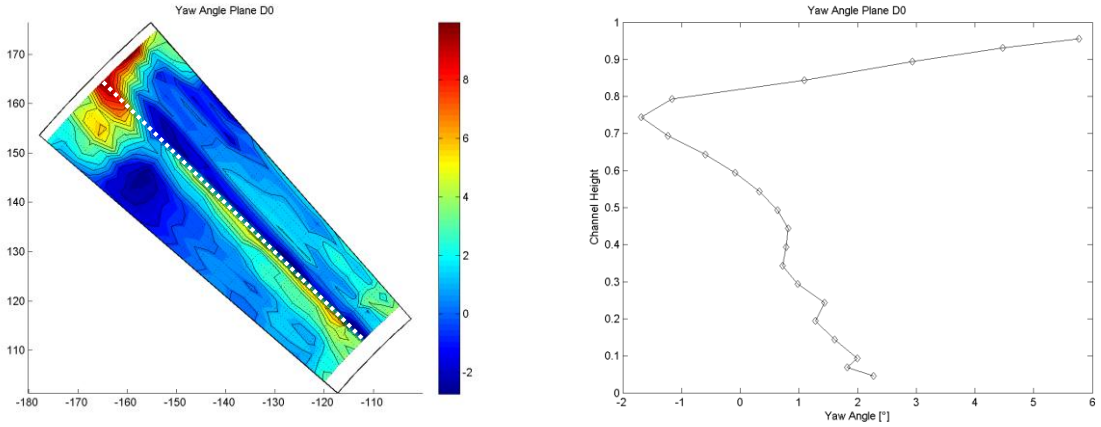

Figure 5-112: Yaw angle distribution plane D0, "Inverse Cut-off" EGV operating point Approach

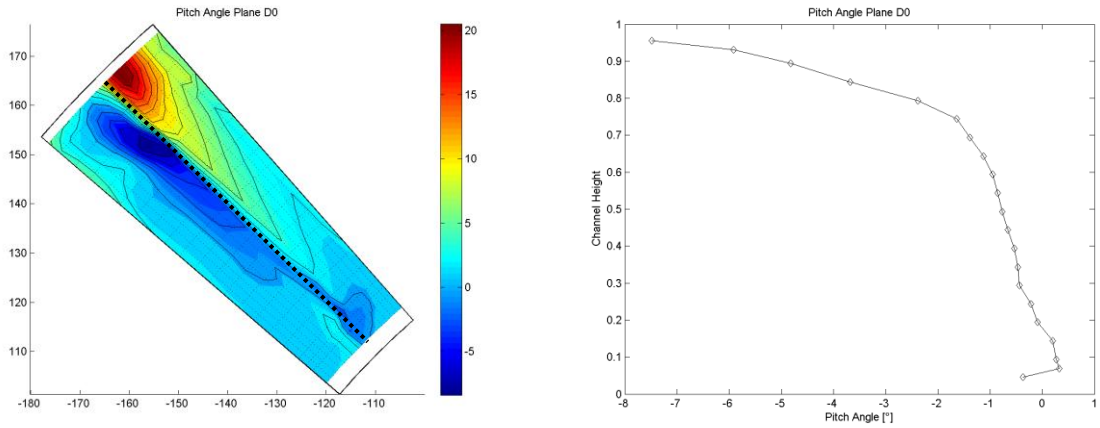

Figure 5-113: Pitch angle distribution plane D0, "Inverse Cut-off" EGV operating point Approach

5-Hole Probe Results Plane D

The following section shows the flow field in plane D, far downstream of the trailing edge.

Figure 5-114 show the total pressure downstream of the wake. The vane, identified by the minimum total pressure along the span is marked with a dotted line. Whether this is the real trace of the wake is difficult to determine due to the fact that mixing has taken place downstream of the trailing edge of the vane and the wake has mixed with the loss cores of the vane. It can be seen that due to the mixing process the region identified as the wake of the vane has become significantly thicker compared to what was seen directly downstream of the vane in Figure 5-109. Close to the casing a large region of low total pressure can be identified that is due to the secondary flows of the EGV migrating downstream. Due to the strong radial flow component the low total pressure fluid associated with the tip leakage flow is migrated from the casing region along the wake towards midspan and creates this low total pressure region.

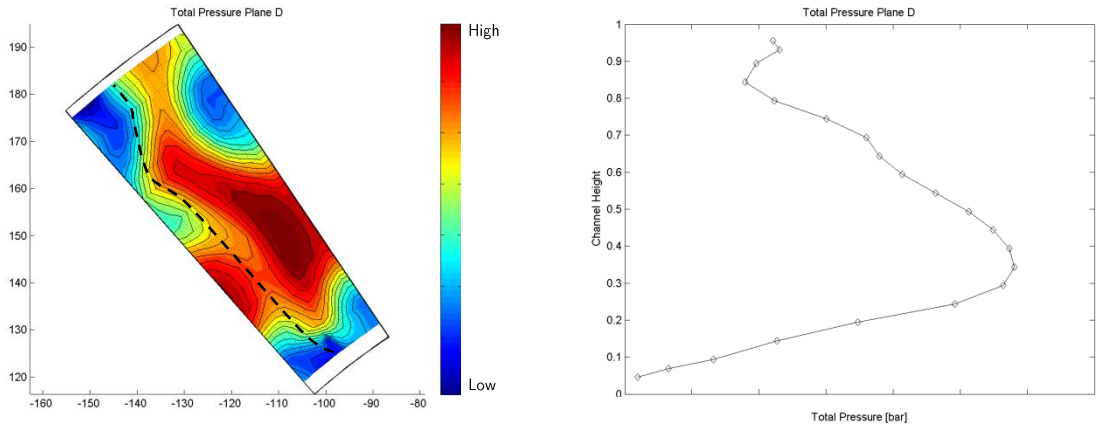

Figure 5-114: Total Pressure distribution plane D, "Inverse Cut-off" EGV operating point Approach

The static pressure distribution in Figure 5-115 shows a static pressure distribution that shows a similar radial distribution to what was seen in plane C upstream of the leading edge of the vane. There is a radial gradient with an increase in static pressure from the hub towards the casing. This is due to the low chord of the vane having only a minor influence on the radial pressure distribution of the vane.

The total temperature distribution in Figure 5-116 shows that the mixing downstream of the vane has resulted in similar averaged total temperature across most of the span. Close to the casing the region of low total temperature that was already seen in plane D0 downstream of the trailing edge can again be identified. The difference in total temperature between this region and the rest of the flow field has not decreased significantly due to the mixing downstream of the vane.

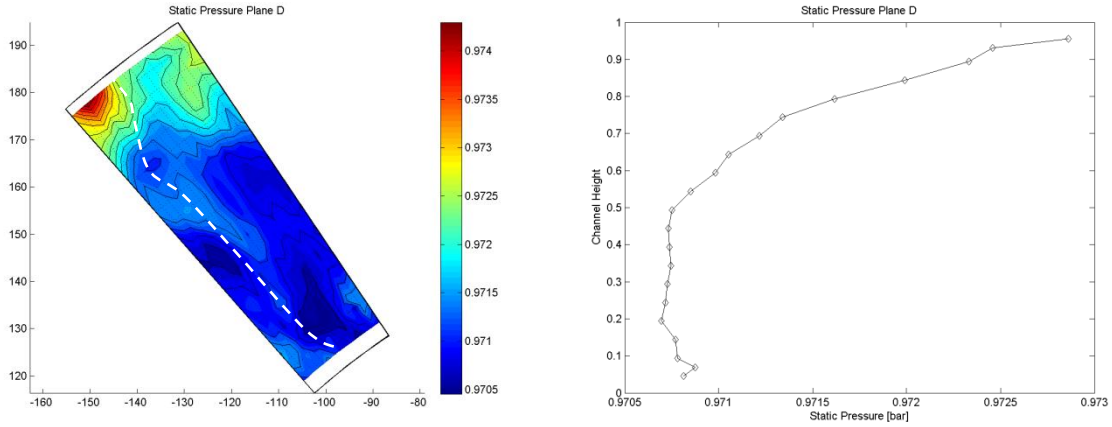

Figure 5-115: Static Pressure distribution plane D, "Inverse Cut-off" EGV operating point Approach

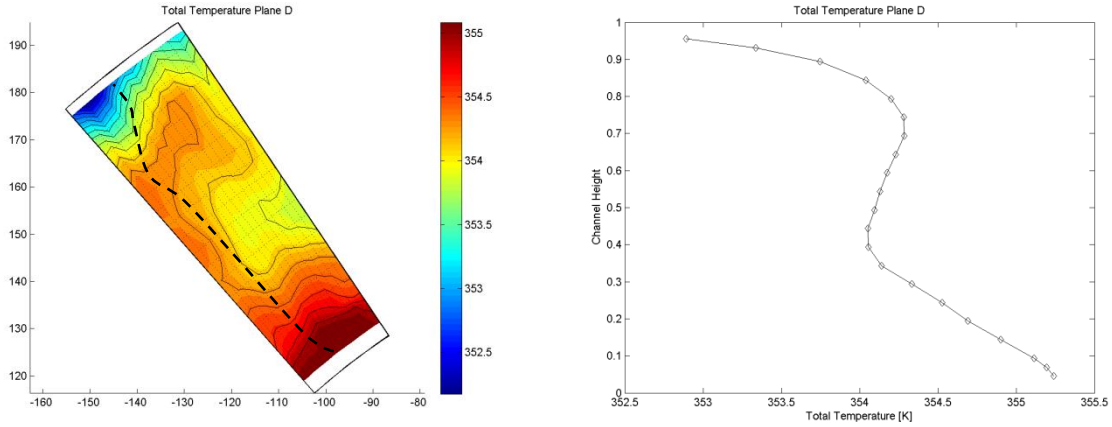

Figure 5-116: Total temperature distribution plane D, "Inverse Cut-off" EGV operating point Approach

While the total pressure distribution shows a smooth distribution across the flow field, the yaw angle distribution in Figure 5-117 has a very unsteady distribution. This is especially visible at midspan, where two radial lines of high yaw angle can be identified. These structures are due to errors measurement of the circumferential velocity components. Still the most important structures can be identified. There is a region of positive yaw angle located at around 70% span that is due to the tip leakage vortex fluid and a negative yaw angle close to the casing that is caused by the rolling up of this structure. Close to the hub the secondary flows due to the passage pressure gradient can be identified. The pitch angle distribution in Figure 5-113 shows that the trailing edge shed vorticity has further increased the size of the regions with positive/negative pitch angle. These regions do now stretch from the casing to a region of almost midspan. The unsteady distribution seen in the yaw angle is not present for this flow property.

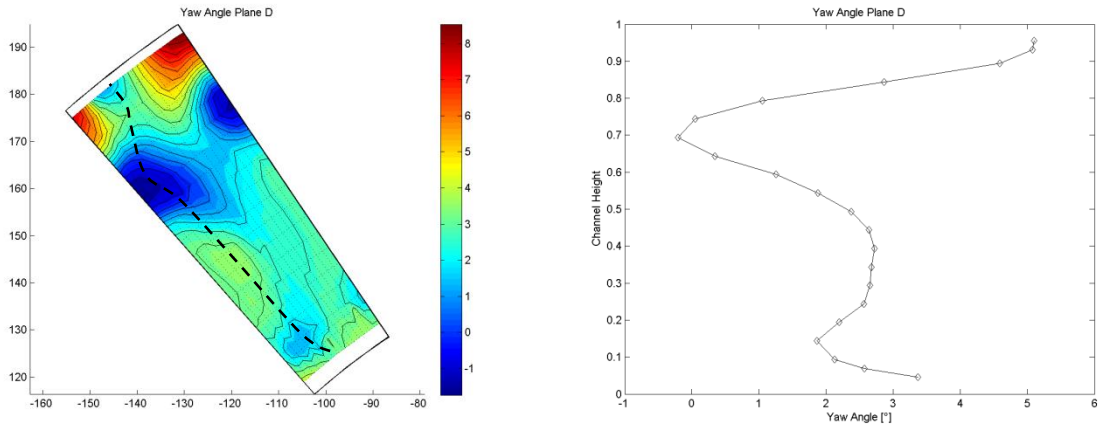

Figure 5-117: Yaw angle distribution plane D, "Inverse Cut-off" EGV operating point Approach

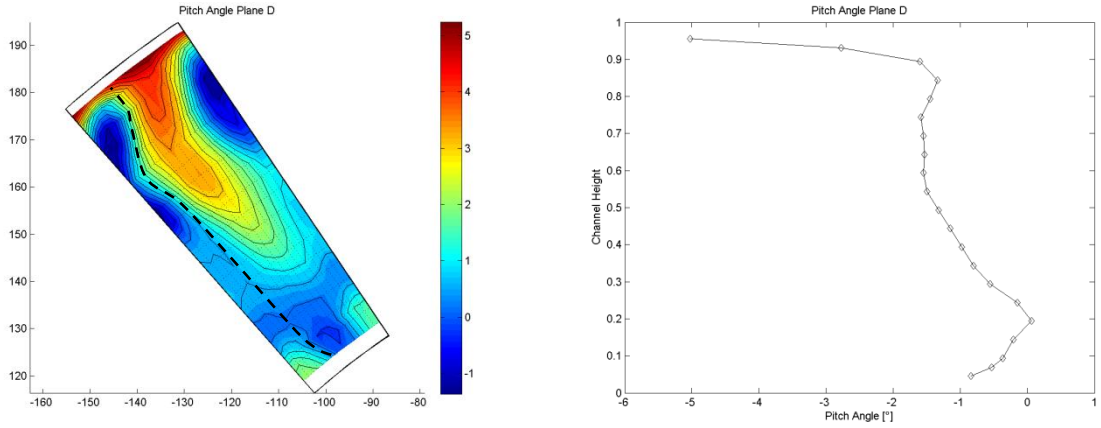

Figure 5-118: Pitch angle distribution plane D, "Inverse Cut-off" EGV operating point Approach

Static Pressure Distribution

The static pressure distribution on the surface of the vane for 4 different radial positions is shown in Figure 5-119. The pressure side distribution for the radial positions 20, 30 and 50% span show almost similar pressure distributions. A small difference can be seen for the first measurement point close to the leading edge at 30% span. The distributions show a strong deceleration just downstream of the leading edge and a slow deceleration downstream of the second static pressure tap. The static pressure distribution at 80% span shows a much lower static pressure along the chord of the vane, except for the first tap at leading edge. Downstream of the leading edge a steady increase in static pressure can be observed. The overall pressure level at 80% span is significantly lower than what can be measured at the other radial positions.

The suction side shows an almost similar distribution for the radial positions 20% and 30% span. There is a strong increase in velocity with a suction peak at approximately 20% axial chord followed by a steady increase in static pressure. The pressure distribution at 50% span shows a later suction peak, at approximately 25% axial chord. At an axial position of 43% a small plateau like feature can be seen for this radial position which could point towards a separation bubble located at this region of the vane. The 80% span position shows a maximum velocity at approximately 30% axial chord, although there is no distinct suction peak but a region extending to almost 50% axial chord. There is a small change in static pressure between 34% and 43% which might indicate a separation bubble

in the area between 43% and 50% axial chord. Downstream of this position a steady increase in static pressure can be seen.

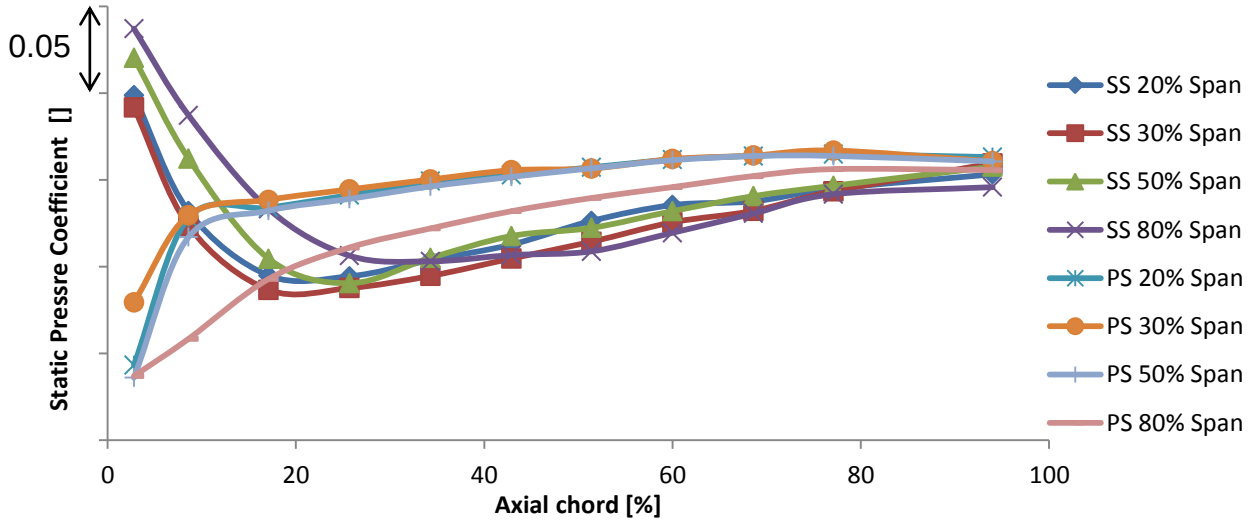

Figure 5-119: Vane surface static pressure distribution, "Inverse Cut-off" EGV operating point Approach

Oil Flow visualisation

The oil flow visualisation for the "Inverse Cut-off" EGV, operating point Approach, is seen in the following section.

Figure 5-120 shows the oil flow visualisation on the casing of the EGV passage. The stagnation point is located on the suction side of the vane and its approximate location is marked with a red "S". The separation line can be easily identified and is marked as well as the main patterns of fluid movement in the passage. Due to the operation point the vane has a negative angle of incidence that causes a flow separation on the pressure side of the vane as seen later in Figure 5-122. This results in a region marked "E" in the oil flow visualisation that is heavily influenced by this separation region. This separated region is also one of the main influences causing a migration of fluid from the pressure towards the suction side.

Figure 5-121 shows the oil flow visualisation on the hub of the vane. The stagnation point is located farther on the pressure side of the vane when compared to the casing. The flow field is dominated by the cross passage gradient. As can be seen the stream lines located at mid-passage at the LE are pushed towards the suction side at the TE of the vane. It can be seen in Figure 5-121 this does not cause a significant radial fluid movement on the suction side of the vane.

Figure 5-122 shows the oil flow visualisation of the suction side (left) and the pressure side (right) of the vane. The suction side of the vane shows similar features as were already seen in earlier flow visualisations. The casing region shows a fluid movement from the casing towards the midspan that is due to the rotor tip leakage and the passage pressure gradient, as seen by the white dotted line close to the casing. Close to the casing two effects can be seen. The unusual flow effect due to the start-up of the test rig is also present on this EGV and can be seen as a black dotted line. Close to the hub a separation line can be identified that starts at approximately 15% axial chord and elevates from the hub to a position of 5% span, therefore staying confined to the hub and only slightly influencing the flow field. There is clear indication neither flow separation nor a strong cross passage

gradient pushing fluid from the hub onto the suction side surface of the vane. At an axial position of approximately 25% chord a change in the texture of the oil flow visualisation can be seen that is marked by a white dotted line reaching from 20% span to 65% span of the vane (marked A). The reason for this change in texture is not fully known. One possible explanation is the occurrence of a separation bubble that might cause such behaviour, yet this is not supported by the static pressure distribution seen in Figure 5-119, where no signs of a separation bubble can be identified in this region of the flow. Yet it has to be remarked that the occurrence of this effect is at a similar axial position as the suction peak of the vane, a region with a large wall shear stress. The pressure side on the right of Figure 5-122 shows a large region of separated flow in the leading edge casing region. The region of separated flow extends from approximately 60% span at the leading edge towards the trailing edge of the vane. This region of separated flow is due to the wrong incidence caused by the rotor tip leakage flow and is marked with an "S". A second structure within this separated region can be identified close to the casing and is marked with a dotted line. This region shows a change in texture of the oil flow visualisation pointing towards a region of very small shear stress at the intersection of pressure side and casing. Close to the hub the oil flow visualisation shows a small radial component of the flow.

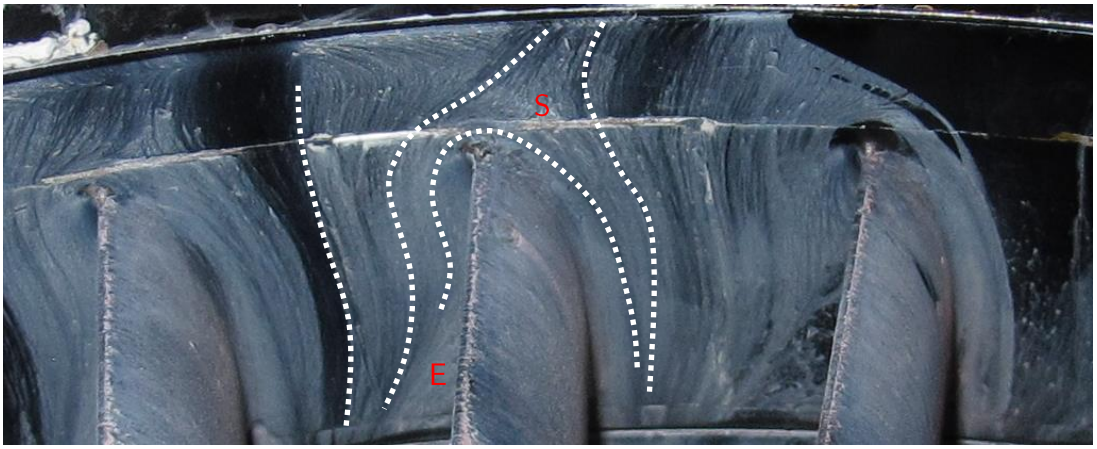

Figure 5-120: Casing Oil Flow visualisation, "Inverse Cut-off" EGV operating point Approach

Figure 5-121: Casing Oil Flow visualisation, "Inverse Cut-off" EGV operating point Approach

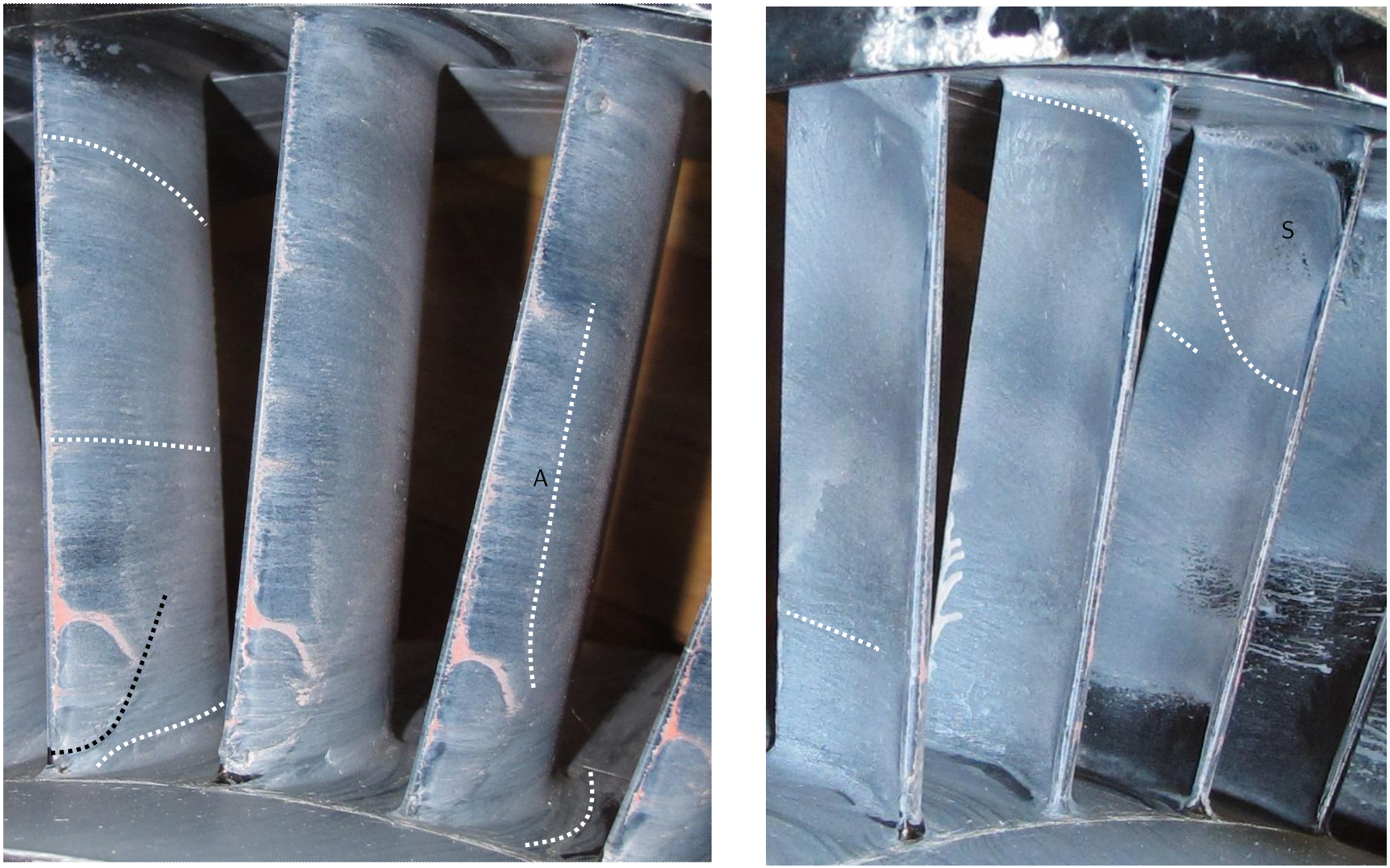

Figure 5-122: Oil Flow visualisation "Inverse Cut-off" EGV, operating point Approach, suction side (left) and pressure side (right), "Inverse Cut-off" EGV operating point Approach

Acoustic

The results of the acoustic post processing are shown in the following section. Figure 5-123 shows an averaged FFT of all microphones used in the acoustic post-processing. The 1st BPF can be seen at a frequency of 5520 Hz as well as the 2nd BPF at 11040 Hz. In addition to these frequencies a peak at approximately 4080 Hz as well as at 8160 Hz can be seen that are due to blade vibration.

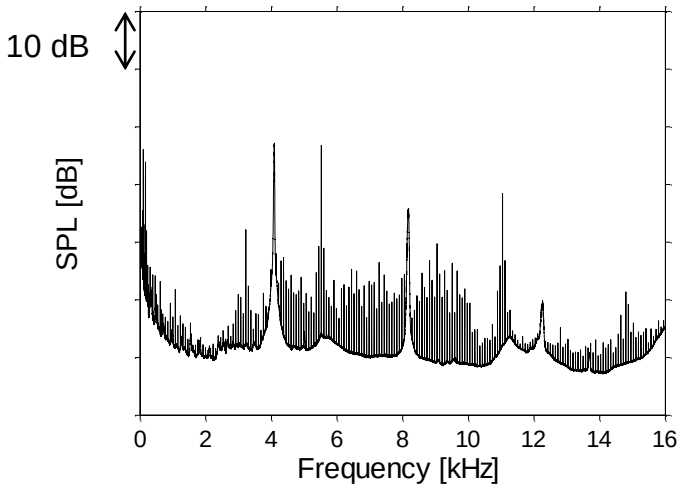

Figure 5-123: Averaged FFT of all microphones for the operating point, "Inverse Cut-off" EGV operating point Approach

The result of the azimuthal mode decomposition is shown in Figure 5-124 where the modes able to propagate are shown as red dotted lines. The results show that there is no clearly dominating mode in the circumferential modes as already seen for the operating point ADP. The highest mode in the decomposition is not due to the modes calculated with the formula of Tyler and Sofrin. This shows that the design intent of the EGV, supressing the propagation of interaction modes, is also valid for the operating point Approach.

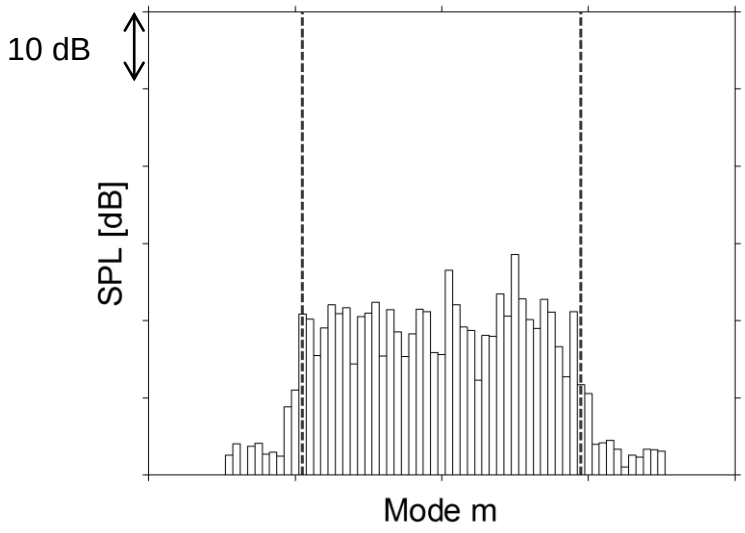

Figure 5-124: Azimutal mode decomposition, "Inverse Cut-off" EGV operating point Approach

The following radial mode decomposition results in the results that can be seen in Figure 5-125. The figure shows the circumferential modes for each radial mode able to propagate. The results are split

into modes propagating in and against streamwise direction. It can be see that the modes propagating in streamwise direction are significantly higher than the modes propagating against streamwise direction. The result of the radial mode decomposition summing up all radial modes can be seen in Figure 5-126. The dominating modes are the modes m=+10 for both radial modes n=0 and n=1 as can be seen in Figure 5-127 left and right.

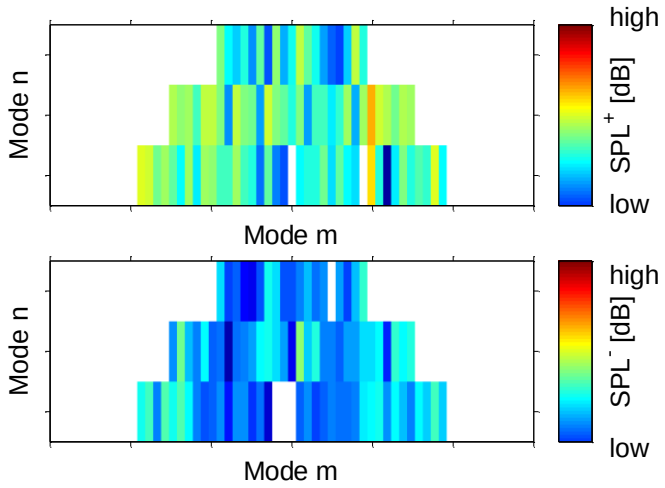

Figure 5-125: Radial mode decomposition for, "Inverse Cut-off" EGV operating point Approach

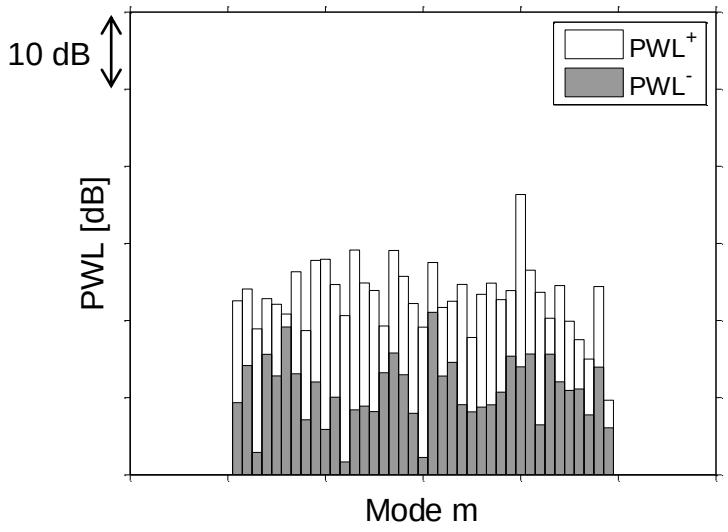

Figure 5-126: Radial mode decomposition, sum of all radial modes, "Inverse Cut-off" EGV operating point Approach

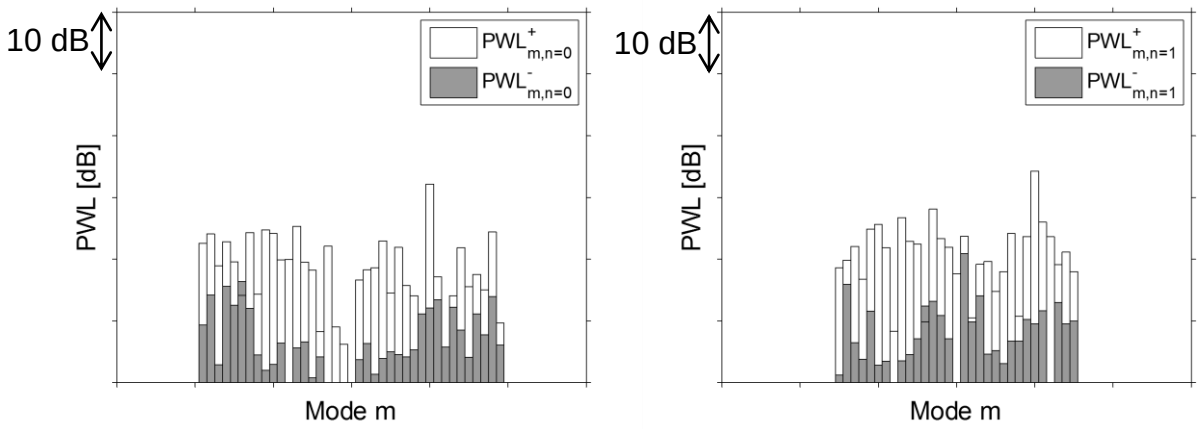

Figure 5-127: Radial mode decomposition, radial mode n=0 (left) and radial mode n=1 (right), "Inverse Cut-off" EGV operating point Approach

5.2.2.4 High loaded EGV

5-hole Probe Plane D0

The total pressure distribution in Figure 5-128 is dominated by the wake of the vane that extends radially from the hub to the casing. A region of low total pressure associated with the hub secondary vortex can be identified close to the hub. The wakes of the upstream stator can still be identified in the total pressure field. There is a pattern of three regions of large total pressure that extend in vertical direction can be identified and are marked with black dotted lines. These are due to the upstream stator wakes that are not yet mixed out. The circumferential averaging shows a local maximum of total pressure at approximately 30% span. This is due to the total pressure distribution downstream of the rotor as seen in Figure 5-74.

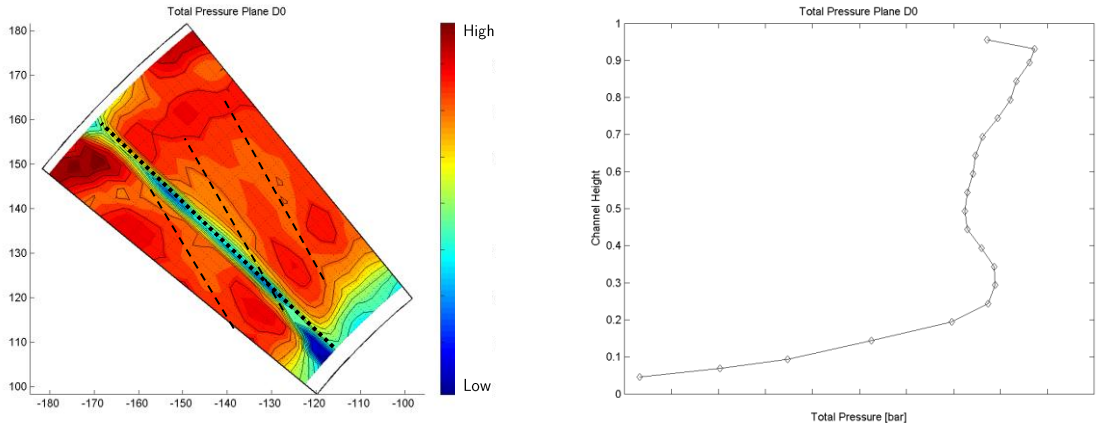

Figure 5-128: total pressure distribution in plane D0, "High Loading" EGV operating point Approach

The Mach number in plane D0 can be seen in Figure 5-129. There are small differences to what was seen in the total pressure distribution. The region of high total pressure close to the casing that was due to the lack of work performed in the tip region of the blade results in a low Mach number region where the tip leakage vortex is present. The regions of low total pressure that were identified as the wakes of the upstream stator vanes result in regions of high Mach number. This is unlike what was seen where the plane C upstream of the EGV TE where the wakes of the stator show a high total pressure as well as Mach number.

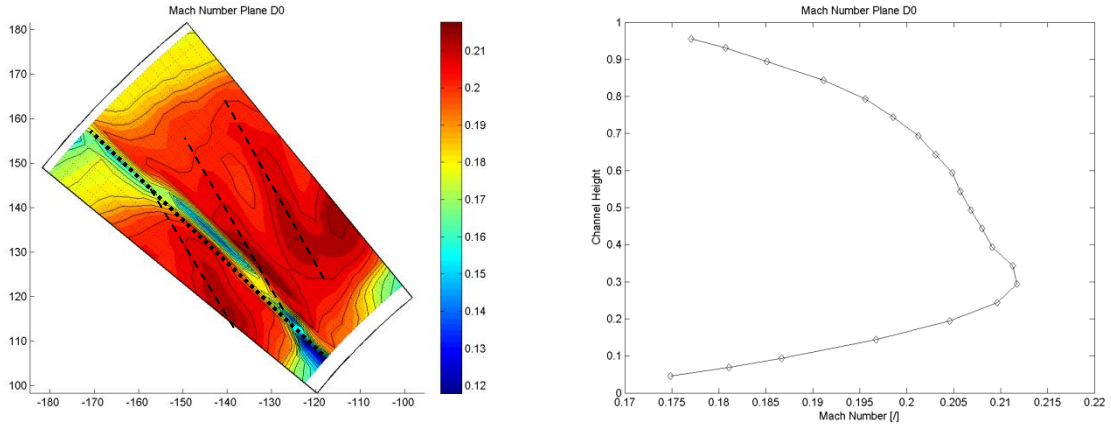

Figure 5-129: Mach number distribution in plane D0, "High Loading" EGV operating point Approach

The total temperature distribution downstream of the vane can be seen in Figure 5-130. A region of high total temperature can be identified close to the casing at the suction side of the wake. This structure is due to the fluid coming from the tip leakage region of the rotor blade. A second region of high total temperature can be identified close to the hub, where the hub secondary flow can be found.

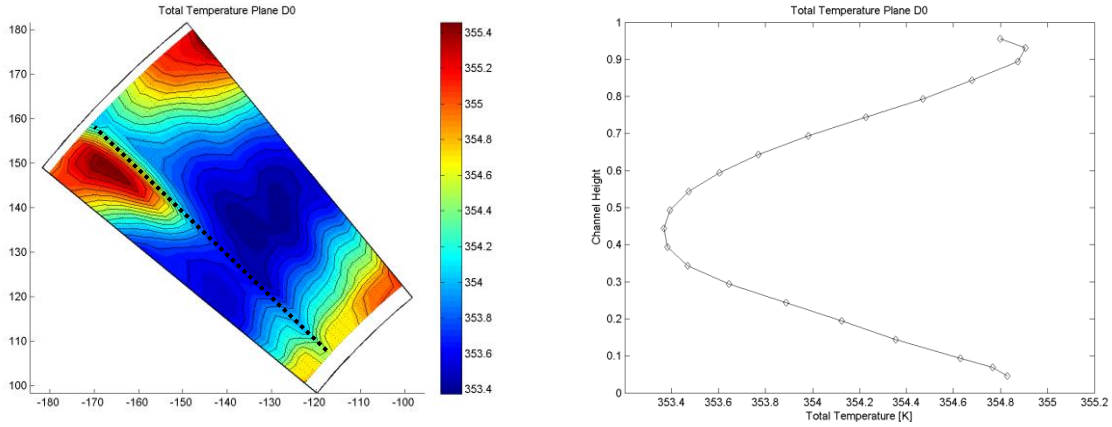

Figure 5-130: Total temperature distribution in plane D0, "High Loading" EGV operating point Approach

The yaw angle distribution in Figure 5-131 shows a region of positive yaw angle close to the outer casing that is due to the fluid coming from the tip leakage. Close to the hub a region of negative yaw angle is dominating in the pressure side corner of the endwall. Around mid-passage at the hub, a small region of positive yaw angle can be identified that is due to the weak hub secondary flow. The wake shows a positive yaw angle along the middle of the wake and a negative yaw angle close to the endwalls.

The pitch angle in Figure 5-132 shows a large region of negative pitch angle on the suction side of the vane. This is due to the fluid migrating from the casing towards midspan. On the pressure side of the vane, a large region of positive pitch angle can be seen. These two regions are a result of the vane secondary flow interacting with the rotor tip leakage causing a strong migration of fluid from the casing towards midspan on the suction side of the vane (see section 12). Below midspan these structures are flipped as to be expected for the lower passage vortex: the suction side shows a positive yaw angle, the pressure side a negative yaw angle.

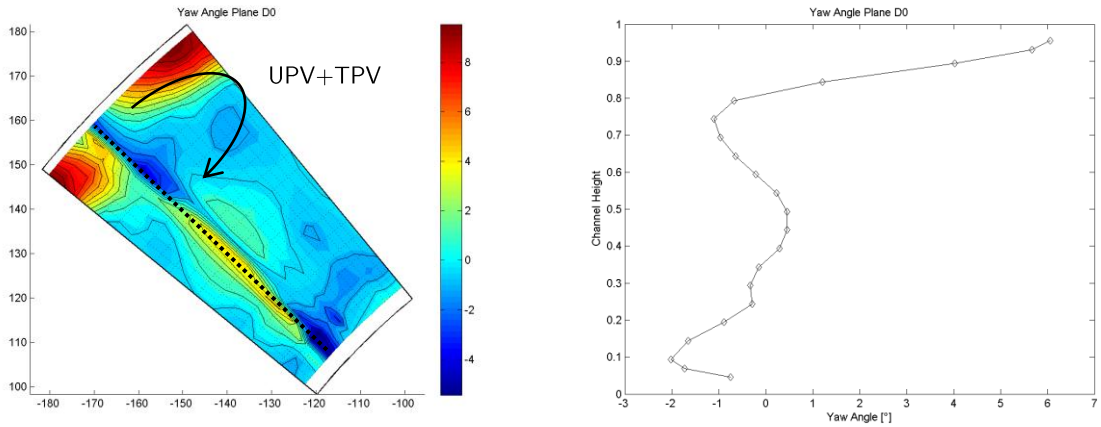

Figure 5-131: yaw angle distribution in plane D0, "High Loading" EGV operating point Approach

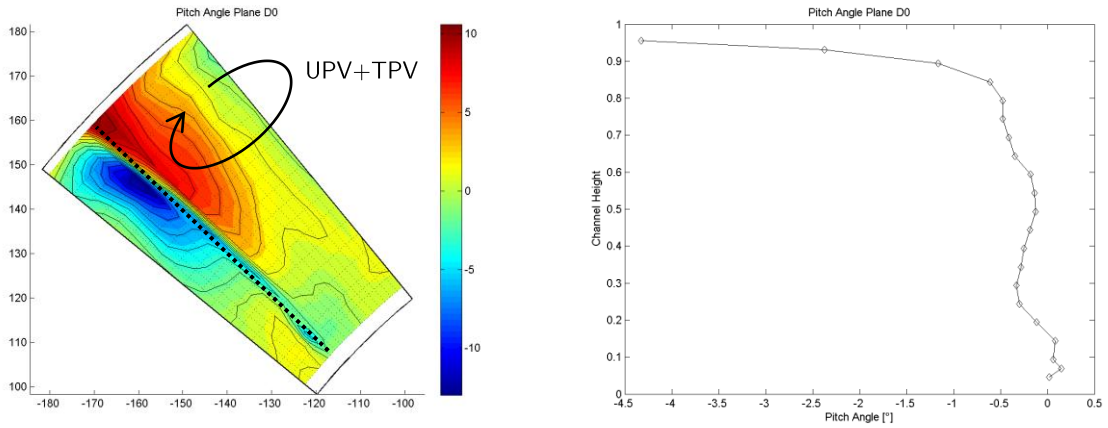

Figure 5-132: pitch angle distribution in plane D0, "High Loading" EGV operating point Approach

5-hole Probe Plane D

The total pressure distribution in plane D, 981% axial chord downstream of the trailing edge is shown in Figure 5-133. The wake of the vane is not yet totally mixed out can still be identified in the figure and is marked as a dotted line. The wake has 3 distinct features. Close to the casing, a region of low total pressure can be identified on the suction side of the wake (marked A). While a region of low total pressure was present in this region in plane D0, the region was confined to a region close to the wall. The long distance between the two planes and pressure gradient present in the flow field push this region further towards mid-channel. Close to the casing, a second region of low total pressure can be identified (marked B). This region was also present in the plane D0 and has now expanded a bit further into the channel.

At approximately 60% span a region of low total pressure and Mach number can be found (marked C). This region was not present in plane D. This structure is caused by rolling up of the trailing edge shear layer caused by the difference in radial velocities as seen by the pitch angle distribution in Figure 5-137 (see Pullan et al. [89] and section 12).

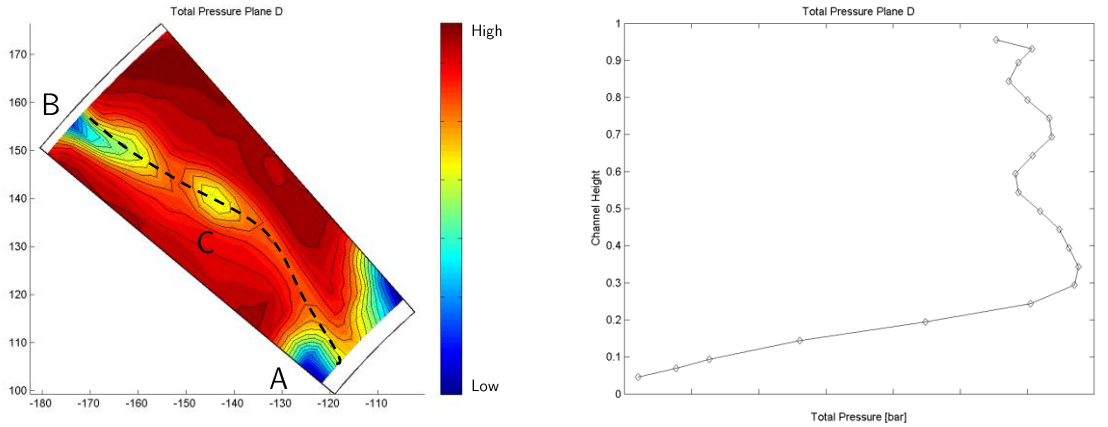

Figure 5-133: Total pressure distribution in plane D, "High Loading" EGV operating point Approach

The static pressure distribution in Figure 5-134 shows a region of low static pressure that is located at approximately midspan on the suction side of the wake. The structure has migrated further towards midspan due to the pressure gradient present in the flow-field. A second region of low static pressure is present close to the hub in the wake/endwall region.

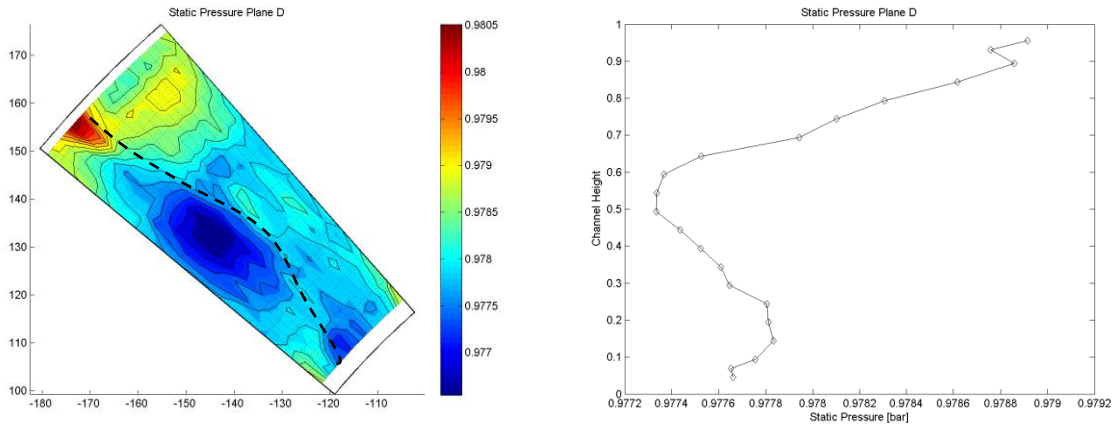

Figure 5-134: Static pressure distribution in plane D, "High Loading" EGV operating point Approach

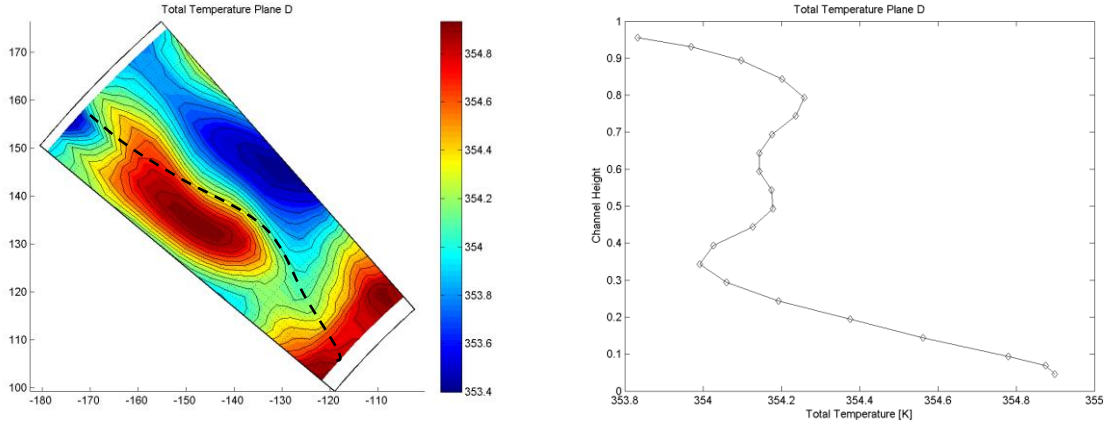

Figure 5-135: Total temperature distribution in plane D, "High Loading" EGV operating point Approach

The yaw angle distribution in Figure 5-136 shows a region of positive yaw angle close to the casing that is due to the tip leakage vortex. While the positive flow angle is rather low (3°) the source (tip leakage) is easily identified. The flow in this region is moving towards the hub in this region as seen from the pitch angle distribution in Figure 5-137. This is consistent with the features seen in Figure 5-132in plane D0. At midspan, a combined region of positive and negative yaw angle can be identified. This region is due to the rollup of the trailing edge shed vorticity as explained by Pullan et al. [89]. Close to the casing a region of positive yaw angle is located close to the hub where the hub secondary flow is located. This structure is very small and can hardly be identified.

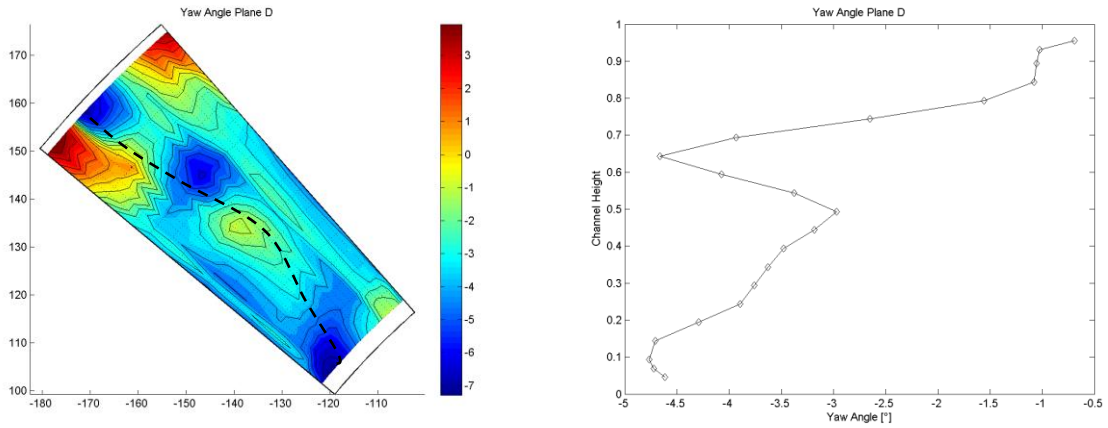

Figure 5-136: Yaw angle distribution in plane D, "High Loading" EGV operating point Approach

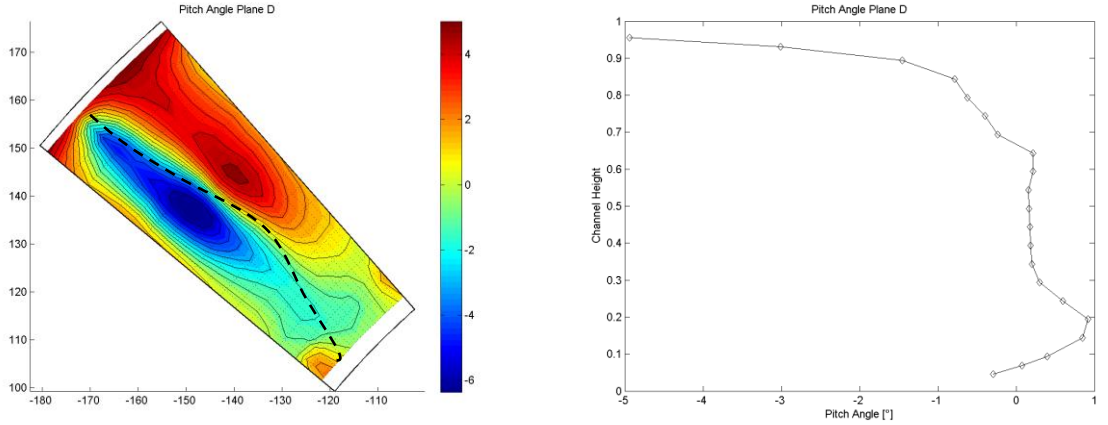

Figure 5-137: Pitch angle distribution in plane D, "High Loading" EGV operating point Approach

Static pressure

The static pressure distribution for both the suction and the pressure side of the vane can be seen in Figure 5-138. The figure shows the static pressure in bar as a function of the percentage axial chord for all 4 different radial positions.

The distribution on the suction side of the vane shows a suction peak that is located at approximately 20-30% axial chord at 20% span, moving towards 25% at 30% span and 30% at 50% span. There is a steady increase in static pressure from the suction peak towards the trailing edge with no significant sign of a separation bubble. The 30% span pressure distribution shows a plateau like pressure distribution. The oil flow visualisation in Figure 5-144 shows a deposition of oil flow in this particular region of the vane.

The suction side pressure distribution at 80% span is different from the other suction side distributions, as the suction peak has moved towards approximately 5% span. At 25% span the distribution shows a plateau with two almost identical pressure values pointing towards a possible separation bubble. In addition the static pressures towards the trailing edge of the vane are higher than for the other radial positions due to the higher static pressure towards the casing.

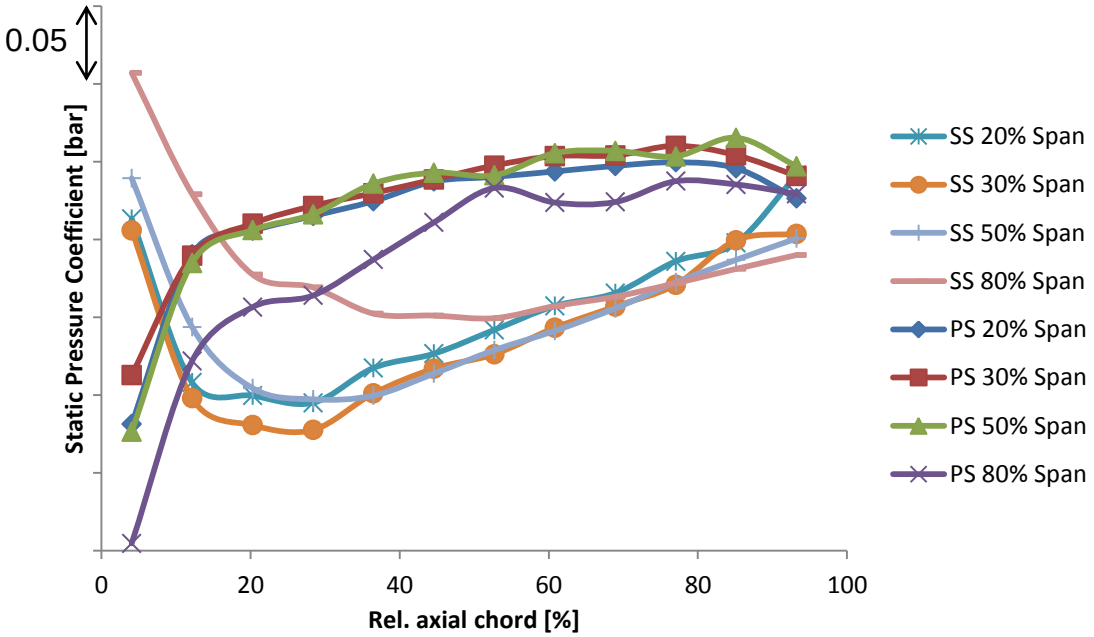

Figure 5-138: Static pressure distribution on the vane surface, suction and pressure side, "High Loading" EGV operating point Approach

The pressure side of the vane shows an almost identical distribution for the values at 20%, 30% and 50% span. There is a small variation close to the leading edge that is due to the change in incidence angle along the span. There is a steady decrease in velocity up to approximately 90% chord with a small acceleration at the last 10% chord.

The 80% span is again different than the other radial positions. The static pressure increases from the leading edge to approximately 20% chord where a small plateau occurs that could indicate a flow separation yet this cannot be seen in the oil flow visualisation. Afterwards the static pressure starts to increase again to 50% chord, where a small plateau with a lowered static pressure occurs between 55% and 70% chord.

Oil flow visualization

The following section shows the oil flow visualization for the operating point Approach.

The following Figure 5-139 and Figure 5-140 show the flow close to the casing of the "High loading" EGV for the operating point Approach. The flow moves from the bottom to the top in both figures. One is able to identify the mean streamlines coming upstream rotor. The stagnation point is located on the pressure side of the vane and the approximate position is marked with an "S". The exact location is hard to determine due to the low shear forces leaving a large amount of oil in the vicinity of this specific location. There is no significant pressure gradient visible between the pressure and the suction side that would encourage a strong cross passage flow. This can also be seen in the vane pressure distribution in Figure 5-138.

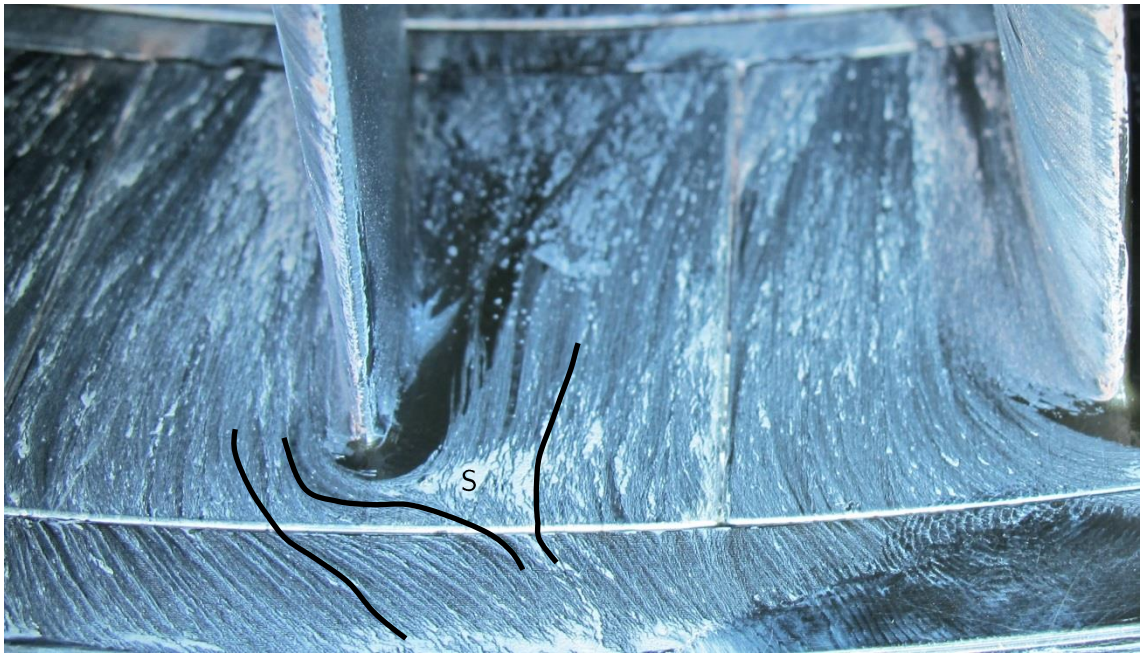

Figure 5-139: Casing Oil Flow visualisation, "High Loading" EGV operating point Approach

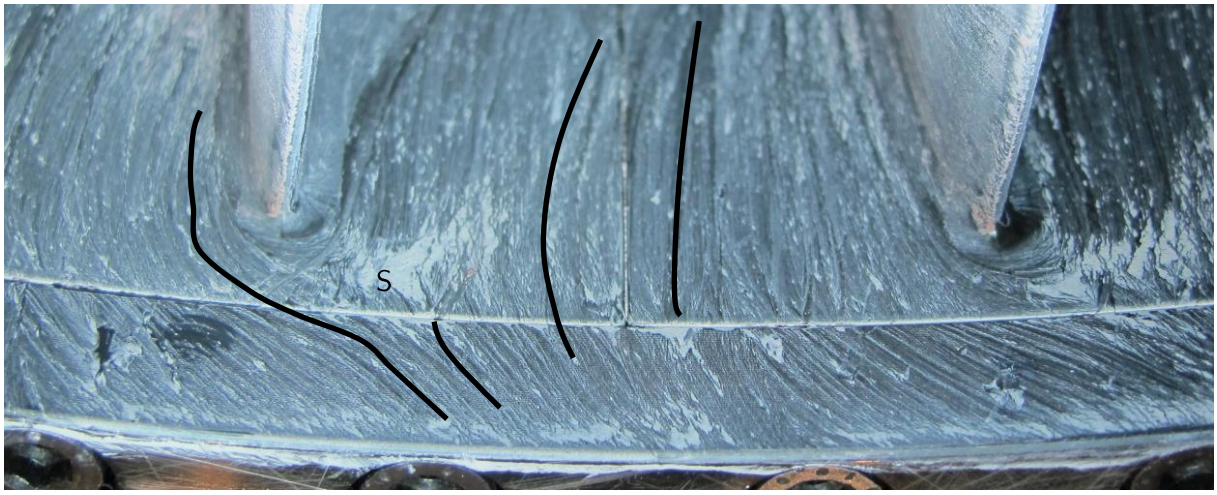

Figure 5-140: Casing Oil Flow visualisation, "High Loading" EGV operating point Approach

The streamlines at the hub of the EGV can be seen in Figure 5-141 and Figure 5-142. The separation point is again to be found on the pressure side of the vane. A strong pressure gradient is present as can be seen by the streamlines from the pressure to the suction side. The separation point is again marked with an "S", and again it is hard to determine the exact point of separation due to the low shear stress. This strong cross passage flow is responsible for a lift-off line on the suction side hub endwall corner of the vane.

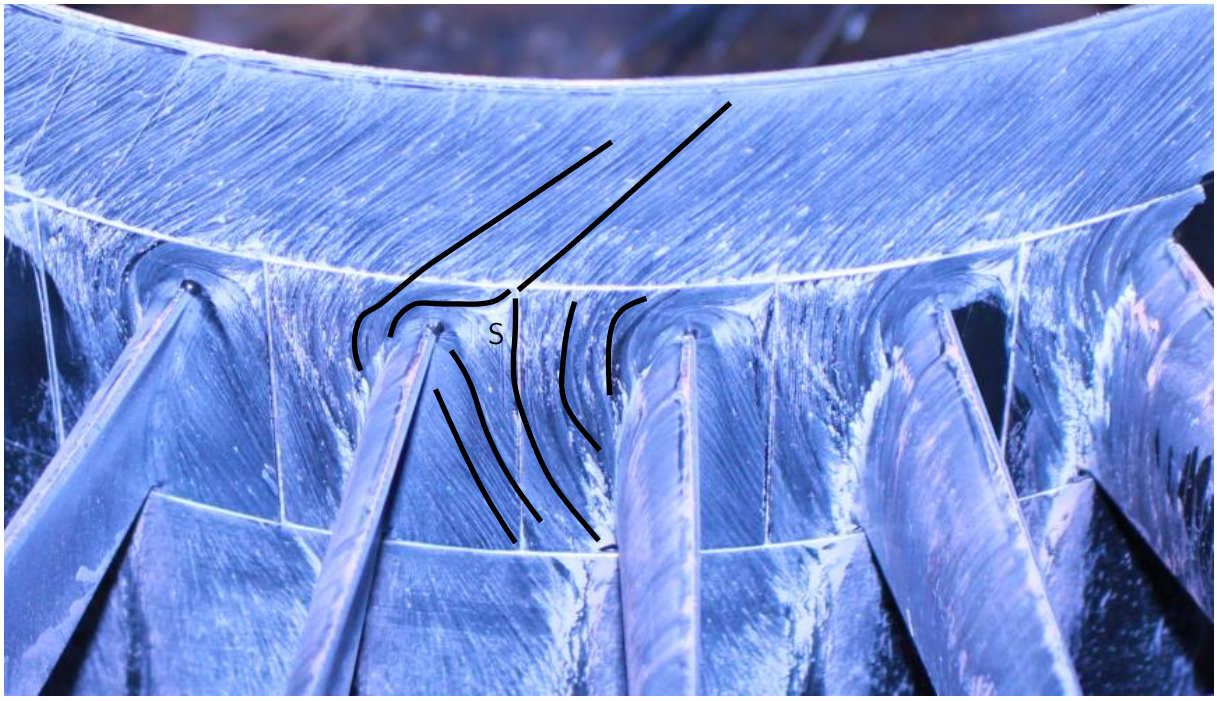

Figure 5-141: Hub Oil Flow visualisation, "High Loading" EGV operating point Approach

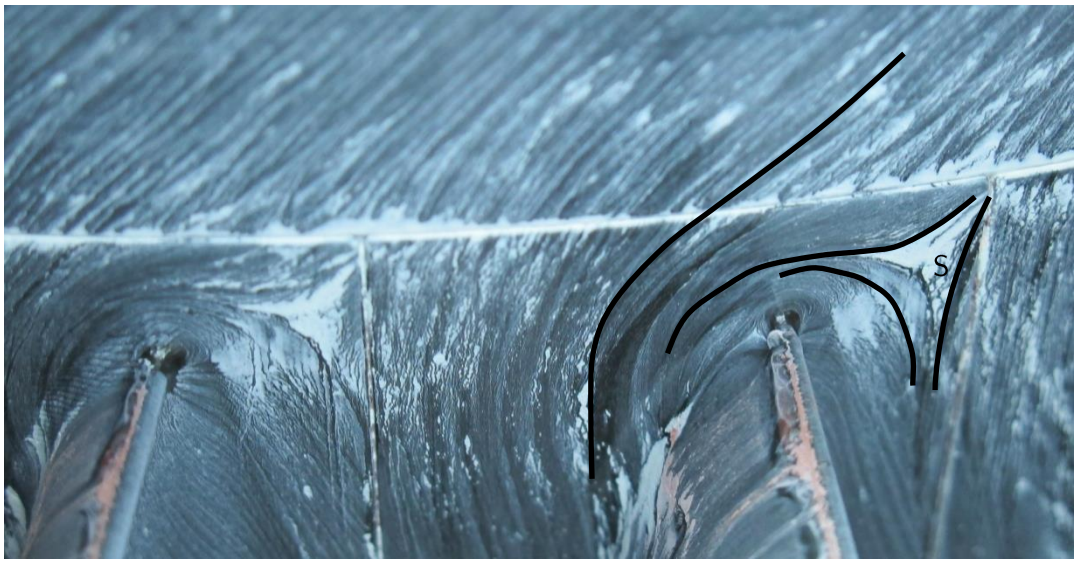

Figure 5-142: Hub Oil Flow visualisation, "High Loading" EGV operating point Approach

Figure 5-143 shows the streamlines on the suction side of the vane. Close to the endwall, a lift-off line can be identified that starts at approximately 25% axial chord as shown in the figure.

A structure can be identified at approximately 15% axial chord that is marked with a dashed line. At this axial position, a deposition of oil can be seen along the dashed line of the vane. A second deposition can be seen around midspan that is marked with a second dashed line. This line starts at

approximately 30% axial chord and bends further back to approximately 70% chord at 60-75% span. Close to the outer casing, the effects of the tip leakage flow interacting with the vane secondary flow can be seen. There is strong fluid motion from the casing towards the hub present. This downward motion is identifiable to a radial position of approximately 70% chord. This downward motion was also seen in the pitch angle distribution in Figure 5-132.

The pressure side oil flow visualization seen in Figure 5-144 shows a flow field that is moving towards the casing from 80% leading edge span upwards. This can be seen by two black lines marked in the figure. Close to the casing, the surface streamlines show a flow towards the casing, corresponding to Figure 5-132. At the hub endwall, the separation line can be seen as a dotted line in the left figure that was already discussed in Figure 5-141.

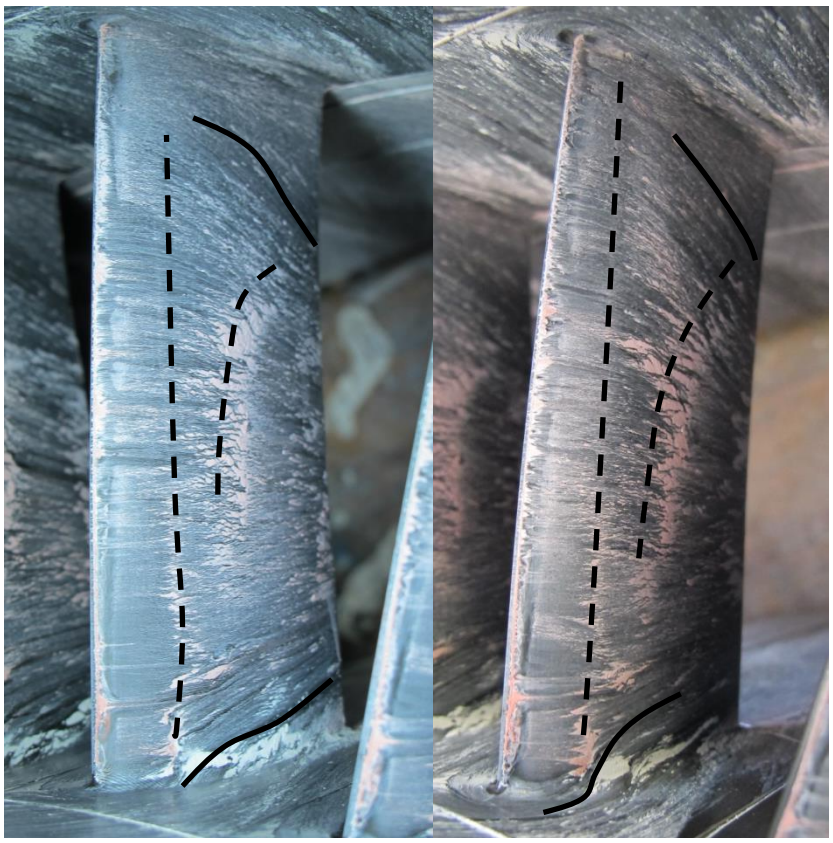

Figure 5-143: Suction Side Oil Flow visualisation, "High Loading" EGV operating point Approach

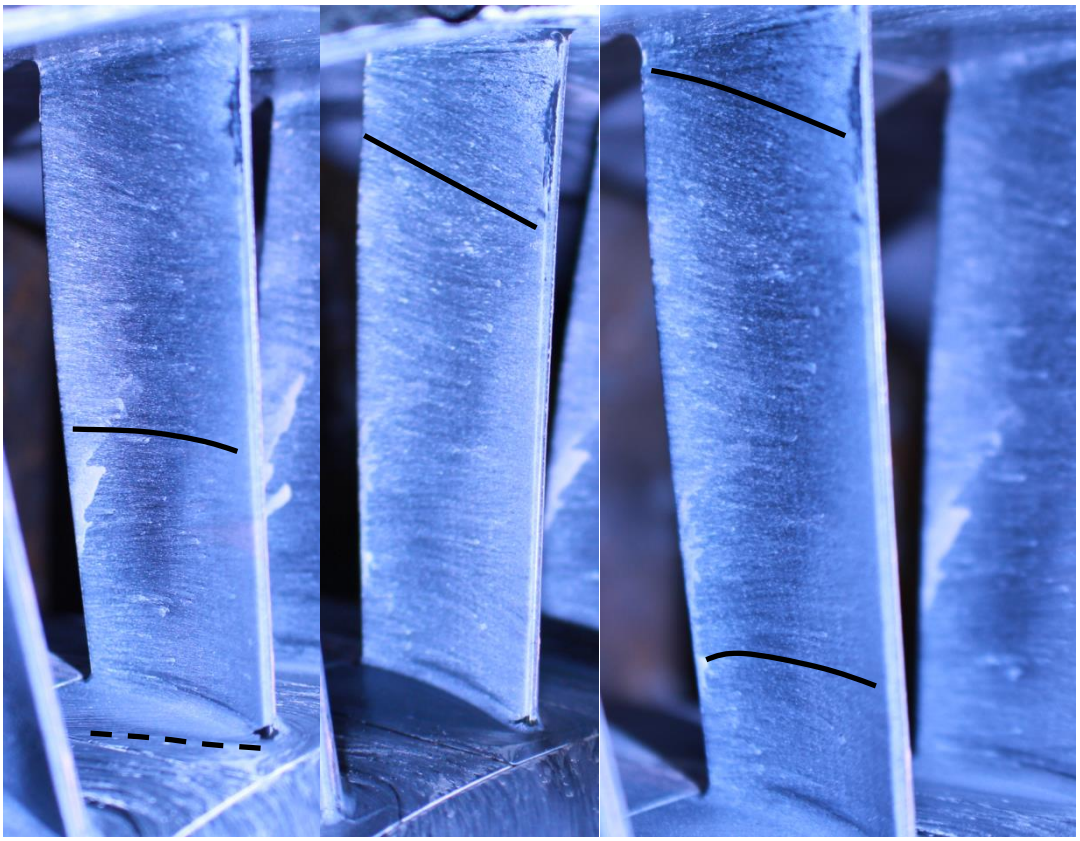

Figure 5-144: Pressure Side Oil Flow visualisation "High loading" EGV, operating point Approach

Acoustic

The acoustic results of "High loading" EGV, operating point Approach, are shown in this section. Figure 5-145 shows the mean FFT of all microphones. The blade passing frequency is 5520Hz and can easily be identified due to the highest peak of the spectrum. The blade eigenfrequency of 4080 Hz seen in the previous operating points can also be seen here.

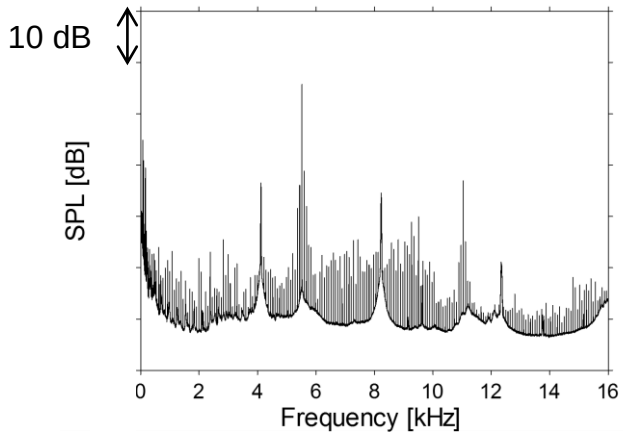

Figure 5-145: Mean FFT of all microphones

The results of the modal decomposition are shown in Figure 5-146. The modes from the Taylor and Sofrin formula are shown as black bars. The limit for modes able to propagate for the given rotational speed is marked as red-dotted lines. All modes between ±21 are able to propagate for the rotational speed 4600 rpm. The dominant mode is by a large margin the mode m=-8 that is due to

two things: an interaction of the rotor with the EGV (32*2-72) as well as a scattering of the mode m=24 resulting from the rotor/stator interaction (96-72) by the exit guide vane (24-32=-8). The mode m=-8 is dominating all other modes by more than 10dB resulting in an overall AMA sound power level of 115.8 dB.

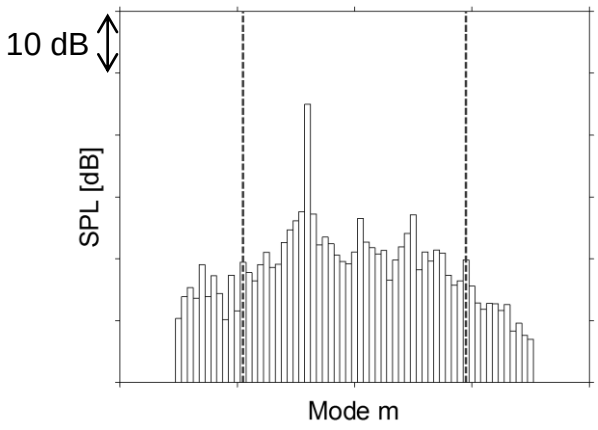

Figure 5-146: AMA decomposition of the modal

The results of the radial mode decomposition can be found in Figure 5-147. All azimuthal and their respective radial modes are seen for both the up- and downstream propagating acoustic field. The dominating mode is again the mode m=-8 for both the up- and downstream moving field. The highest of the radial modes is the radial mode n=0 for the downstream moving modes and the mode n=2 for the upstream moving modes.

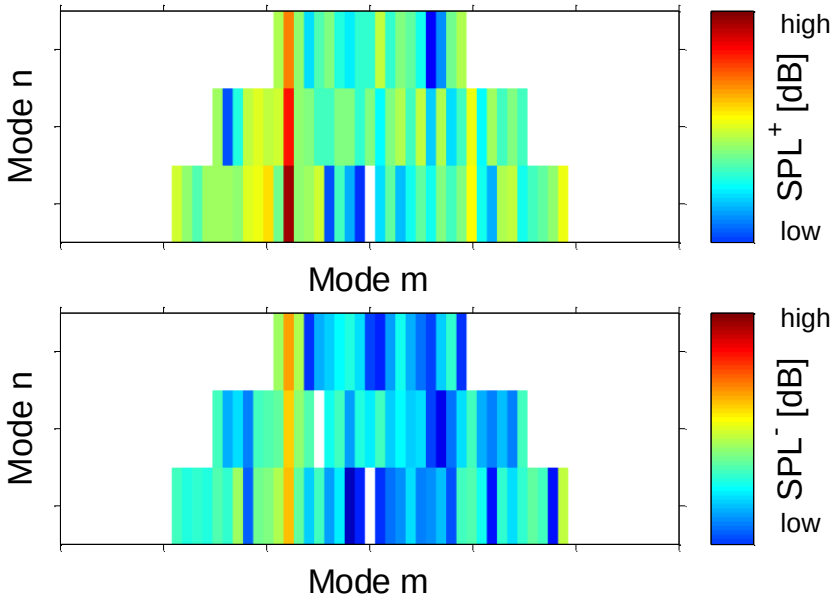

Figure 5-147: Azimuthal and radial modes

The sum of all radial modes is shown for up and downstream extending acoustic modes is shown in Figure 5-148. Again the highest mode is by far the mode m=-8. The same can also be seen in Figure 5-149, where the radial modes n=0 and n=1 can be seen

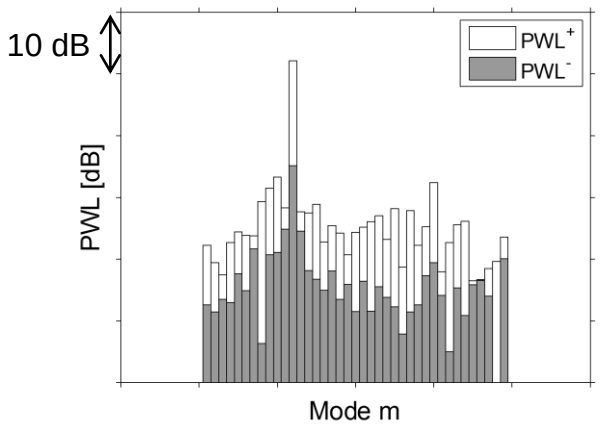

Figure 5-148: Sum of all radial modes for the up- and downstream moving azimuthal modes, "High loading" EGV, operating point Approach

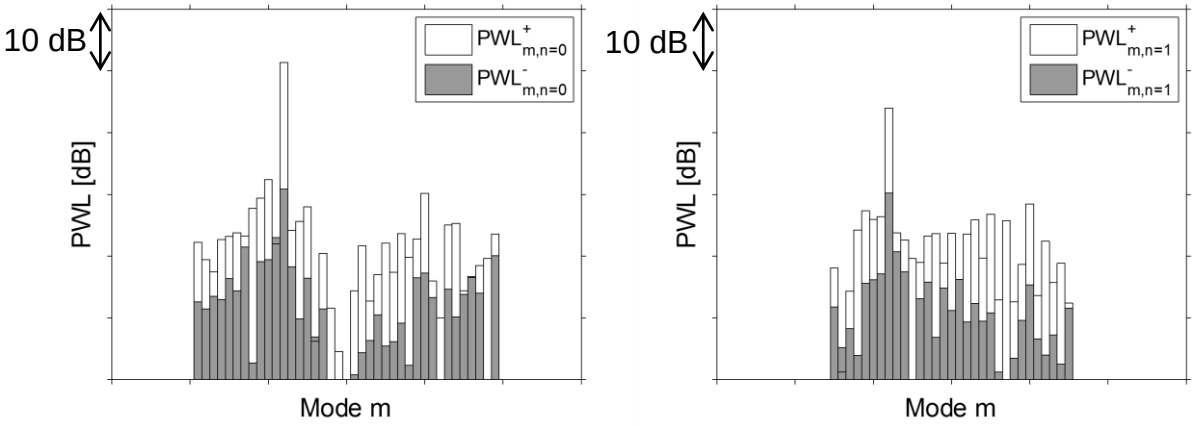

Figure 5-149: radial modes n=0 (left) and n=1(right) for the up- and downstream moving azimuthal modes, "High loading" EGV, operating point Approach

5.2.3 Comparison of the EGVs

The following section directly compares resulting flow and acoustic field downstream of the different EGVs presented in the previous chapters. At first the aerodynamic differences including a comparison of the different total pressure loss coefficients will be presented and then the differences in acoustic performance will be discussed.

Aerodynamic Comparison

The aerodynamic properties of the different EGVs will be discussed in terms of circumferentially averaged distributions of total pressure and yaw angle since these provide the best insight into the flow field downstream of the EGV. Figure 5-150 shows a comparison of the circumferentially averaged total pressure distribution downstream of the EGV for all four EGV configurations for the operating point Approach. The abscissa shows the total pressure and the ordinate the dimensionless height of the channel.

The "Datum" EGV shows a total pressure distribution with a minimum total pressure loss at approximately 60% span. This minimum is due to the strong fluid flow from the casing towards the midspan region caused by the tip leakage flow. The total pressure loss shows a steady increase both towards the hub and the casing, the regions that are heavily influenced by the secondary flows. The region close to the hub shows two regions with a different slope, suggesting the secondary flow is heavily influencing a region from the hub up to approximately 20% span.

The yaw angle distribution seen in Figure 5-151 clearly shows the influence of the secondary flow as well as the rotor tip leakage flow onto the flow field downstream of the vane. The passage pressure gradient, causing a flow from the pressure towards the suction side results in an increase in yaw

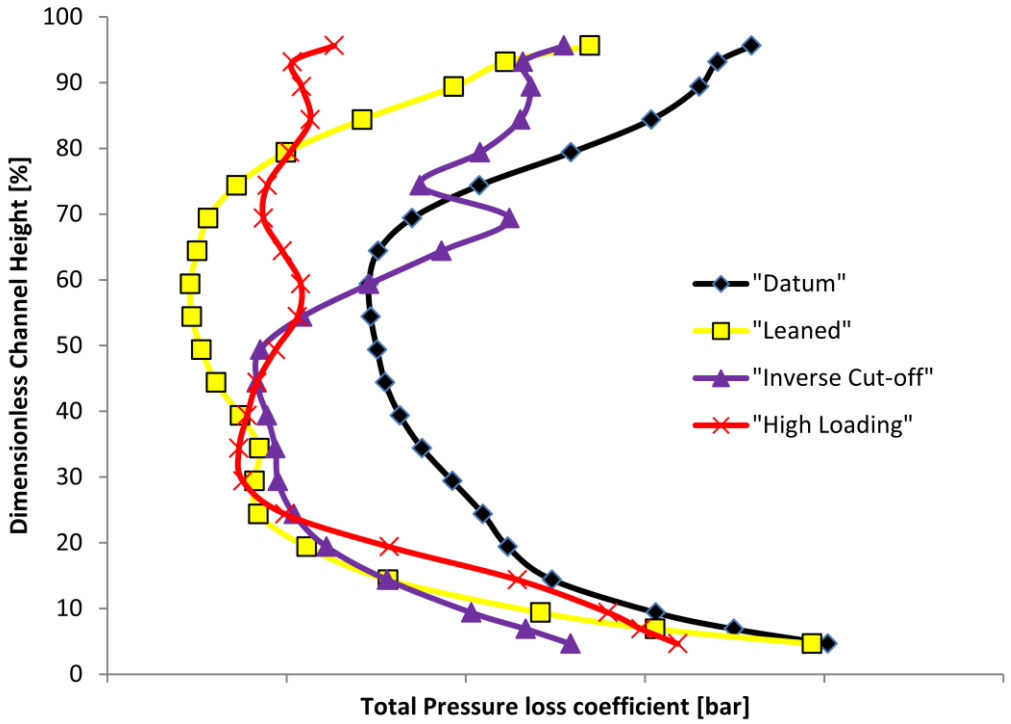

Figure 5-150: Comparison of circumferentially averaged total pressure loss coefficient in plane D, operating point Approach

angle at both the hub and the casing. The casing is, in addition to the secondary flows, subject to the rotor tip leakage flow that causes an increase in yaw angle distribution close to the casing of the vane.

The "Leaned" EGV shows a total pressure distribution in plane D as seen in Figure 5-150 that also shows a local minimum of total pressure loss at approximately 60% span of the vane that is lower than what was seen for the "Datum" EGV. The increase in total pressure loss towards the casing is lower than for the "Datum" EGV resulting in a higher total pressure close to the casing. Towards the hub a change in total pressure loss coefficient can be seen at approximately 30% span. This is due to the pronounced low total pressure region present in the wake at this radial position that is not present for the "Datum" EGV. The yaw angle distribution shows a significantly different behaviour close to the casing than the "Datum" EGV. There is no significant increase in yaw angle close to the casing, but rather an almost constant yaw angle distribution between approximately 55% span, where the minimum averaged yaw angle is located and the casing. This change is due to the fact that the lean of the vane promotes the migration of fluid from the casing along the suction side of the vane that is largely influenced by the tip leakage flow towards midspan. This results in an increased yaw angle in the other regions of the flow field rather than close to the casing of the vane as more fluid is migrating away from the casing. Close to the hub an increase in yaw angle can be seen.

The "Inverse Cut-off" EGV shows a different total pressure loss distribution compared to the low aspect ratio EGVs. There is a low total pressure loss region located between 25% and 50% span with a minimum at approximately 49% that is strongly increasing between 55% span to a local maximum at 70% span. This increase is due to a large region of low total pressure located between 75% span and the casing within the wake region as seen in Figure 5-114 that results from the low total pressure region caused by the rotor tip leakage flow. Close to the hub an increase due to the

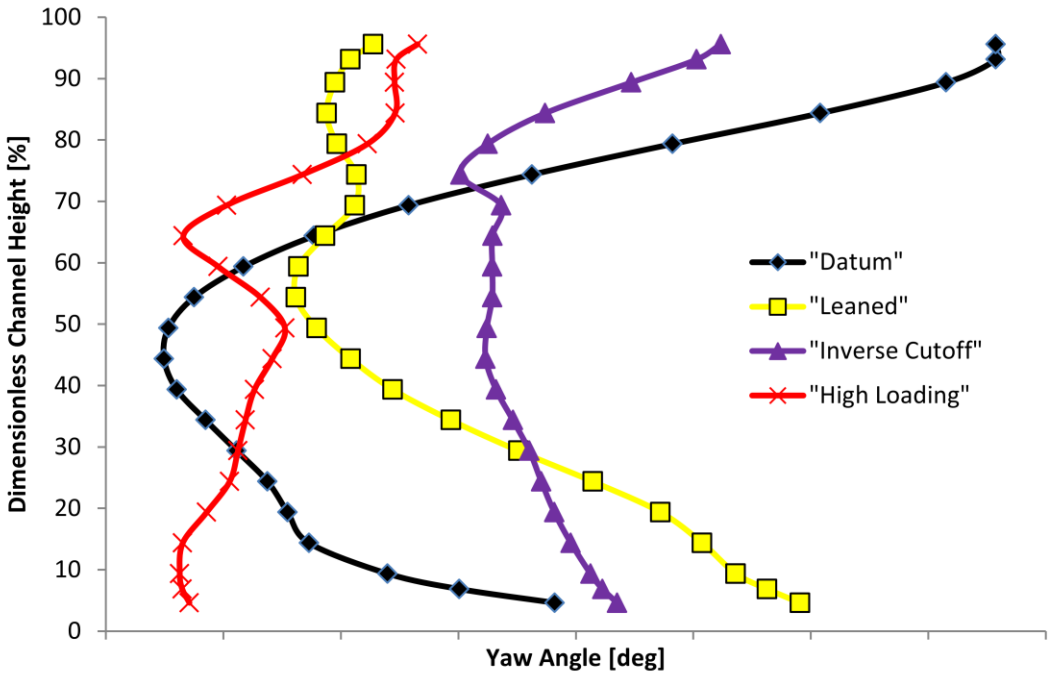

Figure 5-151: Comparison of circumferentially averaged yaw angle in plane D, operating point Approach

hub secondary flows can be seen. The yaw angle distribution of the "Inverse Cut-off" EGV as seen in Figure 5-151 shows an almost constant averaged yaw angle between 45% span and 70% span that shows an increase in yaw angle close to the casing due to the influence of the tip leakage flow. Another small increase in yaw angle can be identified close to the hub.

The total pressure loss distribution of the "High Loading" EGV as seen in Figure 5-150 shows that there is only very little change between 30% span and the casing. The average total pressure loss distribution varies only slightly due to the effects of the secondary flows present in this region. Close to the casing the total pressure loss increases like for all other EGVs. The yaw angle in Figure 5-151 shows an averaged distribution that shows a slight increase in yaw angle across the span of the vane. At a radial position of 65% span a reduction in averaged yaw angle can be identified. This reduction in yaw angle is due to a vortex that is forming at approximately midspan that is rotating in counter clockwise direction and causes this decrease. The strong increase in yaw angle close to the casing that occurs for other EGVs does not occur here.

The relative total pressure losses with respect to the "Datum" EGV between measurement plane C and D can be seen in Table 5-3.

The "Leaned" EGV has a calculated relative loss of 0.57 meaning there is a significant reduction of 43% in the losses generated by the EGV. This holds true despite the fact that the oil flow visualisation of the "Leaned" EGV in section 5.2.2.2 shows a large separation region on the pressure side casing leading edge. This is not visible from the oil flow visualisation of the "Datum" EGV in section 5.2.2.1 all though CFD calculations (not presented in this thesis) suggest a separation on the pressure side of the "Datum" EGV is present.

The "Inverse Cut-off" EGV shows a decrease in total pressure loss coefficient by 29% between plane C and D. There is also a separation region present for this operating point that influences a large part of the passage causing a strong displacement of fluid. This is especially critical due to the fact that most of the chord of the vane is influenced by this structure and therefore an increase in losses compared to the "Datum" EGV. The losses calculated between C and D0 are 54% of those occurring between C and D. With respect to the "Datum" EGV between D and D the losses are 39% of said losses.

The aerodynamically optimised "High Loading" EGV shows a reduction in total pressure loss by 43% compared to the datum configuration. When looking at the losses occurring between the

Table 5-3: EGV total pressure loss comparison Approach

	Total Pressure Loss $\frac{\zeta}{\zeta_{ref}}$	
Configuration	C-D	C-D0
Datum EGV	1	-
Leaned EGV	0.57	-
Inverse Cut-Off EGV	0.71	0.39
High loaded EGV	0.57	0.29

measurement planes C and D0 it can be seen that the losses occurring for the "High Loading" EGV are only 29% of those occurring for the datum configuration. There is an increase in losses between plane D0 and plane D by 33% of the losses occurring for the datum configuration. This also shows that the mixing losses of the "Inverse Cut-off" EGV are higher than those occurring downstream of the "High Loading" EGV.

Acoustic Comparison

A comparison of the acoustic properties for the four EGV at the operating point Approach will be given in the following section.

Figure 5-152 shows the overall sound power level (SPL) as well as of all four EGVs as already separately shown in earlier chapters. The according values can be seen in Table 5-4. It can be seen that the highest PWL is caused by the "High loading" EGV. The PL is significantly, 5.1 dB, higher than the "Datum" EGV. The reason for this is the dominant interaction mode occurring for the "High Loading" EGV. The two EGVs that were optimised for the acoustic performance, the "Leaned" and "Inverse Cut-off" EGV show lower power levels than the "Datum" EGV. The "Leaned" EGV, that was optimised for this particular operating point shows a PWL that is 4.6 dB lower than for the "Datum" EGV and the "Inverse Cut-off" EGV has a level that is 5.9 dB lower. The reason for this decrease for the "Inverse Cut-off" EGV is the fact that the modes associated with the formula by Tyler and Sofrin are not able to propagate and are therefore significantly lower than those of the other EGVs (see chapter 3.3.3 explaining the design process).

Looking at the modes predicted by the Tyler and Sofrin formula, the "High Loading" EGV has significantly higher Tyler and Sofrin modes (+4.7 dB) than the "Datum" EGV.

Figure 5-153 shows a comparison of all modes able to propagate from the radial mode

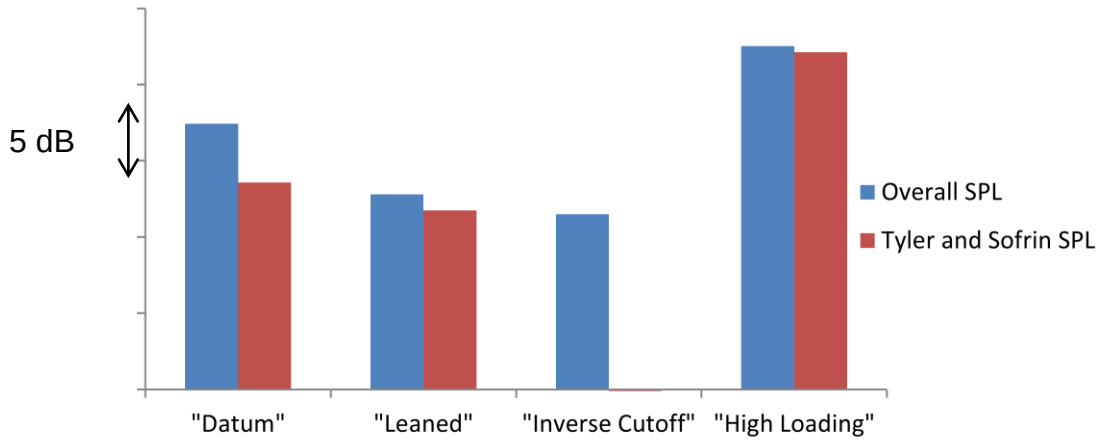

Figure 5-152: EGV Sound Power Level Comparison Approach

Table 5-4: EGV Sound Power Level Comparison Approach

	Datum	Leaned	Inverse Cut-off	High Loading
Overall SPL	Reference	-4.6 dB	-5.9 dB	+5.1 dB
Tyler and Sofrin SPL	-3.8 dB	-5.7 dB	-	+4.7 dB

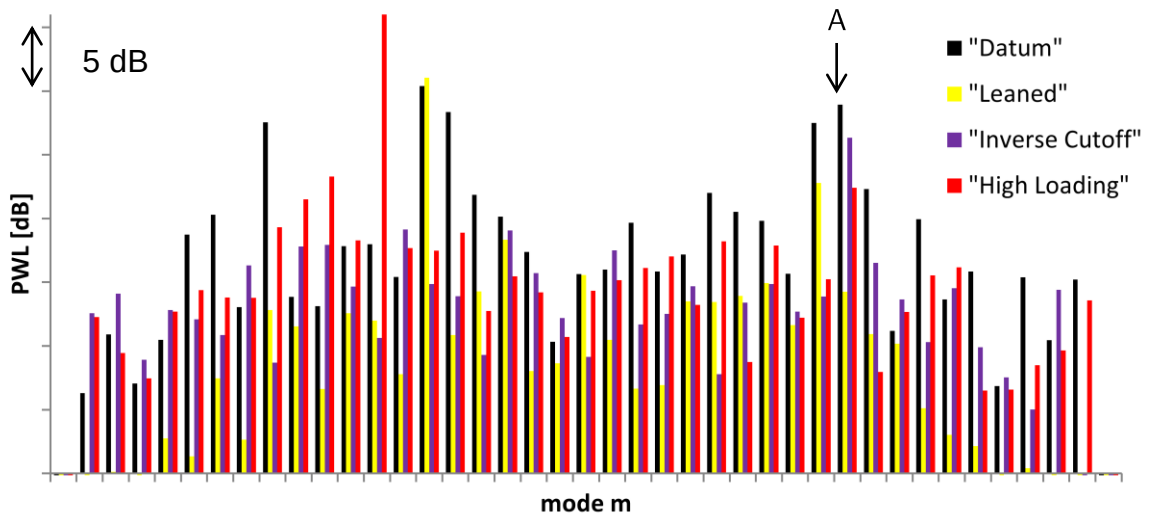

Figure 5-153: EGV Sound power level comparison, all modes, operating point Approach

decomposition performed for the acoustic field downstream of all four EGVs.

The dominant modes for both the "Datum" and "Leaned" EGV are both the rotor/stator interaction scattered by the EGV.

Another interesting fact is that the mode marked A that is amongst the highest modes for all EGVs except the "Leaned" EGV, is a mode that is not predicted by the Tyler and Sofrin formula but rather not associated with the number of vanes and blades.

Overall the goal of reducing the PWL by either a change in vane number ("Inverse Cut-off" EGV) has been successfully applied for this operating point and resulted in a decrease in PWL by 5.9 dB. The stacking of the vane profiles ("Leaned" EGV) resulted in a change in PWL of 4.6 dB that is due to a reduction in the interaction mode m=-12 and m=9 as well as a reduction in non-Tyler & Sofrin Modes. The strong interaction modes occurring for the "High Loading" EGV show to be the dominant source of noise for this EGV.

Overall the goal of reducing the PWL by either a change in vane number ("Inverse Cut-off" EGV) or the stacking of the vane profiles ("Leaned" EGV) has been successfully applied for this operating point resulting in a significant decrease in PWL for the operating point Approach.

6 SUMMARY

In this work four different exit guide vane (EGV) designs were compared at the "Subsonic Test Turbine Facility" (STTF) at the Institute for Thermal Turbomachinery and Machine Dynamics (ITTM). The evaluation of these EGVs was done for two different operating points: the aero design point (ADP) and the operating point "Approach". This operating point represents the engine condition during the landing procedure and is especially relevant from an acoustic point of view, where the LPT is one of the dominant sources of noise.

The four different EGVs were designed in order to understand and evaluate different effects leading to an improvement in acoustic and aerodynamic performance of the EGV itself and the engine as a whole. The "Datum" EGV is derived from current state-of-the-art designs and serves as the status quo in terms of fluid flow and acoustic performance. The "Leaned" EGV is derived from the "Datum" EGV and incorporates a 20° lean in order to reduce the sound power level of the EGV [22]. The "Inverse Cut-off" EGV is designed prohibit the propagation of certain airfoil interactions with the goal of reducing the sound power level downstream of the test rig [76].The "High loading" EGV was designed applying a multi-point optimisation process to the 33% span profile section of the "Datum" EGV.

The aerodynamic evaluation of the EGVs was performed using 5-hole probes and static pressure taps. A single EGV pitch was measured for each of the vanes in order to compare the losses for the two different operating points presented in this thesis.

The acoustic and aerodynamic properties of the "Datum" EGV at the aero design point (ADP) are used as reference results within this final chapter. The values of total pressure loss with respect to the "Datum" EGV at the operating point ADP can be seen in Table 6-1

The flow through the "Datum" EGV at design conditions (chapter 5.1) shows typical flow conditions as found in typical compressor vanes. There is a strong influence of the rotor tip leakage vortex causing a migration of fluid from the casing towards midspan (chapter 12) this increases the trailing edge shed vorticity downstream of the vane which causes a rolling up of this vorticity sheet into a vortex [89]. This rolling up of the vortex causes a significant change in the flow field downstream of the EGV. The off-design point Approach shows an increase in total pressure loss by

Table 6-1: EGV total pressure loss comparison for the operating points ADP and Approach with respect to the "Datum" EGV at ADP

	Total Pressure Loss $\frac{\zeta}{\zeta_{ref}}$	
Configuration	ADP	Approach
Datum EGV	1 (REF)	1.57
Leaned EGV	0.92	0.89
Inverse Cut-Off EGV	0.85	1.11
High loaded EGV	0.81	0.90

a factor of 1.57. This is at least partially caused by the occurrence of a separation on the pressure side of the vane. While this is not clearly visible from the oil flow visualisation, CFD data strongly suggests this occurrence.

The "Leaned" EGV shows a reduction in total pressure loss compared to the "Datum" EGV at ADP by approximately 8%. This occurs despite the fact that a region of suction side hub corner separation is present for the operating point approach as seen in Figure 5-28. While a migration of fluid from the hub onto the suction side endwall due to the hub secondary flow is also visible for the "Datum" EGV, the "Leaned" EGV shows a reverse flow on the hub.

The losses calculated for the operating point Approach show a decrease of 3.3% compared to the operating point ADP. This is rather unusual due to the fact that the losses generate during an off-design condition is usually higher than for the design condition (ADP). The oil flow visualisation of the operating point Approach shows a flow separation on the pressure side close to the leading edge. While this pressure side separation due to the tip leakage flow is also present for the "Datum" EGV, the suction side corner separation is not present for the "Datum" EGV. A more detailed investigation of the losses occurring for the "Leaned" EGV shows that the losses for the operating point "ADP" are significantly higher below 60% span where the influence of the hub secondary flow and the corner separation is influencing the flow field the strongest. On the other hand the operating point "Approach" shows higher losses for the region between 80% span and the casing, where the flow is influenced by the pressure side flow separation. This means that the influence of the reverse flow region on the suction side of the vane is stronger than the combined effect of the negative incidence angle and the resulting separation on the pressure side of the vane.

The "Inverse Cut-Off" EGV at the operating point ADP has total pressure losses that are 15% lower than those of the "Datum" configuration. For the off-design point Approach this is increased by 35% to 1.11 times the reference losses at ADP.

The "High loading" EGV with a highly optimised aerodynamic design has the total pressure losses at ADP reduced by 19%. The losses for the off-design point show only a minor increase by 9% to a total of 0.9 times the reference losses at ADP. This means that there is only a minor difference between the design point and the off-design point in terms of total pressure losses.

Combining these improvements in total pressure loss of the two short chord EGVs for both design and off-design point with a reduction of weight and overall length this provides a valuable improvement for the aero engine.

The acoustic evaluation of the EGV was performed using an acoustic measurement section downstream of the EGV that is rotatable by 360° in order to perform a modal analysis of the flow field. A depiction of the overall sound power levels for all four EGV for both operating points, ADP and Approach, can be seen in Figure 6-1.

Multiple techniques for reducing the overall sound power level downstream of the low pressure turbine were tested within the scope of this thesis, either by reducing the overall sound power level by changing the interaction between the rotor wakes and the vane leading edge ("Leaned" EGV) or by manipulating the interaction modes between the components in order to inhibit certain airfoil interactions from propagating ("Inverse Cut-off" EGV).

The "Datum" EGV shows an overall PWL that is 2.4 dB smaller for the operating point ADP. This is effect results from the difference in rotational speed of the rotor as well as the change in incidence angle of the EGV itself. A comparison of the PWL of the rotor without EGV (not presented in this thesis) shows that the change in PWL between the two operating points ADP and Approach is 2 dB meaning a change of 0.4 dB can be attributed to the EGV and its interactions with the stage.

The "Leaned" EGV was designed to reduce the overall sound power level compared to the "Datum" EGV for the operating point Approach, which was successfully accomplished with a reduction of overall PWL of 4.6 dB. For the operating Point ADP no reduction in PWL was achieved implying that the effect of the lean is heavily dependent on the incidence angle of the vane, since the lean of the vane in the relative system is identical for both operating points. This means that for a given lean, a certain rotor exit flow condition is required in order to fully take advantage of this technique of reducing the PWL.

The "Inverse Cut-off" EGV relies on inhibiting the interaction modes of the EGV, which is mainly dependent on Mach number of the flow and rotational speed of the rotor. Due to a proper selection of the number of exit guide vanes within the TEC, these modes are successfully supressed for both operating points presented in this thesis. The result of eliminating these interaction modes is a reduction in PWL of 3.3 dB for the operating point ADP and 5.9 dB for the operating point Approach, a significant reduction in noise emitted from the LPT.

The acoustic results of the "Highly Loaded" EGV show intensive interactions between the rotor/EGV as well as of the resulting rotor/stator interaction mode with the EGV. These two interactions bot result in an identical circumferential mode that is the dominant acoustic mode. This strong interactions result in a large PWL for both operating points, 1.5 dB larger than the "Datum" EGV for the ADP and 5.1 dB larger for the operating point Approach. This shows that while the "High Loading" EGV shows a significant improvement in terms of aerodynamic performance, the overall noise level significantly increases.

The results presented in this thesis show that the state of the art in EGV design still has a lot of potential for improvement in both aerodynamic and acoustic aspects. The possible changes in the

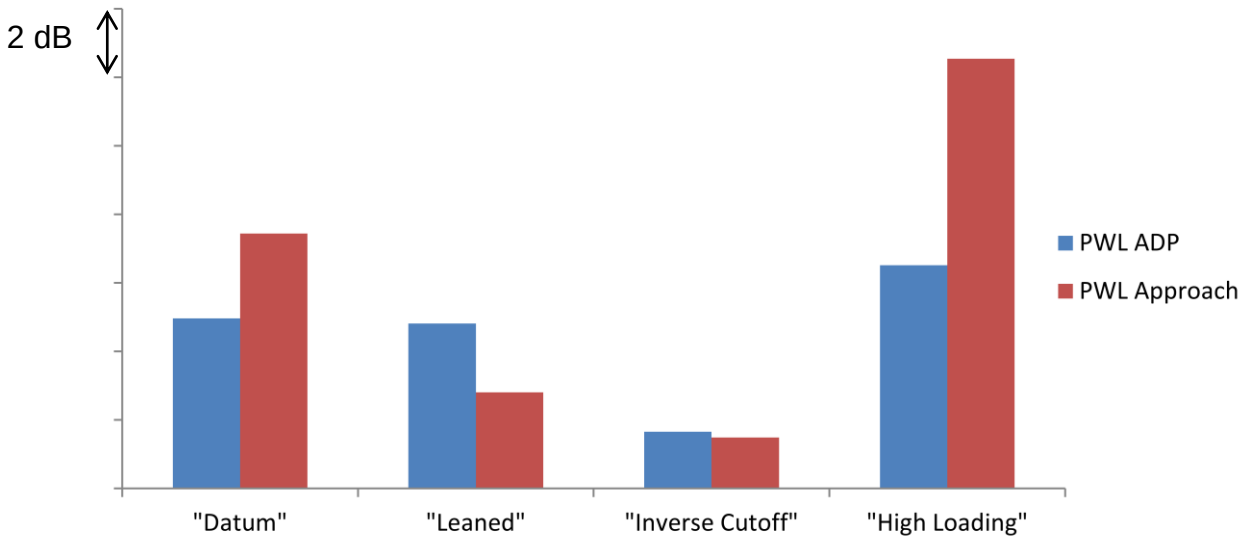

Figure 6-1: comparison of overall PWL for the operating points ADP and Approach for all EGVs

architecture of modern aero engines like the implementation of turning struts in the turbine mid frame and the change in position of the engine mount from the TEC to the mid turbine frame. This opens up the possibility to use the newly gained design space for the EGV.

This thesis has shown that the EGV offers a lot of room for optimisation for both main functions of the EGV: aerodynamic and acoustic.

The acoustic investigations have shown a potential of up to 5.9 dB for the operating point Approach, A reduction of the PWL downstream of the turbine for this operating point plays an important part in fulfilling the aircraft noise certification regulations, extending the operating times of airports and aircrafts. In addition the change in the engine design allows for a possible decrease in engine weight and size leading to an improvement in fuel efficiency and a reduction in the cost of the engine.

Yet this work has shown that an improvement in aerodynamic performance might come hand in hand with an increase in PWL downstream of the EGV. Therefore the designer needs to be concerned with all aspects of the component and anticipate possible negative effects onto other matters as early as possible during the design of the EGV. This does not only hold true for aerodynamic and acoustic aspects but also fatigue and vibrations.

7 Outlook

This thesis has shown that the potential change in aero-engine design caused by the migration of the engine mount offers large possibilities for the turbine exit guide vane. The design of the EGV can be adapted to this new architecture to improve both acoustic and aerodynamic performance further than it is possible now.

While this work has shown the potential improvements of the current state of the art there are a variety of further adaptations to be done in future projects. There are multiple design possibilities presented in this thesis that are not mutually exclusive, meaning it is possible to include both a lean and apply the principles of the "Inverse Cut off" EGV. This can be done in addition to aggressively optimising the aerodynamic performance. In a next step these design concepts can be incorporated in a single EGV.

Further improvements to the acoustic performance of the EGV can be made by applying techniques like absorbers as presented by Broszat et al. [23] for the hub and casing and Serrano et al.[24] for the suction and pressure side of the vane. A possibility of applying these -absorber is e.g. to use a hollow vane with bores on the surface to achieve the effect desired.

These technologies allow for further optimisation of the EGV and allow for future work to be performed. In addition, the interactions of these modifications with the upstream LPT have to be taken into consideration and have to be carefully evaluated.

8 Publications

8.1 Journal Publications

2015 Marn, A.; Broszat, D.; **Selic, T.**; Schönleitner, F.; Heitmeir, F.

"Comparison of the Aerodynamics of Acoustically Designed EGVs and a State-of-the-Art EGV", Journal of Turbomachinery April 2015, Vol.137

Selic, T., Marn, A., Schönleitner, F., Broszat, D., Hoeger, M., Heitmeir, F.

"Comparison of a State of the Art and a High Stage Loading Rotor", Journal of Mechanics Engineering and Automation, Volume 4, Number 11, November 2014

2014 Lengani, D., Kindermann, S., **Selic, T.**, Marn, A., Heitmeir, F.

"Measurement and Decomposition of Periodic Flow Structures of a Test Turbine", Experiments in Fluids, Volume 55, Issue 1

8.2 Conference Publications

2015 Broszat, D., Marn, A., Hoeger, M., **Selic, T.**, Schönleitner, F., Heitmeir, F.

„*Acoustic Comparison of Different Turbine Exit Guide Vane Designs- Part 1: Design Philosophy and Numerical Predictions*", 21st AIAA/CEAS Aeroacosutic Conference, Dallas, USA

Marn, A., **Selic, T.**, Schönleitner, F., Zerobin, S., Broszat, D., Hoeger, M., Heitmeir, F., "*Acoustic Comparison of Different Turbine Exit Guide Vane Designs- Part2: Experimental Analysis*", 21st AIAA/CEAS Aeroacosutic Conference, Dallas, USA

Selic, T., Marn, A., Schönleitner, F., Broszat, D., Hoeger, M., Heitmeir, F.:

"Comparison of an Acoustically Optimised and an Aerodynamically Optimised Exit Guide Vane", 11th European Conference of Turbomachinery, Fluid Dynamics and Thermodynamics, March 2015, Madrid, Spain

2014 **Selic, T.**, Lengani, D., Broszat, D., Schönleitner, F., Marn, A.

"Comparison of a State of the Art and a High Stage Loading Rotor",

ASME Turboexpo 2014, Düsseldorf, Germany

Marn, A.; Broszat, D.; **Selic, T.**; Schönleitner, F.; Heitmeir, F.

"Comparison of the Aerodynamics of Acoustically Designed EGVs and a State-of-the-Art EGV", ASME Turboexpo 2014, Düsseldorf, Germany

Selic T., Marn A.

"On the Influence of Rotor Design on an Acoustically 3d-Designed Turbine Exit guide vane", 20th AIAA/CEAS Aeroacoustic Conference, Atlanta, USA

Schönleitner, F., Koch, H., **Selic, T.**, Höger, M., Marn, A.:

"Comparison of the experimental results between a 2D EGV cascade test and a rig test under engine representative conditions", ASME Turbo Expo 2014, Düsseldorf, Germany

2013 Broszat, D., **Selic, T.**, Marn, A.

"*Verification of the Inverse Cut-Off Effect in a Turbomachinery Stage; Part 2-Comparison to Experimental Results*", 19th AIAA/CEAS Aeroacoustics Conference 2013, Berlin, Germany

2012 **Selic, T.**, Lengani, D., Marn, A., Heitmeir, F.

"Aerodynamic Effects of an Unshrouded Low Pressure Turbine on a Low Aspect Ratio Exit Guide Vane", ASME Turboexpo 2012, Kopenhagen, Denmark

Lengani, D., **Selic, T.**, Spataro, R., Marn, A., Göttlich, E.

"Analysis of the Unsteady Flow Field in Turbines by Means of Modal Decomposition", ASME Turboexpo 2012, Copenhagen, Denmark

Jericha, H., Göttlich, E., **Selic, T.**, Sanz, W.

"Novel Vertical-Axis Wind Turbine With Articulate Blading"

ASME Turboexpo 2012, Copenhagen, Denmark

Broszat, D.; **Selic, T.**; Marn, A.

"Verification of the Inverse Cut-Off Effect in a Turbomachinery Stage Part 1 - Numerical Results", 18th AIAA/CEAS Aeroacoustics Conference 2013, Colorado Springs, USA

9 References

[1] "AirInsight Technical Analysis: The Core of the PW1000G Geared Turbo-Fan." [Online]. Available: http://airinsight.com/2012/10/02/airinsight-technical-analysis-the-core-of-the-pw1000g-geared-turbo-fan/#.VWSKUc-qpBe. [Accessed: 26-May-2015].

[2] A. Marn, "On the Aerodynamics of Intermediate Turbine Ducts for Competitive and Environmentally Friendly Jet Engines," Graz University of Technology, 2008.

[3] J. F. Seda, "Aircraft engine with inter-turbine engine frame," United States Patent 6708482 B2, Nov-2001.

[4] "hdwallpapers.cat." [Online]. Available: https://hdwallpapers.cat/airbus_a380_engine_cutaway_gp7000_aircraft_hd-wallpaper-36478/. [Accessed: 20-May-2015].

[5] S. Stevens and K. Young, "Axial compressor outlet guide vane aerodynamics," in *23rd Joint Propulsion Conference*, American Institute of Aeronautics and Astronautics, 1987.

[6] J. F. Carrotte, K. F. Young, and S. J. Stevens, "Measurements of the Flow Field Within a Compressor Outlet Guide Vane Passage," *J. Turbomach.*, vol. 117, no. 1, pp. 29–37, 1995.

[7] N. Key, K. L. Miller, and R. D. Fulayter, "Lessons Learned from an Aggressive Outlet Vane Design for Axial Compressors," *J. Propuls. Power*, vol. 28, no. 5, pp. 918–926, Sep. 2012.

[8] B. Lakshminarayana, D. E. Thompson, and R. Trunzo, "Strut or guide vane secondary flows and their effect on turbomachinery noise," *J. Aircr.*, vol. 20, no. 2, pp. 178–186, Feb. 1983.

[9] H. Posson and S. Moreau, "Effect of Rotor Shielding on Fan-Outlet Guide Vanes Broadband Noise Prediction," *AIAA J.*, vol. 51, no. 7, pp. 1576–1592, May 2013.

[10] S. Blecherman and T. N. Stankunas, "Composite fan exit guide vanes for high bypass ratio gas turbine engines," *J. Aircr.*, vol. 19, no. 12, pp. 1032–1037, Dec. 1982.

[11] T. Sonoda and H.-A. Schreiber, "Aerodynamic Characteristics of Supercritical Outlet Guide Vanes at Low Reynolds Number Conditions," *J. Turbomach.*, vol. 129, no. 4, pp. 694–704, 2006.

[12] H.-A. Schreiber, W. Steinert, and B. Küsters, "Effects of Reynolds Number and Free-Stream Turbulence on Boundary Layer Transition in a Compressor Cascade," *J. Turbomach.*, vol. 124, no. 1, p. 1, Jan. 2002.

[13] T. Sonoda, Y. Yamaguchi, T. Arima, M. Olhofer, B. Sendhoff, and H.-A. Schreiber, "Advanced High Turning Compressor Airfoils for Low Reynolds Number Condition—Part I: Design and Optimization," *J. Turbomach.*, vol. 126, no. July, p. 350, 2004.

[14] H. G. Rhoden, "Effects of Reynolds Number on the flow of air through a cascade of compressor blades," 1956.

[15] H.-A. Schreiber, W. Steinert, T. Sonoda, and T. Arima, "Advanced High-Turning Compressor Airfoils for Low Reynolds Number Condition—Part II: Experimental and Numerical Analysis," *J. Turbomach.*, vol. 126, no. October, p. 482, 2004.

[16] J. Hjärne, V. Chernoray, J. Larsson, and L. Löfdahl, "An Experimental Investigation of Secondary Flows and Loss Development Downstream of a Highly Loaded Low Pressure Turbine Outlet Guide Vane Cascade," *ASME Conf. Proc.*, vol. 2006, no. 47950, pp. 681–690, 2006.

[17] J. Hjärne, J. Larsson, and L. Löfdahl, "Performance and Off-Design Characteristics for Low Pressure Turbine Outlet Guide Vanes: Measurements and Calculations," *ASME Conf. Proc.*, vol. 2006, no. 90550, pp. 649–658, 2006.

[18] J. Hjärne, V. Chernoray, J. Larsson, L. Löfdahl, J. Hjärne, V. Chernoray, J. Larsson, and L. Löfdahl, "Numerical Validations of Secondary Flows and Loss Development Downstream of a Highly Loaded Low Pressure Turbine Outlet Guide Vane Cascade," in *Volume 6: Turbo Expo 2007, Parts A and B*, 2006, vol. 2006, no. 47950, pp. 681–690.

[19] H. Koch, D. Kozulovic, and M. Hoeger, "Outlet Guide Vane Airfoil for Low Pressure Turbine Configurations," in *42nd AIAA Fluid Dynamics Conference and Exhibit*, American Institute of Aeronautics and Astronautics, 2012.

[20] D. Broszat, D. Korte, U. Tapken, and M. Moser, "Validation of Turbine Noise Prediction Tools with Acoustic Rig Measurements," in *15th AIAA/CEAS Aeroacoustics Conference (30th AIAA Aeroacoustics Conference)*, American Institute of Aeronautics and Astronautics, 2009.

[21] M. Moser, U. Tapken, L. Enghardt, and L. Neuhaus, "An Investigation of Low Pressure Turbine Blade–Vane Interaction Noise: Measurements in a 1.5-Stage Rig," *Proc. Inst. Mech. Eng. Part A J. Power Energy*, vol. 223, no. 6, pp. 687–695, 2009.

[22] D. Broszat, F. Kennepohl, U. Tapken, M. Moser, and F. Heitmeir, "Validation of an Acoustically 3-D-Designed Turbine Exit Guide Vane," in *16th AIAA/CEAS Aeroacoustics Conference*, American Institute of Aeronautics and Astronautics, 2010.

[23] D. Broszat, U. Tapken, L. Enghardt, D. Lengani, and A. Marn, "Validation of an Integrated Acoustic Absorber in a Turbine Exit Guide Vane," in *17th AIAA/CEAS Aeroacoustics Conference (32nd AIAA Aeroacoustics Conference)*, American Institute of Aeronautics and Astronautics, 2011.

[24] A. Serrano and G. Torres, "Estimation of Turbine Noise Benefits Due to Acoustically Treated Outlet Guide Vanes," in *11th European Conference of Turbomachinery Fluid Dynamics and Thermodynamics*, 2015.

[25] N. A. Cumpsty, *Compressor aerodynamics*. Longman Scientific & Technical, 1989.

[26] B. Lakshminarayana and J. H. Horlock, "Review: Secondary flows and losses in cascades and axial-flow turbomachines," *Int. J. Mech. Sci.*, vol. 5, no. 3, pp. 287–307, Jul. 1963.

[27] D. E. Halstead, D. C. Wisler, T. H. Okiishi, G. J. Walker, H. P. Hodson, and H.-W. Shin, "Boundary Layer Development in Axial Compressors and Turbines: Part 1 of 4—Composite Picture," *J. Turbomach.*, vol. 119, no. 1, p. 114, Jan. 1997.

[28] D. E. Halstead, D. C. Wisler, T. H. Okiishi, G. J. Walker, H. P. Hodson, and H.-W. Shin, "Boundary Layer Development in Axial Compressors and Turbines: Part 2 of 4— Compressors," *J. Turbomach.*, vol. 119, no. 3, p. 426, Jul. 1997.

[29] D. E. Halstead, D. C. Wisler, T. H. Okiishi, G. J. Walker, H. P. Hodson, and H.-W. Shin, "Boundary Layer Development in Axial Compressors and Turbines: Part 3 of 4— LP Turbines," *J. Turbomach.*, vol. 119, no. 1, p. 225, Jan. 1997.

[30] D. E. Halstead, D. C. Wisler, T. H. Okiishi, G. J. Walker, H. P. Hodson, and H.-W. Shin, "Boundary Layer Development in Axial Compressors and Turbines: Part 4 of 4— Computations and Analyses," *J. Turbomach.*, vol. 119, no. 1, p. 128, Jan. 1997.

[31] S. Kang and C. Hirsch, "Three Dimensional Flow in a Linear Compressor Cascade at Design Conditions," in *Proceedings of ASME Turbo Expo 1991, June 3-6, Orlando, Florida, ASME Paper No. 91-GT-114*, 1991.

[32] P. K. Chang, *Separation of Flow*. Elsevier Science, 2014.

[33] D. C. Wisler, R. C. Bauer, and T. H. Okiishi, "Secondary Flow, Turbulent Diffusion, and Mixing in Axial-Flow Compressors," *J. Turbomach.*, vol. 109, no. 4, p. 455, Oct. 1987.

[34] D. E. Ashpis, "The NASA Low-Pressure Turbine Flow Physics Program," Jun. 1998.

[35] J. Citavy, Jan, Jilek, "The effect of low Reynolds number on straight compressor cascades," *ASME, Int. Gas Turbine Aeroengine ...*, 1990.

[36] G. V. Hobson, D. J. Hansen, D. G. Schnorenberg, and D. V. Grove, "Effect of Reynolds Number on Separation Bubbles on Compressor Blades in Cascade," *J. Propuls. Power*, vol. 17, no. 1, pp. 154–162, Jan. 2001.

[37] A. N. A. Mukhraiya J. K., "EXPERIMENTAL INVESTIGATION OF AXIAL COMPRESSOR CASCADE PERFORMANCE UNDER THE INFLUENCE OF LOW INTENSITY

TURBULENCE," in *21st Congress of International Council of the Aeronautical Sciences*, 1998.

[38] V. Cyrus, "The Effect of the Reynolds Number on the Three-Dimensional Flow in a Straight Compressor Cascade," *Int. J. Turbo Jet Engines*, vol. 9, no. 2, Jan. 1992.

[39] J. H. Horlock, R. Shaw, D. Pollard, and A. Lewkowicz, "Reynolds Number Effects in Cascades and Axial Flow Compressors," *J. Eng. Power*, vol. 86, no. 3, p. 236, Jul. 1964.

[40] H. J. Preston, "The Determination of Turbulent Skin Friction by Means of Pitot Tubes," *J. R. Aeronaut. Soc.*, vol. 58, pp. 109–121, 1954.

[41] S. A. Gbadebo, N. A. Cumpsty, and T. P. Hynes, "Three-Dimensional Separations in Axial Compressors," *J. Turbomach.*, vol. 127, no. April 2005, p. 331, Apr. 2005.

[42] V.-M. Lei, Z. S. Spakovszky, and E. M. Greitzer, "A Criterion for Axial Compressor Hub-Corner Stall," *J. Turbomach.*, vol. 130, no. 3, p. 031006, Jul. 2008.

[43] Y. Dong, S. J. Gallimore, and H. P. Hodson, "Three-dimensional flows and loss reduction in axial compressors," *J. Turbomach.*, vol. 109, no. 3, pp. 354–361, 1987.

[44] H. D. Joslyn and R. P. Dring, "Axial Compressor Stator Aerodynamics," *J. Eng. Gas Turbines Power*, vol. 107, no. 2, p. 485, Apr. 1985.

[45] D. E. Hobbs and H. D. Weingold, "Development of Controlled Diffusion Airfoils for Multistage Compressor Application," *J. Eng. Gas Turbines Power*, vol. 106, no. 2, p. 271, Apr. 1984.

[46] U. Köller, R. Mönig, B. Küsters, and H.-A. Schreiber, "Development of Advanced Compressor Airfoils for Heavy-Duty Gas Turbines— Part I: Design and Optimization," *J. Turbomach.*, vol. 122, no. 3, p. 397, Jul. 2000.

[47] F. Sieverding, B. Ribi, M. Casey, and M. Meyer, "Design of Industrial Axial Compressor Blade Sections for Optimal Range and Performance," *J. Turbomach.*, vol. 126, no. 2, p. 323, Apr. 2004.

[48] J. D. Denton and L. Xu, "The exploitation of three-dimensional flow in turbomachinery design," *Proc. Inst. Mech. Eng. Part C J. Mech. Eng. Sci.*, vol. 213, no. 2, pp. 125–137, Feb. 1998.

[49] L. S. Langston, "Secondary flows in axial turbines--a review," *Ann. N. Y. Acad. Sci.*, vol. 934, no. 1, pp. 11–26, Jan. 2006.

[50] S. A. Sjolander, "Overview of tip-clearance effects in axial turbines," in *Secondary and tip-clearance flows in axial turbines*, C. H. Sieverding, Ed. von Karman Institute for Fluid Dynamics, 1997.

[51] F. J. G. Heyes and H. P. Hodson, "Measurement and Prediction of Tip Clearance Flow in Linear Turbine Cascades," *J. Turbomach.*, vol. 115, no. 3, p. 376, Jul. 1993.

[52] M. I. Yaras and S. A. Sjolander, "Losses in the tip-leakage flow of a planar cascade of turbine blades," *AGARD, Second. Flows Turbomachines 13 p(SEE N 90-21009 14-07)*, 1990.

[53] M. Sell, M. Treiber, C. Casciaro, and G. Gyarmathy, "Tip-clearance-affected flow fields in a turbine blade row," *Proc. Inst. Mech. Eng. Part A J. Power Energy*, vol. 213, no. 4, pp. 309–318, 1999.

[54] J. Tallman and B. Lakshminarayana, "Numerical Simulation of Tip Leakage Flows in Axial Flow Turbines, With Emphasis on Flow Physics: Part I---Effect of Tip Clearance Height," *J. Turbomach.*, vol. 123, no. 2, pp. 314–323, Apr. 2001.

[55] J. Tallman and B. Lakshminarayana, "Numerical Simulation of Tip Leakage Flows in Axial Flow Turbines, With Emphasis on Flow Physics: Part II—Effect of Outer Casing Relative Motion," *J. Turbomach.*, vol. 123, no. April, p. 324, Apr. 2001.

[56] A. A. McCarter, X. Xiao, and B. Lakshminarayana, "Tip Clearance Effects in a Turbine Rotor: Part II—Velocity Field and Flow Physics," *J. Turbomach.*, vol. 123, no. 2, pp. 305–313, Apr. 2001.

[57] X. Xiao, A. a. McCarter, and B. Lakshminarayana, "Tip Clearance Effects in a Turbine Rotor: Part I—Pressure Field and Loss," *J. Turbomach.*, vol. 123, no. 2, p. 296, Apr. 2001.

[58] S. Yoon, E. Curtis, J. Denton, and J. Longley, "The Effect of Clearance on Shrouded and Unshrouded Turbines at Two Levels of Reaction," *J. Turbomach.*, vol. 136, no. 2, pp. 1231–1241, 2013.

[59] D. Lengani, B. Paradiso, A. Marn, and E. Göttlich, "Identification of Spinning Mode in the Unsteady Flow Field of a Low Pressure Turbine," *J. Turbomach.*, vol. 134, no. 5, p. 051032, Sep. 2012.

[60] J. M. Tyler and T. G. Sofrin, "Axial Flow Compressor Noise," *SAE Trans.*, vol. 70, pp. 309––332, 1962.

[61] N. Arndt, "Blade Row Interaction in a Multistage Low-Pressure Turbine," *ASME J. Turbomach.*, vol. 115, no. 1, pp. 137–146, Jan. 1993.

[62] A. Binder, W. Förster, H. Kruse, H. Rogge, W. Förster, H. Kruse, and H. Rogge, "An Experimental Investigation Into the Effect of Wakes on the Unsteady Turbine Rotor Flow," *J. Eng. Gas Turbines Power*, vol. 107, no. 2, p. 458, Apr. 1985.

[63] M. Tiedemann and F. Kost, "Some aspects of wake-wake interactions regarding turbine stator clocking," *J. Turbomach.*, vol. 123, no. 3, pp. 526–533, 2001.

[64] D. L. Lansing and W. E. Zorumski, "Effects of wall admittance changes on duct transmission and radiation of sound," *J. Sound Vib.*, vol. 27, no. 1, pp. 85–100, Mar. 1973.

[65] J. F. Unruh, "Finite length tuning for low frequency lining design," *J. Sound Vib.*, vol. 45, no. 1, pp. 5–14, Mar. 1976.

[66] M. J. Benzakein and E. . Smith, "Turbine noise generation and suppression," in *ASME Annual Winter Meeting*, 1973, p. ASME PAPER 73–WA/GT–7.

[67] W. J. G. Bräunling, *Flugzeugtriebwerke*. Springer, 2009.

[68] D. L. Sutliff, "Rotating rake turbofan duct mode measurement system," *J. Acoust. Soc. Am.*, vol. 118, no. 3, p. 1864, 2005.

[69] M. J. T. Smith, "Quietening a Quiet Engine-The RB211 Demonstrator Programme," Feb. 1976.

[70] S. W. Rienstra and A. Hirschberg, "An Introduction to Acoustics," 2013.

[71] M. Möser, *Technische Akustik*. Springer, 2009.

[72] R. Lerch, G. Sessler, and D. Wolf, *Technische Akustik: Grundlagen und Anwendungen*. Springer, 2009.

[73] H. . Pirker, H. Jericha, and G. Zhuber-Okrog, "Auslegung und Betriebsverhalten einer Verdichteranlage für die Luftversorgung wissenschaftlicher Versuchseinrichtungen," *VDI Berichte*, vol. 1208, pp. 331–347.

[74] M. Moser, "Untersuchung der Niederdruckturbinenlärmemissionen von Flugtriebwerken in einem neuen Turbinenakustikprüfstand," Graz University Of Technology, 2008.

[75] M. Moser, G. Kahl, G. Kulhanek, and F. Heitmeir, "Construction of a Subsonic Test Turbine Facility for Experimental Investigations of Sound Generation and Propagation for Low Pressure Turbines," in *ISABE conference Beijing, Paper No. ISABE-2007-1366*, 2007.

[76] D. Broszat, T. Selic, and A. Marn, "Verification of the Inverse Cut-off Effect in a Turbomachinery Stage - Part 1 - Numerical results," in *18th AIAA/CEAS Aeroacoustics Conference (33rd AIAA Aeroacoustics Conference)*, American Institute of Aeronautics and Astronautics, 2012.

[77] I. A. Johnsen and R. O. Bullock, "Aerodynamic Design of Axial-Flow Compressors. NASA SP-36," *NASA Spec. Publ.*, vol. 36, 1965.

[78] T. Arnold, "Kalibrierbericht 5-Loch Sonde," 2008.

[79] L. Enghardt, U. Tapken, W. Neise, F. Kennepohl, and K. Heinig, "Turbine Blade/Vane Interaction Noise: Acoustic Mode Analysis Using In-Duct Sensor Rakes," in *Proceedings of the Seventh AIAA/CEAS-Aeroacoustics Conference, Maastricht, The Netherlands, 28–-30 May, Paper No. 2001-2153*, 2001.

[80] N. Instruments, "NI PXI-4498 - National Instruments." [Online]. Available: http://sine.ni.com/nips/cds/view/p/lang/en/nid/203802. [Accessed: 07-May-2015].

[81] Mathworks, "Matlab Documentation. [Online]." [Online]. Available: http://de.mathworks.com/help/matlab/ref/fft.html. [Accessed: 06-May-2015].

[82] A. Hussain and W. Reynolds, "The Mechanics of an Organized Wave in Turbulent Shear Flow," *J. Fluid Mech.*, vol. 41, pp. 241–258, 1970.

[83] L. Munjal, *Acoustics of Ducts and Mufflers*. Wiley, 2014.

[84] P. Sijtsma and J. Zillmann, "In-Duct and Far-Field Mode Detection Techniques," in *13th AIAA/CEAS Aeroacoustics Conference (28th AIAA Aeroacoustics Conference)*, American Institute of Aeronautics and Astronautics, 2007.

[85] U. Tapken and L. Enghardt, "Optimisation of Sensor Arrays for Radial Mode Analysis in Flow Ducts," in *12th AIAA/CEAS Aeroacoustics Conference (27th AIAA Aeroacoustics Conference)*, American Institute of Aeronautics and Astronautics, 2006.

[86] C. C. Paige and M. A. Saunders, "LSQR: An algorithm for sparse linear equations and sparse least squares," *ACM Trans. Math. Softw.*, vol. 8, no. 1, pp. 43–71, 1982.

[87] C. L. Morfey, "Sound transmission and generation in ducts with flow," *J. Sound Vib.*, vol. 14, no. 1, pp. 37–55, 1971.

[88] C. H. Sieverding, "Recent Progress in the Understanding of Basic Aspects of Secondary Flows in Turbine Blade Passages," *J. Eng. Gas Turbines Power*, vol. 107, no. 2, pp. 248–257, 1985.

[89] G. Pullan, J. Denton, and M. Dunkley, "An Experimental and Computational Study of the Formation of a Streamwise Shed Vortex in a Turbine Stage," *ASME Conf. Proc.*, vol. 2002, no. 3610X, pp. 71–79, 2002.

[90] R. J. Astley, R. Sugimoto, G. Gabard, E. Norde, E. J. Grift, and M. Bocquier, "The Effect of Steady Flow Distortion on Mode Propagation in a Turbofan Intake," in *20th AIAA/CEAS Aeroacoustics Conference*, American Institute of Aeronautics and Astronautics, 2014.

[91] "Pratt and Whitney PW1100G Geared Turbofan Engine." [Online]. Available: http://theflyingengineer.com/flightdeck/pw1100g-gtf/. [Accessed: 26-May-2015].

[92] "valiDation of Radical Engine Architecture systeMs." [Online]. Available: http://ec.europa.eu/research/transport/projects/items/dream_en.htm. [Accessed: 17-Feb-2015].

[93] H. Batard, "Development of the quiet aircraft - Industrial needs in terms of aircraft noise and main achievements in Europe Industrial context 2 . 1 Aircraft acoustic regulations Aircraft low noise design," *Measurement*.

[94] M. Möser, *Technische Akustik*. Springer, 2009.

10 List of figures

11 List of tables

12 Annex

12.1 The Influence of the tip leakage vortex

The following section explains the influence of the tip leakage flow onto the downstream vane flow field.

12.1.1 Approach

Due to the change in inlet flow angle the flow field within the downstream guide vane is altered. Figure 12-1 shows the surface shear stress with superimposed surface streamlines for the suction and pressure side of the blade for three different gap configurations: 1.5%, 0.6% and zero gap.

On the suction side, the flow near the hub of the blade shows no significant change, whereas near the tip the influence of the leakage flow is clearly notable.

The most noticeable feature is the migration of fluid from the tip towards midspan as shown by the direction of the streamlines near the trailing edge on the suction side of the vane (marked A). When comparing the different clearances this feature becomes less prominent with decreasing tip clearance and only a minor migration can be seen in Figure 12-1 which is mainly due to the pressure gradient resulting from the radial equilibrium in a swirling flow as well as conventional secondary flow. This means that the influence of the negative vorticity created by the tip leakage flow causes additional migration from the tip towards the hub.

On the pressure side the increase in clearance leads to a flow separation near the tip for the reference clearance case (marked S). This is due to the migration of the leakage flow and thus the position of the maximum of the yaw angle further away from the shroud leading to increased wrong incidence on the vane. In addition the migration of fluid from hub to tip is increased when the rotor

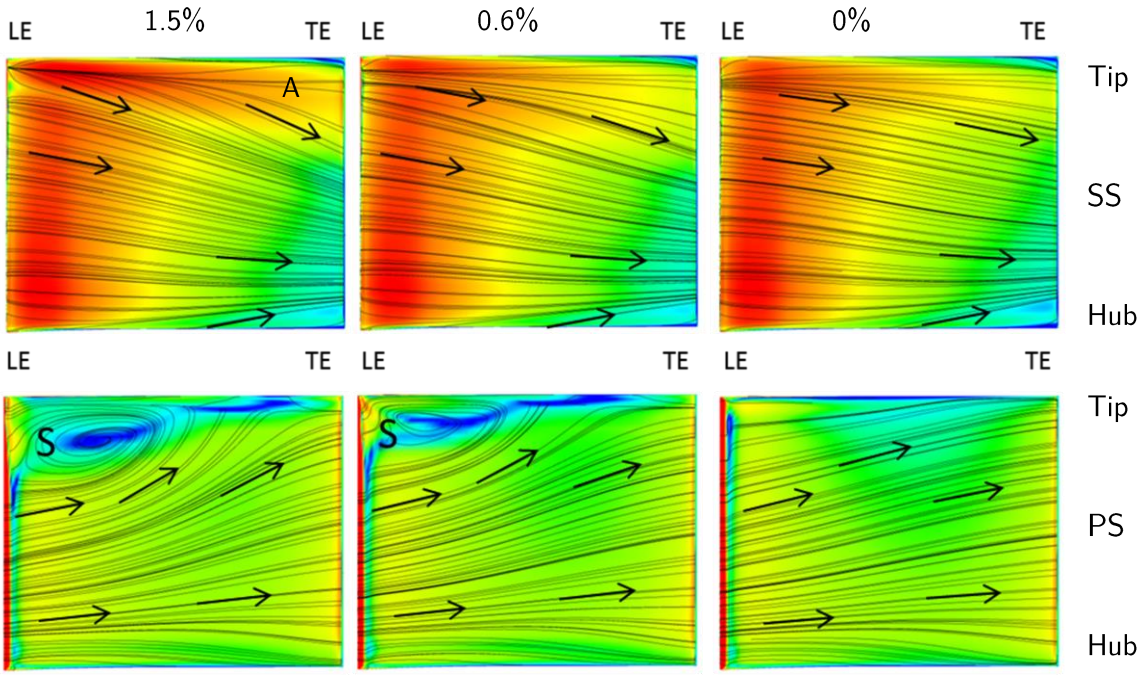

Figure 12-1: Shear stress for the pressure (top) and suction side (bottom) for different tip clearances with surface streamlines

tip clearance is increased. While the oil flow visualisation on the pressure side of the vane in Figure 5-88 shows no clear sign of this separation (when compared to other EGVs) but a change in the consistency of the oil flow visualisation.

Looking at the sear stress distribution, the pressure side shows a change in behaviour at the casing of the vane close to the leading edge. A strong increase in shear stress can be identified at a position where the rotor tip leakage vortex influences the flow field of the vane. In addition a separation line can be identified close to the casing where a corner vortex is forming.

12.1.1 Vane exit flow field

The following section deals with the evolution of the flow by axial cuts through the EGV domain by means of streamwise vorticity. Figure 12-2 shows 4 axial cuts through the computational domain for the 1.5% and zero gap height cases in order to show the differences occurring between those two cases. Red marks a region of positive, blue negative vorticity.

The first two cuts show the streamwise vorticity at 60% axial length the hub for both clearances. The region close to the hub is dominated by a region of positive vorticity due to the hub secondary flows and the boundary layer causing a movement of fluid against rotational direction of the rotor.

At approximately 70-80% span a region of negative vorticity can be identified that stretches from the pressure towards the suction side of the vane that is due to the secondary flows in this region (marked A=. An identical, positive vorticity structure can be seen at 20% span (marked B). At the intersection of the suction side and the casing a small corner vortex with a counter rotation vorticity has formed. Close to the casing a region of negative vorticity due to the boundary layer has formed.

The influence of the rotor tip leakage vortex can easily be identified when looking at the bottom left picture of Figure 12-2. The region of negative vorticity between 70 and 80% span has significantly increased in strength due to the tip leakage vortex that is rotation in rotational direction of the rotor causing a negative vorticity. The influence of the tip leakage vortex, as seen in Figure 12-1, has resulted in a separation on the pressure side of the vane causing a migration of fluid towards the casing downstream of said separation. This causes a region of negative vorticity on the pressure side

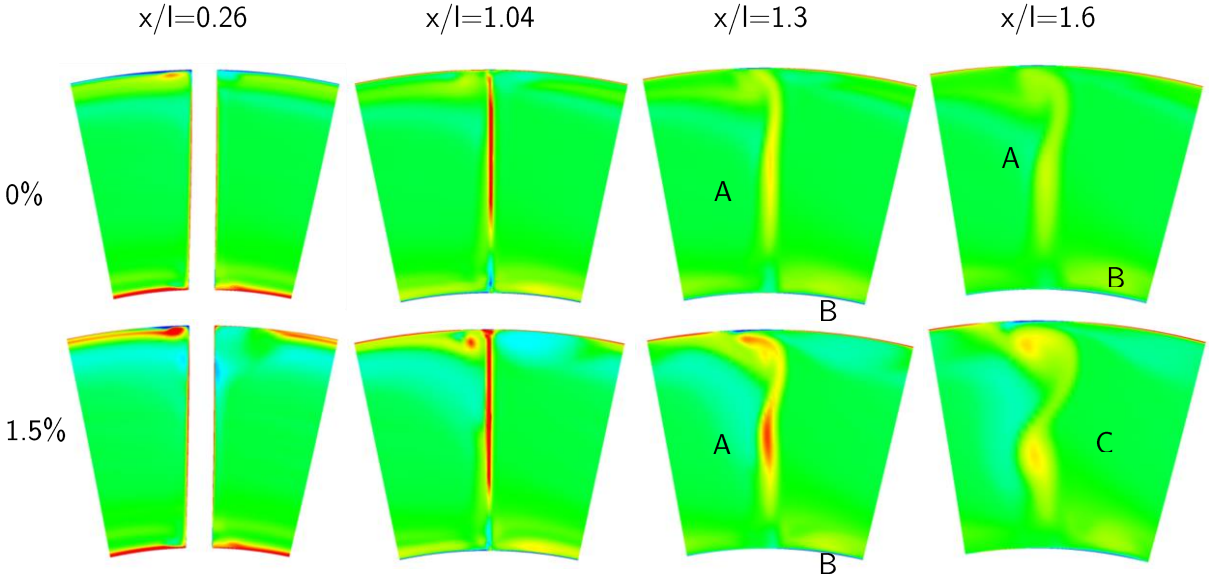

Figure 12-2: Streamwise vorticity for axial cuts of the EGV for zero (top) and 1% (bottom) tip clearance

of the vane. The region of positive vorticity at the intersection between the suction side and the casing has also significantly increased in strength due to the counter-rotation of the tip leakage vortex.

The second axial position shows a cut 4mm downstream of the trailing edge of the EGV. Behind the trailing edge the positive trailing edge vorticity forms a straight line from 20% span upwards, whereas the region below 20% is dominated by a negative vorticity. This is due to the change in radial velocity components on SS and PS caused by the hub secondary vortex. Near the outer casing the SS vortex has started to merge with the trailing edge shed vorticity changing its relative position from the SS towards the PS. The region of negative vorticity associated with the tip leakage vortex has started to migrate towards midspan as seen for the 1.5% leakage case.

In the third picture of Figure 12-2 the leakage flow vorticity has been further bent and extends until 55% span on the suction side of the wake. The positive vorticity of the wake region has split into two distinct regions of high vorticity; one is located at approximately midspan and pairs with the negative vorticity due to the tip leakage flow, whereas the structure close to the casing merges with the corner vortex.

Further downstream, shown in the rightmost picture of Figure 12-2 the leakage vorticity continues to be bowed and continuously gets weaker. The trace of the trailing edge vorticity above midspan (marked C) gets bowed and pushed in clockwise direction for both cases due to the interaction of the casing vortex with the trailing edge vorticity. Near midspan the trailing edge vorticity starts to concentrate leading to a local rolling up of the flow for the leakage case, but not for the zero-tip gap flow field. At approximately 70% span the local shear vorticity gets weakened due to the interaction with the leakage flow leading to two separate vortices at the outer casing and at midspan. In terms of maximum local vorticity the vortex at midspan is significantly stronger than the outer casing vortex.

One can see that the existence of the leakage flow has an important part in the formation of the structures downstream of the EGV. The leakage flow causes an increase in trailing edge shed vorticity due to the increase in hub-wards fluid motion on the vane-SS. This has also consequences on the formation of a shed vortex as shown by Pullan et al. [89]. They showed that a shear layer with discontinuous radial velocity components can cause a rollup of the layer depending on the actual radial as well as circumferential velocity components. The presence of the leakage causes an increase in radial discontinuity as well as a change in yaw angle. While the general flow features at the trailing edge inhibits the rolling up of the vortex as can be seen for the zero-tip gap case, the addition of the vortex flow causes the rolling up of the flow into a streamwise shed vortex as explained by Pullan et al.[89]. The reduced strength of this vortex compared to the vortex shown in [89] is due to the fact that the discontinuities are significantly smaller than used by [89].

The resulting vane exit flow-field for different rotor tip clearances can be seen in Figure 12-3. The figure shows the total pressure as well as the EGV exit yaw angle. When looking at the total pressure in the top of Figure 12-3, the effect of the leakage flow is an increased width of the wake on the suction side. Furthermore, the strength of the vortex B is significantly altered as well as the S-shape of the wake.

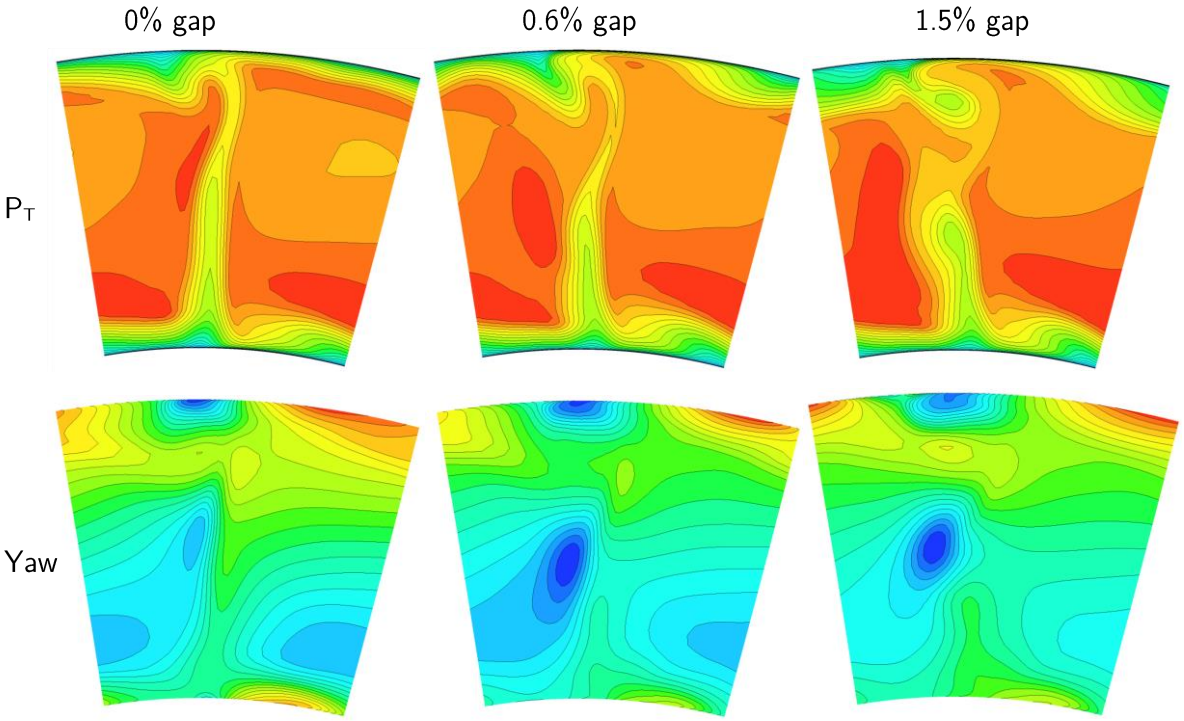

Figure 12-3: Total pressure and yaw angle in plane 3 for different tip gap

This shape is originally a result of the rolling up of the streamwise vorticity shed by the trailing edge (similar to Pullan et al. [89]). This vortex formation is highly influenced by the flow features generated by the EGV. According to the results in [89] the general flow features found in the case without leakage should inhibit rolling into a vortex. This is the case, because the vorticity contribution from yaw and pitch compensate each other and delay the formation. Yet, the addition of the flow features from the rotor tip leakage flow result in a flow field that shows an increased vortex formation. The bottom of Figure 12-3 shows the yaw angle distribution for the flow without tip leakage in the rightmost picture. Again, the flow is dominated by a large vortex in the centre of the passage.

The structure is rotating in clockwise direction, co-rotating with the upstream rotor, which can be observed by the positive yaw angle near the outer casing and the negative near the hub. A hub secondary vortex marked HSV can be identified in the region of positive yaw angle near the hub. Near the tip a region of negative yaw angle marked B shows fluid migrating from the pressure to the suction side.

The pressure gradient from pressure to suction side promotes the formation of a vortex in this region rotating in clockwise direction. The core of this vortex consists of suction side fluid with pressure side fluid wrapping around this core. This vortex is completely removed when the tip clearance is set to zero. This is because the vortex is due to the difference in pitch angle on pressure and suction surface that is dependent on the hub-wards motion of the fluid.

As has been already seen in the previous section, the addition of an inlet vorticity coming from the rotor plays an important role for the formation of the trailing edge vorticity. Figure 12-4 shows the circumferentially averaged values for total pressure and yaw angle for the outlet of the EGV for the two different radial rotor clearances. The figure to the left shows the EGV total pressure. Close to

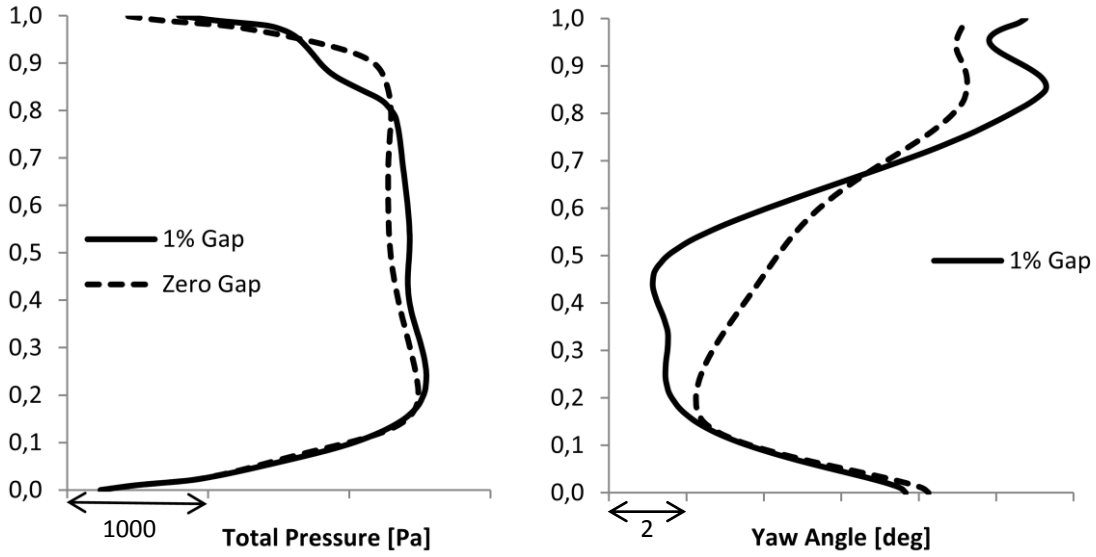

Figure 12-4: Averaged total pressure (left) and yaw angle (right) for the EGV exit plane D from CFD calculations for zero gap and nominal 1% gap, operating point approach

the casing, where the influence of the tip leakage flow is strongest a strong reduction in total pressure can be identified at a region between 80% and 95% span. This is caused by the tip leakage fluid being pushed from the casing towards midspan causing this reduction in total pressure. In contrast, the high total pressure fluid from the leakage flow causes an increase in a region between 20% and 80% span with a maximum difference at 55% span of the vane.

The yaw angle shows that the tip leakage, due to the lack of turning from the rotor, shows an increase in yaw angle close to the casing as expected from the leakage flow. At approximately 95% span a small local minimum can be identified that is due to the vortex forming downstream of the trailing edge close to the casing where the trailing edge shed vorticity interacts with the corner vortex forming on the suction side of the vane.

Between 20% and 60% span the averaged yaw angle of the vane decreases. This is due to the formation of a vortex caused by the interaction of the shed vorticity and the fluid migrating from the tip leakage region towards midspan. This feature is also seen in Figure 12-3 where the bottom right pictures show a region of large negative yaw angle located at approximately this location (marked A). Close to the hub the influence of the leakage flow is negligible.

12.2 ADP

The influence of the tip leakage flow for the operating point ADP is largely identical to what was seen for the operating condition Approach in the previous section.

The two main differences are as follows:

- The separation on the pressure side of the vane that was seen in Figure 12-1 is not present anymore due to the overall change in the yaw angle of the inlet flow.
- There is a much stronger effect of the hub secondary flows resulting in an increase in migration from the hub towards the suction side of the vane. This effect can be seen in Figure 12-5 where this effect is marked with an "A". The effect of the rotor tip leakage flow close to the casing is identical.

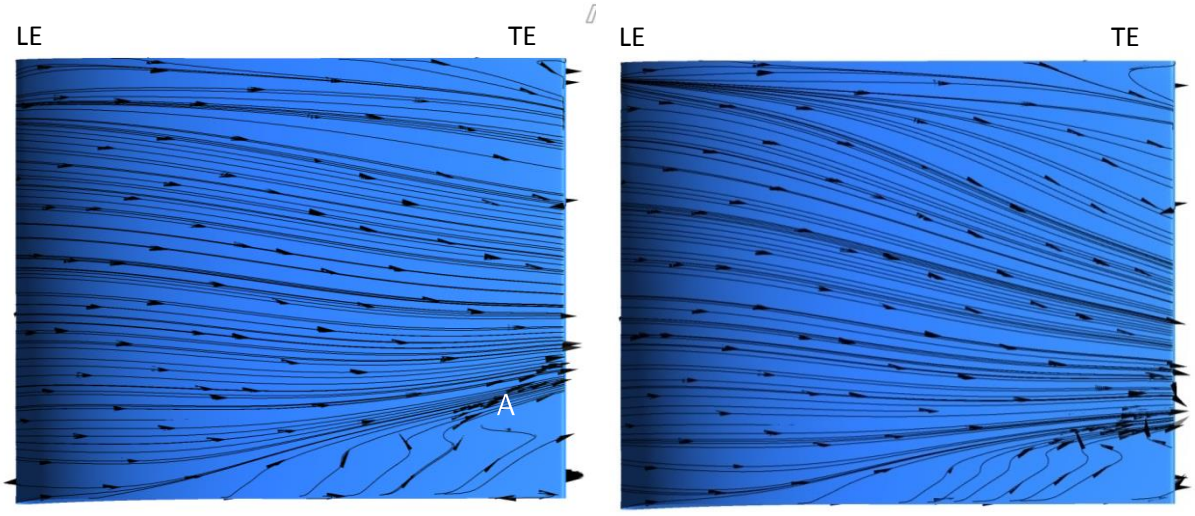

Figure 12-5: Surface Streamlines on the suction side of the EGV; zero gap (left) and nominal gap (right)

12.2 Flow field during start-up

The following section shows the effects in the exit casing (EGV and endwalls) during the short start-up of the facility.

The operating conditions were recorded for the start-up procedure and a typical operating point was selected and put into ANSYS CFX in order to calculate the effects during the start-up procedure. The operating conditions used for the following calculations can be seen in Table 12-1.

Table 12-1: Operating conditions for the start-up simulations

Rotational speed	600 rpm
Inlet Total Pressure	1.03 bar
Inlet Total Temperature	370 K

12.2.1 Datum EGV

The following section shows the flow field at start-up for the "Datum" EGV. Figure 12-6 shows an isometric view of the suction side and the hub of the vane. There is a separation line visible at the suction side of the vane extending from the leading edge at 80% span towards the hub at 30% axial chord. Downstream of this point a region of reverse flow can be seen that extends from the trailing edge to said separation line. This can be better seen in Figure 12-7 where the suction side of the vane is depicted. The results of the start-up CFD calculations as well as the oil flow visualisation can be seen. During the start-up procedure most of the suction side is separated causing a large region of reverse flow with an attractor located at 70% axial chord at approximately 15% span. These structures are only partially visible in the oil flow visualisation of the proper operating point. There is a structure visible in the oil flow that has a different inclination than the separation line seen in the CFD. Other flow features from the start-up are not visible in the suction side oil flow. The flow on the hub of the passage is seen in Figure 12-8. The effect of this reverse flow can be seen by the separation line located close to the suction side at approximately 10% of the channel height. A saddle point can be identified at 35% axial chord of the EGV. None of these structures can be identified in the oil flow visualisation on the hub of the vane.

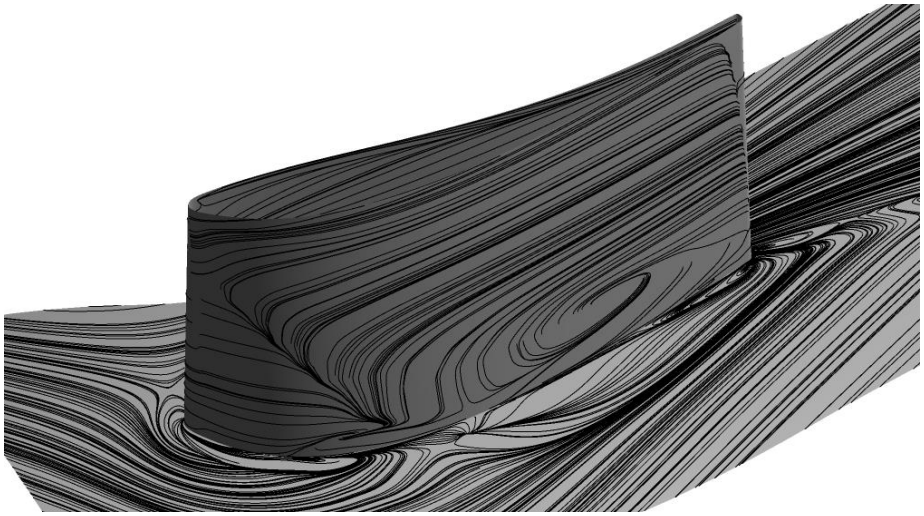

Figure 12-6: Start-up CFD calculation "Datum" EGV, isometric view

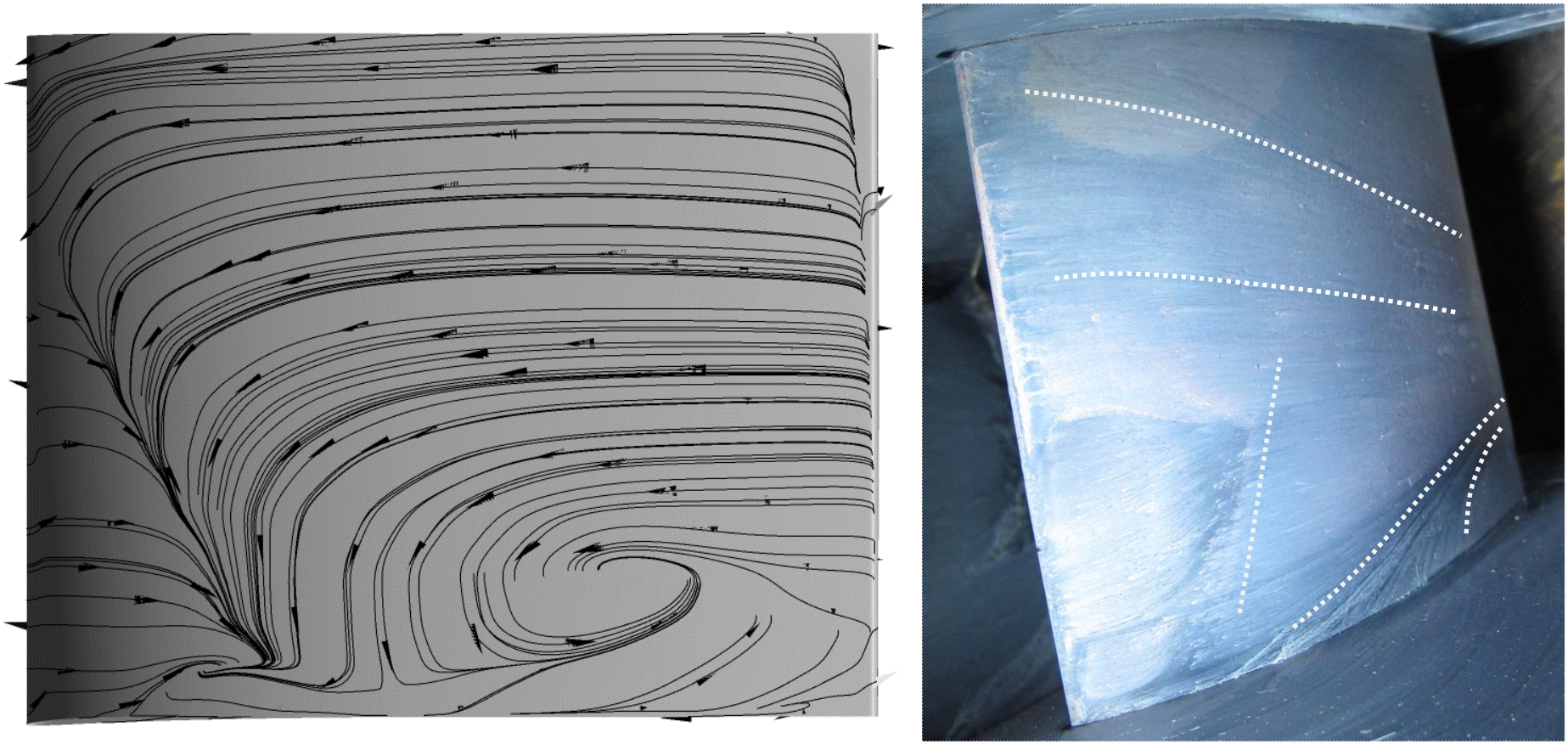

Figure 12-7: Start-up CFD calculation “Datum” EGV, suction side

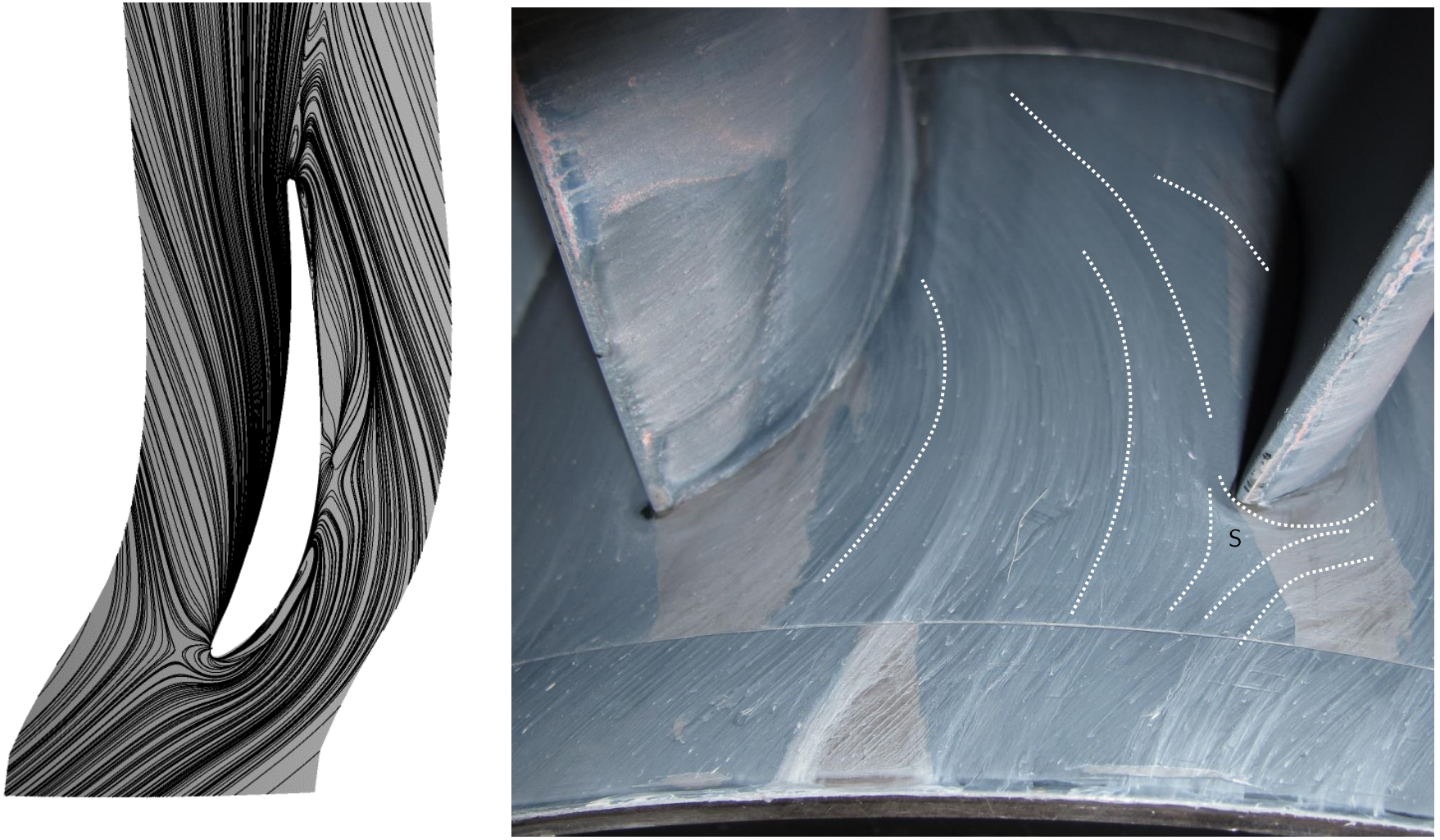

Figure 12-8: Start-up CFD calculation “Datum” EGV, hub

12.2.2 Leaned EGV

The flow field of the EGV during the start-up procedure can be seen in the Figure 12-9 and Figure 12-10

Figure 12-9 shows the flow visualisation for the start-up from CFD on the left, and the oil flow visualisation on the right. The CFD shows a large recirculation zone across approximately 70% of the passage. The recirculation zone starts at approximately 5-10% axial chord of the vane and stretches to a point approximately 20% axial chord downstream of the trailing edge. This recirculation zone extends from the hub along the suction side of the vane until approximately 80% span where the streamlines merge around a single attractor point.

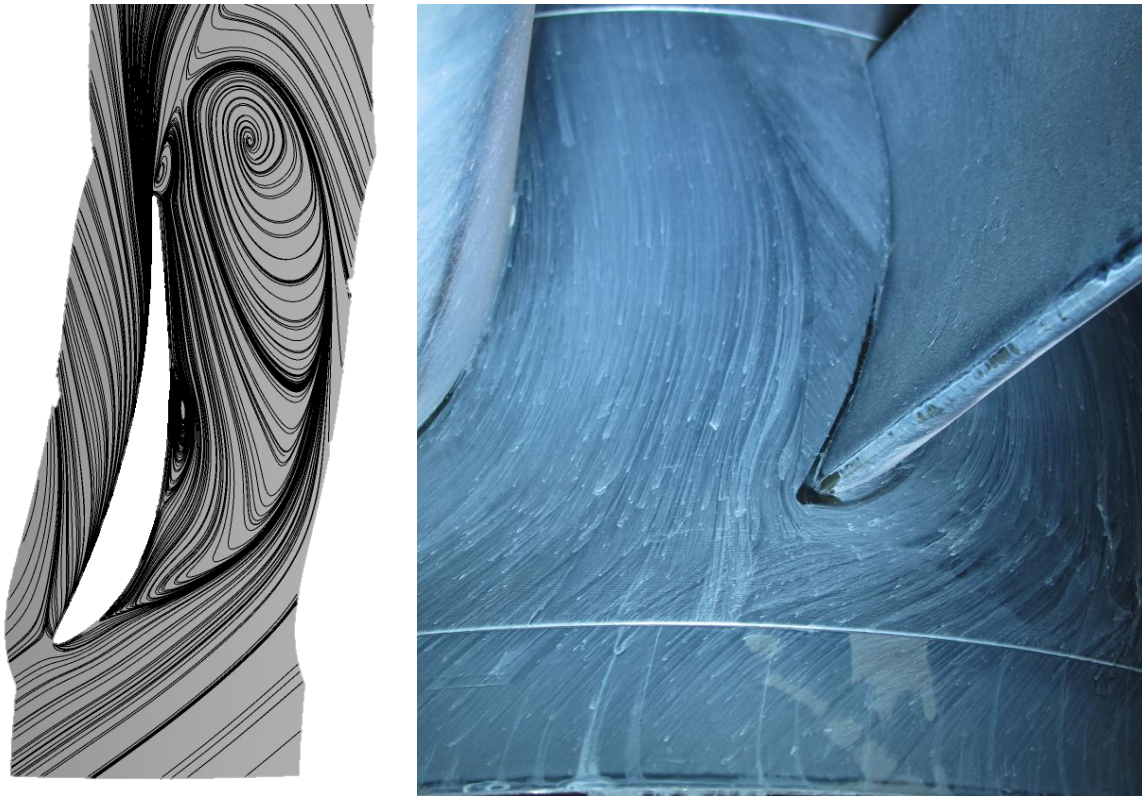

Figure 12-9: Start-up CFD calculation "Leaned" EGV, hub

This can be seen in Figure 12-10, where the suction side is show. This flow feature can also be seen in the oil flow visualisation as a radial line starting at 5-10% axial chord and stretching until approximately 50% span. At this height the shear stresses of the flow, strongly influenced by the tip leakage, is strong enough to later-on mask the effects of start-up of the rig. This explains the structure that can later on be found in the oil flow visualisation .

A second structure can be found within this separation zone that can be identified at approximately mid-chord of the vane.

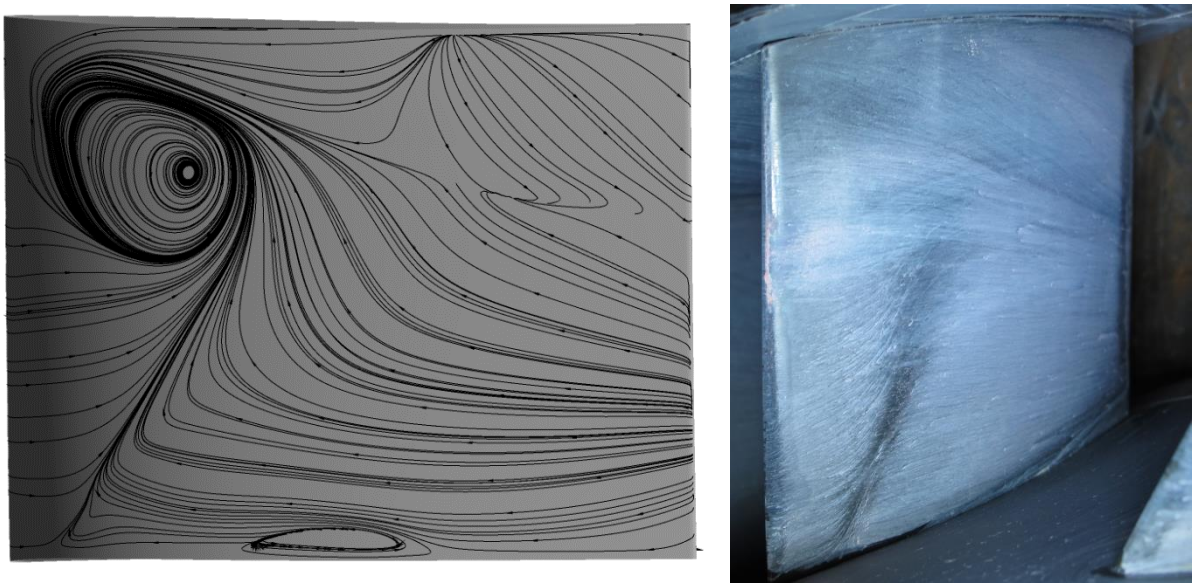

Figure 12-10: Start-up CFD calculation "Leaned" EGV, suction side

12.2.3 Inverse Cutoff EGV

The comparison of CFD and the oil flow visualisation for the hub of the "Inverse Cut-off" EGV can be seen in Figure 12-11. The hub shows a recirculation zone on the suction side of the vane that extends to approximately one third of the passage of the vane. Downstream of the trailing edge another vortex can be identified. None of these structures can be seen in the oil flow visualisation, meaning the shear stresses during the operation at the operating point is sufficiently large enough to be seen in the oil flow visualisation after shutting down the testrig, removing any traces of the startup that might exist on the vane surface.

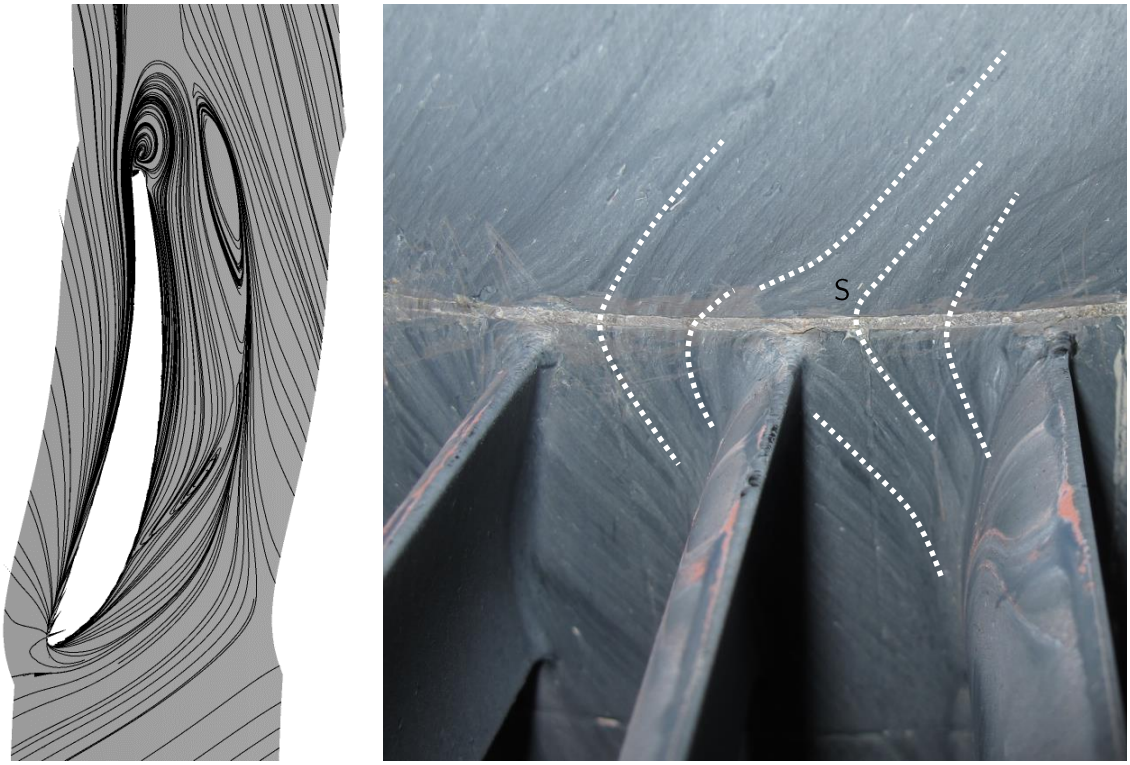

Figure 12-11: Start-up CFD calculation "Inverse Cut-off" EGV, hub

A comparison of the suction side of the vane can be seen in Figure 12-12 where the start-up calculation from CFD and the oil flow visualisation is depicted. The CFD calculations shows a reversed flow between 5% span and approximately 30% span of the vane. This reverse flow exists from a separation line at approximately 5-10% axial chord of the vane until the trailing edge. At approximately 40% span and 60% axial chord an attractor and a saddle point can be seen in the CFD results of the surface streamlines. The flow coming from the leading edge is pushed towards the outer casing at this separation line. Another reverse flow region can be identified close to the casing between 80% span and the casing.

The remainder of the reverse flow structure existing close to the hub can be identified in the oil flow visualisation of the EGV. These lines shown in green depict the remainders of these flow structures existing at the start up of the test rig. Again, it can be seen that the shear stresses caused by the flow close to the hub along the suction side of the vane are not strong enough to superimpose the stream lines of the operating point onto the oil flow visualisation.

The pressure side of the vane shows no significant structures.

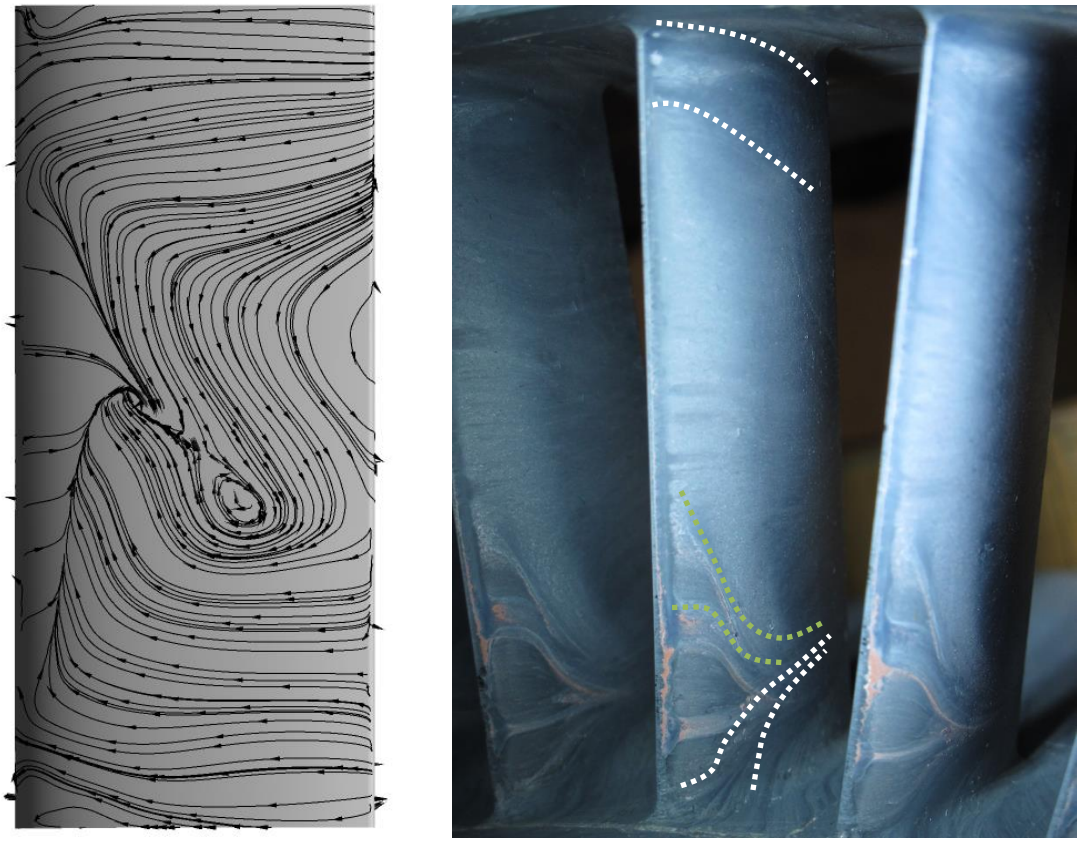

Figure 12-12: Start-up CFD calculation "Inverse Cut-off" EGV, suction side

12.2.4 High loading EGV

The flow feature during the start-up procedure on the hub of the "High Loading" EGV can be seen in Figure 12-13 where the hub is depicted on the left and an isometric view of the surface stream lines is shown on the right. A reverse flow region can be identified between the leading edge of the vane and approximately 40% axial chord close to the suction side of the vane. At this particular operating condition a complex flow pattern is forming as can be seen in the right of Figure 12-13 where the isometric view is seen. There exist multiple reverse flow patterns along the suction side and the hub. The pressure side shows no significant flow features. As seen in the oil flow visualisations for the hub (Figure 5-61 and Figure 5-141) none of this features is visible in the oil flow visualisation.

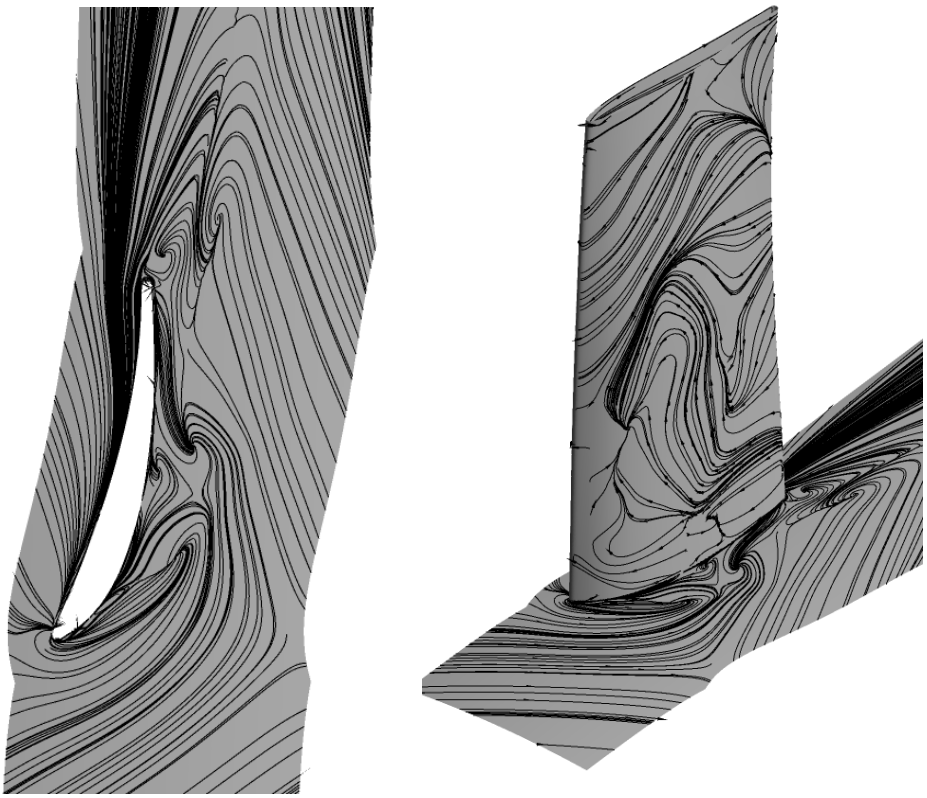

Figure 12-13: Start-up CFD calculation "Highly Loaded" EGV, hub (left) and isometric view (right)

The start-up CFD results can be seen in Figure 12-14. Again the already mentioned complex flow features can be seen on the suction side of the vane. A complex pattern of reverse flow features can be identified for these operating conditions. None of these patterns can be seen in the oil flow visualisation in Figure 5-63 and Figure 5-143

Figure 12-14: Start-up CFD calculation “Highly Loaded” EGV, suction side